



A University of Sussex PhD thesis

Available online via Sussex Research Online:

<http://sro.sussex.ac.uk/>

This thesis is protected by copyright which belongs to the author.

This thesis cannot be reproduced or quoted extensively from without first obtaining permission in writing from the Author

The content must not be changed in any way or sold commercially in any format or medium without the formal permission of the Author

When referring to this work, full bibliographic details including the author, title, awarding institution and date of the thesis must be given

Please visit Sussex Research Online for more information and further details



A Numerical Analysis of a Corrugated Channel Flow by Large Eddy Simulation

Yeru Shang

Submitted for the degree of Doctor of Philosophy

University of Sussex

15th December 2019

Declaration

I hereby declare that I am responsible for the work submitted in this thesis, the original work is my own, and this thesis has not been and will not be submitted in whole or in part to another University for the award of any other degree.

Signature:

Yeru Shang

UNIVERSITY OF SUSSEX

YERU SHANG

DOCTOR OF PHILOSOPHY

A NUMERICAL ANALYSIS OF A CORRUGATED CHANNEL FLOW

BY LARGE EDDY SIMULATION

This thesis presents a detailed numerical analysis of flow through a corrugated channel. The geometry has a rectangular cross section. The bottom wall is corrugated with periodic cavities which is a two-dimensional representation of a commercial stainless steel flexible pipe, and the top and two side walls are flat plates. The Reynolds number based on bulk flow velocity and the hydraulic diameter of the channel is 5300. The principal objective is to understand the flow field in this corrugated channel, which benefits the future design of engineering equipment with corrugated wall. Several Sub-grid Scale (SGS) models are first validated on plane channel flows with different grid densities. Then a Large Eddy Simulation (LES) is performed on the corrugated channel with 128 corrugations and the synthetic turbulence inlet. Flow features of different zones in the channel are analysed in detail, focusing on the time-averaged results, development of the boundary layer, and mechanism of transition. The principal message emerging from this analysis is that the flow in the corrugated channel is more complicated than suggested previously by the experimental study and the two side walls have profound effect on the flow behaviour. The discrepancies between LES predictions and experimental data are also discussed. After a detailed examination, a number of problems and open questions are raised concerning the experimental results and setups. Meanwhile, the LES results are validated from various aspects. In addition, a study of this corrugated channel with 16 corrugations and a periodic boundary condition is also conducted, with the focus on hydrodynamic interaction and vortex evolution. It shows that the case for 16 corrugations with the periodic boundary condition can reproduce the flow characteristics of the fully turbulent region predicted in the case of 128 corrugations. The features of vortex evolution shown in the experiment are reproduced and understood by current LES.

Acknowledgements

I wish to express my appreciation to my supervisor, Dr Esra Sorguven, for everything she has done during the course of my PhD. Her guidance and advice were essential for the completion of the present work.

I want to show my gratitude to Prof. Martin Rose for the great amount he taught me and showing me the beauty of fluid dynamics. I would like to thank Prof. Zhiyin Yang for guiding me to my research field and putting my research on track. I want to give thanks to Prof. Chris Chatwin for his support during the hardest time in my PhD. I am also very thankful to Prof. Jun Peng, for leading me to the path of PhD.

I extend my thanks to my colleagues in the Thermo-Fluid Mechanics Research Centre, especially to Thomas Irps, Huajun Li, Danial Payne, Harri Koivisto and Adam Kosco for their great companionship and support. I would also like to show my gratitude to Prof. Håkan Nilsson in the Chalmers University of Technology, Sweden for his amazing course on OpenFOAM. I also thank Hao Li, Prof. Guoyan Yang and Jianshan Zhou for their help on C++. Thanks also to Marcus Cartwright who kindly offered to proofread my thesis. I also want to acknowledge the computing support from the UK's National Supercomputing Service ARCHER which greatly speed up my research progress.

I am greatly indebted to my mother, Dr Ling Ren, for many years of patience and unfailing support. To my wife Peiying Sun, I am very grateful for her company and support during my hardest time. Finally, to my late grandmother Shuzhen Geng, and my late father Jianxi Shang: Your aspiration and encouragement make it all possible.

Contents

List of Tables	viii
List of Figures	xii
Nomenclature	xvii
1 Introduction	1
2 Background	4
2.1 Literature Review	4
2.1.1 Square Cavity	5
2.1.2 Wavy Cavity	8
2.1.3 Periodic Hill	9
2.2 Turbulence	13
2.2.1 Fundamentals of Turbulence	13
2.2.2 Approaches to Study Turbulence	21
2.2.3 Simulation of Turbulence	23
2.3 Summary	25
3 Governing Equations and Models	27
3.1 Principle of Large Eddy Simulation (LES)	27
3.2 LES Governing Equations	28
3.2.1 Filtering Function	28
3.2.2 Filtered Navier-Stokes Equations	30
3.3 Sub-grid Scale (SGS) Model	33
3.3.1 Principle of Eddy Viscosity SGS Model	33
3.3.2 Standard Smagorinsky SGS model	34
3.3.3 k -equation SGS Model	35
3.3.4 Reynolds Stresses SGS Model	40

3.3.5	Conventional Hybrid Model	40
3.4	Model Selection	41
4	Numerical Methods	42
4.1	Governing Equations	42
4.2	Discretisation Method	44
4.2.1	Finite Difference Method	44
4.2.2	Finite Element Method	45
4.2.3	Finite Volume Method	45
4.3	Discretisation of Governing Equations	47
4.3.1	Spatial Discretisation	48
4.4	Solver	54
5	Validation of SGS Models	56
5.1	General Case Setup	57
5.2	Results	59
5.2.1	Global Flow Quantities	59
5.2.2	Mean Velocity Profiles	61
5.2.3	Velocity Fluctuations	63
5.3	Conclusion	67
6	Analysis of Corrugated Channel	68
6.1	Experimental Setup	68
6.2	Numerical Methods	70
6.3	Grid Independence Study	74
6.3.1	Effect of Grid Density	74
6.3.2	Effect of Corrugated Channel Length	79
6.4	Flow Features in Corrugated Channel	81
6.4.1	Case Setup for 128 Corrugations	81
6.4.2	Overview of Flow Development	83
6.4.3	128 vs 16 Corrugations in Fully Turbulent Region	90
6.4.4	LES Results Validation	94
6.4.5	Details of Flow Development	109
6.4.6	Hydrodynamic Interaction in Fully Turbulent Region	118

7	Conclusions and Suggestions	123
7.1	General Remarks	124
7.2	Recommendations for Future Work	128
	Bibliography	129
	Appendix	142
A	Conventional Hybrid Model	143
A.1	Detached Eddy Simulation	143
A.2	Wall Modelled Large Eddy Simulation	144
A.3	Embedded/Zonal Large Eddy Simulation	144
B	Pressure Correction Equation for PISO Algorithm	145
C	Channel Flow Result Verification	147
D	Comparison of Computing Speeds	150
D.1	Computational Cost of Various SGS models	150
D.2	Computational Speeds of Various HPC	151
E	Results of Two-point correlation	152
F	Discrepancies of Reynolds Stresses Between Each Corrugation	153

List of Tables

3.1	List of SGS models to be validated.	41
5.1	List of SGS models tested in current channel flow case.	56
5.2	Global flow parameter of the channel flow test case.	58
5.3	The mesh used in the simulation.	58
5.4	Global flow quantities of SGS models compared under Mesh1.	59
5.5	Global flow quantities of SGS models compared under Mesh2.	59
5.6	Global flow quantities of SGS models compared under Mesh3.	60
6.1	Configurations of the flow domain.	69
6.2	The dimensions of the flow domain.	75
6.3	Parameters for random generated turbulent inlet BC.	82
6.4	Different zones for flow development in current corrugated channel.	83
6.5	Difference of BL thicknesses and $\langle u \rangle_{max}$ between LES prediction and PIV measurement.	94
6.6	Other SGS models tested in current corrugated channel.	98
D.1	Time cost on different HPC systems for SMAG	151

List of Figures

1.1	The industrial context of the corrugated geometry.	1
1.2	The schematic representation of different corrugation types.	2
1.3	The corrugated pipe studied in current research.	3
2.1	The schematic representation of two different square cavities.	5
2.2	Surface flow patterns around d -type groove.	6
2.3	Surface flow patterns around k -type groove.	6
2.4	Different types of time-averaging processes.	14
2.5	Typical energy spectrum for a turbulent flow.	17
2.6	Sketch of boundary layer natural transition on a flat plate.	18
2.7	A comparison between a typical prediction of velocity distribution near a solid wall and the Universal Laws of the Wall.	20
2.8	A typical distribution of Reynolds stresses near a solid wall.	20
2.9	Decomposition of the energy spectrum of the solution associated with different computational methods.	24
4.1	Discretisation of the solution domain.	47
4.2	Control Volume for Finite Volume discretisation.	47
4.3	Sketch for evaluation of diffusion flux.	51
4.4	A flow chart of the PIMPLE algorithm.	54
5.1	Schematic representation of a channel flow case.	57
5.2	Mean normalised stream-wise velocity in wall coordinates on different mesh densities.	62
5.3	Stream-wise turbulence intensities by wall coordinates on different mesh densities.	64
5.4	Wall normal direction turbulence intensities by wall coordinates on different mesh densities.	65

5.5	Mean shear stress by wall coordinates on different mesh densities.	66
6.1	Schematic of the experimental setups.	69
6.2	Simulation performed in current research.	70
6.3	The time history profile of velocity at $y/h = 0.82$ on the mid-plane.	72
6.4	The time history profile of $\langle u'u' \rangle$ and $\langle v'v' \rangle$ at C8 predicted by SMAG+VD on 16 corrugation case.	73
6.5	Localised views of Grid 1.	74
6.6	The mesh at corrugation for Grid 2	75
6.7	The contour of μ_{sgs}/μ on $x-y$ plane of $z/b = 0.5$ and $y-z$ plane of $x/\lambda = 0$ predicted by SMAG+VD on Grid 1 and 2.	76
6.8	The contour of $k_r\%$ on $x-y$ plane of $z/b = 0.5$ and $y-z$ plane of $x/\lambda = 0$ predicted by SMAG+VD on Grid 1 and 2.	76
6.9	$\langle u \rangle / U_{mean}$ at $z/b = 0.5$ and $x/\lambda = 0$ predicted by SMAG+VD on Grid 1 and Grid 2.	76
6.10	Profile of resolved Reynolds stresses, $\langle v'v' \rangle$, $\langle u'u' \rangle$ and $\langle u'v' \rangle$, normalised by U_{mean}^2 at different z location by SMAG+VD on Grid 1 and Grid 2.	78
6.11	$\langle u \rangle / U_{mean}$ at $z/b = 0.5$ and $x/\lambda = 0$ predicted by SMAG+VD on channels with 8, 16 and 32 corrugations.	79
6.12	The details of the sampling lines for the case with 16 corrugations.	80
6.13	The normalised 2pt correlation of velocity along x direction at $y/h = 0.578$ predicted by SMAG+VD on 16 corrugations with periodic BC.	80
6.14	Setup of case with 128 corrugations.	81
6.15	The overview of the instantaneous U_{mag} on $z/b = 0.5$ predicted by SMAG+VD on 128 corrugation case.	84
6.16	The snapshot of $\langle u \rangle$ and its localised details at $z/b = 0.5$ predicted by SMAG+VD on 128 corrugation case.	86
6.17	The numerical error caused by uniform velocity inlet.	87
6.18	The profiles of BL thicknesses at $x-y$ plane of $z/b = 0.5$ predicted by SMAG+VD on channels with 128 corrugations.	88
6.19	The contour of $\langle u'u' \rangle$ and $\langle v'v' \rangle$ at $z/b = 0.5$ between C55 and C73.	89
6.20	The contour of U_{mag} at $z/b = 0.5$ and the iso-surface of Q-criterion pre- dicted by SMAG+VD on 16 corrugation with periodic BC.	91
6.21	$\langle u \rangle / U_{mean}$ at $z/b = 0.5$ and $x/\lambda = 0$ predicted by SMAG+VD on by cases with 128 and 16 corrugations.	92

6.22	Profile of $\langle u'u' \rangle$ and $\langle v'v' \rangle$ predicted on 16 corrugations.	92
6.23	Profile of $\langle u'u' \rangle$, $\langle v'v' \rangle$ and $\langle u'v' \rangle$ at different locations along z direction predicted on the cases with 128 and 16 corrugations.	93
6.24	Comparison of $\langle u \rangle / U_{mean}$ at $z/b = 0.5$ and $x/\lambda = 0$ between the LES prediction and the PIV measurement.	94
6.25	Comparison of profiles of $\langle u'u' \rangle$, $\langle v'v' \rangle$ and $\langle u'v' \rangle$ at different locations along z direction between the prediction of LES and the measurement of PIV.	96
6.26	Comparison of $\langle u \rangle / U_{mean}$ at $z/b = 0.5$ and $x/\lambda = 0$ between the prediction of different SGS models.	99
6.27	Comparison of $\langle u'u' \rangle$, $\langle v'v' \rangle$ and $\langle u'v' \rangle$ at different locations along z direction predicted by different SGS models.	100
6.28	The contour of $k_r\%$ and μ_{sgs}/μ on mid-plane and $y-z$ plane of $x/\lambda = 0$ predicted by SMAG+VD on 16 corrugation with periodic BC.	101
6.29	The energy spectrum for $y/h = 0.819$ predicted by SMAG+VD on 16 cor- rugations with periodic BC.	102
6.30	Comparison of different sampling frequencies on u data obtained by SMAG+VD at $y/h = 1.4458$ on $z/b = 0.5$ and $x/\lambda = 0$	103
6.31	Comparison between $\langle u \rangle$ obtained by different sampling frequencies on $x/\lambda = 0$ at mid-plane.	104
6.32	Comparison of various Reynolds stresses on $x/\lambda = 0.5$ at different locations along z direction calculated by different sampling frequencies.	106
6.33	Comparison between $\langle u \rangle$ obtained by LES at C57 on $x/\lambda = 0$ at mid-plane and PIV data.	107
6.34	The iso-surface plots of Q-criterion for the flow region between C1 and C9.	110
6.35	The iso-surface plot of Q-criterion coloured by v between C32 and C38.	111
6.36	The iso-surface plots of Q-criterion for the flow region between C32 and C38.	112
6.37	The localised details of the stage of Transition, at $z/b = 0.5$ predicted by SMAG+VD on 128 corrugation case.	115
6.38	The vector plot on x/λ for $y-z$ plane of C101 coloured by the magnitude of $\langle v \rangle$ and $\langle w \rangle$	116
6.39	The time-averaged streamlines coloured by v at C101.	117
6.40	The snapshot of U_{mag} contour and vector at $z/b = 0.5$ for C101 and C102.	117
6.41	Plot of the vortex evolvement at $z/b = 0.5$ predicted by SMAG+VD on 16 corrugations.	119

6.42	The pressure distribution at $z/b = 0$ of the corrugation set at $T = 28.08s$ and $28.09s$ predicted by SMAG+VD for the 16 corrugations case.	120
6.43	The velocity vector plot at $z/b = 0$ of the corrugations set at $T = 28.08s$ and $28.09s$ predicted by SMAG+VD for the 16 corrugations case.	120
6.44	The pressure distribution and velocity vector plot of the corrugation set at $T = 28.11s, 28.12s, 29.14s$ and $28.15s$ predicted by SMAG+VD for the 16 corrugations case.	121
C.1	Velocity time history profile at $y/h = 0.412$ for SMAG+VD on Mesh1. . . .	147
C.2	Spatially and temporally averaged variables along y axis at different flow times for SMAG+VD on Mesh1.	148
C.3	Spatially and temporally averaged variables along y axis at different flow times for KEQ on Mesh2.	149
C.4	Spatially and temporally averaged variables along y axis at different flow times for DyK on Mesh3.	149
D.1	Time cost of various SGS model for channel flow	150
E.1	The normalised 2pt correlation of velocity along x direction at $y/h = 0.265$ and $y/h = 0.819$ predicted by SMAG+VD on 16 corrugations with periodic BC.	152
F.1	The location of data sampling lines.	153
F.2	Comparison between $\langle u'u' \rangle$ of the selected corrugations for SMAG+VD. . .	154
F.3	Comparison between $\langle v'v' \rangle$ of the selected corrugations for KEQ+VD. . . .	155

Nomenclature

Abbreviations

BC	boundary condition
BL	Boundary Layer
CD	Central Differencing
CFD	Computational Fluid Dynamics
CTA	Constant temperature anemometer
CV	Control volume
CVs	Control volumes
DES	Detached-Eddy Simulation
DICGaussSeidel	Diagonal incomplete Cholesky/LU with Gauss-Seidel
DNS	Direct Numerical Simulation
DyK	Dynamic k -equation SGS model
DyLag	Dynamic Lagrangian SGS model
DySMAG	Dynamic Smagorinsky SGS Model
EASM	Explicit algebraic stress model
EVM	Eddy viscosity model
FD	Finite Difference
FDM	Finite difference Method
FE	Finite Element
FRAP	Fast response aerodynamic probes
FV	Finite Volume
FVM	Finite volume Method
GAMG	Geometric-algebraic multi-grid
HPC	High Performance Computing
KEQ	k -equation SGS model
LDA	Laser Doppler Anemometry
LES	Large Eddy Simulation

NSEs	Navier-Stokes equations
PDEs	Partial differential equations
PIMPLE	The combination of PISO and SIMPLE algorithm
PISO	Pressure Implicit with Split Operator
PIV	Particle Image Velocimetry
RANS	Reynolds-averaged Navier-Stokes
RGS	Resolved-Grid Scale
RNG	Renormalized Group
RSSM	Reynolds stresses SGS model
SGS	Sub-grid Scale
SIMPLE	Semi-Implicit Method for Pressure-Linked Equations
SMAG	Smagorinsky SGS model
UD	Upwind Differencing
URANS	Unsteady Reynolds-averaged Navier-Stokes
VD	van Driest damping function
WALE	Wall-Adapting Local Eddy-viscosity SGS model

English Symbols

\mathbf{A}	The group of faces bounding the control volume
C^+	Constant used in Universal Laws of the Wall
C_Δ, A^+	Constant used in van Driest damping function
C_{ij}	Cross stresses
C_{kol}	Kolmogorov constant
C_s	Smagorinsky constant
C_s^{eps}, C_s^k	Constant used in k -equation SGS model
C_w	Constant used in Wall-Adapting Local Eddy-viscosity SGS model
\mathbf{d}	The vector connecting adjacent centres of control volume
$E(\kappa)$	Energy spectral density
F_i	Convective flux parameter
f_i	Interpolation factor
$G(\mathbf{x}, \mathbf{x}', \Delta)$	LES filter
H	Shape factor
h	Half channel height
k	Turbulent kinetic energy per unit mass
k_{sgs}	SGS kinetic energy

ℓ	Turbulence length scale
l	Eddy size
l_0	Length scale of large eddies
L_{ij}	Leonard stresses
L_{ij}^{test}	Leonard stresses at test filter level in Dynamic SGS model
L_x, L_y, L_z	Domain size for channel flow in x, y, z direction
N_x, N_y, N_z	Grid points for channel flow in x, y, z direction
\mathbf{n}	Face normal area vector
p	Kinematic pressure
\bar{p}	Filtered kinematic pressure
Re	Reynolds number
Re_b	Reynolds number based on bulk flow velocity
Re_c	Reynolds number based on centre line velocity
Re_{crit}	Critical Reynolds number
R_{ij}	Two-point velocity correlation tensor
\hat{R}_{ij}	LES Reynolds stresses
Re_{ind}	Indifference Reynolds number
Re_τ	Reynolds number based on friction velocity
\bar{S}	Average strain rate of resolve flow for LES
S_{ij}	Strain rate tensor
\bar{S}_{ij}	Strain rate tensor of resolve flow for LES
$\langle S_{ij} \rangle$	Mean rate of deformation
S_ϕ	Source term in the general transport equations
T	Time duration
\mathfrak{T}_{LM}	Lagrangian average of the tensor products $M_{ij}M_{ij}$
\mathfrak{T}_{MM}	Lagrangian average of the tensor products $L_{ij}^{test}M_{ij}$
t	Time instance
U	Wall parallel velocity
U_b	Bulk flow velocity
U_c	Centre line velocity
U_{mean}	Mean velocity along the sampled line
\mathbf{u}	Instantaneous velocity in vector notation
$\bar{\mathbf{u}}$	Filtered instantaneous velocity in vector notation
u^+	Wall parallel velocity normalised by u_τ

u_0	Velocity scale of large eddies
u_i	Instantaneous velocity in tensor notation
u'', v'', w''	Fluctuating velocity components in x, y, z directions
u_i''	Fluctuating velocity in tensor notation
\bar{u}_i	Filtered instantaneous velocity components in tensor notation
$\langle u_i \rangle$	Temporal average of velocity in tensor notation
\tilde{u}_j	Filtered velocity at test filter level in Dynamic SGS model
u, v, w	Instantaneous velocity components in x, y, z directions
$\bar{u}, \bar{v}, \bar{w}$	Filtered instantaneous velocity components in x, y, z directions
u_τ	Wall friction velocity, $\sqrt{\tau_w/\rho}$
u_η	Kolmogorov velocity scale
V_{cell}	Volume of the grid cell
\mathbf{x}	Position vector in vector notation
x_i	Position vector in tensor notation
x, y, z	Rectangular Cartesian coordinates
x'_1, x'_2, x'_3	Rectangular Cartesian coordinates
y^+	Characteristic wall coordinate for the wall layer, $u_\tau y/\nu$

Greek Symbols

$\Gamma\phi$	Diffusivity coefficient of the transported variable
Δ	LES filter/cutoff length
Δt	Timestep size
Δ^{test}	Test filter in Dynamic SGS model
Δ_{mesh}	Cubic root of cell volume
$\Delta x, \Delta y, \Delta z$	Length, width, height of the grid cell
$\Delta x^+, \Delta y^+, \Delta z^+$	Normalised grid size, $\Delta x^+ = (L_x/N_x)u_\tau/\nu$
$\delta_{99}(x)$	Boundary layer thickness in terms of streamwise location
δ_{ij}	Kronecker Delta
δ^*	Displacement thickness
ϵ	Dissipation per unit mass
ϵ_{sgs}	SGS kinetic energy dissipation rate
η	Kolmogorov length scale
θ	Momentum thickness
θ	Constant used in Dynamic Lagrangian SGS model
ϑ	Turbulent velocity scale

κ	Wavenumber
κ_v	von Karman's constant
μ	Laminar viscosity
ν	Kinematic viscosity
ν_{eff}	Effective kinetic viscosity
ν_{sgs}	Sub-grid Scale viscosity
ν_t	Turbulent/eddy viscosity
ρ	Density
σ^k	Constant used in k -equation SGS model
τ	Shear stress
τ_0	Time scale of large eddies
τ_η	Kolmogorov time scale
τ_w	Wall shear stress
τ_{ij}	Kinematic Sub-grid Scale stresses in tensor notation
$\tau_{ij}^{Newtonian}$	Shear stress of Newtonian flow in tensor notation
τ_{ij}^{RANS}	Reynolds stresses for RANS in tensor notation
τ_{ij}^{SGS}	Sub-grid Scale stresses in tensor notation
τ_{ij}^{test}	SGS stresses at test filter level in Dynamic SGS model
ϕ	Arbitrary transport variable
$\bar{\phi}$	The large scale part of flow variable
ϕ	Arbitrary flow variable
ϕ'	The small scale part of flow variable

Chapter 1

Introduction

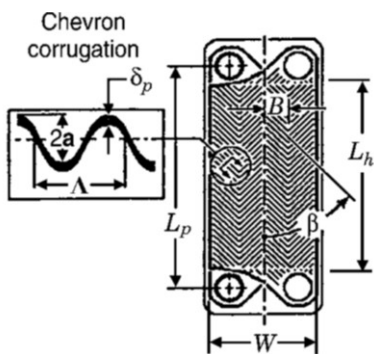
The term "corrugated" describes a surface or material shaped into a series of parallel ridges and grooves [1]. In engineering context, a corrugated structure adds stiffness transverse to the corrugation direction, while maintaining flexibility along the corrugation direction [2]. In addition, the increased surface area enhances the heat and mass transfer [3]. Due to these important features, corrugated channels or sheets widely appear in industrial application and academic research, such as LNG transfer hose, culverts, gasket plate heat exchanger, and structured packing for distillation and absorption.



(A) LNG transfer hose [4]



(B) Culvert [5]



(C) Gasket plat heat exchanger [6]



(D) Structured packaging [7]

FIGURE 1.1. The industrial context of the corrugated geometry.

Although devices with such geometry have been frequently used over the last few decades, the associated physical phenomena are very complex and have not been properly understood, such as the flow separation and reattachment on the corrugated surface, and the momentum exchange between bulk flow and the flow in the corrugation. The combination of these effects leads to a minor modification in corrugation geometry triggering a significant change in flow structures and heat transfer characteristics [8]. This makes it a very interesting and challenging subject to both academia and industry.

Extensive studies [9–11] have been carried out on the three types of corrugated channel shown in Fig. 1.2. They are the corrugation with a square cross section (Fig. 1.2A), sinusoidal wave (Fig. 1.2B) and of the periodic hill (Fig. 1.2C).

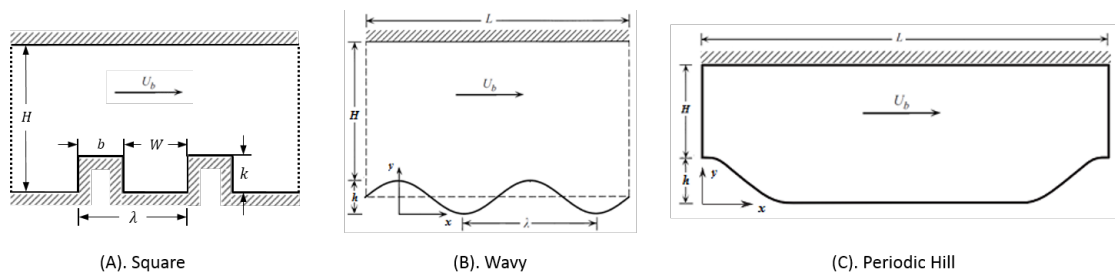


FIGURE 1.2. The schematic representation of different corrugation types.

Nevertheless, research on the flow over realistic corrugated geometries used in industry has not been systematically performed. These geometries, such as the flexible pipes and secondary flow systems in gas turbine engines, tend to have shorter (or even no) post-reattachment-recovery region than the periodic hill, and much smaller length-to-height ratio of a cavity than those corrugations with a sinusoidal wave.

The corrugated channel investigated in present work is shown in Fig. 1.3a. Its corrugation shape is a two-dimensional representation of one of the most widely used commercial stainless steel flexible pipes (with a circular cross section). The flow domain also has two side walls and a top wall, and the flow direction is the x -direction. An experiment with identical geometry and dimensions was carried out using the Particle Image Velocimetry (PIV) technique by Unal et al [3, 12]. The team [8] also recorded instantaneous velocity vectors on the middle plane of the channel for $Re = 17600$ which are shown in Fig 1.3b.

The experimental result shows a three-dimensional, chaotic and unstable flow. More importantly, the flow ejection from the cavities to the outer flow are clearly visible, indicating turbulence, especially the strong momentum exchange between the cavities and the bulk flow, plays a significant role in the flow with such geometry. Despite the findings in the experimental data, there remain many open questions. These include topics such

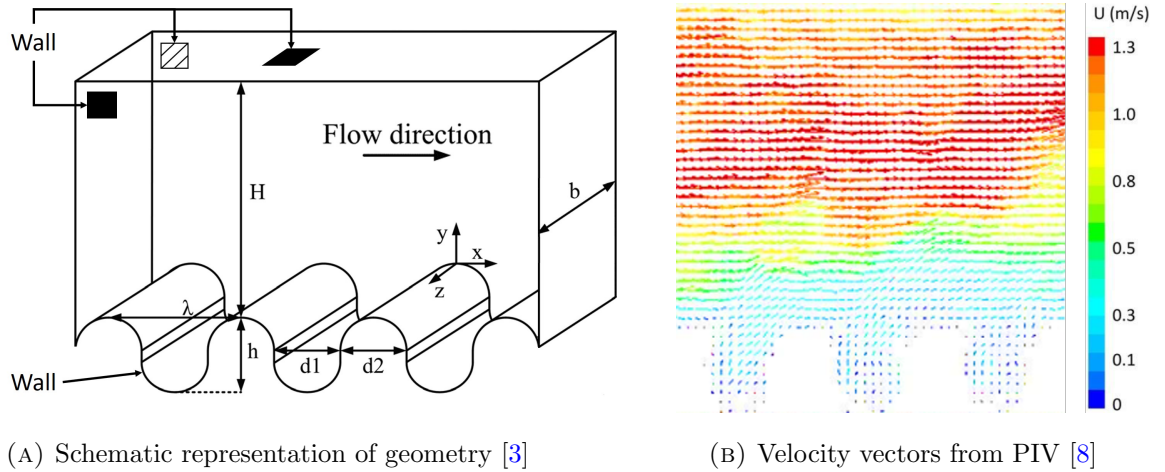


FIGURE 1.3. The corrugated pipe studied in current research.

as the details of flow development, suitability of using a periodic boundary condition on current flow configuration, the interaction between corrugated wall and top and side walls, and mechanisms of hydrodynamic interaction and vortex evolution.

The objective of the current research is to numerically study the flow in the corrugated wall by the Large Eddy Simulation (LES), to find answers for these open questions. The outline of the current thesis is as follow:

- Chapter 2: Literature review and physics associated with the corrugated channel;
- Chapter 3: The governing equations of LES and the Sub-grid Scale (SGS) models used in current research;
- Chapter 4: Discretisation of governing equations and the solver for solutions;
- Chapter 5: The validation of different SGS models on a channel flow case;
- Chapter 6: A comprehensive numerical study on the corrugated channel to study flow field, the interaction between different walls, and detailed hydrodynamic interactions;
- Chapter 7: The conclusions and proposals for further research.

All simulations in current study will be performed by OpenFOAM which is a C++ based fully parallelised CFD software solves the filtered NSEs on non-orthogonal and co-located mesh using the finite volume method.

Chapter 2

Background

2.1 Literature Review

Due to its wide application and the associated complex physical phenomena, the flow in corrugated channels have been attracting researchers and engineers' interest for almost a century. The earliest experimental study can be traced back to 1923 when Hopf (as cited in [13]) carried out experiments on rectangular channels with various roughnesses, including a saw-toothed surface and two other types of corrugated plate. It was the first time that the roughnesses of a rough pipe were divided into two categories, i.e. surface roughness and surface corrugation. Five years later, Fritsch (as cited in [13]) investigated the velocity distribution along the mid-plane of various rough surfaces, including the corrugated (wavy) and toothed shapes. The channel height was between 10 and 35 *mm*, while the width was 150 *mm* to ensure the flow to be two-dimensional. It was reported that if the loss of head among all types of surface were the same, their velocity distributions were same as well, except for the region close to the corrugated wall. In 1929, Treer (as cited in [13]) found from the tests in a channel with extremely coarse roughness that the velocity distribution depends only on the shearing stress, regardless of whether this shearing stress is changed by different roughnesses or Reynolds number (Re). This study indicated that turbulence plays a vital role in corrugated channels.

Since the establishment of a framework on investigating flow over rough surfaces by Nikuradse in 1933 [13], the focuses of the very early studies were on loss of head, velocity distribution, and relationship between the resistance factor and Re , relative roughness and the type of surface [14]. In 1949, Streeter and Chu (as cited in [15]) pointed out that stable vortices were generated by the outer flow inside of a series of grooves with a smooth surface. This was the first time that researchers studied the flow details within a cavity.

Then the research on the flows over corrugated walls were divided into three categories as shown in Fig. 1.2, i.e. the corrugation with a cross section of square, sinusoidal wave and periodic hill.

2.1.1 Square Cavity

Cavities with square cross section were the most widely studied type among the aforementioned three in early years. In 1969, Perry et al. [15] carried out a comprehensive experimental study on the flow characteristics of two types of square-wave groove, i.e. *d*-type and *k*-type which are presented schematically in Fig. 2.1 (reproduced after Perry et al. [15]).

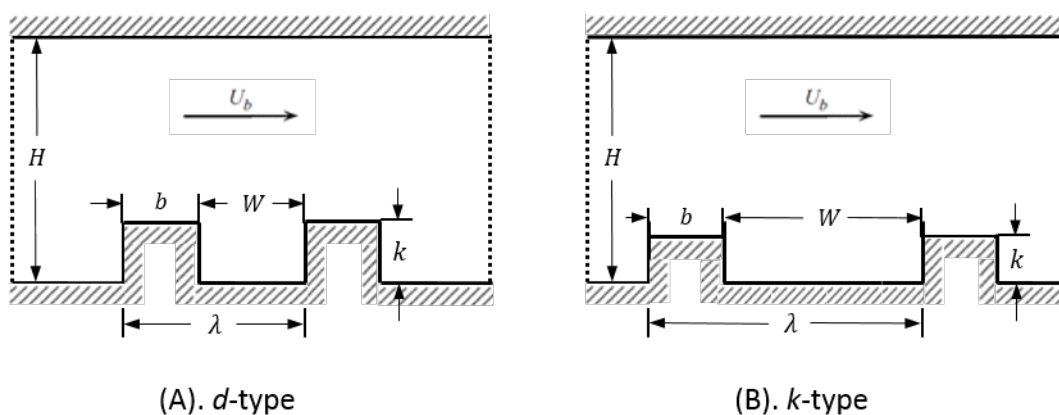


FIGURE 2.1. The schematic representation of two different square cavities.

The *d*-type is typified by the width between two elements being usually equal or similar to its height, i.e. $W \approx k$. The *k*-type has a much larger distance between the two elements than *d*-type, with a width-to-height ratio larger than 4, i.e. $W > 4k$.

Flow visualisation was carried out using a weak suspension of titanium dioxide in kerosene. It was found for the *d*-type (Fig. 2.2, reproduced after Perry et al. [15].) that the outer flow separated at the leading edge of the groove. The flow then impinged on the trailing wall (reaching stagnation). One of the resulting streams goes down to the bottom of the cavity, forming a stable eddy filling up the whole groove. Another stream flows out of the cavity, forming a small separation bubble at the trailing edge of the cavity. Two flattened small eddies are also found at the corners of the cavity.

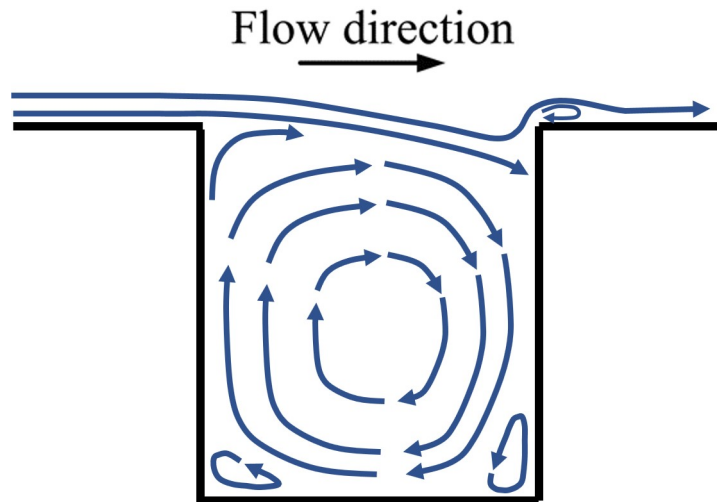


FIGURE 2.2. Surface flow patterns around d -type groove.

Conversely, the flow visualisation of k -type (Fig. 2.3, reproduced after Perry et al. [15].) showed a larger circulating structure filling up the groove, yet the flow structure was not confined to the groove and there was no separation happening at the leading edge nor flow stagnation on the trailing wall.

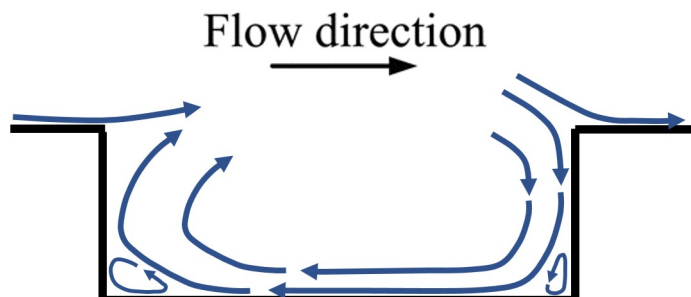


FIGURE 2.3. Surface flow patterns around k -type groove.

Fully developed turbulent boundary layer (BL) flow with d -type roughness was further studied by Wood and Antonia [16] who found the cavity flow appeared to be isolated from the bulk flow. Also the distribution of Reynolds stresses, and skewness and flatness of velocity fluctuation across the BL (measured by hot wires) were similar to those obtained on a flat plate except for the region immediately above the cavity. However, the result from Osaka and Mochizuki [17] showed that discrepancies of flow variable distributions between smooth and d -type walls can be detected even up to 60% of the BL thickness. To overcome the inaccuracy of hot wire measurements close to the wall, Djenidi et al. [18] carried out an experiment with the same flow configuration but using Laser Doppler Anemometry (LDA) for data acquisition. The obtained mean velocity profile confirmed that the outer fluid

entered the cavity at its downstream end, then strengthened the recirculating structure to fill the cavity. Interestingly, the dye visualisation indicated that occasionally the fluid was strongly ejected from the cavity into the bulk flow, and weak ejections were also presented. This enhanced momentum transport over the rough wall was reflected in the increase in the magnitude of wall normal velocity and Reynolds stresses. However the location of maximum magnitudes of wall normal velocity and Reynolds stresses remained the same between the profiles measured on smooth and roughened walls. The effect of the ejection on mean stream-wise velocity was also found to be small. The vortex evolution of a d -type corrugation was later visualised by Elavarasan et al. [19].

A comprehensive review of the study on cavities (of mainly square cross section) was presented by Jimenez [9] who summarised several works and found conflicting results in many experimental studies for d -type cavity. He also listed several reasons of flow ejection proposed by other researchers, such as large scale pressure fluctuations in the outer flow by Townsend [20], the passage of near wall quasi-streamwise vortices/steaks by Elavarasan et al. [19] and [21], and vortices spontaneous bifurcation by Ghaddar et al. [22]. However, their claims were generally not conclusive and detailed mechanism of vortex evolution and flow ejection were far from understood.

Nevertheless, the numerical prediction and experimental data are generally found to be in good agreement on velocity field, turbulent structure and heat transfer characteristics. Saidi and Sunden [23] compared the prediction accuracy of two Reynolds-averaged Navier-Stokes (RANS) models, i.e. eddy viscosity model (EVM) and explicit algebraic stress model (EASM) in a duct with square cross section and two ribbed walls. The result showed both models were able to provide satisfactory agreement with experimental data in terms of friction factor, velocity fields and thermal parameters. It further pointed out that the ribbed duct increased the friction factors five times than the smooth duct with the same cross section, which suggested the enhanced heat transfer rate is accompanied by a large pressure loss penalty.

A parametric numerical study was carried out by Eiamsa-ard and Promvonge [24] for Reynolds number (Re) (based on entrance velocity and the hydraulic diameter of the channel) ranging from 6000 to 18,000, and different pitch-to-height ratios (covering both d -type and k -type) with different RANS turbulence models. It was found the k - ϵ Renormalized Group (RNG) and the standard k - ϵ models gave the best agreement across the full range of experimental data. The study also demonstrated that the grooved channel had higher friction factor than the smooth channel. The friction factor increased with the

increasing of the ratio between groove width and channel height but decreased with the increasing of Re due to the suppression of viscous sub-layer which is also observed in the work of Boulemtafes-Boukadoum and Benzaoui [25].

Simulation results of Lee and Abdel-Moneim [26] and Stel et al. [27] also confirmed that, although the best turbulence model varied, RANS could generally provide accurate predictions for a channel with both k -type and d -type roughness.

2.1.2 Wavy Cavity

The flow over a wavy surface was analytically studied as early as 1932 by Stanton and co-workers [28]. But the primary interest of the early investigations [29, 30] was on the interaction between air and water waves.

In 1972, Beebe and Cermak [31] carried out the first experimental research on a channel with a sinusoidal wavy shape. For these experiments $Re = 1 \times 10^5$. They investigated three wavy shapes with constant wavelength but different amplitudes. The periodicity of the current flow configuration was firstly confirmed by the statistical results. Flow visualisation revealed a single, slow rotating, yet unsteady vortex within the cavity for all cases, and part of the vortex was intermittently shed (rather than ejected) into the outer flow. For the case with the highest amplitude, the flow separated in the area behind the wave crest and reattachment at the trailing face of the cavity, forming a vortex which filled the cavity and the outer flow skimmed over it. The vortex in the case with the lowest amplitude was smaller but more frequently shed, and the outer flow was found to penetrate into the cavity. It was also found that the largest amplitude wave achieved the most flow speed reduction above the surface.

Subsequent experimental studies by Hudson et al. [32], Nakagawa and Hanratty [33], and Kruse et al. [10] provided more insights on this flow configuration. It was found that the turbulence within the cavity was mainly produced by the shear layer due to the flow separation after the wave crest. In addition, this wavy geometry was able to generate flow structures as large as half the channel height. Nevertheless, its impact on the statistical result was shown to be modest, as profiles of normalised Reynolds stresses and turbulent kinetic energy production were found to be independent of the sinusoidal specification at a certain distance away from the cavity.

Numerical study on this type of corrugated flow started relatively early. The sinusoidal wavy channel with low Re was studied numerically by Krettenauer and Schumann [34] in 1992 using direct numerical simulation (DNS) and LES. Different amplitudes and

wavelengths of the sinusoidal shape were tested and the results were compared with the experiment of Adrian et al. [35]. The DNS result indicated the flow field can be turbulent around such curved surfaces at $Re = 100$ (based on convective velocity defined by Deardorff [36] and mean fluid layer height). This parametric study also suggested that the mean flow features, such as profiles of Reynolds stresses and fluxes were not very sensitive to the variations of amplitude, wavelength, domain size, resolution and even the computational methods (DNS or LES). In contrast, details of the flow structure were changed considerably. The study [34] further concluded that the LES could be regarded as reliable as experimental measurement for both high-Reynolds-number and high-Rayleigh-number flows in such cases. Mirzaei et al [37] used LES to study the turbulent flow field in a wavy channel which found that the shape increased the heat transfer rate but suffered from a pressure loss penalty. Another work of the same group has successfully used LES to identified the optimal wave amplitudes to balance the heat transfer gain and pressure loss [38].

There are not many numerical studies on a wavy channel that use RANS. Knotec and Jícha [39] compared various RANS turbulence models on the flow setup. The results showed RANS turbulence models generally provide a poor prediction on flow features, such as mean velocity and Reynolds stresses. The study of Hafez et al. [40] confirmed this finding, although it demonstrated a tailored wall function was able to improve the prediction accuracy of RANS turbulence models significantly.

In comparison, a number of studies have been dedicated to assessing the predictive effectiveness of LES on a wavy channel or using LES to assist experiment to understand the flow features. Gong et al [41] used LES to study the secondary flow in the cavity. The LES solution of Henn and Sykes [42] confirmed the inner layer structure between the wall layer and the outer flow for small amplitude waves with $Re = 1 \times 10^4$ (based on bulk velocity and the channel mean half height). Armenio and Piomelli [43] tested a Lagrangian mixed SGS model on this flow configuration, the LES results were found to agree satisfactorily with previous experimental studies across wide range of flow parameters, both in the case of the moderate-amplitude wavy wall at low Reynolds number, and in the case of the large-amplitude wavy wall at a moderate Reynolds number.

2.1.3 Periodic Hill

For the last three decades, the research focus on the corrugated channel have seen a shift from the cavity with square cross section and sinusoidal wavy shape to a periodic hill,

especially with regard to numerical prediction which is found to be more challenging on curved cavities.

The periodic hill geometry was firstly defined and experimentally studied by Almeida [44] in 1993. The case configuration is characterised by a channel with a periodic flow over a series of consecutive hills equally spaced apart at the bottom of the channel [45]. The flow separates due to the unfavourable pressure gradient downstream of the hills and reattaches at an oblique angle on the upstream surface of the next hill as suggested by the original experiment. This test case was chosen as one of the five test cases in 4th ERCOFTAC/IAHR Workshop on Refined Flow Modelling in 1995 [46]. However, as highlighted by Mellen and co-workers [47], three serious issues surround this test case. The earlier simulations on this test case were carried out based on a periodic boundary condition (BC) along stream-wise direction and without the sidewalls which were the least demanding configuration. However, the result in the ERCOFTAC/IAHR workshop raised doubts concerning the true periodicity of the experimental setup [46]. Also, due to the short spanwise distance in the original experiment, the sidewalls were expected to generate spanwise variation, making the experimental data invalid for benchmarking numerical studies. In addition, the original experiment $Re = 365,000$ (with Re based on the height of the channel and mean centreline velocity) which is very computationally demanding.

In order to get round these issues, Mellen et al. [47] defined a new configuration and carried out a wall-resolving LES using a dynamic SGS model. The new geometry doubled the distance between the two hill crests from $4.5h$ to $9h$, halved the channel height from $6.07h$ to $3.035h$, kept the spanwise distance as $4.5h$ but imposed the spanwise periodicity, and reduced the Reynolds number to 21,560. The new configuration had two benefits. Firstly, the increased distance between hill crests decreases the streamwise correlation and allows a natural reattachment at the flat plate between the hills followed by a recovery region. Secondly, the decrease of channel height and Re make the case more computationally affordable, and the spanwise periodicity eliminates the influence of the sidewalls. This well designed flow configuration soon became a standard benchmark case for studying phenomena such as separation from a curved surface, flow recirculation and reattachment. This test case was also selected by the ERCOFTAC/IAHR/COST Workshop in 2001 [48] and 2002 [49].

Although there was no reliable experimental data, the results of Mellen et al. [47] still provided instructive and useful insight on numerical prediction of flow separation, recir-

ulation and reattachment. It was found that the point of flow separation was insensitive to the SGS model, yet greatly influenced by grid density at the crest of the hill. However, the reattachment location depended on both grid size and SGS model. Wall shear stress profiles were found to be similar between different SGS models and grid densities. In contrast, mean velocity, Reynolds stresses and eddy viscosity content were affected by grid density and SGS model.

The simulation performed by Temmerman and Leschziner [50] and Temerman et al. [51] focused on the effectiveness of the different combinations, including six SGS models and eight wall-functions on three grid densities. The accuracy was judged by a well resolved simulation with a fine grid. The result demonstrated that the prediction of the separation point, and the resultant length of separation bubble and reattachment position, is highly sensitive to grid density (especially for the streamwise resolution close to the separation line) and numerical implementation of the wall laws (more prominently on the coarsest grid). Similar to the findings of Mellen et al. [47], the sensitivity of the solution to SGS models are found to be weaker than grid resolution and wall treatment. This was mainly due to even the coarsest grid having a relatively high resolution resulting a low level of SGS viscosity.

Numerical studies on this test case using RANS are very rare. One such study was carried out by Jang et al. [52] who compared the predictive quality of eight RANS turbulence models with reference to the LES solution of Temmerman and Leschziner [50]. A poor prediction accuracy in terms of reattachment point and Reynolds stresses was generally found for all the RANS models tested. A further study on the RANS regime was conducted by Abe et al. [53] who proposed a new RANS turbulence model. It was found the model showed a significant improvement in terms of normal Reynolds stress when compared to the model tested by Jang et al. [52], but it still provided an unsatisfactory result for the reattachment point and other components of Reynolds stresses. More recently, Jakirlic [54] parametrically assessed the prediction accuracy of various RANS turbulence models and concluded that the conventional RANS turbulence models were not able to correctly capture the flow features of periodic hill configuration, including skin friction, shape and size of the separation bubble and turbulent quantities.

The numerical study of Fröhlich and co-workers [55] was dedicated to the turbulence mechanisms associated with flow separation, recirculation, reattachment and acceleration. Results were studied in detail for mean velocity, Reynolds stresses, two-point correlations and energy spectra. The links between flow structural features and statistical data were

also interpreted. One of the interesting features was that a very high level of spanwise turbulence intensity was found in the post-reattachment-recovery region, especially when the flow hit the upstream surface of the next hill. The result of budgets showed that the energy was diverted from both wall-normal and streamwise components to spanwise component by pressure-strain interaction. This phenomenon was understood as a result of large vortices from the shear layer impinging onto the windward slope. This feature is one of the reasons, suggested by the authors [55], why even a Reynolds stress RANS model could not predict flow features in periodic hill configuration accurately.

A comprehensive study was recently carried out by Breuer et al [11]. The research complemented the work of Fröhlich and co-workers [55] by highly-resolved numerical (DNS and LES) and experimental data (PIV) over a large range of Re (between 100 and 10,595, based on bulk velocity and hill height). The quality of the DNS and LES results were proven by cross-comparison of two independent codes and experimental data. This study did not only confirm the previous findings [55], but also shed new light on these flow features such as the small recirculation on the hill crest (for highest Re) and at the foot of the windward face of the hill, the behaviours of the separation and reattachment as a function of Re . It was also found that at $Re = 100$, the flow was steady and two-dimensional, but it became three-dimensional, instantaneous and chaotic for $Re > 200$. This study clearly demonstrated that LES was able to provide accurate results and assist the experiment to gain more insight into flow fields, especially for higher Re .

It is noted that pressure field and losses seem not to be the focus of the study on Periodic Hill so that no associated pressure loss study has been published.

2.2 Turbulence

2.2.1 Fundamentals of Turbulence

The literature review in Section 2.1 clearly highlights that turbulence plays a vital role in flow in a corrugated channel. This section is dedicated to providing a theoretical background of turbulence and the way to model it.

Turbulent flows, that is flow with irregular characteristics and random variation of quantities with time and space [56], has been regarded as one of the most challenging problems in fluid dynamics [57]. Numerous scientists and researchers have spent a great amount of time to observe, describe and understand turbulent flows. The earliest "informal" study of turbulent flow can be arguably dated back to around 1510 [58], when Leonardo da Vinci sketched a free water jet from a square hole into a pool and observed that the water has eddying motions, one part of which is due to the principle current, and other to the random and reverse motion.

Early fluid mechanics studies generally assumed the fluid to be inviscid, despite the theorem of viscous fluid being established in 1644 by Torricelli [59]. Euler derived the frictionless equation in 1755. However, it was pointed out by d'Alembert that a body immersed in a frictionless flow would not have drag. The paradox, between the existence of drag in real engineering application and the absence of drag due to the assumption of frictionless flow, troubled engineers for over a century. In the early to middle of the nineteenth century, Navier, Cauchy, Poisson and St. Venant advanced the analytical study to add frictional-resistance terms to Euler's inviscid equation, but these terms were associated with an unknown molecular function [59]. In 1845, Stokes derived the equation of viscous flow by adding a Newtonian viscous term [59] resulting in the Navier-Stokes equations (NSEs) which are the governing equations for Newtonian flow.

One of the early experimental attempts at quantifying turbulence was made by Reynolds in 1883 [60], who found the Reynolds number at which turbulence first appears was very sensitive to disturbances at the entrance of the pipe. If no particular effort was taken to minimise this disturbance, the pipe flow would change from laminar state to a turbulent one when $Re > 2000$. In contrast, if the inlet disturbance was minimised, the laminar state could be maintained up to $Re = 13,000$.

The instantaneous flow variable in a turbulent flow is very sensitive to the minor initial difference, but they are steady-on-average under nominally identical conditions. The statistical properties of a turbulent flow are uniquely determined by the boundary and initial conditions [57]. In 1895, Reynolds [61] proposed Reynolds averaging that for

the first time decomposed the flow variable to time-averaged and instantaneous parts and introduced Reynolds stresses. Two types of time-averaging are shown in Fig. 2.4.

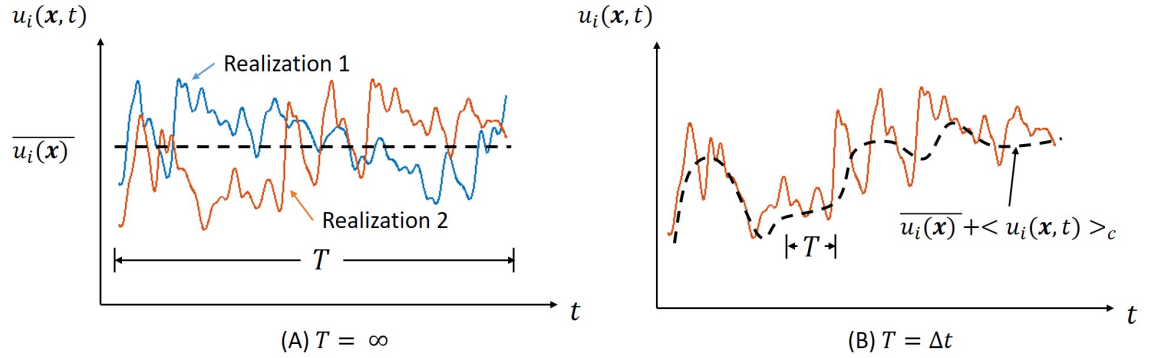


FIGURE 2.4. Different types of time-averaging processes.

Fig. 2.4A shows the time-averaging process with an averaging window of $T = \infty$. The red and blue lines are experiments carried out under nominally identical conditions. Due to the minor discrepancy at the initial conditions, the exact profile of the instantaneous velocity for the two lines vary, but their time-averaged values over the whole period are the same. After Reynolds decomposition, the instantaneous velocity, $u_i(\mathbf{x}, t)$, is represented as

$$u_i(\mathbf{x}, t) = \langle u_i(\mathbf{x}) \rangle + u_i''(\mathbf{x}, t) \quad (2.1)$$

where $\langle u_i(\mathbf{x}) \rangle$ is the statistical average velocity which in operation often associated with a time averaging [62], i.e.

$$\langle u_i(\mathbf{x}) \rangle \approx \overline{u_i(\mathbf{x})} = \lim_{x \rightarrow \infty} \frac{1}{T} \int_0^T u_i(\mathbf{x}, t) dt \quad (2.2)$$

$u_i''(\mathbf{x}, t)$ is the fluctuating part of $u_i(\mathbf{x}, t)$ ¹.

In a large number of turbulent flows, the mean velocity of an unsteady flow can change with respect to time. In this case, certain low frequency modes in time and the average field will need to be solved. This process is depicted in Fig. 2.4B. Now the Eq. 2.1 is replaced with

$$u_i(\mathbf{x}, t) = \overline{u_i(\mathbf{x})} + \langle u_i(\mathbf{x}, t) \rangle_c + u_i''(\mathbf{x}, t) \quad (2.3)$$

¹ $u_i''(\mathbf{x}, t)$ is used here instead of the conventional $u_i'(\mathbf{x}, t)$ is because that $u_i'(\mathbf{x}, t)$ will represent the sub-grid scale velocity component in the later Chapters.

The first term is the time-averaged velocity; the second is its conditional statistical average which is interpreted as the contribution of the coherent modes to the flow dynamics; and the third one is the turbulent fluctuation. The variable used in the numerical model is actually the sum of $\overline{u_i(\mathbf{x})}$ and $\langle u_i(\mathbf{x}, t) \rangle_c$ [62].

The study of Reynolds laid the cornerstone for the Reynolds-averaged Navier-Stokes (RANS) equation. The RANS equation derived from Eq. 2.1 is called steady RANS, while the one derived from Eq. 2.3 is termed unsteady RANS (URANS).

Another important feature of turbulent flow is at any instant, there exists a broad spectrum of eddy sizes. The large eddies migrate across the flow, carrying smaller scale disturbances with them. Richardson [63] summaries this feature at page 66 of his book in 1922 that:

Thus C. K. M. Douglas writing of observations from aeroplanes remarks: "The upward currents of large cumuli give rise to much turbulence within, below, and around the clouds, and the structure of the clouds is often very complex.

...

big whirls have little whirls that feed on their velocity, and little whirls have lesser whirls and so on to viscosity in the molecular sense."

The concept of an energy cascade introduced by Richardson [63] is that the largest eddies, which are created by the instabilities in the mean flow, are unstable and break up or evolve into smaller eddies. The latter are also unstable, and break up after a short life-span and transfer their energy to even smaller eddies. This continual energy cascade stops when the Re based on the eddy length is sufficiently small (order of unity [57]). At this point, the eddy motion is stable and its kinetic energy is dissipated due to the significant viscous forces. The picture of the energy cascade process suggests the dissipation (mainly) happens at the end of the process, and the rate of dissipation on the smallest eddies is (very nearly equal to) the rate they receive the energy from larger eddies. This concept is confirmed mathematically, as by definition, the dissipation rate of kinetic energy in a fluid is $\epsilon = 2\nu S_{ij}S_{ij}$ per unit mass [57]. Here ν is kinematic viscosity, $S_{ij} = \frac{1}{2}(\partial u_i/\partial x_j + \partial u_j/\partial x_i)$ is the strain rate tensor. This suggests dissipation is concentrated in regions with a large instantaneous gradient in velocity (and thereby shear stress), which are the smallest eddies.

The picture of energy cascade was expanded and quantified by Kolmogorov [64]. In 1941, he stated three hypotheses. The first one related to the local isotropy of sufficiently small scale motions within the flow with very large Re . He argued that all informa-

tion of the large eddies, which was determined by flow geometry and Re including the directional information, was lost during the energy cascade process. So the small scale turbulent motions (an order of magnitude smaller than the large eddies [57]) were statistically isotropic/universal. As shown in the energy cascade concept of Richardson [63], two important parameters during the process were ϵ and ν . This then led to the second hypothesis of Kolmogorov, i.e. "The first hypothesis of similarity", which stated that the statistics of the locally isotropic turbulence (small scale turbulent motions) are uniquely determined by ϵ and ν . The size range no larger than this small scale was referred to as the universal equilibrium range [65]. Following the derivation process shown in the book of Davidson [57], Kolmogorov scales of length, velocity and time can be obtained as

$$\eta = (\nu^3/\epsilon)^{1/4} \sim l_0 Re^{-3/4} \quad (2.4a)$$

$$u_\eta = (\epsilon\nu)^{1/4} \sim u_0 Re^{-1/4} \quad (2.4b)$$

$$\tau_\eta = (\nu/\epsilon)^{1/2} \sim \tau_0 Re^{-1/2} \quad (2.4c)$$

where Re , l_0 , u_0 and τ_0 are the Reynolds number, length, velocity and time scale of the eddies in the largest size range, respectively. The equations show that increasing Re will decrease η/l_0 . Inevitably, a large number of eddies whose size should fall between η and l_0 , having a relatively large Re and little effect from ν . Here comes the second hypothesis of Kolmogorov that the statistics of eddies, whose size l fall within the universal equilibrium range yet one to two orders of magnitude [57] larger than η , are uniquely determined by ϵ and independent of ν . Thus, the universal equilibrium range is split into two subranges, inertial subrange and dissipation range. The size range above universal equilibrium range is termed as the "energy containing range". The rate of energy transferred from the large scales does not only determine the dissipation rate, but also the constant rate of energy transfer throughout the inertial subrange [65]. Combining both similarity hypotheses, Kolmogorov further proposed the famous power law for inertial subrange²

$$E(\kappa) = C_{kol}\epsilon^{2/3}\kappa^{-5/3} \quad (2.5)$$

where $E(\kappa)$ is the energy spectrum function in respect of wavenumber, $\kappa = 2\pi/l$ and l is the length scale of turbulent motion; C_{kol} is Kolmogorov constant. A typical energy spectrum for a turbulent flow is shown in Fig. 2.5.

²In the original article of Kolmogorov, the formulae contains $r^{2/3}$ instead of $\kappa^{-5/3}$, where r is a length scale larger than Kolmogorov length scale. A detailed derivation of the $-5/3$ law can be found in the work of Levandowski and Pinier [66]

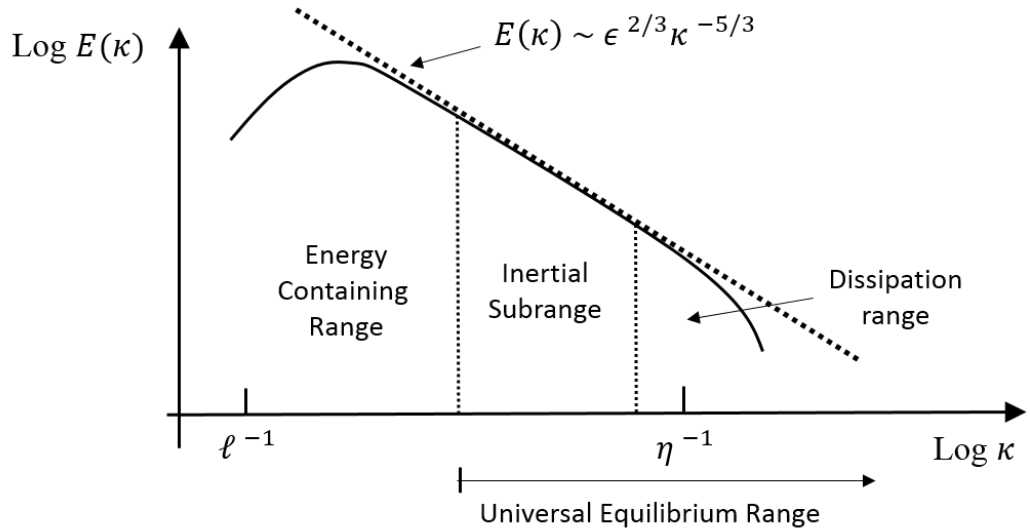


FIGURE 2.5. Typical energy spectrum for a turbulent flow.

The length scale, ℓ , can be the integral length scale [67]. The energy spectrum function $E(\kappa)$ should follow the slope of $-5/3$ during the inertial subrange. The hypotheses of Kolmogorov is the foundation of large eddy simulation (LES). The isotropy and dissipation of small scales have been the fundamental assumption of the commonly used sub-grid scale (SGS) models for LES.

The presence of a boundary also has a significant impact on a turbulent shear flow. This is due to the fact that viscosity and velocity and its fluctuation must fall to zero on/near the wall [57]. In an internal flow, one of the influences of the boundary is the boundary layer (BL). The BL or frictional layer was discovered by Prandtl in 1904 [68]. The thin layer attached to the boundary divides the flow into two regions: the bulk flow region in which viscosity can be neglected under high Re , and the BL where the effect of viscosity must be considered. There are two types of BL, i.e. laminar and turbulent.

In the current research, the fluid flows into the channel at a relatively low Re . a laminar BL is expected to form at the beginning. The thickness of this layer will increase as the fluid flows from inlet to outlet. Then a transition process happens so that the laminar BL eventually becomes a turbulent BL. The natural transition process is shown in Fig. 2.6 [69].

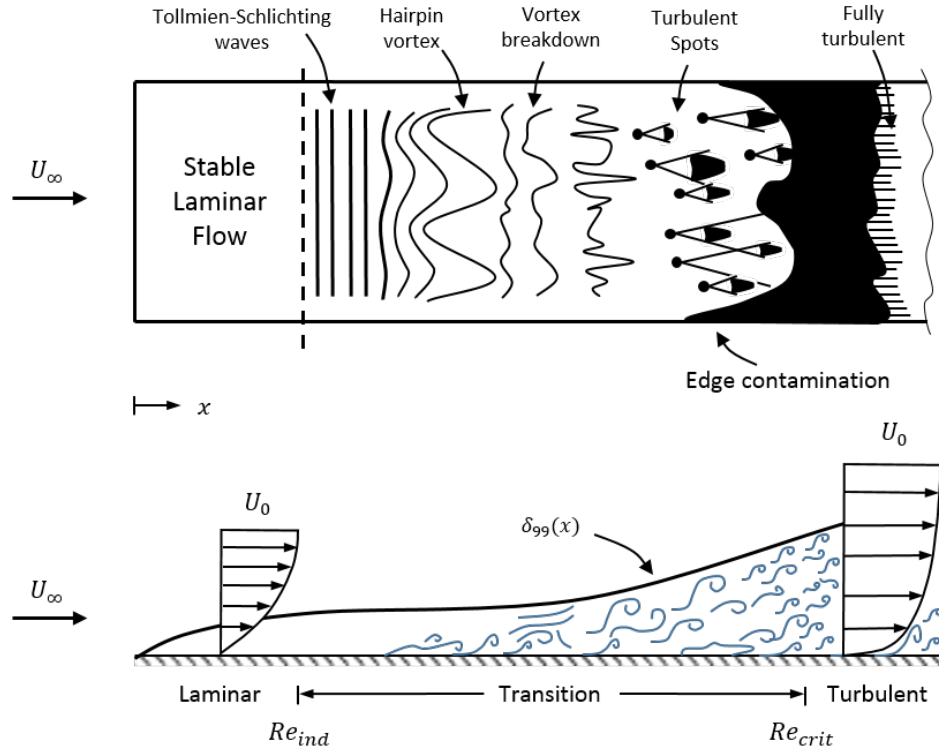


FIGURE 2.6. Sketch of boundary layer natural transition on a flat plate.

It shows that when the indifference Reynolds number³, Re_{ind} , is reached, a two-dimensional undulation, the so-called Tollmien-Schlichting waves, is superimposed onto the laminar BL [69]. Further downstream, three-dimensional hairpin vortices erupt from the wall. These structures are long, arch-like tube with modest diameter. The total length of the tube may be of the order of BL thickness, $\delta_{99}(x)$. The erupted vortices then break down and decay away from the wall. After a short distance, turbulence spots start appearing at various places initiating the transition from laminar to turbulent. The generated localised turbulent flows finally merge together when critical Reynolds number, Re_{crit} , is reached and the flow further downstream is fully turbulent.

BL transition is strongly influenced by many parameters, such as Re , roughness, heat transfer, pressure distribution and turbulence intensity in the bulk flow. In addition, natural transition does not always happen in real engineering applications. In most cases, one or more steps listed in Fig. 2.6 are bypassed. Such transition processes are called by-pass transition, such as in the studies of Irs and Kanjirakkad [70] and Langari and Yang [71].

One difference between laminar and turbulent BLs is their velocity profile. As shown

³ $Re_{ind} = \rho ux/\mu$, where x is the distance from leading edge where Tollmien-Schlichting waves first appear in a natural transition.

in Fig. 2.6, the time averaged velocity distribution along wall normal direction is more uniform in turbulent flows than in laminar ones. This is due to the transverse movement enhancing mixing and momentum exchange in the transverse direction [69]. Another difference is that the whole of the laminar BL is affected by viscosity, whereas in the turbulent BL, the effect of viscosity is restricted to a layer thinner than the BL and very close to the wall, called the linear or viscous sublayer. The region within a turbulent BL but above the viscous sublayer is full of turbulent fluctuations and is almost unaffected by the viscosity.

The viscous sublayer in a turbulent BL is extremely thin ($y^+ < 5$ [72]). It is assumed the shear stresses in this sublayer are constant and equal to the wall shear stresses

$$\tau(y) = \mu \frac{\partial U}{\partial y} \cong \tau_w = \mu \left(\frac{\partial U}{\partial y} \right)_w \quad (2.6)$$

where τ_w is the wall shear stress obtained by Newton's law of friction; μ is laminar viscosity; U is wall parallel velocity and y is wall normal distance. After integration and applying boundary conditions (BC), the first part of Universal Laws of the Wall for a flat plate can be obtained

$$u^+ = y^+ \quad (2.7)$$

where $u^+ = U/u_\tau$ and $u_\tau = \sqrt{\tau_w/\rho}$ is the friction velocity, ρ is the density of fluid; $y^+ = yu_\tau/\nu$ is the characteristic wall coordinate for the wall layer. The equation for the log-law layer can also be derived for the region outside the viscous sublayer ($70 < y^+$) as [69]

$$u^+ = \frac{1}{\kappa_v} \ln(y^+) + C^+ \quad (2.8)$$

where $\kappa_v = 0.41$ is the von Karman's constant; $C^+ = 5.0$. The layer in between the viscous sublayer and log-law layer is called the buffer layer. The universal laws of the wall can be used as a first validation test for a turbulent model in plane channel flow test case as shown in Fig. 2.7.

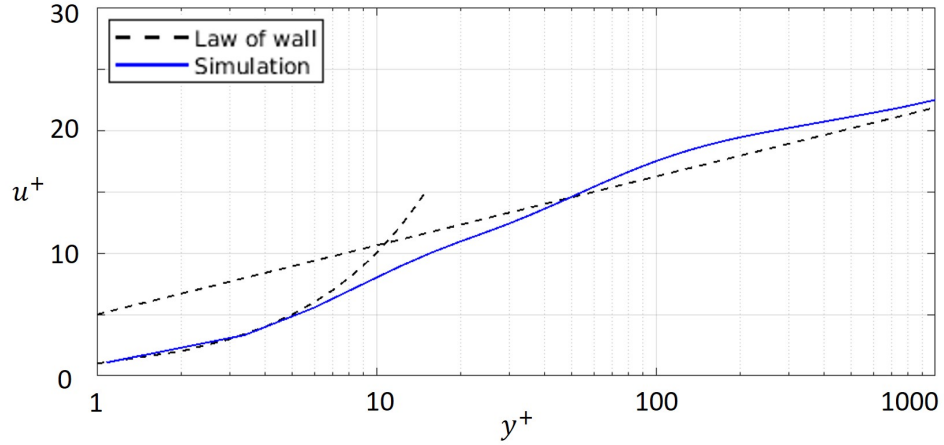


FIGURE 2.7. A comparison between a typical prediction of velocity distribution near a solid wall and the Universal Laws of the Wall.

Other important parameters of the plane channel flow are the distributions of the time-averaged Reynolds stresses, as these directly link with turbulence kinetic energy. Fig. 2.8 depicts a typical profile of normalised time-averaged Reynolds stresses, i.e, the root mean square of $\langle u''u'' \rangle$, $\langle v''v'' \rangle$, $\langle w''w'' \rangle$, and $\langle u''v'' \rangle$ ⁴.

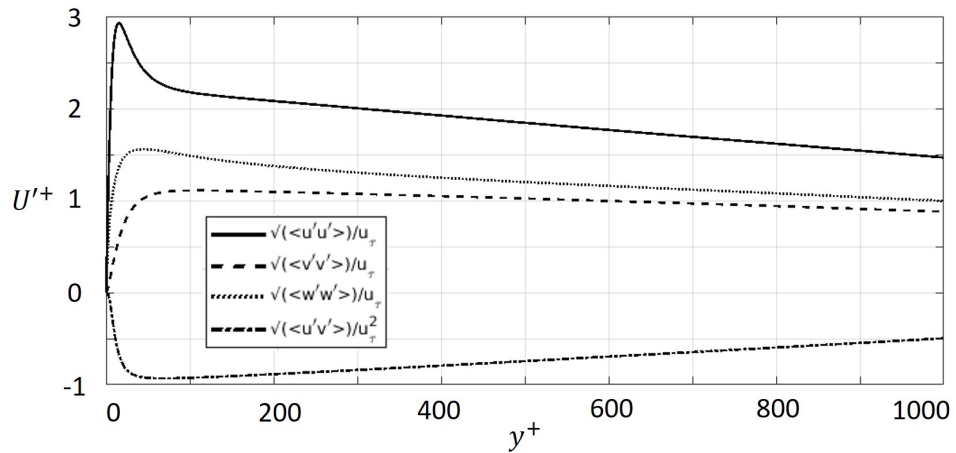


FIGURE 2.8. A typical distribution of Reynolds stresses near a solid wall.

Unlike the mean velocity profile, there is no universal law for Reynolds stresses, so the validation for turbulence models on these parameters is done using comparisons with experimental or DNS data.

⁴Due to the fact that the channel flow is symmetric along wall normal direction, its $\langle u''w'' \rangle$ and $\langle v''w'' \rangle$ are equal to zero [73].

2.2.2 Approaches to Study Turbulence

Given the importance of turbulence in practical engineering applications, engineers have tried many ways to study and predict its behaviour in a system in order to get better designs or optimise systems' operation. Three approaches are normally used, i.e. experimental, analytical and computational [74], which will be discussed in following sections.

Experimental Method

Experimental measurement generally gives the most reliable information about physical phenomena. Performing experiments allows engineers to understand the system directly or to build mathematical models to present the system under certain conditions. However, in most practical engineering applications, an experiment involving full scale testing under given conditions is either difficult, very expensive or even not possible at all, such as in circumstances where there is no wind tunnel that can simultaneously test the high Mach numbers and high flow field temperature to be encountered by trans-atmospheric vehicles [75].

A common alternative approach is to carry out the experiments on small scale models or a certain part of those models. Although dimensional scaling enables the small scale model to capture the features of the full scale system, some key features are very difficult to measure in the small scale model, such as the velocity after turbine blade root section for wind turbine generators. Also a part of the model does not usually have the desired working condition for testing. In addition, even these alternative approaches are turned out to be very time and cost consuming to design and build [76].

Another aspect which should not be neglected is the limitation of the measuring equipment. Some intrusive instrumentation, such as constant temperature anemometer (CTA) need to be inserted into the flow field to get measurements and potentially interfere with the flow conditions. Furthermore, CTA suffers from short life spans in high speed flows, and is only sensitive to the velocity perpendicular to the wire/film so that multiple wires probes are required which disturb the flow field more strongly [77].

One solution to the issue of intrusive probes is the non-intrusive techniques, such as laser doppler anemometry (LDA) and particle image velocimetry (PIV). Both techniques have been used to experimentally study the flow in corrugated walls as shown in the literature review. However, as pointed out by DroZdZ and Uruba [78] that although the mean velocity profile can be well captured by PIV comparing with hot wire, PIV tends to greatly underestimate the near-wall peak for Reynolds stresses, especially for the

wall normal component. Such underestimation might be due to the smaller structures in the flow which are not be able to be resolved using the large field of view in the PIV methods. In addition, the study of Scharnowski et al. [79] shows that the quality of PIV measurements is sensitive to the suitability of interrogation window size and displacement on the image plane. Nevertheless, due to the small flow domain size, the experiment of the corrugated channel to be investigated in the current research was carried out by Unal et al. with PIV techniques [3].

Analytical Method

In an analytical method, physical phenomena are represented by a mathematical model, mainly consisting of a set of differential equations, and solved analytically with various assumptions and simplifications.

Analytical methods played a significant role in the past and together with experimental methods were the only options for fluid dynamics research at the early stage. They helped researchers to understand the macro behaviours of flow, interpret experimental results, and validate the results obtained by computational fluid dynamics (CFD).

Nevertheless, only a small number of flow problems are adequately simple to have an analytical solution. Too many assumptions and simplifications limit their validity in more complex flows. Therefore, analytical methods have been limited to simple flows, such as Couette flow and Poiseuille flow, etc [80].

Computational Fluid Dynamics

Computational fluid dynamics is a branch of fluid dynamics that solves the equations of fluid motion numerically to quantitatively predict fluid flows and their associated phenomena, such as turbulence, heat transfer and chemical reaction, etc.

CFD have expanded rapidly with the advent of digital computers. Since the 1950's, the continuous improvement of computing power has been boosting its development [74]. From the 1960s the aerospace industry has integrated CFD techniques into the design, and research and development of aircraft and jet engines [72]. More recently the methods have been applied to the automotive industry for drag prediction, internal and external air flow, and internal combustion engine design [81]. Recent years have also seen a trend of CFD being spread to areas which are not traditionally engineering related, such as the food industry [82] and physiological applications [83]. The increase in availability of high performance computing (HPC) and the introduction of user-friendly interfaces have made

CFD a vital tool for industry and research.

CFD offers many advantages. Firstly, it provides a cost effective way to supplement experiments in fluid flow studies. Thanks to the more complete set of information and details of results, CFD has been extensively used in research to explain experimental data and lead the experimental focus. Secondly, CFD is applicable to complex geometries where it is impossible for analytical study. Thirdly, CFD can achieve a substantial reduction of lead times and costs of new designs over experimental-based approach. Finally, CFD is able to simulate a situation which is too difficult or impossible for experiment, such as very large systems or hazardous conditions.

Current research will use CFD to numerically study the current corrugated channel to try to answer those questions raised from the experiment.

2.2.3 Simulation of Turbulence

Three techniques are currently used to solve the NSEs, the governing equations for viscous flow. They are DNS, RANS and LES. Each method resolves a different range of the turbulent kinetic energy spectrum shown in Fig. 2.5. Consider a turbulent flow that has a predominant frequency. The solved and modelled parts of energy for each method can be indicatively illustrated by Fig. 2.9 (reproduced after Sagaut [62]).

DNS directly solves the NSEs under very fine spatial and temporal resolutions which allow it to resolve the length scale down the energy dissipating Kolmogorov length scale, η , and the turnover time of the energy-dissipating eddies. Therefore its energy spectrum most complete and nothing is modelled. The challenge of DNS is that its computational requirements are prohibitively high for real engineering applications. This is due to the fact that the number of grid points required for sufficient spatial resolution is of the order of $Re^{9/4}$ and Re^3 for the CPU time [65]. Therefore, at the current stage, DNS is still limited to the fundamental study of flows on relatively simple geometries.

The common approach, therefore, is to account for the approximate effects of turbulence by employing appropriate turbulence models. A large range of turbulence models have been developed and turbulence modelling is a subject of active ongoing research. Two main classes involving modelling of turbulence at different levels are RANS and LES. Some hybrid models have also been developed to utilise benefits of both RANS and LES approaches e.g. Detached-Eddy Simulation (DES) modelling where near-wall regions are solved using RANS mode and the rest of the flow is treated using the LES approach.

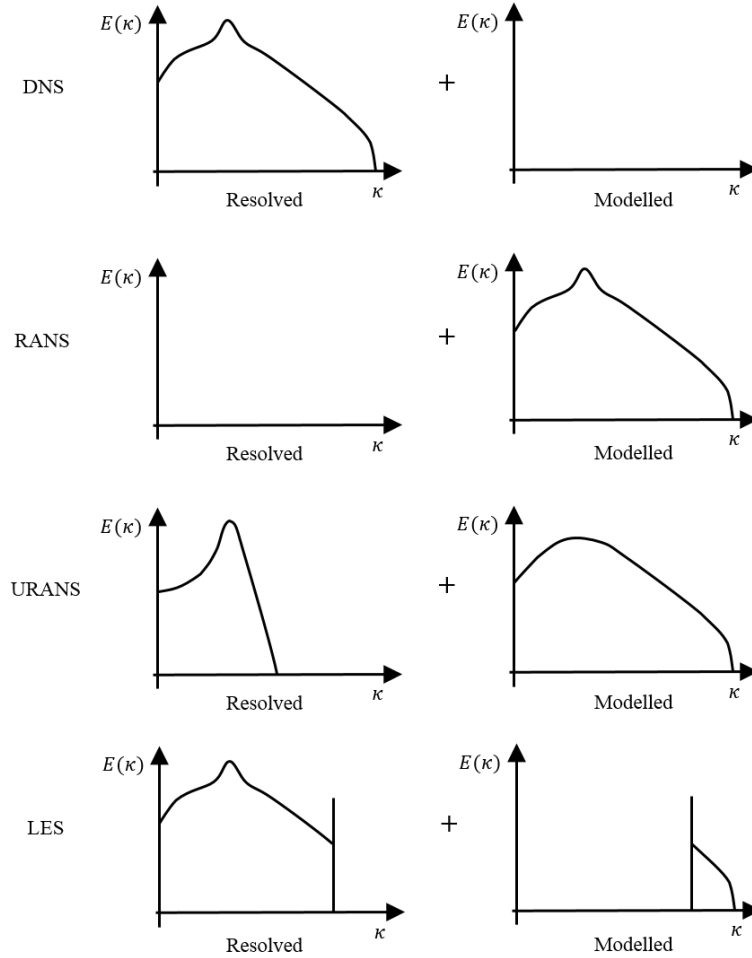


FIGURE 2.9. Decomposition of the energy spectrum of the solution associated with different computational methods.

The RANS approach stems from the Reynolds average as shown in Eq. 2.1 where the instantaneous flow variable is decomposed into a time-averaged part and a fluctuating part. Then the time-averaged part is calculated directly, and the effect of fluctuating part is modelled. Therefore, as shown in Fig. 2.9, RANS is a complete opposite to DNS, as it models all turbulent kinetic energy by a turbulence model. RANS uses the least computational effort among the methods shown in Fig. 2.9 and it has been used mostly for engineering calculations [62]. The statistical solution, however, prevents a fine description of the physical mechanisms. This approach, therefore, is not usable for fundamental studies.

A variant of RANS is called unsteady RANS (URANS). Its decomposition of flow variables follows Eq. 2.3, i.e. the time-averaged flow variable changes with time. Thus, URANS contains more information than RANS, especially when a predominant low frequency exists in the flow field. Nevertheless, due to modelling most turbulent kinetic

energy, URANS is not able to capture most flow structures apart from the the ones contributing to the predominant frequency of the flow.

LES falls in between DNS and RANS. LES does not have any averaging, rather, it introduces a filter with certain spatial cut-off length to filter the high frequency motions out and only calculate the low frequency motion in the space. This process can be found in Fig. 2.9. The high frequency motion is effectively the small eddies. Their effect on the flow field is modelled by a SGS model. Therefore, the size of the cut-off length should locate within the range of inertial subrange in which the eddies are assumed by Kolmogorov to be isotropic and solely characterised by ϵ , yet being able to resolve under a lower resolution than DNS. LES is able to return more complete information of the flow field, i.e. a three-dimensional time-dependent solution of the governing equations. This is because the contribution of the large energy-carrying structures to momentum and energy transfer is computed directly and the effects of only the small structures are modelled.

If referring to the energy spectrum plot in Fig. 2.5, it is found that the grid size of the URANS method can be located in the energy containing range, as it only captures the mean flow and some turbulent scales. However, the grid size of DNS is required to locate within the dissipation range, as it needs to resolve all the turbulent structures. Given the x -axis in the plot is log scale, the grid size of LES, which falls in the inertial subrange, can be larger than DNS and smaller than URANS by one to two orders of magnitude depending on Re . Therefore, LES is perfectly suited for studying a fundamental problems with a relatively lower computing resource.

2.3 Summary

Past studies on various corrugated channels have been reviewed. A comparison between well studied geometries and the geometry in current research reveals that the latter assembles many of the interesting features of the previous cavities. Unlike the periodic hill and the sinusoidal wavy shape, the geometry to be studied in this research does not have a flow reattachment at the bottom of the corrugation. Instead, similar to the square shape, it has a large vortex formed in the corrugation that ejects out from time to time. Yet, its flow separates on the curved surface, unlike the geometry inducted separation for the square shape. In addition, the smaller length-to-height ratio may cause stronger flow ejection for current geometry than any of the previously studied geometries. Finally, the side wall may bring some unexpected effects to the flow field.

Turbulence is the dominant physics in the corrugated channels and its computational

strategies are compared. Combing the findings in the literature, the RANS method cannot accurately predict the separation location so that it fails to capture main characteristics of the cavity with curved wall. The RANS calculation carried out by Unal et al. [8] on the same geometry with the current study confirmed this. On the other hand, DNS has been used on the study of cavities with a curved surface, but its high demand on computing power limited its usage to fairly low Re . The review also shows LES has been more extensively used than DNS to study the flow features in corrugated walls and is recognised to have a high accuracy. For these reasons, LES is used as the computational method in the current numerical study.

Chapter 3

Governing Equations and Models

Having investigated the characteristics of turbulence and selected LES as the tool to numerically study the corrugated channel flow, it is necessary to turn the focus to the principles of LES and its relevant modelling approaches.

This chapter starts with an introduction of the principle of LES, followed by an overview of LES Governing equations. A comprehensive review of currently available and dominant Eddy Viscosity SGS models is then given together with a detailed investigation and comparison of their pros and cons. The variety of LES, such as Hybrid-LES will also be briefly discussed. Finally, the selected SGS models for current research are presented.

3.1 Principle of Large Eddy Simulation (LES)

The LES approach was first proposed by Smagorinsky in 1963 [84]. Due to the limited computational resources, it has only been widely developed in recent decades [85]. According to the theory of Kolmogorov [86], the smallest scales of motion were isotropic. In addition, the function of these small scales is assumed to mainly drain energy from the larger scales, suggesting that these small scales can be successfully approximated. The principle of LES is fundamentally different from RANS. RANS uses a time or ensemble averaging approach and solves with additional transport equations to calculate the resulting Reynolds stresses. In LES, The large scales motion (large eddies) which contain most of the energy (thereby strongly related with boundary conditions) are calculated directly. Meanwhile, the small eddies of SGS are represented by a model. LES is much more accurate than RANS as the characteristics of large eddies which are energy intensive and carry out most of momentum transport and turbulent mixing can be fully captured while they are completely modelled in the RANS approach [62].

3.2 LES Governing Equations

3.2.1 Filtering Function

In LES, any flow variable or function $\varphi(\mathbf{x}, t)$ can be defined as a combination of a large scale and a small scale as shown in Eq 3.1

$$\varphi(\mathbf{x}, t) = \bar{\varphi}(\mathbf{x}, t) + \varphi'(\mathbf{x}, t) \quad (3.1)$$

where the overbar denotes the larger scales (resolved scales), while the prime represents the small scales (modelled scale).

In order to extract the large scale components (separated from small scales), a filter function or kernel, $G(\mathbf{x}, \mathbf{x}', \Delta)$, is introduced to conduct spatially filtering which is defined as Eq 3.2 [87]

$$\bar{\varphi}(\mathbf{x}, t) = \int_{-\infty}^{\infty} \int_{-\infty}^{\infty} \int_{-\infty}^{\infty} G(\mathbf{x}, \mathbf{x}', \Delta) \varphi(\mathbf{x}, t) dx'_1 dx'_2 dx'_3 \quad (3.2)$$

Where:

Δ = filter or cutoff width;

$\bar{\varphi}(\mathbf{x}, t)$ = filtered function for spatial variations larger than Δ ;

$\varphi(\mathbf{x}, t)$ = original function.

The filter function $G(\mathbf{x}, \mathbf{x}', \Delta)$ has to satisfy the following property in order to manipulate the NSEs [62]:

1. Conservation of constants:

$$\bar{a} = a \Leftrightarrow \int_{-\infty}^{\infty} \int_{-\infty}^{\infty} \int_{-\infty}^{\infty} G(\mathbf{x}, \mathbf{x}', \Delta) dx'_1 dx'_2 dx'_3 = 1 \quad (3.3)$$

2. Linearity

$$\overline{\varphi_1 + \varphi_2} = \bar{\varphi}_1 + \bar{\varphi}_2 \quad (3.4)$$

3. Commutation with derivation or differentiation

$$\overline{\frac{\partial \varphi(\mathbf{x}, t)}{\partial s}} = \frac{\partial \overline{\varphi(\mathbf{x}, t)}}{\partial s}, \quad s = \mathbf{x}, t \quad (3.5)$$

The filter or cutoff width, Δ , which is introduced in Eq 3.2 is a characteristic length scale which determines the size of eddies in resolved-grid scale (RGS). There will be retained in the flow field to be directly resolved by the NSE, while eddies with a length scale smaller than Δ are of SGS will be represented by modelling. It is noteworthy that the

overbar in Eq 3.2 denotes spatial filtering which is an integration in 3D space rather than time-averaging in RANS which is an integration in the time domain.

Three filters are commonly used in LES for spatial scale separation [62]:

1. Box or Top-hat filter:

$$G(\mathbf{x}, \mathbf{x}', \Delta) = \begin{cases} \frac{1}{\Delta^3} & |\mathbf{x} - \mathbf{x}'| \leq \Delta/2 \\ 0 & |\mathbf{x} - \mathbf{x}'| \geq \Delta/2 \end{cases} \quad (3.6)$$

This is an average over a rectangular (box) region.

2. Gaussian filter:

$$G(\mathbf{x}, \mathbf{x}', \Delta) = \sqrt{\frac{6}{\pi\Delta^2}} \exp\left(-\frac{6|\mathbf{x} - \mathbf{x}'|^2}{\Delta^2}\right) \quad (3.7)$$

This filter was introduced in the finite difference method (FDM) by the Stanford group. It is smooth and differentiable. Over a long period, it has been the research focus of LES and its theory and modelling have been well established [72].

3. Spectral or sharp cutoff filter:

$$G(\mathbf{x}, \mathbf{x}', \Delta) = \prod_{i=1}^3 \frac{\sin[(x_i - x'_i)/\Delta]}{(x_i - x'_i)} \quad (3.8)$$

This filter is applied together with spectral methods which use Fourier series to describe the flow variables. This filter eliminates all the wave numbers above a chosen frequency and gives a sharp cutoff in the energy spectrum at a wavelength of Δ/π . This filter has an advantage in terms of separation of the large and small eddy scales, but it is difficult to apply to inhomogeneous flow. So the spectral method cannot be used in general-purpose CFD [72].

There also are two options for filtering operation: Explicit and implicit filtering. “Explicit filtering” applies a filter such as a Gaussian one with arbitrary filter size Δ on the flow governing equations. “Implicit filtering” can be regarded as applying a box filter with Δ directly related to grid spacing [85]. In the finite volume method (FVM), it is pointless to choose a Δ smaller than the grid size since the value of flow variable $\varphi(\mathbf{x}, t)$ is stored as a single cell centre value on each grid cell, or face centre value at the boundary, destroying the details of the finer resolution. Therefore, “implicit filtering” is adopted in the current research. A box filter with cutoff width Δ to be of the same order as the grid size will be imposed on the flow governing equation. In a three-dimensional flow domain, Δ is ordinarily defined as the cube root of grid cell volume

$$\Delta = \sqrt[3]{\Delta x \Delta y \Delta z} = \sqrt[3]{V_{cell}} \quad (3.9)$$

Where Δx , Δy and Δz are length, width and height of the grid cells.

In short, eddies with length scale larger than grid size (Δ) are classified as ‘‘large eddy’’ and will be calculated directly, while the eddy smaller than Δ are in SGS and will be modelled.

3.2.2 Filtered Navier-Stokes Equations

Recall the incompressible, unsteady NSEs for a fluid with constant kinematic viscosity, ν , in Cartesian coordinates

$$\nabla \cdot \mathbf{u} = 0 \quad (3.10a)$$

$$\frac{\partial u}{\partial t} + \nabla \cdot (u\mathbf{u}) = -\frac{\partial p}{\partial x} + \nu \nabla^2 u \quad (3.10b)$$

$$\frac{\partial v}{\partial t} + \nabla \cdot (v\mathbf{u}) = -\frac{\partial p}{\partial y} + \nu \nabla^2 v \quad (3.10c)$$

$$\frac{\partial w}{\partial t} + \nabla \cdot (w\mathbf{u}) = -\frac{\partial p}{\partial z} + \nu \nabla^2 w \quad (3.10d)$$

where p is kinematic pressure obtained as static pressure, P , divided by density, ρ .

By applying a uniform filter (whose filtering function satisfies the properties of linearity and commutation with differentiation) with respect to space and time, one can derive LES NSEs as

$$\nabla \cdot \bar{\mathbf{u}} = 0 \quad (3.11a)$$

$$\frac{\partial \bar{u}}{\partial t} + \nabla \cdot (\overline{u\mathbf{u}}) = -\frac{\partial \bar{p}}{\partial x} + \nu \nabla^2 \bar{u} \quad (3.11b)$$

$$\frac{\partial \bar{v}}{\partial t} + \nabla \cdot (\overline{v\mathbf{u}}) = -\frac{\partial \bar{p}}{\partial y} + \nu \nabla^2 \bar{v} \quad (3.11c)$$

$$\frac{\partial \bar{w}}{\partial t} + \nabla \cdot (\overline{w\mathbf{u}}) = -\frac{\partial \bar{p}}{\partial z} + \nu \nabla^2 \bar{w} \quad (3.11d)$$

where \bar{p} is the filtered kinematic pressure, \bar{u} , \bar{v} and \bar{w} are x , y and z direction components of filtered velocity vector $\bar{\mathbf{u}}$.

As in RANS, the filtered momentum Equations (3.11b to 3.11d) create a non-linear convective term $\nabla \cdot (\overline{\varphi\mathbf{u}})$. This term can be easily rearranged as

$$\nabla \cdot (\overline{\varphi\mathbf{u}}) = \nabla \cdot (\varphi\bar{\mathbf{u}}) + \nabla \cdot (\overline{\varphi\mathbf{u}} - \varphi\bar{\mathbf{u}}) \quad (3.12)$$

It is clear that the 1st term in the r.h.s of the above equation can be calculated from the filtered field, whereas the second term needs to be modelled. By substituting Eq 3.12 into Eq 3.11b to 3.11d, one can obtain the LES momentum equations

$$\frac{\partial \bar{u}}{\partial t} + \nabla \cdot (\bar{u}\bar{\mathbf{u}}) = -\frac{\partial \bar{p}}{\partial x} + \nu \nabla^2 \bar{u} - \nabla \cdot (\overline{u\mathbf{u}} - \bar{u}\bar{\mathbf{u}}) \quad (3.13a)$$

$$\frac{\partial \bar{v}}{\partial t} + \nabla \cdot (\bar{v}\bar{\mathbf{u}}) = -\frac{\partial \bar{p}}{\partial y} + \nu \nabla^2 \bar{v} - \nabla \cdot (\overline{v\mathbf{u}} - \bar{v}\bar{\mathbf{u}}) \quad (3.13b)$$

$$\underbrace{\frac{\partial \bar{w}}{\partial t}}_{(I)} + \underbrace{\nabla \cdot (\bar{w}\bar{\mathbf{u}})}_{(II)} = -\underbrace{\frac{\partial \bar{p}}{\partial z}}_{(III)} + \underbrace{\nu \nabla^2 \bar{w}}_{(IV)} - \underbrace{\nabla \cdot (\overline{w\mathbf{u}} - \bar{w}\bar{\mathbf{u}})}_{(V)} \quad (3.13c)$$

where terms (I) are the rate of change of the filtered velocity of the x , y and z directions; terms (II) are the filtered convective fluxes of the x , y and z directions; terms (III) are the filtered pressure gradients of the x , y and z directions; terms (IV) are the filtered diffusive fluxes of the x , y and z directions; and terms (V) are the terms caused by filtering, which can be rewritten into suffix notation as

$$\nabla \cdot (\overline{u_i\mathbf{u}} - \bar{u}_i\bar{\mathbf{u}}) = \frac{\partial (\overline{u_i u_j} - \bar{u}_i \bar{u}_j)}{\partial x_j} \quad (3.14)$$

Then the kinematic SGS stresses can be introduced as

$$\tau_{ij} = \overline{u_i u_j} - \bar{u}_i \bar{u}_j = \overline{u_i \mathbf{u}} - \bar{u}_i \bar{\mathbf{u}} \quad (3.15)$$

where kinematic SGS stresses, equal SGS stresses divided by density, are normally used in calculating incompressible flow in which density is constant.

The SGS stresses are introduced by a filtering operation. It is easy to see that when $\Delta \rightarrow 0$, $\tau_{ij} \rightarrow 0$. As the mesh is refined, the model effect from τ_{ij} will decrease. Eventually DNS will be reached if the numerical order is sufficiently high. Although SGS stresses look similar to Reynolds stresses in RANS, their attributes are different:

1. SGS stresses only account for much smaller portions of turbulent energy in a flow domain than Reynolds stresses, so the accuracy of the model is not as demanding as in RANS calculation;
2. SGS stresses contain further contributions.

In order to have an insight of the contributions in SGS stresses, one can substitute the decomposition of $\varphi(\mathbf{x}, t)$ in Eq 3.1 into τ_{ij} to obtain

$$\tau_{ij} = \overline{(\bar{u}_i + u'_i)(\bar{u}_j + u'_j)} - \bar{u}_i \bar{u}_j = \underbrace{\overline{\bar{u}_i \bar{u}_j} - \bar{u}_i \bar{u}_j}_{L_{ij}} + \underbrace{\overline{\bar{u}_i u'_j} + \overline{u'_i \bar{u}_j}}_{C_{ij}} + \underbrace{\overline{u'_i u'_j}}_{R_{ij}} \quad (3.16)$$

This process is referred to as the Leonard or triple decomposition [62]. There are three terms in Eq 3.16

1. L_{ij} = Leonard stresses

This term represents interaction among the large scales. It can be calculated from the resolved velocity field. A method has been given by Leonard to calculate it from the filtered flow field [88].

2. C_{ij} = Cross stresses

This term reflects the interaction between large and small scales. It relates to the energy transfer between the two scales, although the energy can be transferred in either direction, transfer from large to small scale is dominant. Ferziger [89] developed an approximate method for this term.

3. R_{ij} = LES Reynolds stresses

This term expresses the interaction along the small scales and needs to be modelled.

Strictly speaking, the SGS model only deals with LES Reynolds stresses, however, even though the features of the three stresses are different, the decomposition of SGS stresses was almost abandoned leaving the whole SGS stresses τ_{ij} to be modelled as a single SGS model [90]. This may be attributed to the observation that the accumulated errors from an approximation of each term have a greater negative effect on the model accuracy than modelling as a whole [91].

3.3 Sub-grid Scale (SGS) Model

After over 50 years of development, many kinds of SGS models have been proposed and developed. They can be classified into several groups, such as eddy viscosity models (EVM) by Berselli et al. [92], gradient (Taylor) models by Clark et al. [93], rational models by Gladi and Layton [94] and scale similarity models by Bardina et al. [95]. Current research will only focus on the eddy viscosity approach because it is the most widely used SGS closure approach.

3.3.1 Principle of Eddy Viscosity SGS Model

The theory of SGS EVM is rooted in RANS modelling. It is based on the presumption that the function of viscous stresses is analogous to Reynolds stresses in RANS. It is well known that in Newton's law of viscosity for incompressible flow

$$\tau_{ij}^{Newtonian} = 2\nu S_{ij} = \nu \left(\frac{\partial u_i}{\partial x_j} + \frac{\partial u_j}{\partial x_i} \right) \quad (3.17)$$

It has been found that the turbulent stresses increase as the mean rate of deformation increases [72]. The Boussinesq hypothesis proposed that the Reynolds stress in RANS is proportional to the mean rates of deformation

$$\tau_{ij}^{RANS} = -\overline{u_i'' u_j''} = \nu_t \langle S_{ij} \rangle = \nu \left(\frac{\partial \langle u_i \rangle}{\partial x_j} + \frac{\partial \langle u_j \rangle}{\partial x_i} \right) - \frac{2}{3} k \delta_{ij} \quad (3.18)$$

where u_i'' , u_j'' and u_k'' are the fluctuating components (modelled); $\langle u_i \rangle$, $\langle u_j \rangle$ and $\langle u_k \rangle$ are the mean components of velocity (calculated); $\mathbf{u} = \langle u_i \rangle + u_i''$; $k = \frac{1}{2} \langle u_i''^2 \rangle$ is the turbulent kinetic energy per unit mass; ν_t is the turbulent or eddy viscosity in RANS; and δ_{ij} is the Kronecker delta. Details of the derivation of Reynolds stress can be consulted in general CFD textbooks [72].

The underlying assumption of EVMs is that turbulence kinematic viscosity (or SGS kinematic viscosity in LES) ν_t is isotropic which means the ratios between Reynolds stresses (or SGS kinematic stresses in LES) and mean rate of deformation (or resolved strain rate in LES) are the same in all directions. Although this assumption cannot hold true in many complex flows, it has been proven to give a good prediction accuracy on a wide range of flow types [96].

On dimensional grounds, it is assumed that ν_t can be expressed as a product of a turbulent velocity scale, ϑ , and a turbulent length scale, ℓ , as

$$\nu_t = C\vartheta\ell \quad (3.19)$$

where C is a dimensionless constant. Therefore, in EVM, an appropriate representation of ϑ and ℓ is required to obtain ν_t (or ν_{sgs} in LES), and then solve the unclosed NSEs.

3.3.2 Standard Smagorinsky SGS model

Boussinesq's hypothesis assumes that the turbulence production and dissipation are in balance, i.e. equilibrium, and the turbulence structure at small scale should be largely isotropic. Smagorinsky [84] suggested that due to small turbulent eddies being more isotropic and dissipating its energy which is transferred from resolved scales, Boussinesq's EVM is likely to give good representation for the SGS eddies. The SGS stresses are modelled as

$$\tau_{ij}^{SGS} = \overline{u'_i u'_j} = -2\nu_{sgs}\bar{S}_{ij} + \frac{1}{3}\tau_{ii}\delta_{ij} = -\nu_{sgs}\left(\frac{\partial\bar{u}_i}{\partial x_j} + \frac{\partial\bar{u}_j}{\partial x_i}\right) + \frac{1}{3}\tau_{ii}^{SGS}\delta_{ij} \quad (3.20)$$

where ν_{sgs} is SGS kinematic turbulent viscosity, $\bar{S}_{ij} = \frac{1}{2}\left(\frac{\partial\bar{u}_i}{\partial x_j} + \frac{\partial\bar{u}_j}{\partial x_i}\right)$ is the strain rate of the resolved flow and the term $\frac{1}{3}\tau_{ii}^{SGS}\delta_{ij}$ ensures the sum of modelled normal SGS stresses is equal to the kinetic energy of the SGS eddies.

Following Prandtl's mixing length model equation (Eq 3.19), the Smagorinsky-Lilly SGS model proposed

$$\ell = \Delta, \quad \vartheta = \Delta \times |\bar{S}| \quad (3.21)$$

then, ν_{sgs} can be described as

$$\nu_{sgs} = (C_s\Delta)^2|\bar{S}| \quad (3.22)$$

where $|\bar{S}| = \sqrt{2\bar{S}_{ij}\bar{S}_{ij}} = \sqrt{2(\bar{S}_{11}^2 + \bar{S}_{22}^2 + \bar{S}_{33}^2 + 2\bar{S}_{12}^2 + 2\bar{S}_{13}^2 + 2\bar{S}_{23}^2)}$ is the average strain rate of the resolved flow, Δ is the filter cutoff length and chosen as the cubic root of the cell volume; and C_s is the Smagorinsky constant, its value varies from 0.11 to 0.22 depending on the flow type [97]. In OpenFOAM v1612, the value is taken as 0.168 [98]. Thus, in the Smagorinsky SGS Model (SMAG), the SGS stresses is expressed as

$$\tau_{ij}^{SGS} = -2(C_s\Delta)^2|\bar{S}|\bar{S}_{ij} + \frac{1}{3}\tau_{ii}^{SGS}\delta_{ij} \quad (3.23)$$

Since this model only utilises an algebraic formulation to represent ν_{sgs} without involving any transport equation, it is also referred to as an algebraic or zero equation SGS

Model. It has high stability and simplicity [99] and is the simplest and most commonly used model in the EVM group [65].

3.3.3 k -equation SGS Model

The Smagorinsky SGS model is based on the equilibrium assumption which in theory only works well in the situation that resolved flow changes very slowly and small eddies can dissipate the energy received from resolved scales instantaneously. However, in real industrial applications non-equilibrium conditions are extremely common, such as free shear layers, separation and reattachment. So one can borrow the turbulence models in RANS that adds transport equations to account for the transport effect of one or more SGS turbulence parameters. The simplest model of this kind is the k -equation SGS model (KEQ).

KEQ solves a transport equation for one or more SGS quantity to evaluate the velocity scale, ϑ , and length scale, ℓ , then obtain the SGS eddy viscosity to close the governing equations. In 1975 Schumann [100] proposed the first KEQ for SGS kinetic energy

$$k_{sgs} = \frac{1}{2} \sum_{n=1} \tau_{ii}^{SGS} = \frac{1}{2} (\overline{u'^2} + \overline{v'^2} + \overline{w'^2}) \quad (3.24)$$

The KEQ incorporates rate of change, convection, diffusion, production and dissipation of SGS turbulent kinetic energy. The form adopted in OpenFOAM v1612 is from the work of Yoshizawa [101]

$$\frac{\partial k_{sgs}}{\partial t} + \nabla \cdot (k_{sgs} \bar{\mathbf{u}}) = \nabla \cdot \left(\frac{\nu + \nu_{sgs}}{\sigma_k} \nabla k_{sgs} \right) + 2\nu_{sgs} \bar{S}_{ij} \cdot \bar{S}_{ij} - \epsilon_{sgs} \quad (3.25)$$

where ν is molecular viscosity, $\sigma_k = 1$ [72] and ϵ_{sgs} is the SGS turbulent kinetic energy dissipation rate and

$$\epsilon_{sgs} = C_s^{eps} \frac{k_{sgs}^{3/2}}{\Delta} \quad (3.26)$$

where $C_s^{eps} = 1.048^1$ [101].

In this model SGS eddies Length scale ℓ is still equal to Δ , while the velocity scale ϑ is evaluated by square root of the SGS turbulent kinetic energy $\sqrt{k_{sgs}}$ rather than $\Delta \times |\bar{S}|$ used in SMAG. Therefore, the formulation of SGS eddy viscosity is

$$\nu_{sgs} = C_s^k \Delta \sqrt{k_{sgs}} \quad (3.27)$$

¹In the work of Fureby et al. [102], $C_s^{eps} = 1$.

where $C_s^k = 0.094^2$ [101]. Thus SGS stresses in KEQ are calculated as

$$\tau_{ij} = -2C_s^k \Delta \sqrt{k_{sgs}} \bar{S}_{ij} + \frac{1}{3} \tau_{ii}^{SGS} \delta_{ij} \quad (3.28)$$

Although, theoretically, under equilibrium condition the SMAG and KEQ should provide similar results, it was reported by Fureby et al [102] that KEQ is more effective and superior to SMAG.

van Driest damping function

One drawback of SMAG and KEQ is that there is no universal value of C_s in the fluid domain. So ν_{sgs} does not become 0 in the viscous sublayer where the flow is laminar. C_s is suggested to be in the range of 0.17 and 0.21 in the inertial subrange, while due to an excessive eddy viscosity predicted from the mean shear it was reported that the near-wall region was too dissipative [103] and spurious dissipation generated by this model dampens the perturbations which stop transition to the turbulence phase. C_s is suggested to be 0.1 in this region [104, 105]. One way of solving it is to couple the SMAG and KEQ models with the van Driest damping function (VD) [106] to reduce ν_{sgs} as the flow approach the wall.

The form used in OpenFOAM v1612 is

$$\Delta = \min \left(\Delta_{mesh}, \left(\frac{\kappa_v}{C_\Delta} \right) \right) y \left(1 - e^{-y^+/A^+} \right) \quad (3.29)$$

rather than the form suggested by Ferziger and Peric [107] which modifies C_s while approaching the wall.

In Eq. 3.29, Δ_{mesh} is the cubic root of cell volume; $\kappa = 0.4187$ is the von Karman constant; $C_\Delta = 0.158$, $A^+ = 26$; y is the distance from the wall; and y^+ is the dimensionless distance from the wall calculated the wall shear stress [108]. The SMAG and KEQ models which are used in conjunction with the van-Driest damping function are referred to as SMAG+VD and KEQ+VD, respectively.

Dynamic Lagrangian SGS model

Although the van Driest damping function is widely used together with SMAG and KEQ, it directly links the distance from the wall which is problematic in the case of complex geometries such as curved boundaries and corners. C_s is a dynamical variable that adjusts

²The value is same as the one proposed by Schumann [100], but in the work of Fureby et al. [102], $C_s^k = 0.05$.

itself to each flow [97]. Due to different effects from main flow strain and shear plus the anisotropy of small eddies, run-time adjustment of C_s is required to improve the prediction accuracy.

To overcome the negative effect of the variability of C_s in LES, the dynamic Smagorinsky SGS model (DySMAG) was firstly introduced by Germano and co-workers in 1992 [109] to compute the local value of C_s based on the energy content of the smallest resolved scale rather than a priori. This model is based on the scale-similarity Model [95] which assumes the interaction between smallest resolved eddies (with the size of Δ) and both slightly larger resolved eddies (with the size of 2Δ) and SGS eddies is similar. Therefore, the C_s calculated between the eddies with size of Δ and 2Δ should be similar to the value calculated between eddies with size of Δ and SGS eddies.

In DySMAG, apart from the cutoff filter Δ originally imposed on NSEs which generates SGS stresses

$$\tau_{ij} = \overline{u_i u_j} - \bar{u}_i \bar{u}_j \quad (3.30)$$

a new test filter with cutoff width of Δ^{test} (normally $\Delta^{test} = 2\Delta$ [72]) will also be applied on filtered NSEs to introduce SGS stresses in the test filter level as

$$\tau_{ij}^{test} = \widetilde{\overline{u_i u_j}} - \tilde{u}_i \tilde{u}_j \quad (3.31)$$

The Leonard stresses L_{ij}^{test} part of SGS stresses τ_{ij}^{test} at test filter level can be calculated from the resolved field of LES as

$$L_{ij}^{test} = \widetilde{\overline{\tilde{u}_i \tilde{u}_j}} - \tilde{u}_i \tilde{u}_j \quad (3.32)$$

Then one can obtain

$$L_{ij}^{test} = \tau_{ij}^{test} - \tilde{\tau}_{ij} \quad (3.33)$$

which is called the Germano identity. By applying the Smagorinsky model on both τ_{ij} and τ_{ij}^{test} , after rearrangement, one can get [110]

$$L_{ij}^{test} = C_s^2 M_{ij} + \frac{1}{3} L_{kk} \delta_{ij} \quad (3.34)$$

where

$$M_{ij} = -2\Delta^{test2} |\tilde{S}| \tilde{S}_{ij} + 2\Delta^2 \widetilde{|\tilde{S}| \tilde{S}_{ij}} = 2\Delta^2 (\widetilde{|\tilde{S}| \tilde{S}_{ij}} - 4|\tilde{S}| \tilde{S}_{ij}) \quad (3.35)$$

Lilly [110] proposed a least squares approach to calculate local value of C_s as

$$C_s = \sqrt{\frac{\langle L_{ij}^{test} M_{ij} \rangle}{\langle M_{ij} M_{ij} \rangle}} \quad (3.36)$$

where $\langle \rangle$ denotes an appropriate averaging procedure, whose purpose is to remove or smooth the sharp fluctuation of local C_s . DySMAG achieved a significant improvement in LES and solved a troublesome issue in the Smagorinsky SGS Model: in high shear and near wall regions the Dynamic SGS Model automatically adjusted the C_s , and eddy viscosity automatically changed to 0 in the laminar region.

However, it was found [72, 95, 109] that early dynamic SGS models can predict huge or negative eddy viscosity. Locally negative eddy viscosity indicates an energy backscatter and is a physically plausible feature. This is because DNS data [111] confirmed that the forward and backward energy cascades are within the same order of magnitude but the former is larger giving an overall energy transfer from large to small eddies. Nevertheless, the negative eddy viscosity predicted in DySMAG does not correspond to real physics of backscatter [102] and can cause instability in LES computation. The calculated C_s has a large auto-correlation time which means once it becomes negative in some region it may stay in a negative value for a very long time, causing the growth of local velocity fields, leading to a divergence of the total energy [112].

To alleviate this problem, several averaging procedures have been proposed. For flow with high homogeneity, the averaging will be conducted over a homogeneous direction [109]. For more complex flow, the averaging takes place over a small time interval [113]; or introducing an integral formulation of the Germano identity together with an equation for the SGS kinetic energy budget and solving them in every time-step [114]. In current research, the averaging procedure proposed by Meneveau and co-workers [115] is applied. It averages along the fluid-particle trajectories. In essence the dynamic Lagrangian model (DyLag) is solving two transport equations for the Lagrangian average of the tensor products $L_{ij}^{test} M_{ij}$ and $M_{ij} M_{ij}$ as \mathfrak{T}_{LM} and \mathfrak{T}_{MM} respectively

$$\frac{\partial \mathfrak{T}_{LM}}{\partial t} + \bar{\mathbf{u}} \cdot \nabla (\mathfrak{T}_{LM}) = \frac{1}{T} (L_{ij}^{test} M_{ij} - \mathfrak{T}_{LM}) \quad (3.37a)$$

$$\frac{\partial \mathfrak{T}_{MM}}{\partial t} + \bar{\mathbf{u}} \cdot \nabla (\mathfrak{T}_{MM}) = \frac{1}{T} (M_{ij} M_{ij} - \mathfrak{T}_{MM}) \quad (3.37b)$$

where the time scale T represents the memory length of the Lagrangian averaging and is proposed by Meneveau et al. [115] as

$$T = \theta \Delta (\mathfrak{T}_{LM} \mathfrak{T}_{MM})^{(-1/8)}; \quad \theta = 1.5. \quad (3.38)$$

the C_s is then evaluated as

$$C_s = \sqrt{\frac{\mathfrak{T}_{LM}}{\mathfrak{T}_{MM}}} \quad (3.39)$$

Dynamic k -equation SGS model

The dynamic k -equation SGS model (DyK) is the dynamic variant of the KEQ model [116]. This SGS model also evaluates ν_{sgs} and k_{sgs} by Eq. 3.27 and Eq. 3.25, respectively, but dynamically determines C_s^k and C_s^{eps} by [117]

$$C_s^k = \frac{L_{ij}^{test} M_{ij}}{2M_{ij} \widetilde{M}_{ij}} \quad (3.40a)$$

$$C_s^{eps} = \frac{(\nu_{sgs} + \nu)(\widetilde{S}_{ij} \widetilde{S}_{ij} - \widetilde{S}_{ij} \widetilde{S}_{ij})}{K_k^{3/2}/(2\Delta)} \quad (3.40b)$$

where

$$L_{ij}^{test} = \widetilde{u}_i \widetilde{u}_j - \widetilde{u}_i \widetilde{u}_j \quad (3.41a)$$

$$M_{ij} = -2\Delta \widetilde{S}_{ij} \sqrt{\max(K_k, 0)} \quad (3.41b)$$

$$K_k = \frac{1}{2}(\widetilde{u}_i \widetilde{u}_i - \widetilde{u}_i \widetilde{u}_i) \quad (3.41c)$$

The values of C_s^k and C_s^{eps} are kept positive, if a negative value occurs, the negative value will be replaced by the average of the positive value.

Wall-Adapting Local Eddy-viscosity SGS model

The Wall-Adapting Local Eddy-viscosity SGS model (WALE) was proposed by Nicoud & Ducros [118] to recover the $\nu_{sgs} = O(y^3)$ near wall scaling without using extra transport equation, damping functions as dynamic procedures. This model also calculates ν_{sgs} by Eq. 3.27 and keeps the constant $C_s^k = 0.094$, but instead of solving a transport equation for k_{sgs} , it uses an algebraic formulation

$$k_{sgs} = \left(\frac{C_w^2 \Delta}{C_k} \right)^2 \frac{\left(\overline{S}_{ij}^d \overline{S}_{ij}^d \right)^3}{\left[\left(\overline{S}_{ij} \overline{S}_{ij} \right)^{5/2} + \left(\overline{S}_{ij}^d \overline{S}_{ij}^d \right)^{5/4} \right]^2} \quad (3.42)$$

where

$$\overline{S}_{ij}^d = \frac{1}{2} \left(\frac{\partial \overline{u}_k}{\partial x_i} \frac{\partial \overline{u}_j}{\partial x_k} + \frac{\partial \overline{u}_k}{\partial x_j} \frac{\partial \overline{u}_i}{\partial x_k} \right) - \frac{1}{3} \delta_{ij} \frac{\partial \overline{u}_k}{\partial x_l} \frac{\partial \overline{u}_l}{\partial x_k} \quad (3.43)$$

and the constant $C_w = 1.048$

3.3.4 Reynolds Stresses SGS Model

The aforementioned SGS models are all based the Boussinesq hypothesis which assumes the SGS eddy viscosity has no direction preference (isotropic) and the SGS stresses can be expressed by a SGS eddy viscosity and the strain rate of resolved flow. Although this assumption can provide good predictions in many kinds of flow, the universal validity of this theory is still questionable. Challenging the assumption will naturally lead to Reynolds Stress SGS models (RSSM). This is similar to its counterpart in RANS modelling, using transport equations to directly calculate SGS stresses. The model was first derived by Deardorff [119] in 1973. In this model six transport equations for each SGS stress are solved along with a modelled isotropic dissipation rate and a total of 18 empirical constants. Also, ν_{sgs} still appears in each transport equation and is modelled in the same way in the k -equation SGS model. Therefore, it can be classified as half EVM. Theoretically, it should be the model with the potential to predict SGS stresses most accurately, however, Fureby et al [120] reported that RSSM only gives a small improvement and predicted similar results to other EVM models at low and moderate Re and behaved more like an EVM model on a coarse mesh. Additionally, solving six transport equations is considerably more computationally expensive even in low Re channel flow. In addition, the number of model constants in RSSM may affect the universality of the model.

3.3.5 Conventional Hybrid Model

There is another group of LES methods which mostly focus on reducing computation cost rather than improving the LES model itself. Most of them are hybrid Models and share a common principle that large eddies are resolved away from walls (in the detached region) and the wall boundary layers (in the attached region) are covered by a RANS model. Examples of these Hybrid Models are summarised by Menter [121] and ANSYS [122] as detached eddy simulation (DES), wall-modelled LES (WMLES) and zonal or embedded LES (ZLES/ELES). These models are listed in Appendix A.

3.4 Model Selection

As aforementioned, each modelling approach has its pros and cons, but due to the fact that the current research is to numerically study the flow characteristics in a corrugated channel, the flow domain should be resolved as much as possible. To this end, the hybrid models and wall functions are excluded for the current study, as they will use RANS or predefined functions to model the flow features close to the wall which are key for the current study. The Reynolds stresses SGS model will also not be included because of its complexity and marginal accuracy gains. Therefore, only EVMs are selected to go through the validation test on a plane channel flow case. They are listed in Table 3.1 and include SMAG and KEQ, and their variants with van Driest Damping function and dynamic features, as well as the WALE models.

SGS Models	Model Description
SMAG	Smagorinsky
SMAG+VD	Smagorinsky SGS model with van-Driest wall damping function
DyLag	Dynamic Lagrangian SGS model
KEQ	k -equation SGS model
KEQ+VD	k -equation SGS model with van-Driest wall damping function
DyK	Dynamic k -equation SGS model
WALE	Wall-adapting local eddy-viscosity SGS model

TABLE 3.1. List of SGS models to be validated.

Chapter 4

Numerical Methods

The governing equations and models presented in the last chapter are only a comparatively small part of what constitutes a functional LES solution method. The process of obtaining the computational solution consists of two stages, discretisation and solution, which are collectively referred to as the numerical method. The first stage involves the conversion of the filtered Navier-Stokes equations, i.e. several sets of partial differential equations (PDEs) and auxiliary (boundary and initial) conditions into a system of discretised algebraic equations. The second stage is to solve the discretised algebraic equations by a method such as the Pressure Implicit with Split Operator (PISO) algorithm [123].

The selection of numerical methods follows the following principles. It is crucial to maintaining the order of accuracy of the discretisation method to minimise its error in the solution. Moreover, the methods are also required to be flexible enough to accommodate unstructured meshes and for application to complex geometries in engineering flows. Finally, the discretisation of the governing equations should facilitate efficient parallelisation, without which only very limited LES would be possible.

The numerical methods that are related directly to current research are presented in this Chapter. The description starts by recalling the governing equations and their form with the SGS model, followed by a comparison of different discretisation methods. Then the detailed discretisation of the governing equation will be given for each term. Finally, the solver used in the current LES is presented.

4.1 Governing Equations

In the current research, the SGS model will mainly be applied to aerodynamic cases at low Mach numbers. Therefore, incompressible and Newtonian flows with constant thermo-

physical properties are considered. The governing equations for current LES, which have been convoluted with a filter of uniform width, Δ , are given by

$$\nabla \cdot \bar{\mathbf{u}} = 0 \quad (4.1a)$$

$$\frac{\partial \bar{\mathbf{u}}}{\partial t} + \nabla \cdot (\bar{\mathbf{u}}\bar{\mathbf{u}}) = -\nabla \bar{p} + \nabla \cdot \nu \nabla \bar{\mathbf{u}} - \nabla \cdot \boldsymbol{\tau} \quad (4.1b)$$

Here, \bar{p} is filtered pressure divided by the constant density; $\bar{\mathbf{u}}$ is the filtered velocity vector; ν is kinematic viscosity; $\boldsymbol{\tau}$ are the SGS stress tensors which have to be modelled to close the system.

Then, due to $\nabla \cdot \bar{\mathbf{u}} = 0$ for incompressible flow, $\nabla \cdot \nu \nabla \bar{\mathbf{u}}^T$, where $\nabla \bar{\mathbf{u}}^T$ is the transpose of $\nabla \bar{\mathbf{u}}$, can be added into above equation without affecting its conservation property. As discussed in Chapter 3, the EVM will be applied, i.e. $\boldsymbol{\tau} = -\nu_{sgs}(\nabla \bar{\mathbf{u}} + \nabla \bar{\mathbf{u}}^T)$, therefore, Eq 3.13 is changed to

$$\frac{\partial \bar{\mathbf{u}}}{\partial t} + \nabla \cdot (\bar{\mathbf{u}}\bar{\mathbf{u}}) = -\nabla \bar{p} + \nabla \cdot \nu_{eff}(\nabla \bar{\mathbf{u}} + \nabla \bar{\mathbf{u}}^T) \quad (4.2)$$

where ν_{eff} is the sum of the kinematic and SGS viscosities.

4.2 Discretisation Method

The process of obtaining a numerical solution to a differential equation can be viewed in the same way as conducting an experiment. The physical quantity, flow velocity, for example, is measured at a set of discretised points in the domain of interest using a measurement device. A picture of the flow variation can then be constructed by connecting the measurement points allowing visualisation of the flow. If the flow quantities between the measurement points are required, some interpolation technique can be used which may be a linear or a higher order interpolation. This will depend on how far the points are from each other, or the required accuracy. Similarly, numerical techniques convert the continuous differential equation to the discretised points in space i.e. grid points, and find the solution on it.

Several discretisation methods are currently used for LES of engineering flows, including finite volume (FV), finite difference (FD), finite element (FE) [74, 91, 107, 124] which will be discussed and compared in this section. There are also other methods such as spectral methods and Lattice-Boltzmann methods, but they will not be discussed here, due to their limited application in complex engineering flow.

4.2.1 Finite Difference Method

The FD method is the oldest and simplest method for the discretisation of PDEs. It can be traced back to 1768 when Euler developed it for hand calculation of PDEs [124]. The flow variables are calculated and stored at each nodal point of the grid. Taylor series expansions are used to convert the PDEs of the governing equations into several sets of algebraic equations for flow solution at each grid point.

The FD method can theoretically be applied to any type of grid system and up to any degree of accuracy. However, the method is more commonly applied to structured grids due to its requirement of a high degree of mesh regularity, and limited grid stretching or distortion. Despite that the use of body-fitted coordinate system extends its usage to more complex shapes [124], generally, the FD structured grids are still constrained to the general coordinate systems, such as Cartesian grids with six-sided computational domains. It is also reported not to work well in the convection-dominated problem [124].

One of the major advantages of the FD method is its high-order accuracy [125] on regular grids. It therefore has some popularity in research-oriented investigations [126–129]. But, its main disadvantage is that the flow property is not usually conserved unless special care is taken [124] and the requirement of body fitted coordinates limits its application to

fairly complex cases [91]. For this reason, FD is not widely used in modern LES.

4.2.2 Finite Element Method

The FE method was initially developed for structural analysis between 1940 and 1960 to calculate stress and strain displacements, and then extended to CFD [74]. The FE method discretises the flow domain with non-overlapping cells called elements and the flow variables are stored at the nodes comprising the element. It can accommodate a wide range of element shapes, such as tetrahedral prisms and Hexahedrons. Therefore, unlike the FD method, it is suitable for irregular computational domains and able to handle complex arbitrary geometries [124].

Another distinguishing feature of the FE method is that a shape/interpolation/basis function needs to be selected in the FE method to represent the variation of the solution over the element. The derivative can then be written as a matrix of the nodal value and distance. The next step is to substitute this approximation into weighted residuals over the solution domain and make these equal to zero to generate sets of algebraic equations [74, 124].

The FE method has not been extensively used in CFD, although there are a number of codes available that employ it, such as FEniCS [130] and COMSOL [131]. This is mainly due to the fact that the FE method requires greater computational resources than the equivalent FV method [124]. Moreover, the formulation of the FE method does not guarantee the local conservation of flow variables, such as mass [91].

4.2.3 Finite Volume Method

The FV method was introduced in 1971 for two-dimensional flow and later extended to three-dimensional flow in 1973 by Rizzi and Inuoye [124]. Similar to the FE method, the FV method divides the computational domain into continuous and non-overlapping control volumes called cells. The scalar flow variables, such as p and ν_{sgs} are stored at the cell centre, and a vector variable, such as \mathbf{U} is either stored at the cell centre or at the surface surrounding the cell as the flow of flux [72]. The distinctive advantage of FV method over the FD and FE methods is that it discretises the integral form of the governing equation directly, so that by nature the FV method guarantees the conservation of flow properties for each cell, regardless of the cell shape [107]. Nevertheless, it does have disadvantages when compared to the FD method, i.e. third order approximation and above are more difficult to develop in three dimensions for the FV method [124].

From a practical Engineering application perspective, the FV method has more advantages than disadvantages. Firstly, it can accommodate any type of grid and handle very complex geometries without worrying about the conservation of flow variables. Secondly, no transformation of equations in terms of a body-fitted coordinate system is required as in FD method. Thirdly, second order accuracy is easily maintained for LES solution.

Governing Equations For Finite Volume Method

Taking account of the pros and cons of all methods discussed in this subsection, the FV method, which is employed in the majority of all CFD codes today, was found to offer the best balance between flexibility and accuracy and will be used in current research.

The governing equations Eq 4.1a and 4.2 (rearranged to incorporate ν_{eff}) represent the conservation of mass and momentum respectively and will be applied to an infinitesimal region of space. In the FV method, they are integrated over a control volume and in time to produce the integral form of the governing equations

$$\int_V \nabla \cdot \bar{\mathbf{u}} dV = \int_A \mathbf{n} \cdot \bar{\mathbf{u}} dA = 0 \quad (4.3a)$$

$$\int_t^{t+\Delta t} \left[\frac{\partial}{\partial t} \int_V \bar{\mathbf{u}} dV + \int_V \nabla \cdot (\bar{\mathbf{u}}\bar{\mathbf{u}}) dV - \int_V \nabla \cdot \nu_{eff} (\nabla \bar{\mathbf{u}} + \nabla \bar{\mathbf{u}}^T) dV \right] dt \quad (4.3b)$$

$$= - \int_t^{t+\Delta t} \left[\int_V \nabla \bar{p} \right] dt$$

where the A is the area of the entire surface of the control volume and dA represents an infinitesimal surface element. $\mathbf{n} \cdot \bar{\mathbf{u}}$ is the component of the vector $\bar{\mathbf{u}}$ in the direction of the outward unit vector \mathbf{n} normal to dA .

The above governing equation is second order, as a second derivative appears in the diffusion term [91]. It is recognised that the numerical discretisation scheme is one of the primary error sources for LES (with another one being the SGS modelling). Therefore, higher-order numerical schemes (at least second order) are desirable [132] which however are difficult to implement for the complex geometry. Hence, second order discretisation scheme are normally used for complex engineering configurations in order to balance the accuracy and practicability [85]. In addition, since the time steps for LES are normally small, the temporal discretisation are usually chosen to be second order as well, rather than higher order [85]. Details about the discretisation method used in current research are presented in Section 4.3.

4.3 Discretisation of Governing Equations

Discretisation in the current research involves spatial discretisation and temporal discretisation. In spatial discretisation, the space domain is sub-divided into a finite number of non-overlapping and contiguous control volumes (CVs) as seen in Fig. 4.1. The governing equations, i.e. Eq 4.3 is then discretised onto this mesh. The discretisation of time is done by breaking the total simulation time period into a set of time steps, Δt , whose size may be changed during the simulation as required by some calculation criteria.

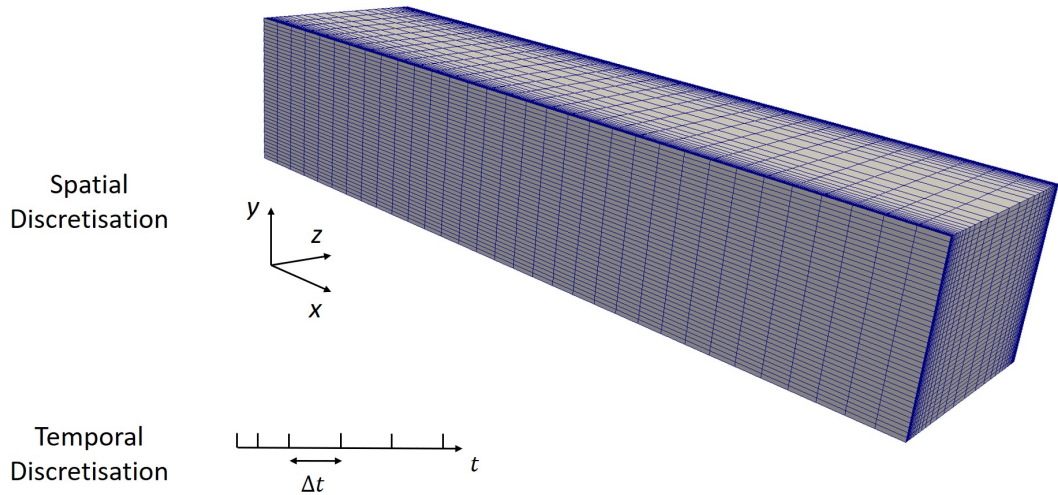


FIGURE 4.1. Discretisation of the solution domain.

A detailed view of two adjacent CVs is shown in Fig. 4.2. Each of these CV encapsulates a computational point at its centroid, such as point P for the left cell, at which dependent variables, such as $\bar{\mathbf{u}}$ and \bar{p} , etc., and other properties are stored. The CV is bounded by a number of flat faces, collectively referred to as A . These faces can have arbitrary shapes and unstructured alignments which provide greater flexibility in complex geometries. \mathbf{d} is the vector connecting adjacent cell centres P and Q , and \mathbf{n} is the face normal area vector for the common face between the cells.

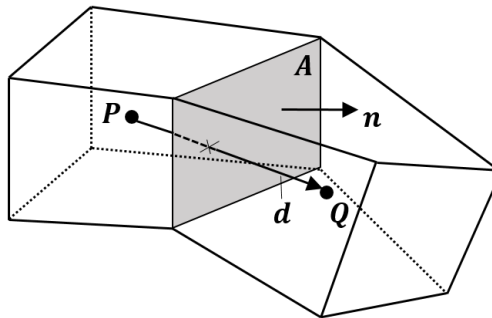


FIGURE 4.2. Control Volume for Finite Volume discretisation.

4.3.1 Spatial Discretisation

The governing equations (Eq. 4.3) are effectively transport equations, it is beneficial to examine the discretisation for each term of a generic transport equation. Recalling the integral form of the general transport equations

$$\underbrace{\frac{d}{dt} \int_{CV} \phi dV}_{\text{Temporal derivative}} + \underbrace{\int_{CV} \nabla \cdot (\bar{\mathbf{u}}\phi) dV}_{\text{Convective term}} - \underbrace{\int_{CV} \nabla \cdot (\Gamma_\phi \nabla \phi) dV}_{\text{Diffusion term}} = \underbrace{\int_{CV} S_\phi dV}_{\text{Source term}} \quad (4.4)$$

where ϕ is any transported variable, such as u or p ; Γ_ϕ is the diffusivity coefficient of this transported variable; S_ϕ is the source term in this equation. If all flow variables are assumed to vary linearly around the point \mathbf{P} and time t , one can get

$$\phi_{\mathbf{Q}} = \phi_{\mathbf{P}} + (\mathbf{X}_{\mathbf{Q}} - \mathbf{X}_{\mathbf{P}}) \cdot (\nabla \phi)_{\mathbf{P}} \quad (4.5a)$$

$$\phi^{(t+\Delta t)} = \phi^t + \Delta t \left(\frac{\partial \phi}{\partial t} \right)_t \quad (4.5b)$$

where $\phi_{\mathbf{Q}}$ and $\phi_{\mathbf{P}}$ are values of ϕ at point \mathbf{Q} and \mathbf{P} respectively, $\mathbf{X}_{\mathbf{Q}} - \mathbf{X}_{\mathbf{P}}$ is the distance between Point \mathbf{Q} and \mathbf{P} , $(\nabla \phi)_{\mathbf{P}}$ is the gradient of ϕ at point \mathbf{P} ; $\phi^{(t+\Delta t)}$ and ϕ^t are values of ϕ at time t and $t + \Delta t$ respectively, Δt is the time interval and $\left(\frac{\partial \phi}{\partial t} \right)_t$ is the time derivative of ϕ at time t .

Recalling Gauss's theorem

$$\int_{CV} \nabla \cdot \phi dV = \int_A \mathbf{n} \cdot \phi dA \quad (4.6)$$

indicates the surface integration needs to be performed over area A of the CV. As in Eq. 4.3, the physical interpretation of $\mathbf{n} \cdot \phi$ is the component of ϕ (if ϕ is a vector) in the direction of the outward unit vector \mathbf{n} normal to dA . Applying Gauss's theorem to Eq 4.4 gives

$$\frac{d}{dt} \int_{CV} \phi dV + \int_A \mathbf{n} \cdot (\bar{\mathbf{u}}\phi) dA - \int_A \mathbf{n} \cdot (\Gamma_\phi \nabla \phi) dA = \int_{CV} S_\phi dV \quad (4.7)$$

where A is the area of the entire cell surface bounding the CV and dA is an infinitesimal surface element belonging to A . The area integration is then performed over all surface elements to get

$$\frac{d}{dt} \int_{CV} \phi dV + \sum_{\text{all}} \int_{\Delta A_i} \mathbf{n}_i \cdot (\bar{\mathbf{u}}\phi) dA - \sum_{\text{all}} \int_{\Delta A_i} \mathbf{n}_i \cdot (\Gamma_\phi \nabla \phi) dA = \int_{CV} S_\phi dV \quad (4.8)$$

Where ΔA_i is the area of specific surface among the entire control surface, and \mathbf{n}_i is the normal unit vector to that specific surface. Each term in Eq 4.8 is treated separately in the following sections.

Convection Term

The convective term of Eq 4.8 is

$$\sum_{all} \int_{\Delta A_i} \mathbf{n}_i \cdot (\bar{\mathbf{u}}\phi) dA$$

The area integration is the summation of the integrals over all ΔA_i . Each of these integrals is evaluated as the dot product of \mathbf{n}_i and the multiplication between a convective flux vector $\bar{\mathbf{u}}\phi$ and ΔA_i . The convective flux parameter F_i is defined as the flow rate normal to the surface element

$$F_i = \int_{\Delta A_i} \mathbf{n}_i \cdot \bar{\mathbf{u}} dA \cong \mathbf{n}_i \cdot \bar{\mathbf{u}} \Delta A_i \quad (4.9)$$

then, the convective term can be written as

$$\sum_{all} \int_{\Delta A_i} \mathbf{n}_i \cdot (\bar{\mathbf{u}}\phi) dA = \sum_{all} F_i \phi_i \quad (4.10)$$

where ϕ_i is the value of ϕ at the centre of surface area element dA_i . It is worthwhile pointing out that due to the continuity equation, the flux should satisfy

$$\int_{CV} \nabla \cdot \bar{\mathbf{u}} dV = \int_A \mathbf{n} \cdot \bar{\mathbf{u}} dA = \sum_{all} \int_{\Delta A_i} \mathbf{n}_i \cdot \bar{\mathbf{u}} dA = \sum_{all} F_i = 0 \quad (4.11)$$

As discussed before, linear variation of the dependent variable is assumed. The face value can be evaluated by applying a Central Differencing (CD) scheme which is done by conducting an interpolation between the cell values at \mathbf{P} and \mathbf{Q} as

$$\phi_i = f_i \phi_{\mathbf{P}} + (1 - f_i) \phi_{\mathbf{Q}} \quad (4.12)$$

where f_i is the interpolation factor which is defined as the ratio of the distances between \mathbf{Q} to surface, $D_{f\mathbf{P}}$, and \mathbf{PQ} , $D_{\mathbf{PQ}}$

$$f_i = \frac{D_{f\mathbf{P}}}{D_{\mathbf{PQ}}} \quad (4.13)$$

The CD scheme is able to offer second order accuracy even on unstructured meshes [107]. However, A disadvantage of the CD scheme is its unboundedness when the convection

term strongly dominates the system which can lead to non-physical oscillations in the solution or even divergence [72].

An alternative approach, the upwind differencing (UD) scheme, has been widely used to improve the instability and unboundedness issues brought by the CD scheme. In this scheme the face value, ϕ_i , is determined according to the direction of the flux

$$\phi_i = \begin{cases} \phi_{\mathbf{P}} & F_i \leq 0 \\ \phi_{\mathbf{Q}} & F_i \geq 0 \end{cases} \quad (4.14)$$

The UD scheme by nature complies with boundedness, but a major drawback of the scheme is that it introduces diffusion-like erroneous results when the grid lines are misaligned with the flow, which is well known as numerical diffusion or false diffusion [107]. Due to the fact that the turbulent diffusivity predicted by LES is generally very small, even a modest numerical diffusion can contaminate the result. Therefore, the UD scheme is only used in LES to increase the stability of the calculation when the CD scheme cannot guarantee convergence of solution. Therefore, the central differencing scheme will be used throughout the research.

Diffusion Term

The diffusion term of Eq 4.8 is

$$\sum_{all} \int_{\Delta A_i} \mathbf{n}_i \cdot (\Gamma_\phi \nabla \phi) dA$$

Similar to the the convective term, the area integration is the summation of the integrals over all ΔA_i . Each of these integrals is evaluated as the dot product of \mathbf{n}_i and the multiplication between a diffusive flux vector $\Gamma_\phi \nabla \phi$ and ΔA_i

$$\sum_{all} \int_{\Delta A_i} \mathbf{n}_i \cdot (\Gamma_\phi \nabla \phi) dA \cong \sum_{all} \mathbf{n}_i \cdot (\Gamma_\phi \nabla \phi) \Delta A_i \quad (4.15)$$

If the mesh is orthogonal, i.e. surface unit normal vector \mathbf{n}_i , \mathbf{d} , and the line joining nodes \mathbf{P} and \mathbf{Q} are in the same direction, the equation above can be approximated by using the CD scheme along line \mathbf{PQ} :

$$\sum_{all} \mathbf{n}_i \cdot (\Gamma_\phi \nabla \phi) \Delta A_i \cong \Gamma_i \frac{\phi_{\mathbf{Q}} - \phi_{\mathbf{P}}}{|d|} \Delta A_i \quad (4.16)$$

where the $|d|$ is the distance between the centroids \mathbf{P} and \mathbf{Q} , Γ_i is the diffusion coefficient on the surface dA_i that can be calculated by the CD scheme in Eq 4.12. However, in

more complex geometries such as the corrugated channel in the current research, the mesh will have some degrees of skewness and non-orthogonality so that line PQ is not parallel to \mathbf{n}_i . In this case, a correction is needed for Eq. 4.16 to offset the error brought by non-orthogonality. This research adopts the method of introducing a term called cross-diffusion [72] as in Eq. 4.17. By considering an arbitrary geometry in Fig. 4.3, vector \mathbf{d} is the direction of line joining centroids P and Q of adjacent cells, vector \mathbf{c} is the direction of the line joining vertices a and b , \mathbf{n} is the unit vector normal to surface A , m is the midpoint of ab , and θ is the angle between \mathbf{n} and \mathbf{d} . The diffusion flux through each CV face can then be evaluated as

$$\mathbf{n}_i \cdot (\Gamma_\phi \nabla \phi) \Delta A_i = \underbrace{\Gamma \cdot \frac{1}{\cos\theta} \frac{(\phi_Q - \phi_P)}{|d|} \Delta A_i}_{\text{Direct gradient term}} - \underbrace{\Gamma \cdot \tan\theta \frac{(\phi_Q - \phi_P)}{|c|} \Delta A_i}_{\text{Cross-diffusion term}} \quad (4.17)$$

where $|c|$ is the distance between vertices a and b , and will be ΔA_i in 3D mesh, and ϕ_a and ϕ_b can be calculated by taking an average over the neighbouring nodal cell centre value

$$\phi_a = \frac{\phi_Q + \phi_P + \dots}{N} \quad (4.18)$$

where N is the number of cells surrounding the vertex a .

It should be noted that a further error term can be introduced by skewness, as the CD scheme is only second order accurate if the integration of the control surface element uses the midpoint value of $\mathbf{n}_i \cdot (\Gamma_\phi \nabla \phi) \Delta A_i$. In the case of mesh having high skewness, the lines PQ and ab do not intersect at the midpoint m of ab . This error increases with the rise of skewness and aspect ratio, indicating it is important to minimise the non-orthogonality, skewness and aspect ratio in the mesh.

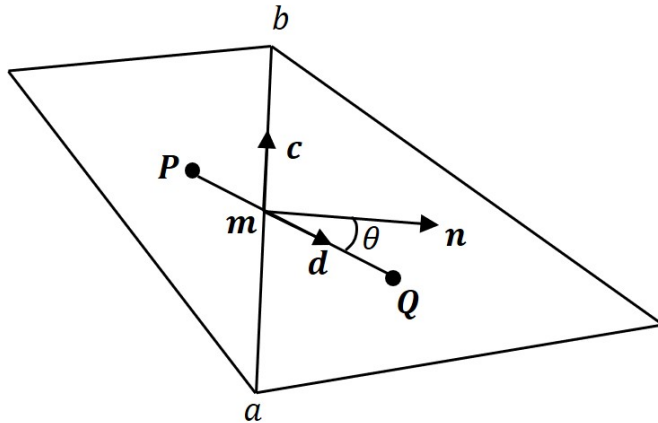


FIGURE 4.3. Sketch for evaluation of diffusion flux.

Source Terms

In the current research, all terms which are not convection, diffusion or temporal contributions are classified as source terms. The volume integration in the source term on the r.h.s and transient term on the l.h.s of Eq 4.8 can be approximated by the product of the cell volume and the centroid value of the variable, i.e.

$$\int_{CV} \phi dV = \phi_{\mathbf{P}} V_{\mathbf{P}} \quad (4.19)$$

where $V_{\mathbf{P}}$ is the cell volume, and

$$\int_{CV} S_{\phi} dV = \bar{S}_{\phi} \Delta V \quad (4.20)$$

Where \bar{S}_{ϕ} is the average of S_{ϕ} over the CV and ΔV is the volume of the CV. By using the midpoint rule, replacing \bar{S}_{ϕ} by the value at the centroid of the CV offers second-order accuracy. The source term is then introduced to the discretised equation as

$$\bar{S}_{\phi} \Delta V = S_u V_{\mathbf{P}} + S_p V_{\mathbf{P}} \phi_{\mathbf{P}} \quad (4.21)$$

The integral relation for the generic transport equation without time integration can be written as

$$\frac{d}{dt} \int_V \phi dV + \int_V \nabla \cdot (\bar{\mathbf{u}}\phi) dV - \int_V \nabla \cdot (\Gamma_{\phi} \nabla \phi) dV = \int_V S_{\phi} dV \quad (4.22)$$

This can be written with time integration as

$$\int_t^{t+\Delta t} \left[\frac{d}{dt} \int_V \phi dV + \int_V \nabla \cdot (\bar{\mathbf{u}}\phi) dV - \int_V \nabla \cdot (\Gamma_{\phi} \nabla \phi) dV \right] dt = \int_t^{t+\Delta t} \left[\int_V S_{\phi} dV \right] dt \quad (4.23)$$

By substituting the equations discussed above, Eq. 4.22 can now be rewritten as

$$\frac{d(\phi_{\mathbf{P}} V_{\mathbf{P}})}{dt} + \sum_{all} F_i \phi_i - \sum_{all} \mathbf{n}_i \cdot (\Gamma_{\phi} \nabla \phi) \Delta A_i = S_u V_{\mathbf{P}} + S_p V_{\mathbf{P}} \phi_{\mathbf{P}} \quad (4.24)$$

Eq. 4.23 can now be rewritten as

$$\int_t^{t+\Delta t} \left[\frac{d(\phi_{\mathbf{P}} V_{\mathbf{P}})}{dt} + \sum_{all} F_i \phi_i - \sum_{all} \mathbf{n}_i \cdot (\Gamma_{\phi} \nabla \phi) \Delta A_i \right] dt = \int_t^{t+\Delta t} [S_u V_{\mathbf{P}} + S_p V_{\mathbf{P}} \phi_{\mathbf{P}}] dt \quad (4.25)$$

Temporal Discretisation

The time integration in Eq. 4.25 can be treated by the Crank Nicholson scheme which is an equal blend of first order explicit and implicit Euler schemes and only offers second order accuracy for equal blending [107]. It is shown that Crank-Nicholson scheme requires extra inner-iterations during each time step to evaluate the diffusion term using the properties at the new time, and has a large memory overhead due to the stored variables [91].

In this research the second order backward differencing scheme will be used to treat the time derivative. The scheme is fully implicit, of second order accuracy and unconditionally stable [89]. Although it has a larger truncation error than the Crank Nicholson scheme, the backward differencing scheme is cheaper to run and less prone to producing oscillatory solutions than the latter. Given that the time step for current research is very small ($C_o < 1$), the size of numerical diffusion caused by the temporal scheme is kept to a minimum [91]. In the backward differencing scheme, the temporal derivative is approximated as

$$\left[\frac{d(\phi_{\mathbf{P}}V_{\mathbf{P}})}{dt} \right]^{n+1} = \frac{3(\phi_{\mathbf{P}}V_{\mathbf{P}})^{n+1} - 4(\phi_{\mathbf{P}}V_{\mathbf{P}})^n + (\phi_{\mathbf{P}}V_{\mathbf{P}})^{n-1}}{2\Delta t} \quad (4.26)$$

where $(\phi_{\mathbf{P}}V_{\mathbf{P}})^{n+1} = (\phi_{\mathbf{P}}V_{\mathbf{P}})^{t+\Delta t}$ is at the new time level, i.e. the time step being solved for; $(\phi_{\mathbf{P}}V_{\mathbf{P}})^n = (\phi_{\mathbf{P}}V_{\mathbf{P}})^t$ is at the current time level, the value is stored from the previous time step; and $(\phi_{\mathbf{P}}V_{\mathbf{P}})^{n-1} = (\phi_{\mathbf{P}}V_{\mathbf{P}})^{t-\Delta t}$ is at the old time level, the value is stored from the time step before the last.

The other terms are evaluated only at the new time level, neglecting the temporal variation. Then Eq. 4.24 becomes

$$\begin{aligned} \frac{3(\phi_{\mathbf{P}}V_{\mathbf{P}})^{n+1} - 4(\phi_{\mathbf{P}}V_{\mathbf{P}})^n + (\phi_{\mathbf{P}}V_{\mathbf{P}})^{n-1}}{2\Delta t} + \sum_{all} F_i \phi_i^{n+1} - \sum_{all} \mathbf{n}_i \cdot (\Gamma_\phi \nabla \phi)^{n+1} \Delta A_i \\ = S_u V_{\mathbf{P}} + S_p V_{\mathbf{P}} \phi_{\mathbf{P}}^{n+1} \end{aligned} \quad (4.27)$$

4.4 Solver

The solver selected in the current research is the PIMPLE algorithm¹. This algorithm is a combination of PISO (Pressure Implicit with Splitting of Operator) [123] and SIMPLE (Semi-Implicit Method for Pressure-Linked Equations) [133]. The PIMPLE algorithm allows users to specify the number of outer loops other than the default value of 1 for PISO. However, if 1 outer corrector step and 2 inner corrector steps are specified, this algorithm is effectively a PISO algorithm. The flow chart of the PIMPLE algorithm is shown in Fig. 4.4 followed by the explanations of various steps in the flow chart².

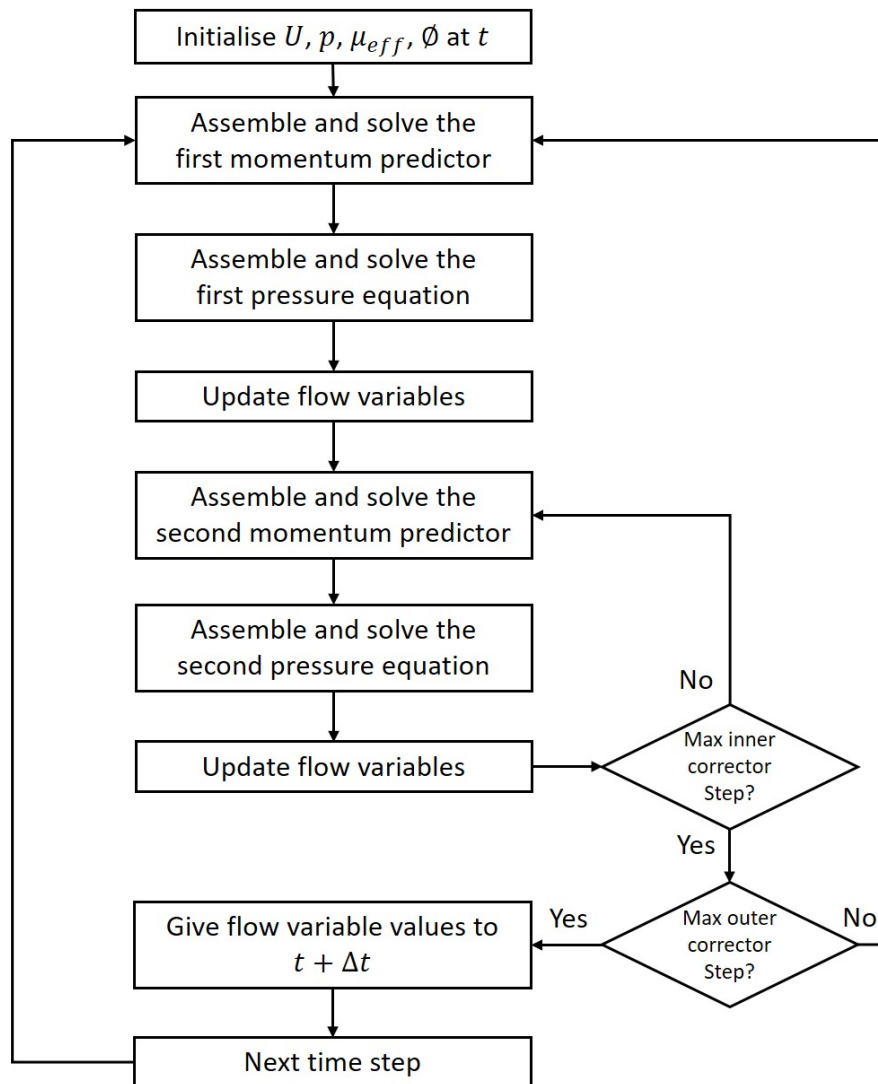


FIGURE 4.4. A flow chart of the PIMPLE algorithm.

¹There is no literature about this algorithm, but it exists in OpenFOAM v1612, and is regarded as more robust than PISO by the OpenFOAM community.

²The flow chart is made by combining the information in the source code of OpenFOAM and the information about SIMPLE and PISO algorithms in various textbooks [72, 107, 134].

1. The flow variables at $t = 0$ (the initial condition) is used as an initial guess for computing the flow solution at $t + \Delta t$.
2. Assemble and solve the first momentum equations/predictor to obtain a tentative velocity. The solution of velocity components is obtained by a smooth solvers with a symmetric Gauss-Seidel smoother. The resultant velocity field does not normally satisfy the mass conservation.
3. Assemble and solve the first pressure correction equation. The solution of matrix is achieved by a generalised geometric-algebraic multi-grid (GAMG) solver with a Gauss-Seidel smoother. Despite that the pressure correction equation has been presented in various literature [72, 91, 107, 135], for the sake of completeness, the pressur correction equation is described in Appendix B.
4. Update \mathbf{U} , p and F_i using the flow variable calculated in momentum and pressure correction equations and the value at t .
5. Use the latest \mathbf{U} , p and F_i to assemble and solve the second momentum corrector/predictor.
6. Use the newly solved \mathbf{U} to assemble and solve the second pressure correction equation. The solution is obtained by GAMG but smoothed by diagonal incomplete-Cholesky/LU with Gauss-Seidel (DICGaussSeidel).
7. Update \mathbf{U} , p and F_i by summing the flow variable calculated in the second momentum and pressure correction equations and their intermediate value generated after Step 4.
8. Step 5-7 is now performed repeatedly until the maximum number of inner corrector steps is reached. Due to the fact that the time step size in current research is very small, convergence can generally be reached within 2 iterations.
9. When the maximum number of inner corrector steps is reached, \mathbf{U} , p and F_i will be assigned as the initial value back to Step 2. Then step 2-8 is repeated iteratively until the maximum number of outer corrector steps is reached.
10. Set the value at $t + \Delta t$ to be the final solution.
11. Advance to next time step.

Chapter 5

Validation of SGS Models

Fig. 1.3a shows clearly that the top wall and the two side walls of the corrugated channel are flat plates. Therefore, although the modelling accuracy of various SGS models is unclear on the corrugated wall, their performances can be assessed on the fully developed turbulent channel flow. Due to the simplicity of its geometry and abundant experimental and DNS data, channel flow is generally used as the first test case to validate SGS models.

In this test case, the performance of different SGS models from Chapter 3 (summarised in Table. 5.1) are compared in terms of streamwise velocity profile, mean shear stress profile and second order velocity moments. The effects of grid density on the prediction accuracy of SGS models are also analysed. Finally, the computing cost of various SGS models are compared leading to the conclusions of the current chapter.

SGS Models	Model Description
SMAG	Smagorinsky SGS model
SMAG+VD	Smagorinsky SGS model with van-Driest wall damping function
DyLag	Dynamic Lagrangian SGS model
KEQ	k -equation SGS model
KEQ+VD	k -equation SGS model with van-Driest wall damping function
DyK	Dynamic k -equation SGS model
WALE	Wall-adapting local eddy-viscosity (WALE) SGS model

TABLE 5.1. List of SGS models tested in current channel flow case.

5.1 General Case Setup

The channel flow case is shown schematically in Fig 5.1. A channel flow case should consist of two infinite (at least long enough) parallel plates within which there is an equilibrium turbulent flow. It is non-practical to simulate the whole domain. Thus an approximation is made that a finite sub-domain of this channel is taken and periodic boundaries are applied in the streamwise, x , and spanwise, z , directions. This BC has been shown to be the best practice in similar research [11, 27, 103, 136], since this method removes the need for specification of inflow conditions and significantly reduces the computational domain. When the required streamwise bulk velocity, U_b , is defined, a pressure gradient is calculated at each time step, acting as an additional external force term into the momentum equation, in order to keep U_b constant across the channel.

The distance between the paired boundaries should be sufficiently far that the largest eddy structure will not interfere with itself. It was reported that an adequate dimensions of the computational domain should be around $2\pi h \times 2h \times 1.5\pi h$ [91, 100, 137] in the x , y and z directions respectively (h is the half channel height), although it is also shown by Fureby et al. [136] that a smaller channel dimension ($4h \times 2h \times 2h$) is also viable.

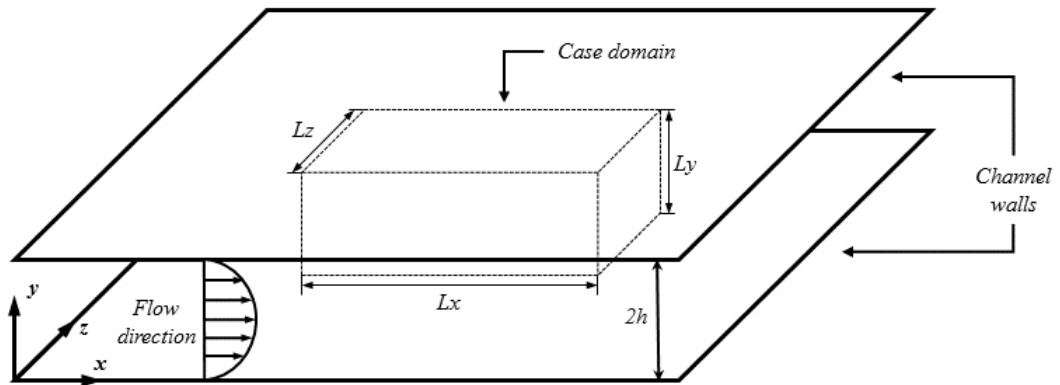


FIGURE 5.1. Schematic representation of a channel flow case.

The emphasis of current testing is on the flow with medium Re . The Re based on h and U_b is 38000. The experiment was done by Wei and Willmarth [138] using a water tunnel and flow variables were measured by Laser Doppler Anemometer (LDA). The relevant LES on this test case was originally done by Poimelli [113] to test a dynamic SGS model based on a spectral method. It was then used by Shah and Ferziger [139] to test a non-eddy viscosity based SGS model. Tang et al. [140] also tested a multigrid 3D pressure solver on the same configuration. A DNS study was recently performed by Lee and Moser [141]. The flow domain and parameters are given in Table. 5.2.

Parameter	Notation	Value	Expression
Bulk Reynolds number	Re_b	38000	$U_b h / \nu$
Centre Reynolds number	Re_c	39582	$U_c h / \nu$
Friction Reynolds number	Re_τ	1800	$u_\tau h / \nu$
Domain size	$L_x \times L_y \times L_z$	$2.5\pi h \times 2h \times 0.5\pi h$	—

TABLE 5.2. Global flow parameter of the channel flow test case.

One objective of current validation is to investigate the effect of grid density on the result of the simulation. So three different mesh sizes are tested and referred to as Mesh1, Mesh2 and Mesh3. Mesh1 is the coarsest among the three. The mesh is uniform in the x and z directions, and stretched in the y direction. Mesh2 doubles the number of grid lines of mesh1 along all dimensions. By using the same way of refinement on Mesh2, Mesh3 is obtained as the finest mesh. The mesh information is summarised in Table. 5.3¹. The configurations of Mesh2 are the same as those used by Piomelli [113], Shah and Ferziger [139] and Voloudis et al [142]. For Mesh1 the ratio between the largest and smallest cell size along y -axis is 75, this ratio for Mesh2 and Mesh3 is 90. It is acknowledged that the required grid resolution to obtain accurate LES results for turbulent channel flow is $(\Delta x^+, \Delta y^+, \Delta z^+) \simeq (100, 1, 30)$ [143]. Therefore, even Mesh3 is not fine enough for accurate results. However, in the real engineering application, the mesh density and quality may not always follow the best practice due to the complexity of the geometry and computing power. Therefore, current mesh densities serve the purpose of assessing SGS models on sub-optimal meshes.

Mesh name	$N_x \times N_y \times N_z$	Δx^+	Δz^+	Δy^+
Mesh1	$32 \times 40 \times 40$	442	71	2.5-185
Mesh2	$64 \times 80 \times 80$	221	35	1.1-99
Mesh3	$128 \times 160 \times 160$	110	18	0.56-50

TABLE 5.3. The mesh used in the simulation.

Constant mean velocity is imposed in the x direction with periodic BC being set in both x and z directions. No-slip is applied on the wall and $y^+ < 3$ for all three meshes, meaning the flow field close to the wall is explicitly computed. Time step size, Δt , is set

¹Note that Δx^+ , Δy^+ , Δz^+ are calculated based on the Re_τ value in Table. 5.2. $\Delta x^+ = (L_x/N_x) \times u_\tau/\nu$, and $Re_\tau = h \times u_\tau/\nu$, so $\Delta x^+ = (Re_\tau \times L_x)/(N_x \times h)$.

to be $2 \times 10^{-5}s$, making the Courant Number, Co , less than one.

Initial turbulence was generated by using utilities provided by the community of OpenFOAM [144]. LES simulation started with the model KEQ+VD. the simulation is run for first 5s (43 flow through, 250,000 time steps) in order to allow the flow field to fully develop and reach a statistically stationary state. Then the time averaging is carried out from 5s to 8s (26 flow through, 150,000 time steps). Result verification can be found in Appendix C.

5.2 Results

5.2.1 Global Flow Quantities

Global flow quantities include the computed friction velocity and mean centreline velocity which characterise the flow. These values predicted by various SGS models under different mesh densities are summarised in Table. 5.4 to 5.6. The target value is from the work of Shah and Ferziger [139].

Parameter	SMAG	SMAG+VD	DyLag	KEQ	KEQ+VD	DyK	WALE
U_c/U_b	1.177	1.098	1.066	1.164	1.092	1.069	1.066
Target value	1.124	1.124	1.124	1.124	1.124	1.124	1.124
Error (%)	4.69%	-2.28%	-5.15%	3.51%	-2.87%	-4.94%	-5.14%
Re_τ	699	1683	1333	908	1684	1384	1324
Target value	1800	1800	1800	1800	1800	1800	1800
Error (%)	-61.17%	-6.50%	-25.94%	-49.56%	-6.44%	-23.11%	-26.44%

TABLE 5.4. Global flow quantities of SGS models compared under Mesh1.

Parameter	SMAG	SMAG+VD	DyLag	KEQ	KEQ+VD	DyK	WALE
U_c/U_b	1.133	1.092	1.078	1.128	1.088	1.076	1.077
Target value	1.124	1.124	1.124	1.124	1.124	1.124	1.124
Error (%)	0.79%	-2.84%	-4.11%	0.34%	-3.22%	-4.23%	-4.18%
Re_τ	936	1764	1596	1230	1770	1614	1576
Target value	1800	1800	1800	1800	1800	1800	1800
Error (%)	-48.00%	-2.00%	-11.33%	-31.67%	-1.67%	-10.33%	-12.44%

TABLE 5.5. Global flow quantities of SGS models compared under Mesh2.

Parameter	SMAG	SMAG+VD	DyLag	KEQ	KEQ+VD	DyK	WALE
U_c/U_b	1.137	1.108	1.108	1.137	1.109	1.103	1.104
Target value	1.124	1.124	1.124	1.124	1.124	1.124	1.124
Error (%)	1.17%	-1.44%	-1.46%	1.13%	-1.37%	-1.84%	-1.75%
Re_τ	1202	1824	1760	1528	1828	1770	1751
Target value	1800	1800	1800	1800	1800	1800	1800
Error (%)	-33.22%	1.33%	-2.22%	-15.11%	1.56%	-1.67%	-2.72%

TABLE 5.6. Global flow quantities of SGS models compared under Mesh3.

The results demonstrate the targeted centreline to bulk velocity ratio, U_c/U_b , can be well captured by all models. Even under Mesh1, the smallest error is -2.28% obtained by KEQ+VD, and the largest error is -5.15% obtained by DyLag. In addition, as expected, increasing the mesh density will increase the prediction accuracy for all the models, as on Mesh3 all errors on predicting U_c/U_b are within 2%.

In terms of Re_τ , however, most SGS models tend to under-predict the value and the accuracy of each model varies considerably. Also a close link between accuracy and mesh density is observed. The SMAG under Mesh1 has the highest error and it under-predicts the target value by 61.17%. By adding an extra k -equation, KEQ reduces the error but the value is still around 50%. Their dynamic variants, DyLag and DyK future reduce the error to around 25%, which is at the same level with WALE. The best accuracy is obtained by adding the van-Driest Damping function to SMAG and KEQ. It is found SMAG+VD and KEQ+VD both under-predict the target value by less than 7% on Mesh1. The accuracy is found to be improved by increasing the mesh density. In Mesh2, the error obtained by SMAG+VD and KEQ+VD is reduced to 2%, but their dynamic counterparts, DyLag and DyK, still under-predict the target value by over 10%. In Mesh3, all SGS models see a further improvement in accuracy, and apart from SMAG and KEQ, all other SGS model have reduced the error to less than 3%.

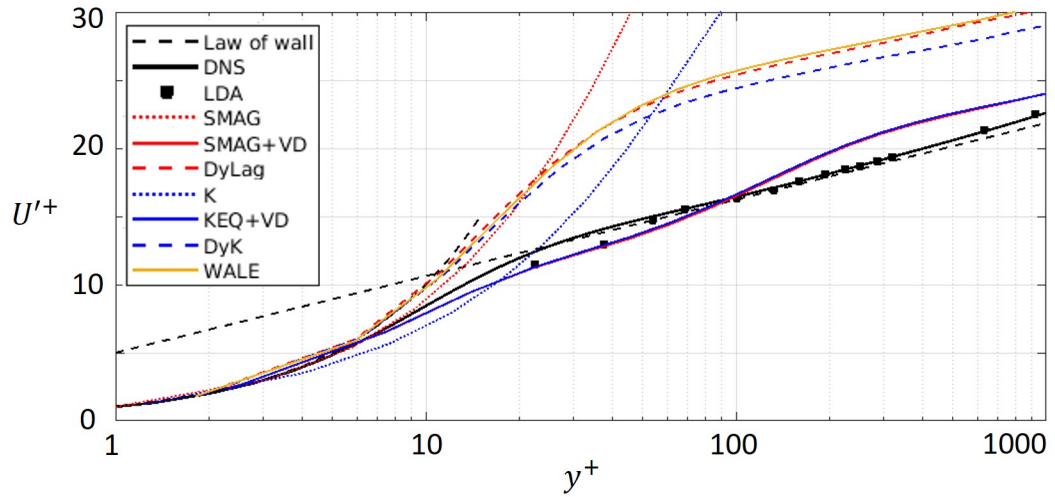
5.2.2 Mean Velocity Profiles

The profile of the averaged stream-wise velocity, $\langle u \rangle$, is inspected in this section. The result of mean flow field for each SGS model under different mesh densities is shown in Fig. 5.2. The profile is presented in wall coordinates, $y^+ = u_\tau y / \nu$, and streamwise velocity is scaled with friction velocity, i.e. $U^+ = \langle u \rangle / u_\tau$. The red and blue dotted lines represent the SGS models without van-Driest damping function (VD), i.e. SMAG and KEQ respectively. The red and blue solid lines show the results of SMAG+VD and KEQ+VD respectively. The coloured dashed lines are for dynamic models, i.e. DyLag and DyK. Finally, the yellow solid line is for WALE.

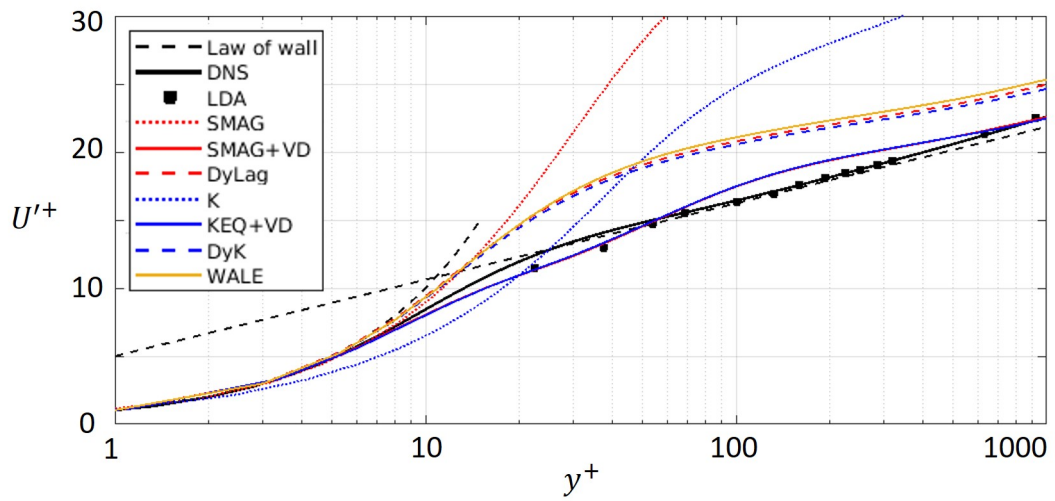
It appears that apart from KEQ, all the results of the SGS models match the profile within viscous layer even with Mesh1. However, both SMAG and KEQ completely fail to reproduce the profile within the log layer region. Their VD counterparts, SMAG+VD and KEQ+VD, predict a similar result and generally match the profile predicted by DNS and observed by LDA, although slight under-prediction is shown between y^+ of 10 and 100, and over-prediction is exhibited beyond $y^+ = 100$. The result of DyLag, DyK and WALE are similar, they present an over-prediction of the profile from $y^+ = 70$ to the end. But at log layer region, those three models are able to match the gradient of the profile.

As the mesh density increases for Mesh2, the accuracy of all SGS models improves. The difference between the prediction of DyLag, DyK and WALE and the correct log layer profile reduces by 5 units on U^+ axis, compared with the prediction under for Mesh1. Their results are similar to the standard Smagorinsky and k -equation with another wall damping function proposed by Yoshizawa [101] which were reported by Veloudis et al. [142]. Due to the result predicted by SMAG+VD and KEQ+VD being close to the correct profile in Mesh1 already, the mesh refinement has less impact on their result, despite a small improvement of prediction accuracy being visible within the log layer region. The profile predicted by SMAG+VD and KEQ+VD are comparable to the results reported by Piomelli [113] and Shah and Ferziger [139].

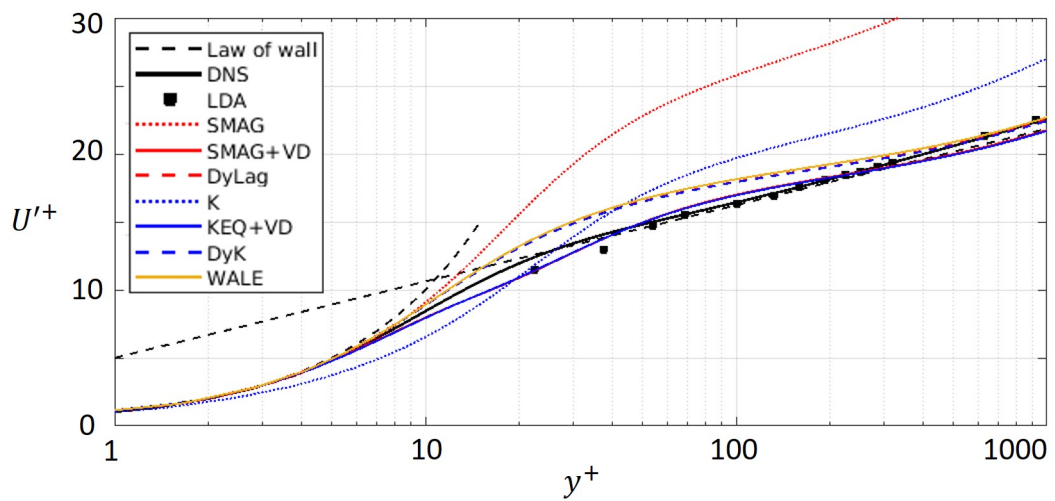
Further refining to Mesh3, the prediction of both models with VD are now very close to the correct profile. The difference between the results of DyLag, DyK and WALE and DNS data further decreases, although a bulge still exists between the y^+ value of 20 and 100. The refinement also sees that the SMAG and KEQ approaches the correct profile. It is expected that the prediction of all SGS models will be closer to the DNS result under further refinement and will eventually match it if the numerical scheme is adequately high and numerical errors are properly controlled.



(A) Mesh1



(B) Mesh2



(C) Mesh3

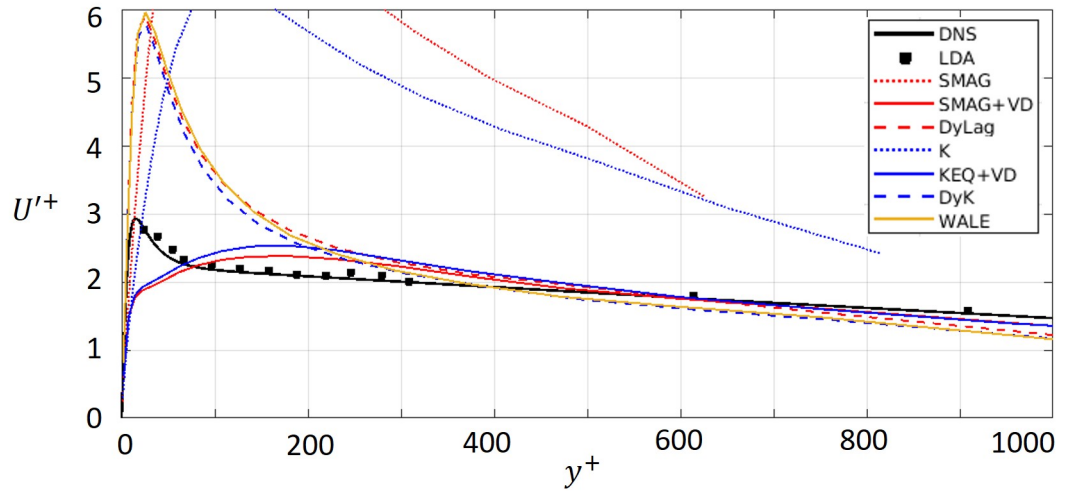
FIGURE 5.2. Mean normalised stream-wise velocity in wall coordinates on different mesh densities.

5.2.3 Velocity Fluctuations

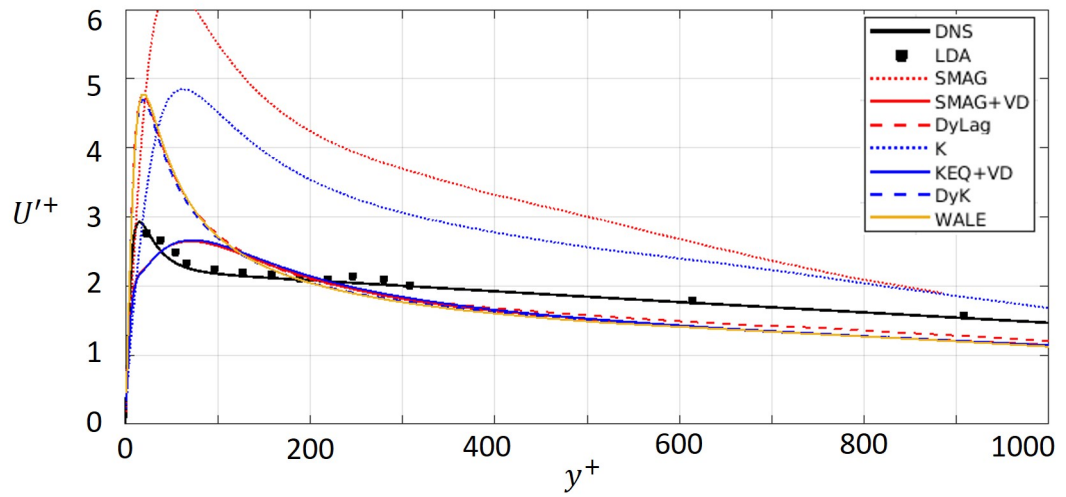
This section is devoted to the analysis of each component of the Reynolds stress tensor obtained from various SGS models under different mesh densities. The Reynolds stresses tensor, $u'_i u'_j$, is the variances of velocity components which are the primary quantities describing the turbulent fluctuations. The root-mean-square value (standard deviation) of its diagonal components, $\sqrt{\langle u_i'^2 \rangle}$, are often non-dimensionalised by friction velocity, u_τ , (referred to as u_i^+) and compared against y^+ . Since the channel flow is symmetric in the wall normal direction, its $\langle u'w' \rangle$ and $\langle v'w' \rangle$ components are equal to zero [73]. So the $\langle u'v' \rangle$ component, whose negative value is referred to as turbulent shear stress, is the only component left to be analysed. It is customary to normalise the time-averaged turbulent shear stress, $\langle -u'v' \rangle$, by u_τ^2 (refers to as $u'v'^+$) and compare against y^+ .

Fig. 5.3 to Fig. 5.5 compare the u'^+ , v'^+ and $u'v'^+$ with y^+ predicted by each SGS model under different mesh densities with data obtained by DNS and LDA. From those figures, a general trend of improvement is observed as the mesh is refined. Also, SMAG+VD and KEQ+VD provide similar results, and results predicted by DyLag, DyK and WALE are almost identical, and SMAG and KEQ fail to predict a correct profile completely under Mesh1.

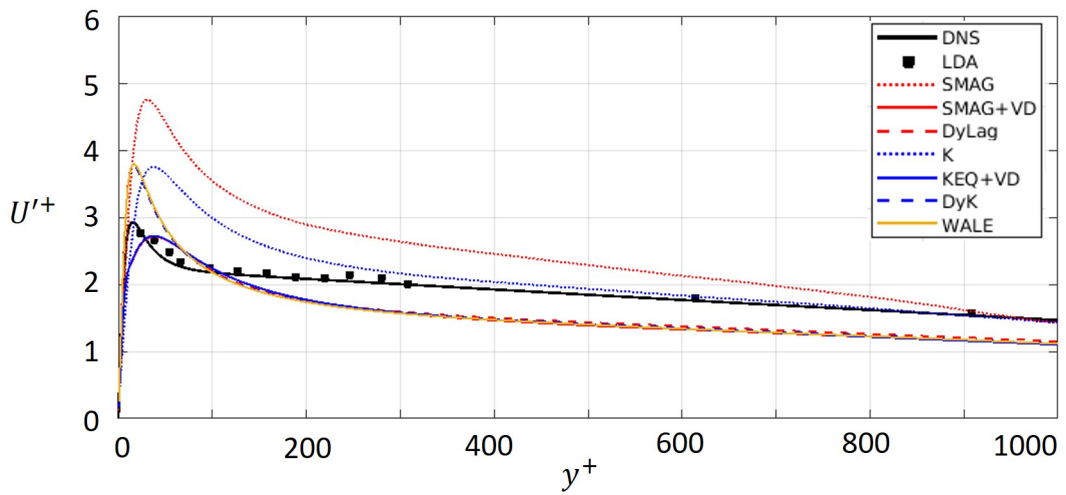
For u'^+ in Fig 5.3, it is found that SMAG+VD and KEQ+VD are able to capture the right level of turbulence intensity (with slight under-prediction) even under Mesh1, but fail to predict where the highest intensity occurs. On the opposite, DyLag, DyK and WALE tend to over-predict the highest value of turbulence intensity, but they are better at predicting the location where the highest turbulence in intensity happens under very coarse mesh. In Fig 5.4, DyLag, DyK and WALE demonstrate better accuracy in predicting the profile of v'^+ than SMAG+VD and KEQ+VD in all mesh densities, despite that all SGS models are not able to match the exact DNS profile. In terms of $u'v'^+$ in Fig. 5.5, DyLag, DyK and WALE still outperform SMAG+VD and KEQ+VD. The first three SGS models predict a profile which is close to DNS result under the coarsest mesh and match it well when refining to Mesh3, whereas, SMAG+VD and KEQ+VD show considerable difference with DNS data under Mesh1. Although their accuracy benefits from increasing the mesh density, their results still depict discrepancy within $y^+ < 100$.



(A) Mesh1

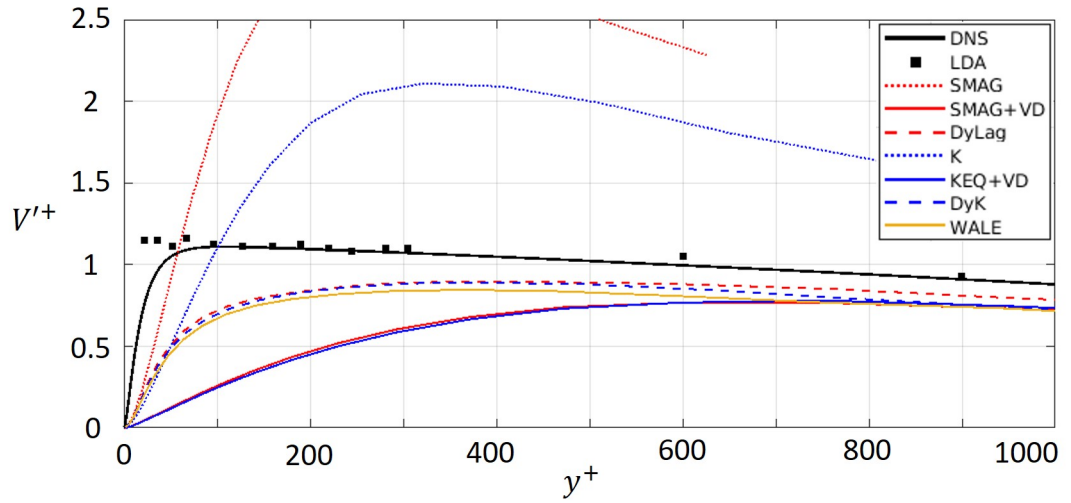


(B) Mesh2

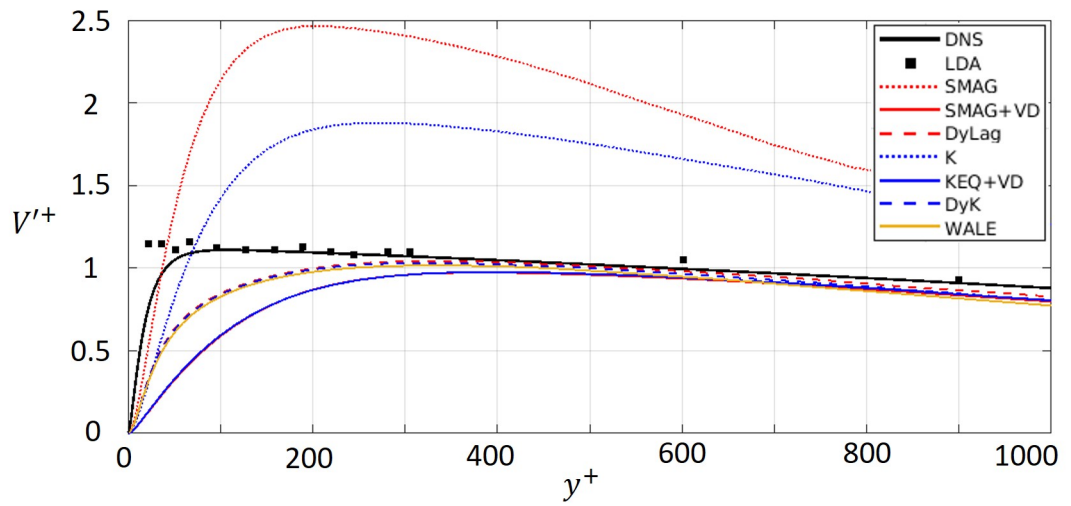


(C) Mesh3

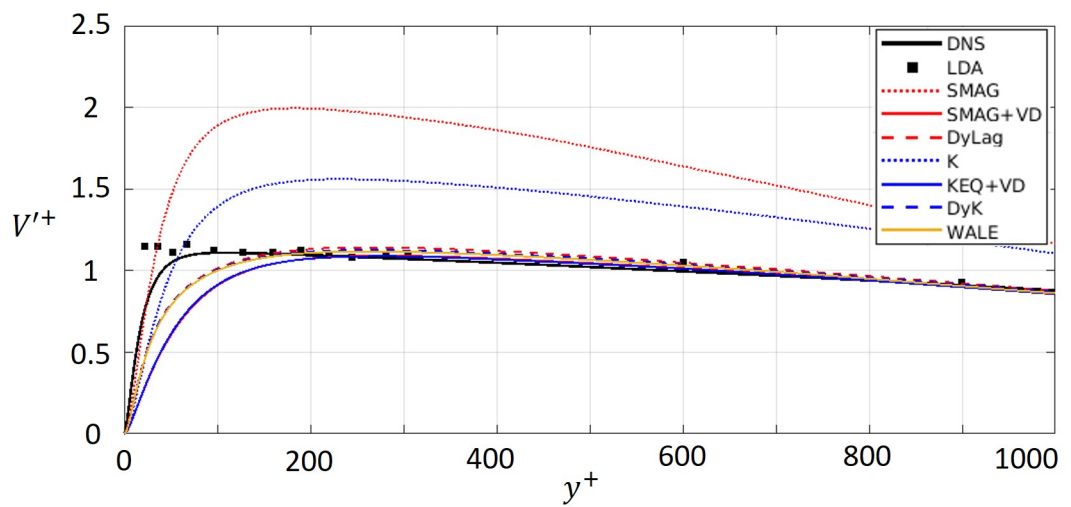
FIGURE 5.3. Stream-wise turbulence intensities by wall coordinates on different mesh densities.



(A) Mesh1

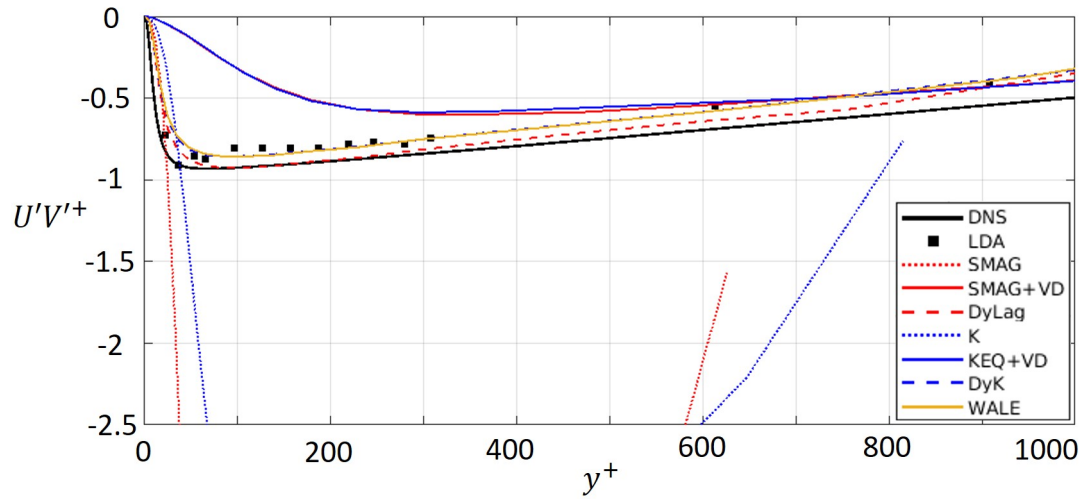


(B) Mesh2

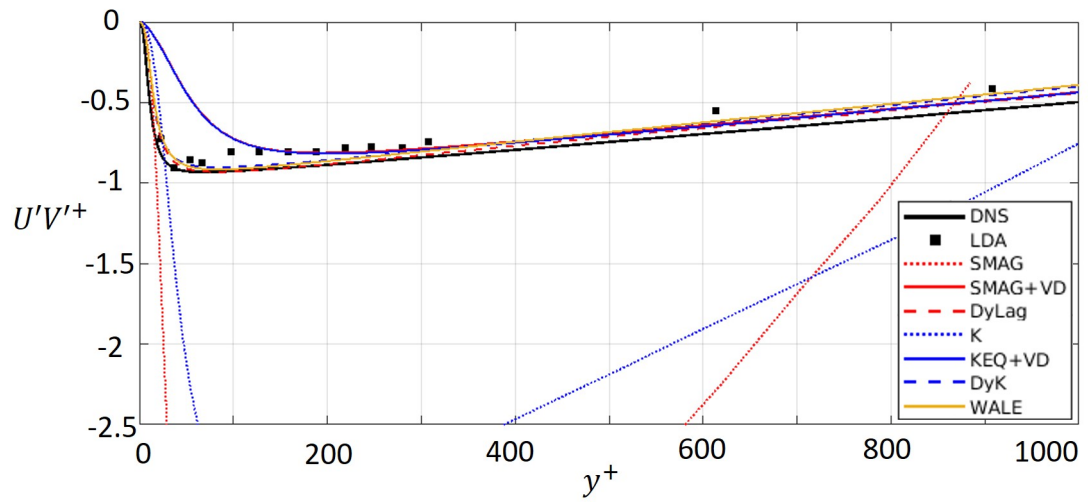


(C) Mesh3

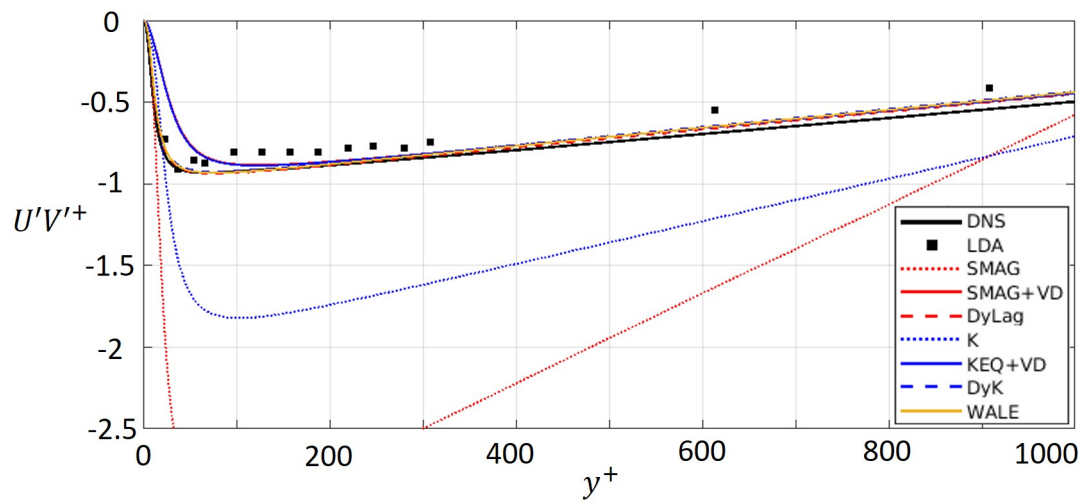
FIGURE 5.4. Wall normal direction turbulence intensities by wall coordinates on different mesh densities.



(A) Mesh1



(B) Mesh2



(C) Mesh3

FIGURE 5.5. Mean shear stress by wall coordinates on different mesh densities.

5.3 Conclusion

Several SGS models are tested under different mesh densities on a well documented channel flow configuration. It is found that under every mesh density, results obtained by SMAG+VD and KEQ+VD are very similar, and DyLag, DyK and WALE predict almost identical profiles. All these models can predict flow profile close to the data of DNS and LDA on Mesh3 ($[\Delta x^+, \Delta y_{min}^+, \Delta z^+] = [110, 0.56, 18]$). However, SMAG and KEQ failed to provide satisfactory results even under the finest mesh (Mesh3).

Although the prediction accuracy of all SGS models should deteriorate as the mesh is coarsened, in terms of predicting mean velocity profile, decreasing mesh density has less effect on SMAG+VD and KEQ+VD than DyLag, DyK and WALE. As the mesh density coarsens by a factor of 64 (i.e. under Mesh1), SMAG+VD and KEQ+VD are still able to provide a reasonably accurate result, whereas DyLag, DyK and WALE show a considerable over-prediction in log layer region, despite the gradient being well retained. In addition, DyLag, DyK and WALE tend to over-predict the value of the highest turbulence intensities, although they are able to capture the location of the highest turbulence intensities (except for $\langle v'v' \rangle$) even under the coarsest mesh. Conversely, SMAG+VD and KEQ+VD tend to slightly under-predict the highest turbulence intensities, but have worse accuracy on predicting their locations, especially the wall normal turbulence intensity.

Combing the aforementioned findings, SMAG+VD will be used in the study of the corrugated channel flow, as it is able to produce an overall more satisfactory result on Mesh3 at lower computing cost².

²The comparison of computing cost between different SGS models is presented in Appendix D.

Chapter 6

Analysis of Corrugated Channel

The main objectives of the current research are to numerically investigate the flow in a corrugated channel, including its flow development, mean flow profiles, and vortex evolution mechanisms within the corrugations. In what follows, Section 6.1 discusses the key features of the flow domain. Section 6.2 outlines the numerical setup and the BCs employed, followed by the grid independence study in Section 6.3. Results are presented and discussed in Section 6.4.

6.1 Experimental Setup

As mentioned in Chapter 1, an experiment study has been carried out to compare with the numerical predictions. The experimental results were acquired by PIV technique and the schematic of the experimental setups are shown in 6.1.

Two experimental setups were used for testing under different Re ranges. The first one is shown in Fig. 6.1a in which flow through the channel is driven by the pressure difference (700mm elevation difference) between the reservoir and the flow control valve at the exit. The flow rate changes 3-4% during a typical run¹ due to the change of pressure head as water in the reservoir discharges. Due to the limitation of pressure head, this setup is only able to achieve $Re = 6000$. Therefore another setup with pump, as shown in 6.1b, was built to measure flows with higher Re . In this setup, the pump was located downstream of the test section to minimise turbulence [12].

The corrugated channel investigated in the present work has a rectangular cross section, as shown in Fig. 1.3a, the bottom wall has a wavy shape with periodic grooves, whereas the top wall and two sidewalls are both flat plates. The dimensions of the geometry is

¹The duration for a typical run was not reported in the work of Unal et al. [3]

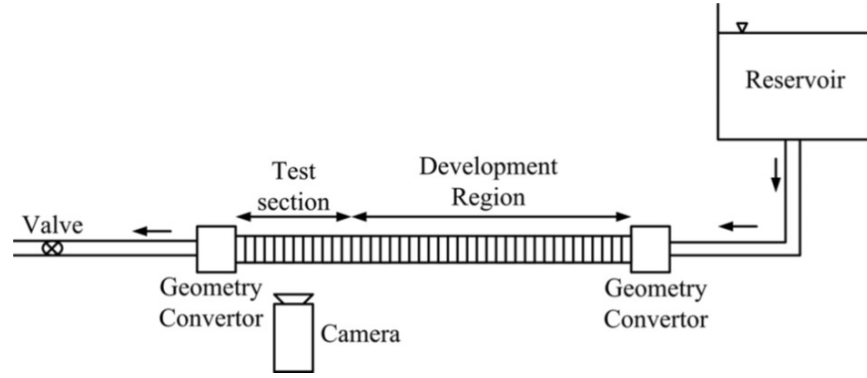
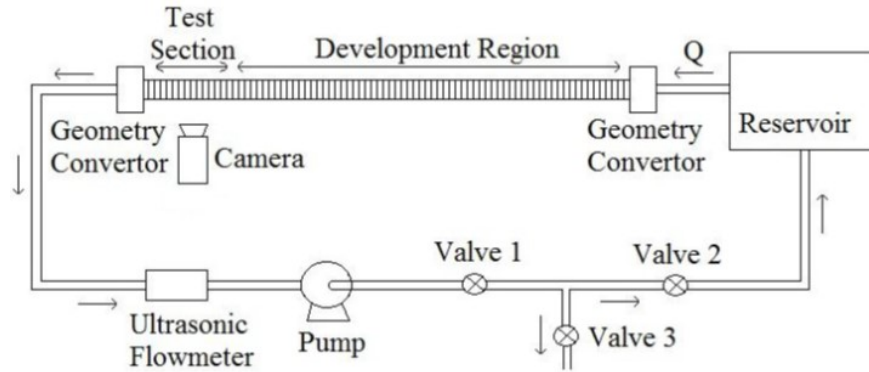
(A) Experimental setup for Re up to 6000 [3](B) Experimental setup for Re above 6000 [12]

FIGURE 6.1. Schematic of the experimental setups.

shown in Table. 6.1.

Variables	Description	Value (mm)
H	channel height	15.85
h	corrugation height	4.15
λ	wavelength of the corrugation	6.6
d_1	diameter of the groove	3.0
d_2	corrugation diameter	3.6
b	channel width	20

TABLE 6.1. Configurations of the flow domain.

The PIV experiment reports that the flow in current configurations became turbulent at $Re_b > 2000$, based on bulk velocity, U_b , and hydraulic diameter of the channel, $2bH/(b+H)$. In this research, simulations are performed for $Re = 5300$. The density and laminar viscosity of the fluid are kept the same as in the work of Unal et al [8], i.e $\rho = 998.2 \text{ kg/m}^3$ and $\mu = 0.001 \text{ Pa s}$, leading to $U_b = 0.3 \text{ m/s}$. Detailed descriptions of the experimental

setup can be found in the work of Unal et al [3, 12].

6.2 Numerical Methods

Three simulations are performed in the current research as listed in Fig. 6.2. BCs on the walls are no slip for U , i.e. $\mathbf{U}_w = (0, 0, 0)m/s$, zero gradient for p and ν_{sgs} , i.e. $\partial(p|\nu_{sgs})/\partial\mathbf{n}_w = 0$, where \mathbf{n}_w is the unit normal vector on the wall, and there is a fixed value of 0 for k_{sgs} , i.e. $k_{sgs_w} = 0$.

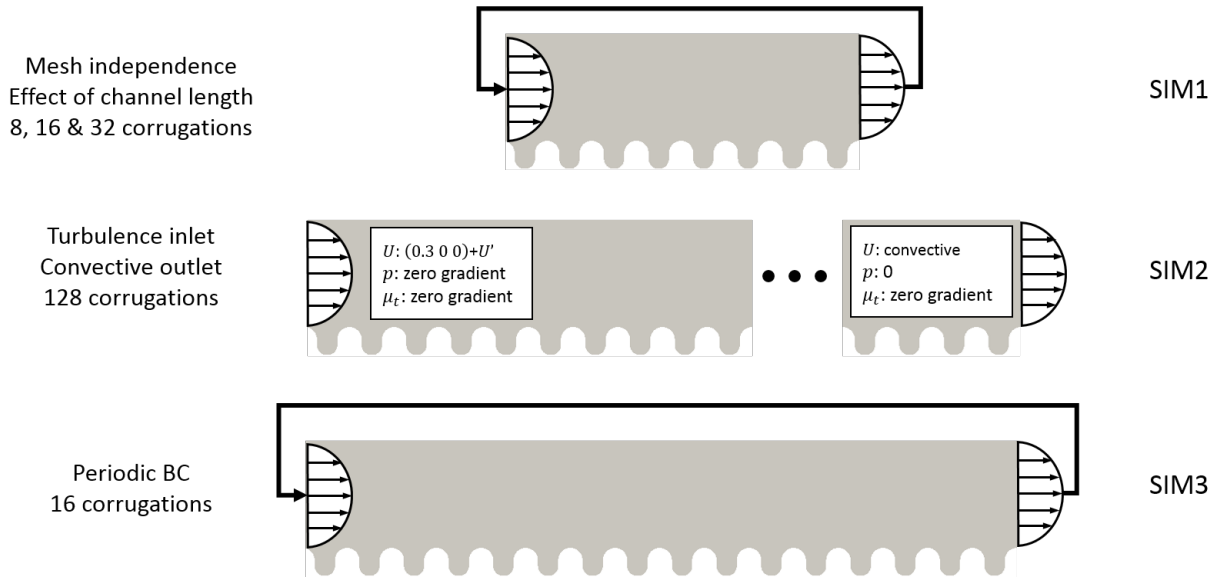


FIGURE 6.2. Simulation performed in current research.

Detailed BCs for inlet and outlet of each simulation are listed below:

1. SIM1

- Purpose:

To investigate mesh independence and the effect of corrugated channel length.

- BCs:

Inlet and outlet are coupled for periodic BC. Mesh independence study compares the results obtained by different mesh densities on cases with 8 corrugations. The study of the effect of corrugated channel length will use the same mesh density but compares results from cases with 8, 16 and 32 corrugations.

2. SIM2

- Purpose:

To investigate flow development in the corrugated channel.

- BCs:

At the inlet, $\langle \mathbf{U} \rangle = (0.3, 0, 0) m/s$ with randomly generated turbulence having a maximum turbulence intensity of $\mathbf{U}'/\langle \mathbf{U} \rangle = (22.4\%, 11\%, 11.85\%)$; zero gradient for p and ν_{sgs} . At the outlet, convective BC is for \mathbf{U} , i.e. $\partial \mathbf{U} / \partial t + \mathbf{U}_n \cdot (\partial \mathbf{U} / \partial \mathbf{n}) = 0$, where \mathbf{n} is the outward pointing unit normal vector at the outlet; p is set to be reference level and zero gradient for ν_{sgs} .

3. SIM3:

- Purpose:

To investigate hydrodynamic interaction and vortex evolution.

- BCs:

Inlet and outlet are coupled for periodic BC. Simulation is performed on the appropriate mesh density and channel length found in SIM1.

All simulations in current study are performed with OpenFOAM v1612+. Spatial interpolation of convection and diffusion terms is based on Gauss integration and second order central differencing schemes (Green-Gauss scheme). The gradient term is based on the least-squares method rather than the default Green-Gauss scheme. This is because the recent study of Syrakos et al. [145] suggests that when calculating the gradient, the Green-Gauss scheme is second-order accurate only on a structured mesh yet zeroth-order accurate on a general unstructured mesh. In contrast the least-squares gradient scheme is able to provide a second-order accurate result on both meshes. Time marching is approximated by a second-order backwards differencing implicit scheme with a time step of $\Delta t = 5 \times 10^{-5} s$ for cases with 8 corrugations and of $\Delta t = 1 \times 10^{-4} s$ for cases with more than 8 corrugations. A posterior analysis shows the maximum Courant number is less than 1 and its mean value within the flow domain is below 0.1, if $\Delta t = 1 \times 10^{-4} s$ is used.

In the first simulation, the periodic flow in the 8 corrugation channel is calculated by initialising the entire flow domain with a uniform velocity of $(0.267, 0, 0) m/s$, pressure of reference value, and ν_{sgs} of $1 \times 10^{-6} m^2/s$. This initial calculation is allowed to achieve a statistically steady state and stops at 10s. Then the resulting fully developed flow field is used as the initial condition for all cases.

For each simulation, in order to demonstrate that the flow reaches a statistically steady state, time series data at various points are evaluated before post-processing. Fig 6.3 shows the time history of velocity and its fluctuation at the point $y/h = 0.82$, $x = 52.8 mm$

and $z/b = 0.5$ (mid-plane) predicted by SMAG+VD on 16 corrugations. The grey line represents the time history of u . The blue and red lines are $\langle u \rangle$ and $\langle u'^2 \rangle$ obtained by OpenFOAM. The blue and red circle are the moving average of u and u'^2 calculated from u by a self-written code².

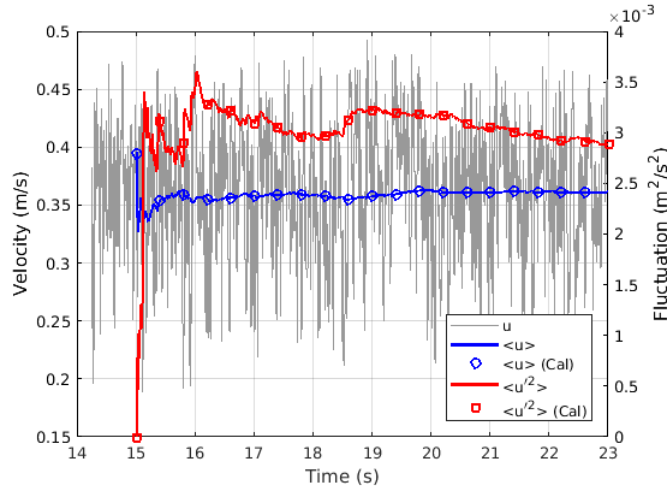


FIGURE 6.3. The time history profile of velocity at $y/h = 0.82$ on the mid-plane.

It is found that the $\langle u \rangle$ reaches the statistically steady state after taking the average for few simulation seconds. However, value for $\langle u'^2 \rangle$ seems not to reach statistically stationary after 8 simulation seconds' averaging. In order to determine whether the 8 seconds time-averaging window is adequate long, the time history data of $\langle u'u' \rangle$ and $\langle v'v' \rangle$ at same corrugation predicted by SMAG+VD are studied. The average was taken from $T = 15$ to $23s$, data between $T = 18$ and $23s$ are displayed in Fig. 6.4 with time interval of $1s$.

The time history data below reveals that after $T = 21s$ the flow variable is almost statistically stationary. The largest discrepancy between results at $T = 22$ (peach solid line) and $23s$ (dashed black line) is less than 1% at $y/h = 0.5$ for $\langle u'^2 \rangle$. Therefore, the flow at $T = 22s$ is deemed to reach the statistically stationary state. It is therefore concluded that the time-averaging window of 8 seconds is adequately long to obtain a statistical steady state.

²The self-written code is used to verify every average obtained by OpenFOAM, as a bug was found in the software which could stop it from taking average correctly if the correct procedure or setup was not followed.

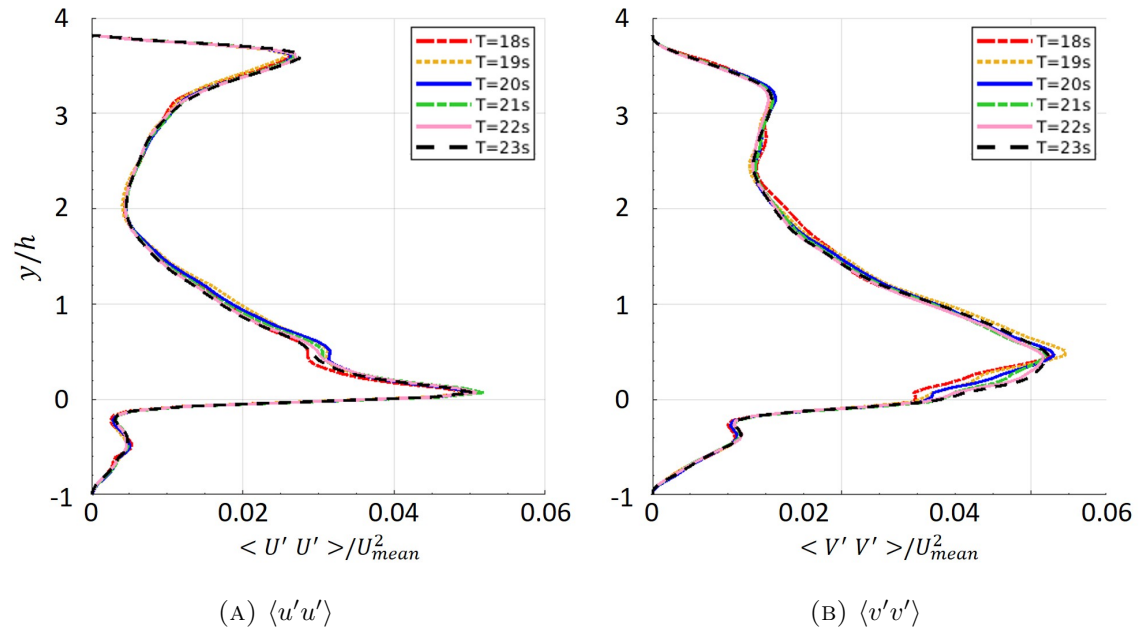


FIGURE 6.4. The time history profile of $\langle u'u' \rangle$ and $\langle v'v' \rangle$ at C8 predicted by SMAG+VD on 16 corrugation case.

6.3 Grid Independence Study

6.3.1 Effect of Grid Density

A hexahedral mesh is used for spatial discretisation. Fig. 6.5 shows that the mesh (referred to as Grid 1) is increasingly dense when approaching the wall. The first layer thickness on the corrugated wall is 0.005 mm for the bottom, 0.0044 mm for the side, and 0.0058 mm for the top. The first layer thickness on the top wall is 0.01 mm and 0.05 mm for the side walls.

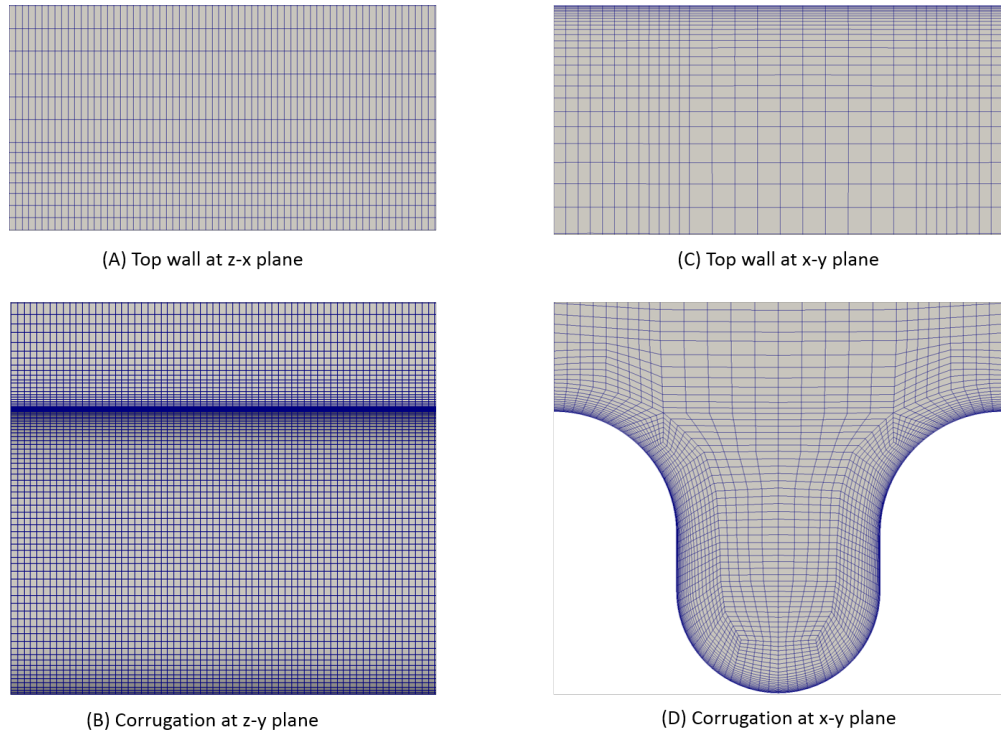


FIGURE 6.5. Localised views of Grid 1.

A finer grid (Grid 2) is constructed for the grid independence study. The density of Grid 2 doubles along each direction compared with Grid 1. The mesh for Grid 2 at the corrugation are shown in Fig. 6.6.

Simulations are performed by applying SMAG+VD and the same BCs on both grids. The properties and resultant $\langle y^+ \rangle$ and relevant details of both grids are listed in Table 6.2. The y direction for this y^+ is the direction perpendicular to the wall. Therefore y^+ for the side wall actually indicates the mesh density for z direction in current coordinate system.

Despite not being shown here, the contour plots of $\langle U \rangle$ and $\langle U'U' \rangle$ predicted by both grids are very similar. The differences mainly appear on the ratio between the SGS and

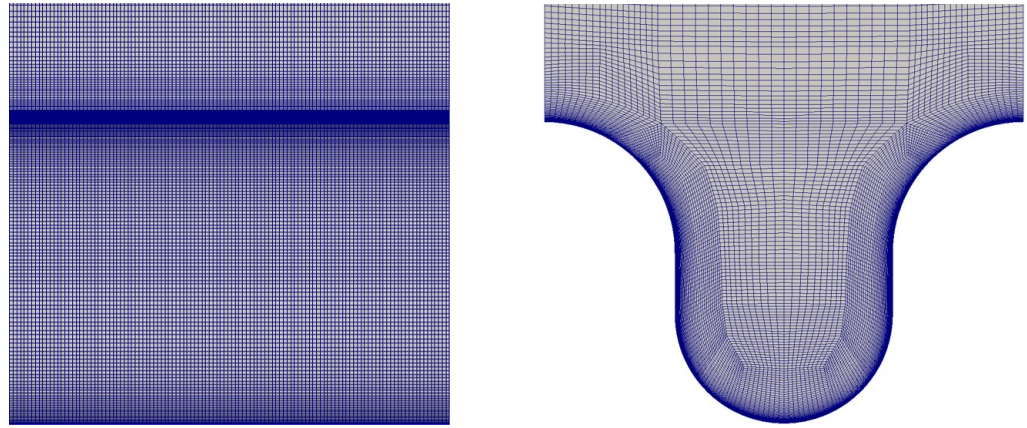
(A) Corrugation at z - y plan for Grid 2(B) Corrugation at x - y plane for Grid 2

FIGURE 6.6. The mesh at corrugation for Grid 2

Grid	CV per corrugation	$\langle y^+ \rangle$ (max, spatial average)		
		Top wall	Side wall	Corrugated wall
Grid1	0.9 million	0.12, 0.10	1.86, 0.69	0.17, 0.04
Grid2	7.2 million	0.06, 0.05	0.98, 0.35	0.09, 0.02

TABLE 6.2. The dimensions of the flow domain.

the laminar viscosity, μ_{sgs}/μ (Fig. 6.7), and the percentages of the resolved turbulent kinetic energy, $k_r\% = k_r/(k_r + k_{sgs})$ (Fig. 6.8). The figures indicate that, as expected, simulation on Grid 2 predicts a smaller value of ν_{sgs} globally and resolves more turbulent kinetic energy, but the flow field simulated on Grid 1 is well resolved. This is because the predicted value of μ_{sgs} on Grid 1 is generally lower than 25% of the value of μ , with only a few regions reaching up to 50%, also the maximum value (68%) only occurs at a very small spot close to the side wall. In addition, although there are some under-resolved flow regions ($k_r\% < 80\%$ ³) close to the top and side walls, most turbulent kinetic energy is resolved on Grid 1.

The normalised time-averaged stream-wise velocity, $\langle u \rangle / U_{mean}$, also confirms that Grid 1 is adequately fine to provide a well resolved LES solution. The comparison of $\langle u \rangle / U_{mean}$, at mid-plane ($z/b = 0.5$) and $x/\lambda = 0$ ⁴ between Grid 1 and Grid 2 is presented in Fig. 6.9. It is found the results obtained by both grids are very similar. Only a marginal difference of $\langle u \rangle_{max}$ location between the results of the two grids is visible. For Grid 1, $\langle u \rangle_{max}$ is at

³When 80% of the turbulent kinetic energy is resolved, the LES can be considered to be well-resolved [143].

⁴ $x/\lambda = 0$ means the vertical line originated from the top of the corrugation.

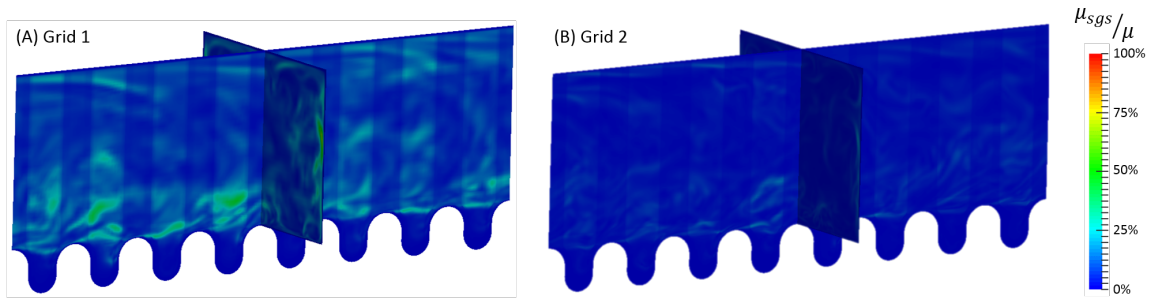


FIGURE 6.7. The contour of μ_{sgs}/μ on $x-y$ plane of $z/b = 0.5$ and $y-z$ plane of $x/\lambda = 0$ predicted by SMAG+VD on Grid 1 and 2.

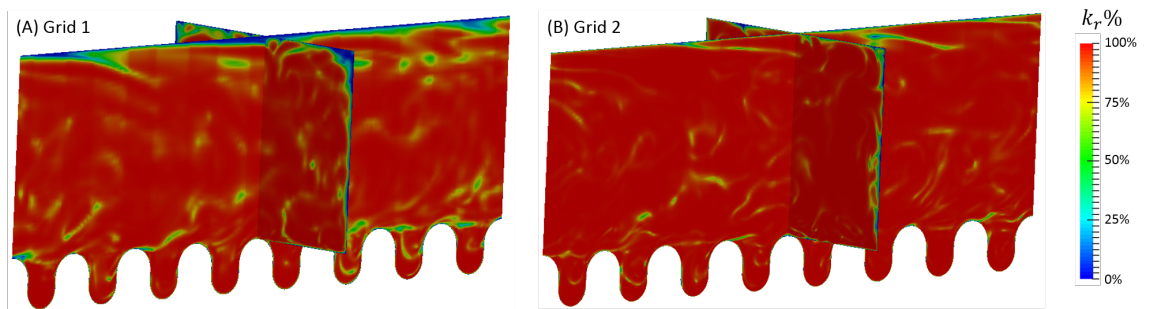


FIGURE 6.8. The contour of $k_r\%$ on $x-y$ plane of $z/b = 0.5$ and $y-z$ plane of $x/\lambda = 0$ predicted by SMAG+VD on Grid 1 and 2.

$y/h = 1.89$ ⁵ and 1.85 for Grid 2, the difference is only 2%.

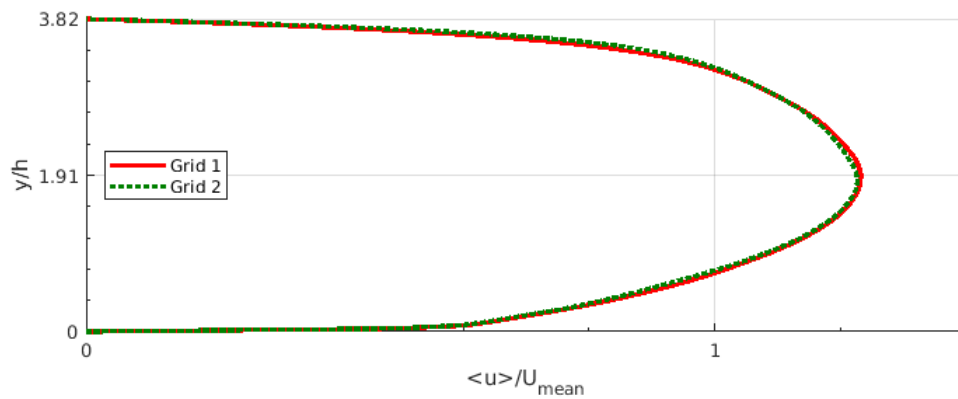


FIGURE 6.9. $\langle u \rangle / U_{mean}$ at $z/b = 0.5$ and $x/\lambda = 0$ predicted by SMAG+VD on Grid 1 and Grid 2.

The normalised time-averaged Reynolds stresses, i.e. $\langle v'v' \rangle$, $\langle u'u' \rangle$ and $\langle u'v' \rangle$, obtained by Grid 1 and Grid 2 are compared in Fig. 6.10. Fig. 6.10a, Fig. 6.10b and Fig. 6.10c are for the Reynolds stresses at $z/b = 0.5$, $z/b = 0.75$ and $z/b = 0.85$, respectively. It is worth

⁵ $y/h = 0$ is at the top of the corrugation.

pointing out that as discussed later in the Section 6.3.2 the distribution and magnitude of the high Reynolds stresses vary from corrugation to corrugation. Therefore, the profile compared in Fig. 6.10 is obtained from a spatial average of the profile of all corrugations.

It is found that the result predicted on Grid 1 generally matches well with that on Grid 2, especially for the region close to the corrugated wall. The y/h location and magnitude for the maximum Reynolds stresses predicted by both grids are very close. The largest discrepancies for these two parameters both occur on $\langle v'v' \rangle$ at $z/b = 0.5$, the value are 0.2% and 0.28%, respectively.

However, most discrepancies are found at regions above $y/h = 2$. For $z/b = 0.5$ and 0.75, although curves for Grid 1 are similar with those for Grid 2, the largest discrepancies for the location of maximum Reynolds stresses (6.5%) occurs at $\langle v'v' \rangle$ for $z/b = 0.5$, and the largest under-prediction of Grid 1 comparing to Grid 2 (20%) occurs at $\langle u'u' \rangle$ at $z/b = 0.5$. However, the the curve obtained on Grid one at $z/b = 0.5$ follows the curve obtained by Grid 2 better than the case for $z/b = 0.75$.

The discrepancies for the same flow region at $z/b = 0.85$ are more obvious than the two other locations. Despite the the general trends of the curve simulated by both grids are similar, the result obtained by Grid 1 are more apart from the Grid 2 than the results for other two z/b locations. The largest discrepancies for the location of maximum Reynolds stresses (6.5%) occurs at $\langle v'v' \rangle$ and the largest under-prediction of Grid 1 comparing to Grid 2 (43%) occurs at $\langle u'u' \rangle$.

The discrepancies and under-predictions of Grid 1 at $z/b = 0.5$ and 0.75 are due to the mesh density, as the finer mesh (Grid 2) should be able to resolve more turbulent kinetic energy. While, the discrepancies at $z/b = 0.85$ are more due to the effect of the side wall. As shown in Chapter 5, the Reynolds stresses predicted by SMAG+VD on channel flow are sensitive to the mesh density and can predict Reynolds stresses at a good agreement with DNS data when $\langle y^+ \rangle < 1.1$. Whereas the maximum y^+ for side wall is 1.86, even though its spatial averaged value is 0.69. Nevertheless, the effects caused by this are deemed limited, as the trends of the profiles and the locations of maximum Reynolds stresses obtained by the two grids are generally very close. In addition, the computing resource for Grid 1 is only 1/8 of Grid 2. It is therefore concluded that Grid 1 offers a good balance between computing resource and accuracy and is able to produce a well resolved LES solution.

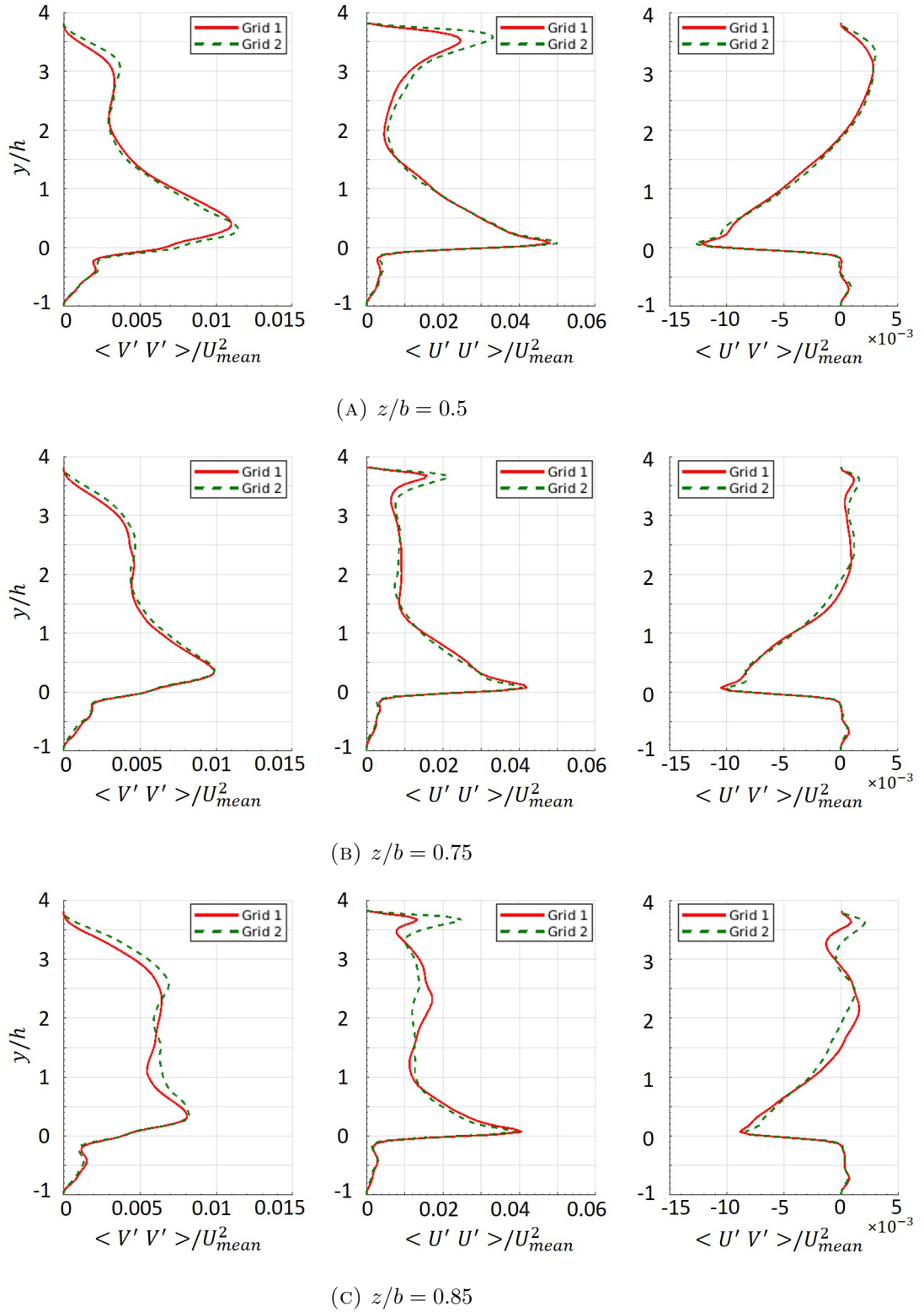


FIGURE 6.10. Profile of resolved Reynolds stresses, $\langle v'v' \rangle$, $\langle u'u' \rangle$ and $\langle u'v' \rangle$, normalised by U_{mean}^2 at different z location by SMAG+VD on Grid 1 and Grid 2.

6.3.2 Effect of Corrugated Channel Length

Stream-wise decorrelation is crucial for simulations with periodic BC [91, 137]. In order to determine a suitable total length of the computational domain in the streamwise direction, three simulations are performed with different corrugation counts: 8 corrugations, total length $L_8 = 8\lambda = 52.8 \text{ mm}$, 16 corrugations, $L_{16} = 16\lambda = 105.6 \text{ mm}$ and 32 corrugations, $L_{32} = 32\lambda = 211.2 \text{ mm}$. The results are shown in Fig. 6.11. The red, yellow and blue solid lines represent results predicted by SMAG+VD with mesh density of Grid 1 on 8, 16 and 32 corrugations, respectively.

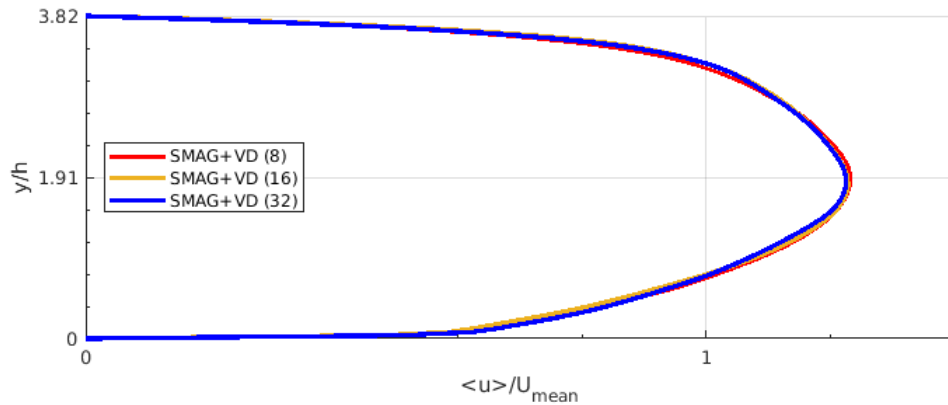


FIGURE 6.11. $\langle u \rangle / U_{mean}$ at $z/b = 0.5$ and $x/\lambda = 0$ predicted by SMAG+VD on channels with 8, 16 and 32 corrugations.

It is shown that the results predicted with the three different channel lengths are very similar. However the $\langle u \rangle_{max}$ for case with the 8 corrugation is at $y/h = 1.89$, whereas the value for cases with 16 and 32 corrugations is at $y/h = 1.81$. The difference is 4.25%.

A study on the two-point (2pt) correlation is conducted to find the suitable computational domain. The definition of the 2pt-correlation is

$$R_{ij}(\mathbf{r}, \mathbf{x}, t) = \langle u'_i(\mathbf{x}, t) u'_j(\mathbf{x} + \mathbf{r}, t) \rangle \quad (6.1)$$

where \mathbf{x} represents the location of the starting point for evaluating the 2pt-correlation; $\mathbf{x} + \mathbf{r}$ is the location of points away from the starting point; $\langle \rangle$ is the time-averaging operator; and u'_i and u'_j are the instantaneous velocity fluctuations of i and j components respectively. After spatial and temporal average, $R_{ij}(\mathbf{r}, \mathbf{x}, t)$ becomes $R_{ij}(\mathbf{r})$.

The data is extracted along three lines at mid-plane which are located at $y/h = 0.265$, $y/h = 0.578$, and $y/h = 0.819$, respectively. Those three locations cover the region of high Reynolds stresses close to the corrugated wall. The locations of the sampling lines are shown in Fig. 6.12. The start point of the sampling line of $y = 1.1 \text{ mm}$ is shown in detail.

The sampling line is divided into 10559 pieces with distance, dr , between each sampling point being $1 \times 10^{-5}m$.

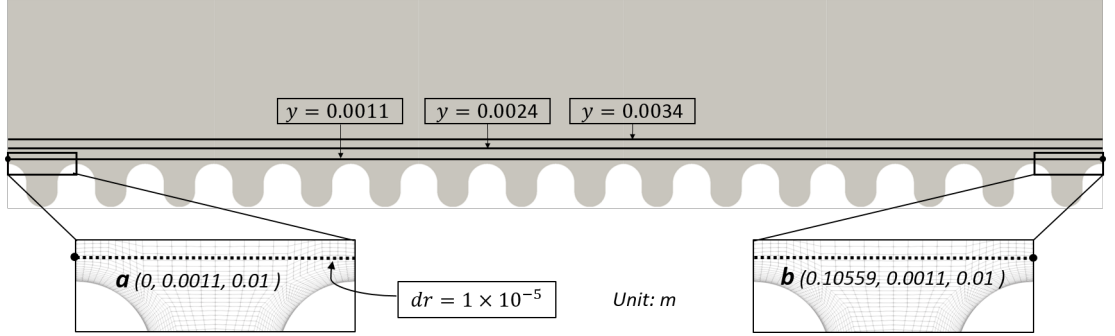


FIGURE 6.12. The details of the sampling lines for the case with 16 corrugations.

The result of the two-point correlation along the line of $y/h = 0.578$ is shown in Fig. 6.13. The profiles at $y/h = 0.265$ and $y/h = 0.819$ are similar to the one at $y/h = 0.578$, and are shown in Appendix E.

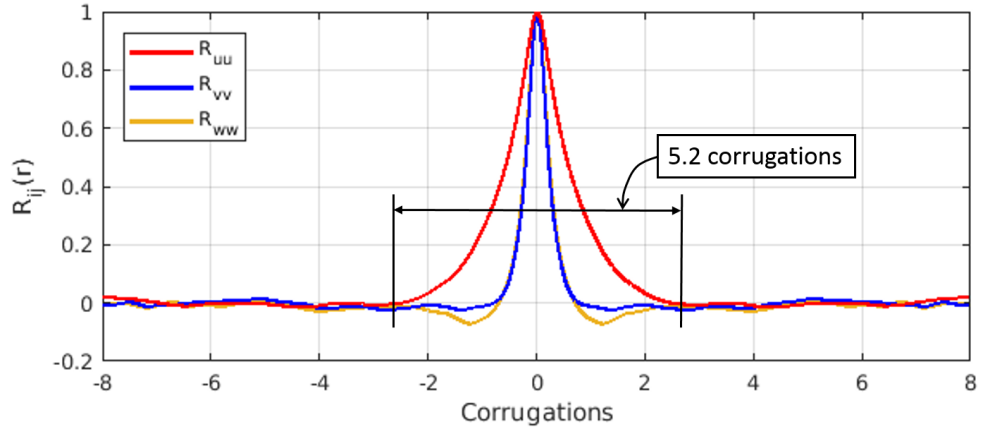


FIGURE 6.13. The normalised 2pt correlation of velocity along x direction at $y/h = 0.578$ predicted by SMAG+VD on 16 corrugations with periodic BC.

The 2pt-correlation is normalised to be 1 at the location where the 2pt-correlation calculation starts, i.e. 0 point on x -axis. Its value then reduces along both positive and negative directions of the x -axis due to the periodic BC. The spatial and temporal averaged correlation is visible for around 5.2 corrugations. It suggests that at some locations and time instants, the correlation exists at a longer distance between two points. Therefore, 8 corrugations may not be large enough to accommodate all the relevant turbulent structures. Given the aforementioned reasons, the 16 corrugations (L_{16}), $\Delta t = 1 \times 10^{-4}s$ and Grid 1 are used for all the simulations with periodic BC.

6.4 Flow Features in Corrugated Channel

6.4.1 Case Setup for 128 Corrugations

To investigate how flow develops over the entire region, a case with 128 corrugations is simulated with a turbulent inlet and non-reflective outlet BCs.

The case setup is referred to as SIM2 and briefly elaborated in Fig. 6.2 in Section 6.2 and is re-plotted in Fig. 6.14. The mesh density and numerical schemes of SIM2 are the same as the cases in the study of the effect of corrugated channel length (Section 6.3.2). The details of BCs are explained below.



FIGURE 6.14. Setup of case with 128 corrugations.

At the inlet, both pressure and SGS viscosity are set to be zero gradient as

$$\frac{\partial(p|\nu_{sgs})}{\partial \mathbf{n}_b} = 0 \quad (6.2)$$

where \mathbf{n}_b is the unit normal outward-pointing vector on the boundary, i.e. inlet and outlet. A uniform velocity of $0.3m/s$ plus the random perturbations are imposed by applying Eq. 6.3⁶

$$\mathbf{U}_p = (1 - \alpha)\mathbf{U}_p^{n-1} + \alpha(\mathbf{U}_{ref} + \mathfrak{S}\{(\mathbf{r} - \mathbf{0.5}), \mathbf{s}\}C_{RMS}|\mathbf{U}_{ref}|) \quad (6.3)$$

where \mathbf{U}_p is the velocity vector used for the current time step; α is the fraction of the new random component added by the previous time step (the default value is 0.1); \mathbf{U}_{ref} is the reference velocity vector, in this case $\mathbf{U}_{ref} = 0.3m/s$; n is time level, so $n - 1$ represents the previous time step; C_{RMS} is the RMS coefficient used to compensate for the loss of RMS fluctuation due to the temporal correlation introduced by α , its formula is $C_{RMS} = \sqrt{12 \times (2\alpha - \alpha^2)}/\alpha$; \mathbf{r} is a random vector with the value of each component being between 0 and 1; $\mathbf{s} = (\sqrt{\langle u'^2 \rangle}/|\mathbf{U}_{ref}|, \sqrt{\langle v'^2 \rangle}/|\mathbf{U}_{ref}|, \sqrt{\langle w'^2 \rangle}/|\mathbf{U}_{ref}|)$ is the vector of turbulence intensity for three dimensions; and \mathfrak{S} is the scale operator for two vectors, i.e. $\mathfrak{S}\{\mathbf{a}, \mathbf{b}\} = (a_1b_1, a_2b_2, a_3b_3)$ [117]. The parameters for Eq. 6.3 are listed in Table 6.3.

There is no best practice to choose the value of \mathbf{s} . In the current study, $\sqrt{\langle u'^2 \rangle}/|\mathbf{U}_{ref}|$ and $\sqrt{\langle v'^2 \rangle}/|\mathbf{U}_{ref}|$ were chosen to be the largest value in PIV data (calculated from Fig.6

⁶The equation is directly interpreted from the source code of OpenFOAM v1612+

Variables	Value
\mathbf{U}_{ref}	(0.3, 0, 0) m/s
\mathbf{s}	(22.4%, 11%, 11.85%)
α	Default value (0.1)

TABLE 6.3. Parameters for random generated turbulent inlet BC.

of Unal et al's work [3]). The $\sqrt{\langle w'^2 \rangle} / |\mathbf{U}_{ref}|$ is less crucial in this case. It was obtained by taking the integrated average of $\sqrt{\langle w'^2 \rangle} / |\mathbf{U}_{ref}|$ at the inlet for the 32 corrugation case with periodic BC. Despite that the sensitivity study of the result on the perturbation levels is not carried out, it is believed that the bulk flow behaviour will be dominantly affected by the flow from the corrugation. Therefore, the level of perturbation should have minimum effect on the result, especially for the fully turbulent region.

At the outlet, the pressure is set to the reference value. ν_{sgs} is zero gradient. As suggested by Versteeg and Malalasekera [72], the convective BC

$$\frac{\partial \phi}{\partial t} + \mathbf{U}_n \cdot \frac{\partial \phi}{\partial \mathbf{n}} = 0 \quad (6.4)$$

is used for velocity, where \mathbf{n} is the outward-pointing unit normal vector at outlet.

The simulation is started from the case with 32 corrugations, then the flow domain is extended to 64 corrugations, and the resulting flow fields from the first 32 corrugations are mapped onto the newly added 32 corrugations.. After 4s run, the result of 64 corrugations is mapped onto the case with 128 corrugations by the same way. After a further simulation of 8s case time, the statistical result is obtained by a time-averaging of another 8s case time (80,000 time steps).

6.4.2 Overview of Flow Development

Fig. 6.15 shows the overview of the instantaneous velocity magnitude, U_{mag} , on the mid-plane (x - y plane at $z/b = 0.5$) predicted by SMAG+VD. Fig. 6.15a to 6.15d are the localised snapshots of regions in Zone 1 to 4, respectively. Different stages of flow development can be identified from Fig. 6.15 and summarised in Table 6.4.

Zone	Top BL	Corrugated Wall BL	Range
1	Fast development, visually laminar	Fast development, gradually becoming chaotic	C1 ~ C15
2	Slow development, visually laminar	Slow development, unsteady and chaotic	C16 ~ C41
3	Transition to turbulent	Unsteady and chaotic	C42 ~ C78
4	Unsteady and chaotic	Unsteady and chaotic	C79 ~ C128

TABLE 6.4. Different zones for flow development in current corrugated channel.

Within Zone 1, as shown in Fig. 6.15a the BL at the top wall is visually laminar and develops faster than the flow in other zones. The development of the BL at the corrugated wall is also visible. Prior to the 7th corrugation (C7), the increase of the BL thickness at the corrugated wall is almost laminar and there is no momentum exchange between the flow in corrugations and bulk flow. However, this exchange starts becoming visible at C7 and being intensified downstream with several flow ejections being found at C11 and C14. The flow ejections from the corrugations affect the flow field in the bulk flow and make the BL at the corrugated wall chaotic.

In Zone 2, shown in Fig. 6.15b, the BL at the top wall is still visually laminar, but develops much slower than Zone 1. The flow close to the corrugated wall is chaotic and its BL thickness remains largely unchanged across the Zone.

Fig. 6.15c suggests that at Zone 3, the top wall BL seems to experience transition from laminar to turbulent, despite that the transition process was not studied in the experimental work [3]. At the beginning of this Zone, some undulations are observed at the BL of the top wall. This BL is distorted downstream and finally breaks up at the end of this Zone. This process also affects the bulk flow region. From Zone 1 to the beginning of Zone 3, the region of bulk flow with $y/h > 0.5$ is relatively uniform. But at the end of Zone 3, the whole region of bulk flow becomes chaotic.

In Zone 4, Fig. 6.15d demonstrates a chaotic bulk flow which has momentum interaction with every corrugation. This characteristics is very similar to the observation of the PIV (Shown in Fig. 1.3b).

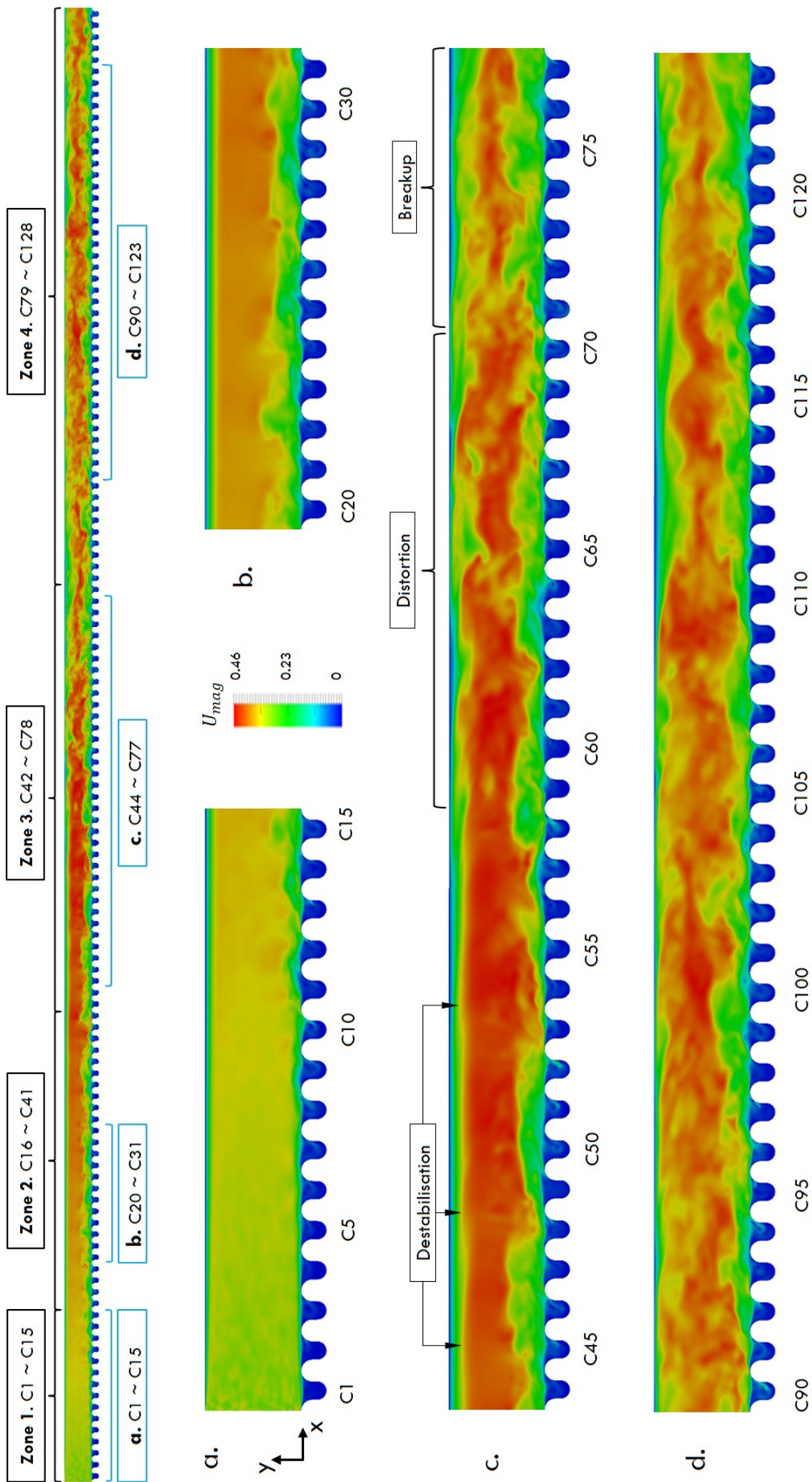


FIGURE 6.15. The overview of the instantaneous U_{mag} on $z/b = 0.5$ predicted by SMAG+VD on 128 corrugation case.

The plot of time-averaged velocity magnitude, $\langle U_{mag} \rangle$, reveals how flow develops in a time-averaged manner. The overview of $\langle U_{mag} \rangle$ on the mid-Zplane is presented in Fig. 6.16. Fig. 6.16a to 6.16g are the localised snapshots of regions in the flow field. Fig. 6.16h and 6.16i show the normalised stream-wise velocity, $\langle u \rangle / U_{mean}$ ⁷, profile along the black lines in Fig. 6.16a to 6.16g. For the sake of clarity, $\langle u \rangle$ profiles of the sampled lines at the first half of the corrugated channel are placed in Fig. 6.16h, the profiles for the second half are shown in Fig. 6.16i. The profile of C62 appears at both figures to maintain the continuity between them.

The profile at C4 in Fig. 6.16h is examined first. It is noted that the velocity peaks close to the walls are non-physical. Although there is no available experimental data to compare with, it is believed that these velocity peaks are caused by a numerical error which can be demonstrated in Fig. 6.17a⁸.

It is known that the flow velocity should be close to zero at the wall regions due to the non-slip BC. Current simulation specifies a uniform velocity at the inlet, i.e, the flow velocity at the near wall region is the same as the bulk flow. When the flow enters the computational domain, the velocity of the flow close to the wall regions will experience a sudden decrease which leads to a static pressure increase, generating local high static pressure regions close to the top wall and two side walls (Fig. 6.17a). These high pressure regions accelerate the flow close to the wall for the first few corrugations, such as C4, creating the local velocity peaks in the profile of C4 in Fig. 6.16h and Fig. 6.17b ($\langle u \rangle$ along the z -axis). Therefore, it is good practice to apply a fully developed flow velocity profile as the inlet condition to eliminate this error. But as shown by the $\langle u \rangle$ profile of C33 in Fig. 6.16h and Fig. 6.17b the effect of this numerical error is not identifiable after C33. Considering the length of the current computational domain (up to C128), this error is not expected to affect the results in Zone 3 and Zone 4.

⁷ $U_{mean} = 0.3m/s$.

⁸Applying a uniform velocity with zero turbulence intensities on the inlet.

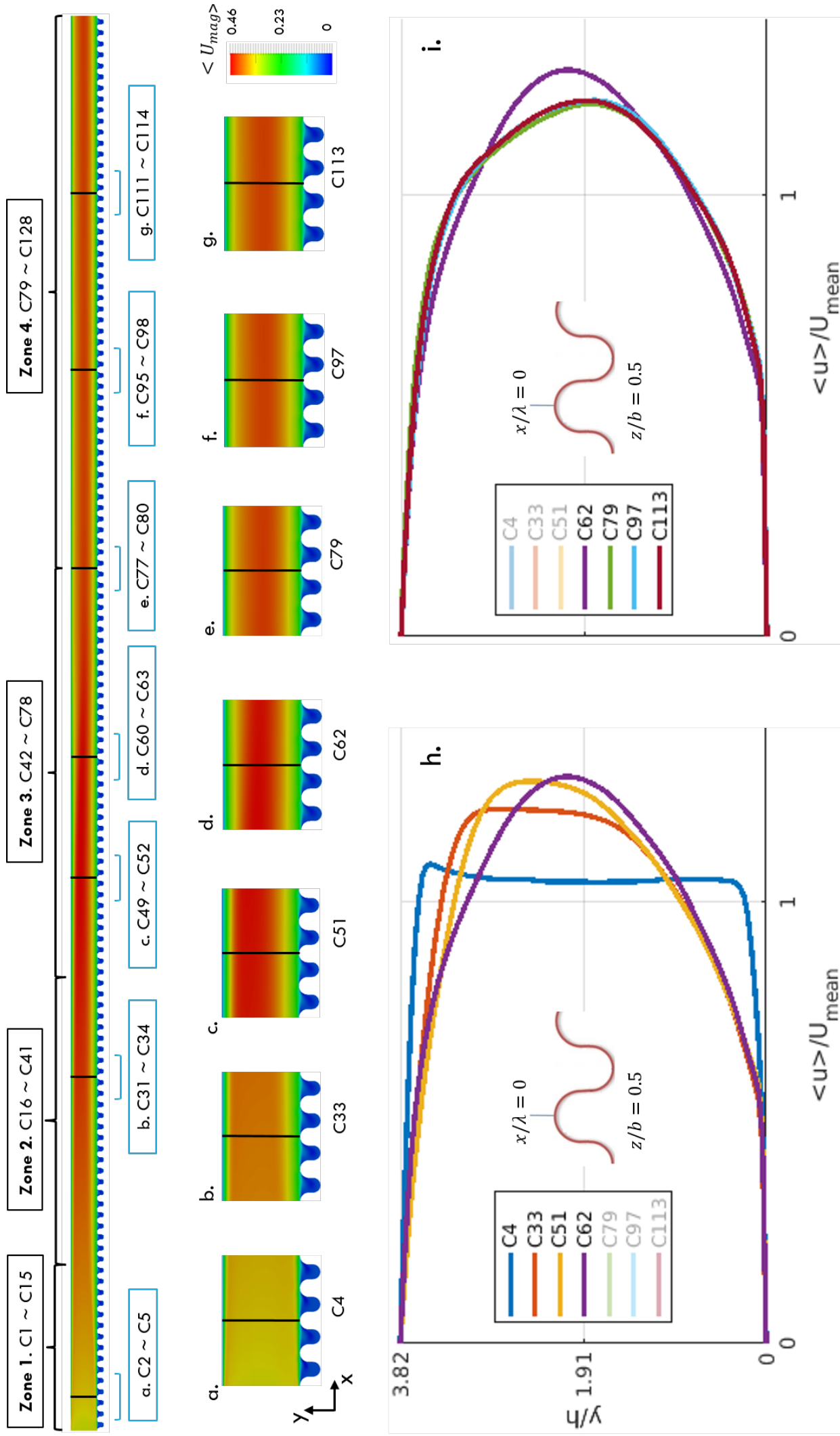


FIGURE 6.16. The snapshot of $\langle u \rangle$ and its localised details at $z/b = 0.5$ predicted by SMAG+VD on 128 corrugation case.

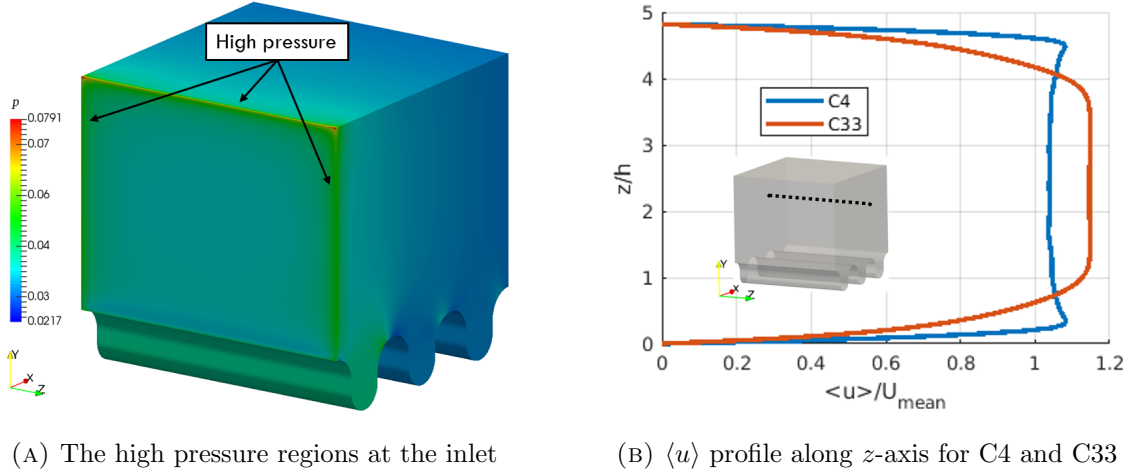


FIGURE 6.17. The numerical error caused by uniform velocity inlet.

From C33, different BL thicknesses are calculated based on the method in the book of Mayes et al. [69]. The u_{max} for $x/\lambda = 0$ of each corrugation is chosen to be the free stream velocity. The calculated displacement and momentum thicknesses are plotted in Fig. 6.18. Fig. 6.18a is for the displacement thickness, δ^* , which is a parameter to quantify the reduction of mass flow rate (blockage) caused by the BL. Fig. 6.18b shows the profile of the momentum thickness, θ , which quantifies the amount of the momentum that the BL destroys. The shape factor, $H = \delta^*/\theta$, is presented in Fig. 6.18c. H is an indicator of whether the BL is turbulent or laminar. The laminar BL in a flow with uniform static pressure (Blasius BL) has $H = 2.59$ and $H \sim 1.4$ is the indication of a turbulent BL [69].

At C33, the differences between the BL of the top and corrugated walls are apparent. The rate of BL development at the corrugated wall is much faster than at the top wall. This is not only shown by the $\langle u \rangle$ profile of C33 in Fig. 6.16h, but is also reflected on the value of δ^* , θ , and H . At C33, the BL of the corrugated wall is turbulent ($H = 1.6$), while the one at the top wall is laminar ($H = 2.34$). The turbulence close to the corrugated wall causes considerably greater (52% and 122% respectively) reduction of mass flow rate and flow momentum than at the top wall.

The BL thicknesses at the corrugated wall increase until δ^* and θ reach their maximum levels at C55 and C51 respectively ($\delta^*_{max} = 0.46h$ and $\theta_{max} = 0.29h$). Then the values of these BL thicknesses decrease continuously at roughly the same rate until C89. At the same corrugations range, the H of the top wall sees a rapid decline from 2.26 at C51 to 1.67 at C79, indicating the BL at the top wall experiences a transition from laminar to turbulent. This suggests the undulation-distortion-breakup process observed in the U_{mag} snapshot (Fig. 6.16c) is a transition process.

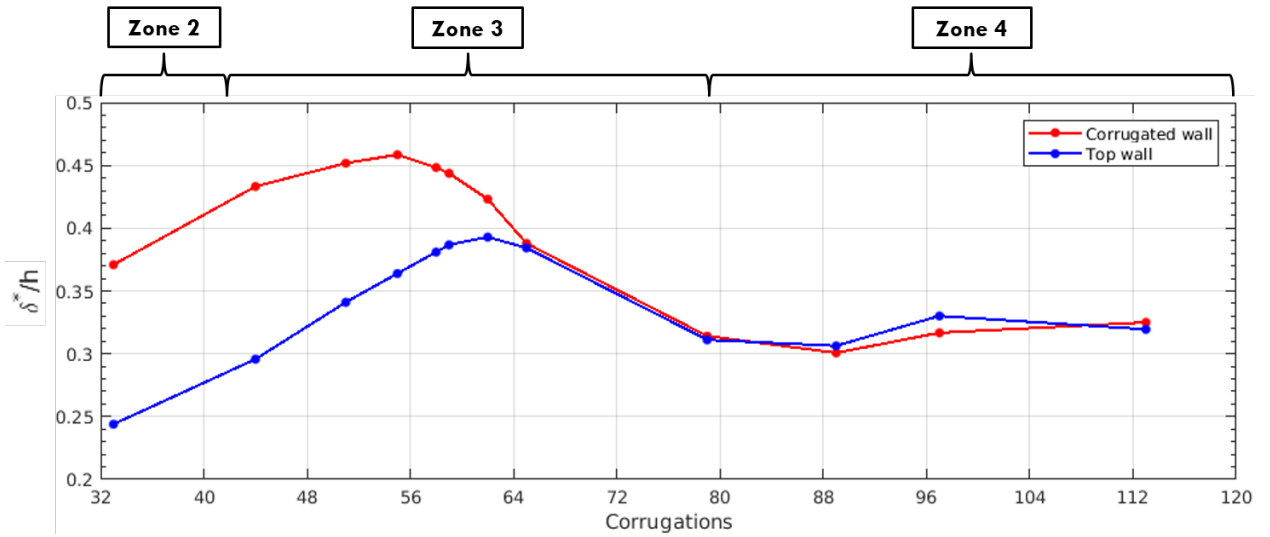
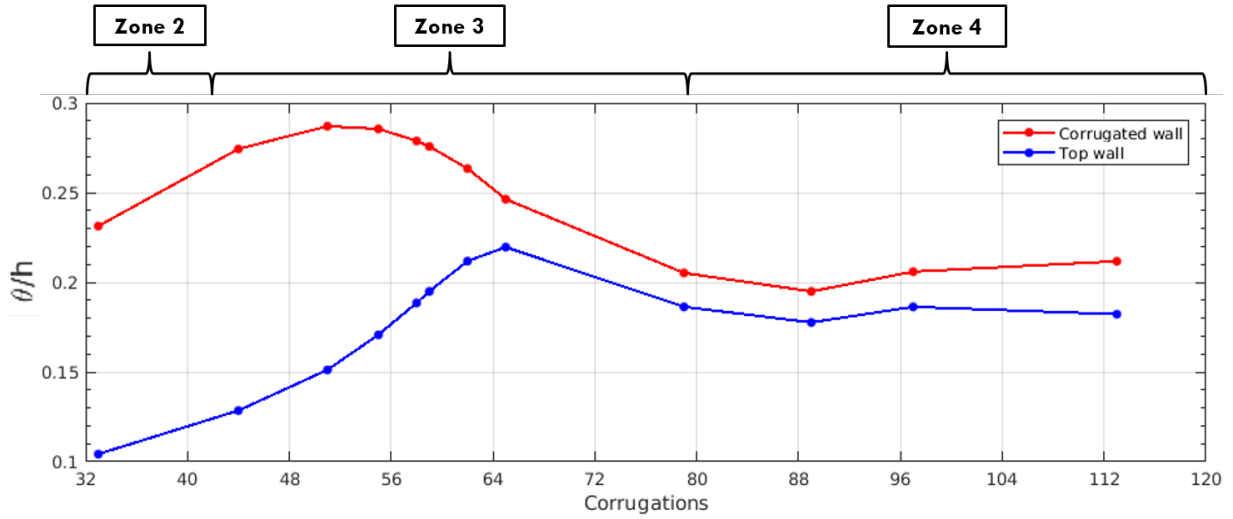
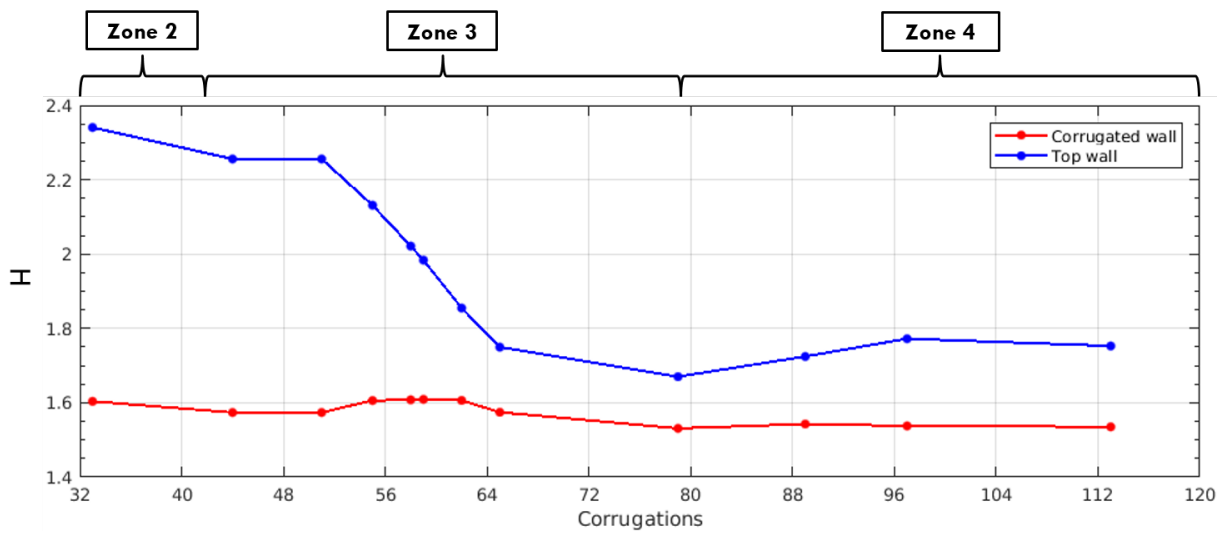
(A) Displacement thickness, δ^* .(B) Momentum thickness, θ .(C) Shape factor, H .

FIGURE 6.18. The profiles of BL thicknesses at $x - y$ plane of $z/b = 0.5$ predicted by SMAG+VD on channels with 128 corrugations.

During the BL transition, the trend of the BL thicknesses at the top wall seems to correlate with the development of the Reynolds stresses at same region. The contour plots of $\langle u'u' \rangle$ and $\langle v'v' \rangle$ between C55 and C73 on the mid-plane are shown in Fig. 6.19.

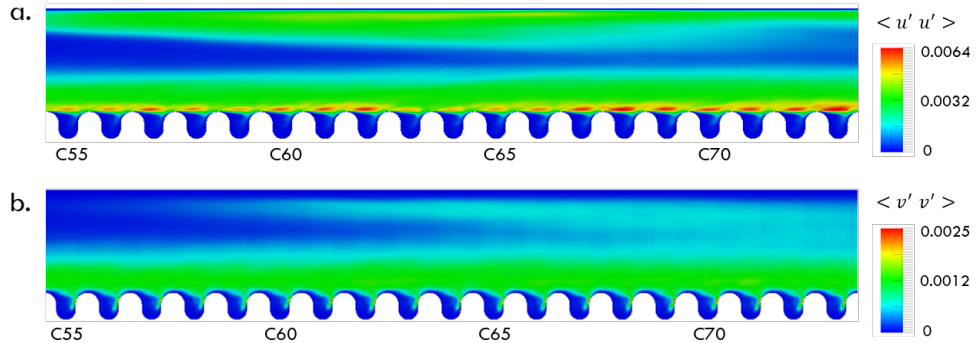


FIGURE 6.19. The contour of $\langle u'u' \rangle$ and $\langle v'v' \rangle$ at $z/b = 0.5$ between C55 and C73.

At the beginning of the transition, the BL thicknesses of the top wall increase, so does the area of the regions with high $\langle u'u' \rangle$ and $\langle v'v' \rangle$ value close to the top wall, as seen in Fig. 6.19a and Fig. 6.19b, respectively. The δ^* and θ reach their maximum values at C62 and C65 respectively. Around the similar location, the upper casing thickness for high turbulence intensity regions reach their maximum values as well. Then the BL thicknesses at the top wall join the declining trend of that at the corrugated wall. Similarly, the sizes of the regions with high turbulent intensity at the top wall decrease after C65 (not very clear for $\langle v'v' \rangle$). However, the reason for the upper casing thickness increase first then decrease beyond C64 remains to be explored and there is no experimental data available to compare with.

At C65, $H = 1.75$ indicates that the BL at the top wall becomes turbulent. Interestingly, the δ^* at top wall reaches the same value with the one at the corrugated wall at C65 and follows the similar trend further downstream. Also from C65, θ for both the top and corrugated walls starts following a similar trend, although the value at the corrugated wall is around 10% larger than the one at the top wall. This suggests that when the BL and also the entire flow in the corrugated channel become turbulent, the blockages and momentum reductions caused by the BL at both top and corrugated walls are roughly the same.

This is reflected in the profiles of $\langle u \rangle$ across the channel. As shown in Fig. 6.16h and 6.16i, unlike C51, the profile at C62 is largely symmetric and has a $\langle u \rangle_{max}$ value around the centreline. As the values of δ^* and θ keep on reducing, the bulk flow becomes more uniform. Finally, in Zone 4 the flow reaches its fully developed profile and has the $\langle u \rangle_{max}$

value at $y/h = 1.813$ which is just below the centreline of the channel ($y/h = 1.91$).

The findings from the overview of flow development in this corrugated channel suggest that the BL development of the corrugated wall is suppressed by the BL transition at the top wall, and the time-averaged effects of BL at the top and corrugated walls on the fully developed turbulent flow are similar. After the overview one may naturally come up with following questions:

1. Can the features of the fully developed turbulent flow region (Zone 4) be captured by 16 corrugations with periodic BC?
2. How does the LES prediction compare with available experimental data?
3. What are the details of flow development and how the transition happens?
4. How are the hydrodynamic interaction and vortices evolution in the fully developed turbulent flow region?

The following sections are dedicated to answering these questions.

6.4.3 128 vs 16 Corrugations in Fully Turbulent Region

As shown in the literature review, the study of fully developed turbulent flow over multiple cavities is normally performed on one or several cavities with streamwise (or spanwise) periodicity, rather than on a full length channel. This method greatly reduces the required computing resources, but it is not applicable to every case with multiple cavities, such as the first case of periodic hill by Almeida et al [44].

This section will compare the flow features and time-averaged results predicted by SMAG+VD on the 128 corrugations with turbulent inlet and 16 corrugations with periodic BC. The data between C97 and C112 is used to represent the fully turbulent region in the 128 corrugations case, as this corrugation range falls in the middle of Zone 4. The data for 16 corrugations with periodic BC from in Section 6.3.2 is used to study the effects of different channel lengths.

Contours of U_{mag} , $\langle U_{mag} \rangle$ and Reynolds stresses predicted for the 128 and 16 corrugations cases are similar. Therefore, only the contours obtained with 16 corrugations and periodic BC are presented here. Fig. 6.20a shows the U_{mag} contours on the mid-plane ($z/b = 0.5$) and Fig. 6.20b is an iso-surface of Q-criterion coloured by v .

The two figures collectively demonstrate a chaotic bulk flow with a wide spectrum of vortex sizes being affected by the flow bursting from corrugations. Various regions of velocity reduction caused by the turbulent BL at the top wall and strong interaction between

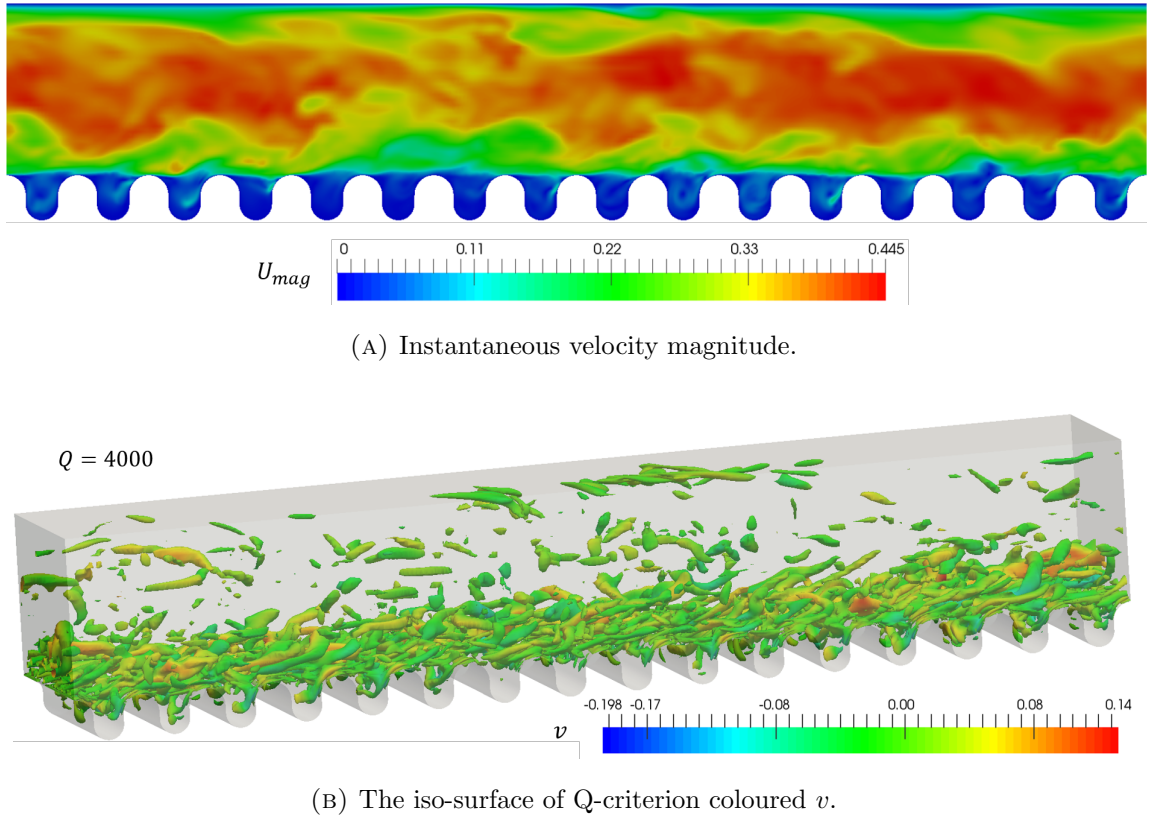


FIGURE 6.20. The contour of U_{mag} at $z/b = 0.5$ and the iso-surface of Q-criterion predicted by SMAG+VD on 16 corrugation with periodic BC.

the eddies in corrugation and bulk flow are clearly visible. The result also shows that multiple vortices with different sizes co-exist at different locations in each corrugation. All these phenomena are in agreement with the observation of the case with 128 corrugation and the experiment by Unal et al. [12].

The profile of $\langle u \rangle / U_{mean}$ at $x/\lambda = 0$ and $z/b = 0.5$ predicted by 128 and 16 corrugations cases are compared in Fig. 6.21. It shows the two profiles match well and their $\langle u \rangle_{max}$ locate at $y/h = 1.813$.

The contours of $\langle u'u' \rangle$ and $\langle v'v' \rangle$ predicted on 16 corrugations are shown in Fig. 6.22. It is observed that each corrugation in Fig. 6.22a has a region with high $\langle u'u' \rangle$ over the exit of the corrugation. These are the regions where the momentum exchange in the x direction occurs. However, the shape and the magnitude of the high intensity region of $\langle u'u' \rangle$ varies from corrugation to corrugation. This feature is also observed in the case with 128 corrugations. The discrepancies between the shape of high turbulence intensity regions are studied in Appendix F. It is found this discrepancies are caused by the nature of this type of flow. Thus, a spatial-averaging of Reynolds stresses is performed across all the corrugations before they are compared between different cases.

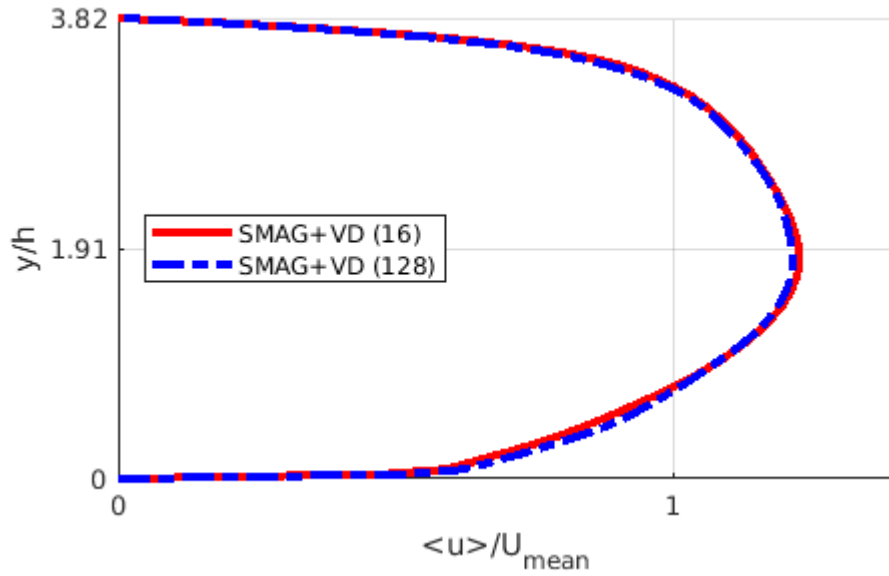


FIGURE 6.21. $\langle u \rangle / U_{mean}$ at $z/b = 0.5$ and $x/\lambda = 0$ predicted by SMAG+VD on by cases with 128 and 16 corrugations.

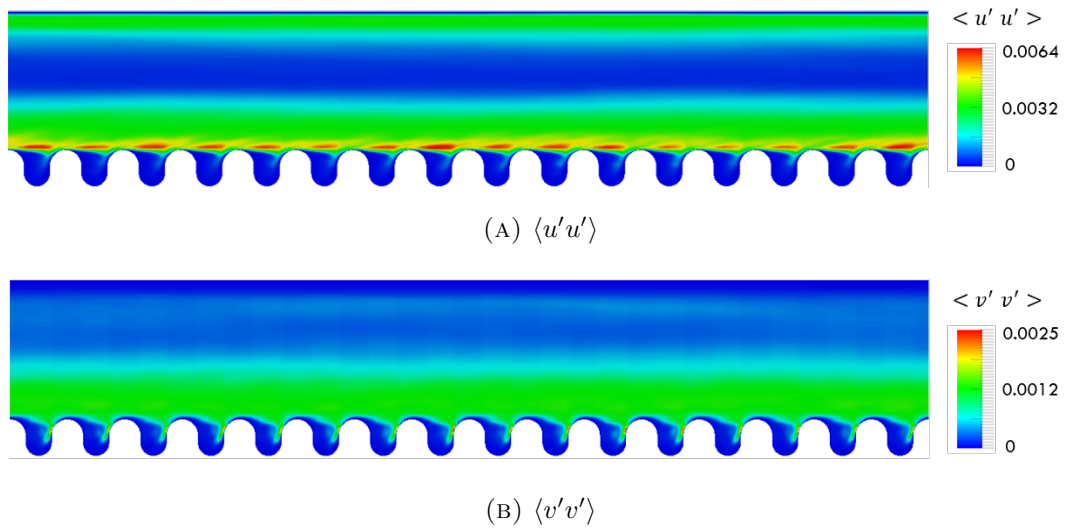


FIGURE 6.22. Profile of $\langle u' u' \rangle$ and $\langle v' v' \rangle$ predicted on 16 corrugations.

Profiles of $\langle u' u' \rangle$, $\langle v' v' \rangle$ and $\langle u' v' \rangle$ at different locations along z direction predicted on the cases with 128 and 16 corrugations are shown in Fig. 6.23. It is found that Reynolds stresses predicted on the case with 16 corrugations are in a very good agreement with the profile predicted on 128 corrugations. Although there are some discrepancies, they are very minor, and the differences are even smaller than the difference between each corrugation.

It is therefore concluded that flow simulated on 16 corrugations with periodic BC is able to reproduce the characteristics of the fully developed turbulent region produced on the case with 128 corrugations and turbulent inlet.

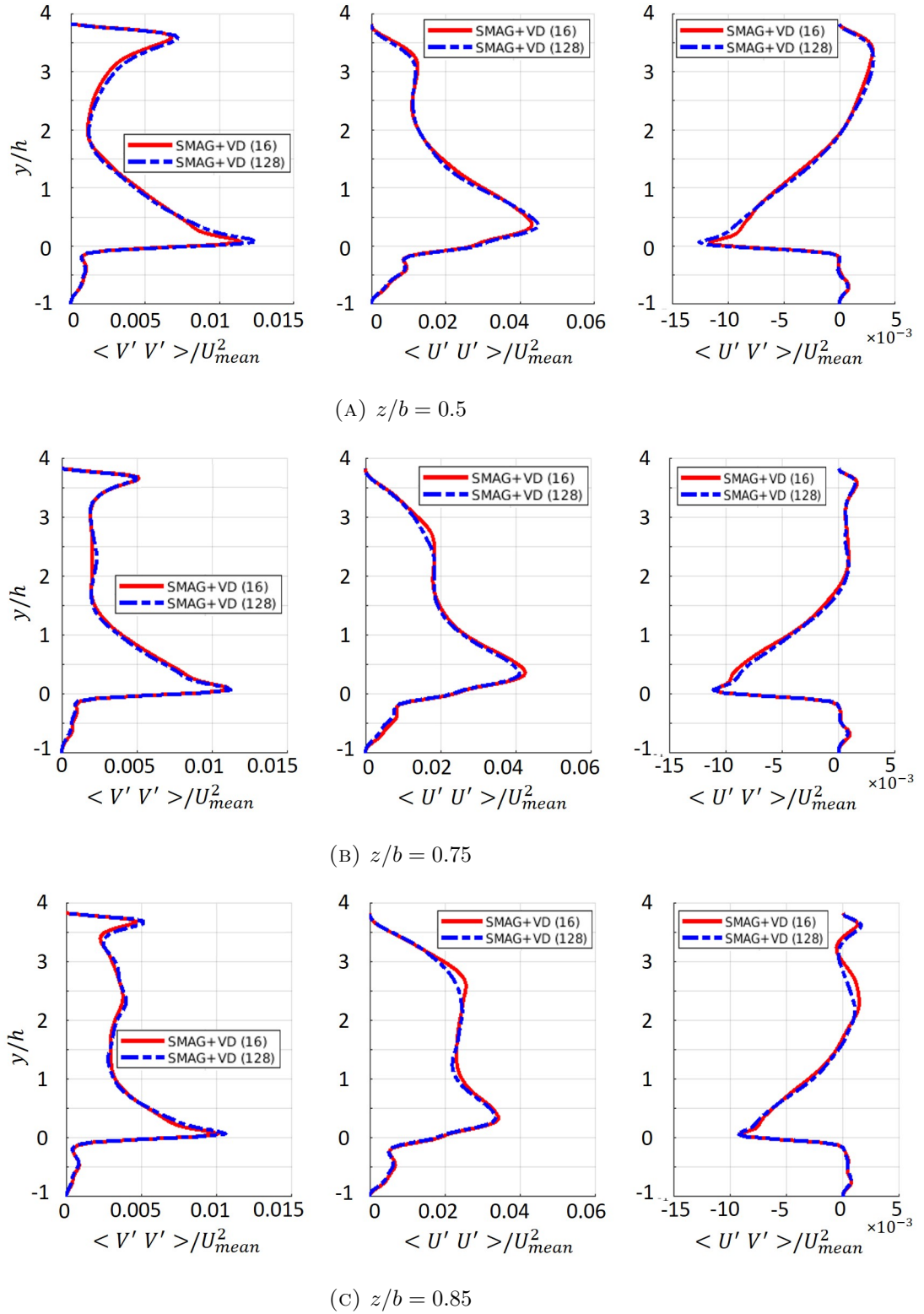


FIGURE 6.23. Profile of $\langle u'u' \rangle$, $\langle v'v' \rangle$ and $\langle u'v' \rangle$ at different locations along z direction predicted on the cases with 128 and 16 corrugations.

6.4.4 LES Results Validation

In this section, the time-averaged flow features obtained by SMAG+VD on 16 corrugations with periodic BC are compared with the PIV measurement for the fully developed turbulent region in current corrugated channel. Their differences are also analysed and discussed.

The profiles of $\langle u \rangle / U_{mean}$ at $x/\lambda = 0$ and $z/b = 0.5$ predicted by LES and measured by PIV are compared in Fig. 6.24.

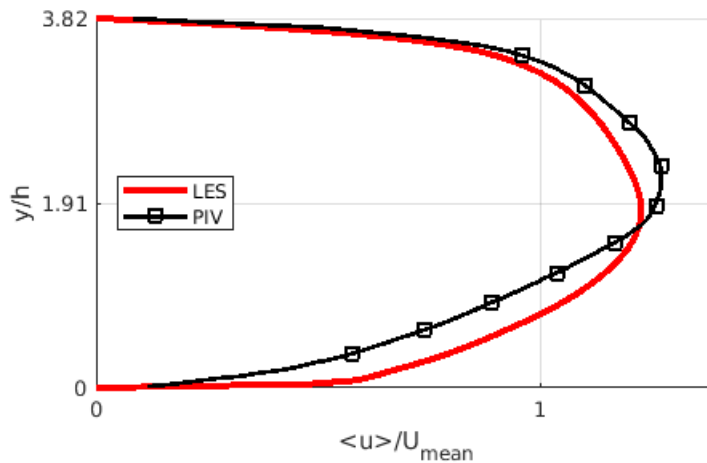


FIGURE 6.24. Comparison of $\langle u \rangle / U_{mean}$ at $z/b = 0.5$ and $x/\lambda = 0$ between the LES prediction and the PIV measurement.

A noticeable difference between LES prediction and PIV measurements of $\langle u \rangle$ is observed. The PIV data is not as symmetric as the LES prediction and their differences on various BL thicknesses are summarised in Table. 6.5.

		PIV	LES	Difference
Top wall	H	1.661	1.745	5.1%
	δ^*/h	0.282	0.331	17.4%
	θ/h	0.170	0.190	11.8%
Corrugated wall	H	1.948	1.589	-48.7%
	δ^*/h	0.585	0.347	-40.7%
	θ/h	0.301	0.218	-27.6%
$\langle u \rangle_{max}$ location	y/h	2.164	1.813	-16.2%

TABLE 6.5. Difference of BL thicknesses and $\langle u \rangle_{max}$ between LES prediction and PIV measurement.

It was found the profile of the PIV data is generally shifted towards the top wall when compared with the more symmetric profile of the LES prediction. This is also reflected by the fact that the $\langle u \rangle_{max}$ location of LES prediction is 16.2% lower than the PIV data. The LES predicted profile is only in good agreement with the PIV data at the region very close to the top wall, but differences start being apparent after $\langle u \rangle / U_{mean} > 1$. The comparison of various BL thicknesses suggests that LES predicts the top wall to cause more blockage and momentum reduction than measured by PIV. At the lower half of the channel, the discrepancies between the two profiles are observable even from the beginning, but the rate of increase of the two profiles seems to be similar. The comparison of various BL thicknesses suggests the LES predicts the corrugated wall to have considerably less blockage and momentum reduction effects than measured by PIV.

The discrepancies between the LES predictions and PIV measurements also exist in Reynolds stresses. Profiles of the normalised $\langle u'u' \rangle$, $\langle v'v' \rangle$ and $\langle u'v' \rangle$ at different locations along z direction predicted by LES and measured by PIV are shown in Fig. 6.25.

The plots show that the discrepancies between the LES prediction and PIV measurement is noticeable, although LES predictions capture the general trend of the PIV profiles and have a better agreement at the region close to the top wall than the corrugated wall. It is also found LES predictions do not match well with the PIV data in terms of the magnitudes and locations of Reynolds stresses. However, the $\langle v'v' \rangle$ profiles predicted by LES are in agreement with the PIV profile at the region very close to the corrugated wall, which is closely associated with flow ejection from the corrugations.

The discrepancies between the LES predictions and PIV data may be attributed to two reasons, i.e. the inaccuracy of the SGS model used in LES and/or the uncertainties in the experiment. These two aspects will be discussed in detail in the next two subsections, respectively.

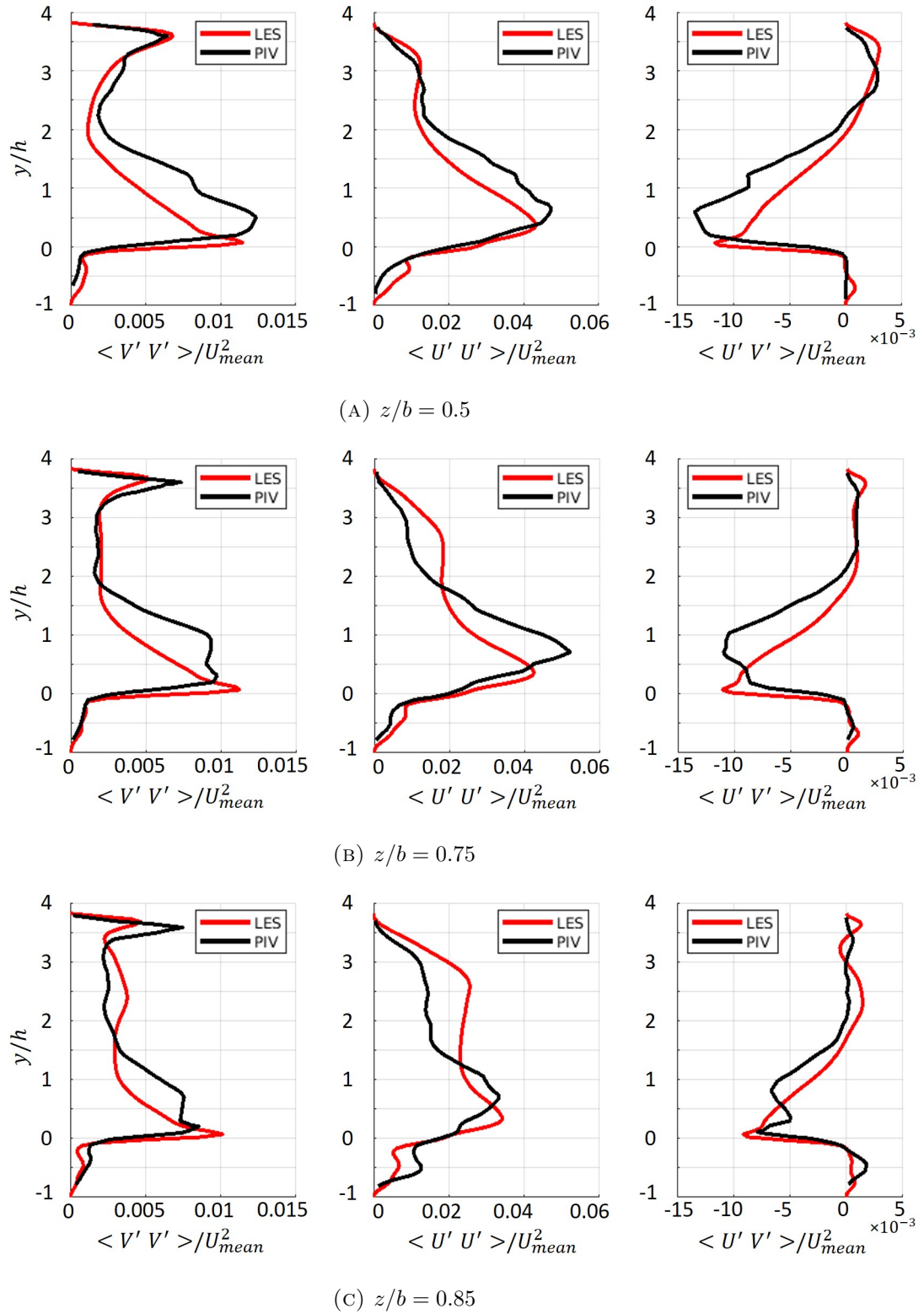


FIGURE 6.25. Comparison of profiles of $\langle u'u' \rangle$, $\langle v'v' \rangle$ and $\langle u'v' \rangle$ at different locations along z direction between the prediction of LES and the measurement of PIV.

Validation of LES Predictions

The numerical result should be firstly validated against the pressure loss correlation. Although the pressure loss is not reported in experimental data, the pressure drop predicted on current configuration should be within the range between the pressure drop due to a smooth pipe with a same cross section and a circular corrugated pipe with similar (if the same one is not available) area of cross section and corrugated pitch and depth.

The pressure drop for flow in ducts of non-circular section is [146]

$$-\frac{dp}{dx} = \frac{4f}{D_E} \frac{1}{2} \rho U^2 \quad (6.5)$$

where f is the friction factor and D_E is the equivalent diameter, defined as

$$D_E = \frac{4A}{P_w} \quad (6.6)$$

where A is the cross section area and P_w is the wetted perimeter of the duct.

The friction factor, f , is determined from the data for ducts of circular section at a Reynolds number $Re = UD_E/\nu$ [146]. The Moody chart shows that $f = 0.03727$ for a smooth pipe with current cross section configuration [147]. This leads to $-dp/dx = 94.67Pa/m$.

A circular corrugated pipe which has a similar cross section area with current configuration will have a diameter of $20.09mm$. The closest corrugated pipe which has available data is Witzeman's HYDRA metal hoses RS331S12-D20, which has a diameter of $20.2mm$, a cross section of $320.3mm^2$, a corrugation depth of $4.05mm$, and a ratio between corrugation depth and inner diameter of 0.2 (2.9% smaller than current configuration). The Manual of Witzeman's HYDRA metal hoses RS331S12-D20 shows its friction factor is around 0.7 [148]. This leads to $-dp/dx = 156.51Pa/m$ for such circular corrugated pipe. The calculated pressure drop for current configuration is $-dp/dx = 135.52Pa/m$, which suggests that the simulation result is in the correct range.

The test on channel flow in Chapter 5 has already shown that SMAG+VD is able to provide an accurate prediction for the flow over a flat wall, on the grid density used in the simulation of current corrugated channel. It is still beneficial to cross-check the results predicted by different SGS models to make sure the discrepancies between the previous LES prediction and PIV data is not due to the inaccuracy of SMAG+VD.

Three other SGS models listed in Table. 6.6 are tested on 16 corrugations with periodic BC. They are all validated by the channel flow test case.

SGS Models	Model Description
KEQ+VD	k -equation SGS model with van-Driest wall damping function
DyK	Dynamic k -equation SGS model
WALE	Wall-adapting local eddy-viscosity SGS model

TABLE 6.6. Other SGS models tested in current corrugated channel.

The reasons for choosing the above SGS models are given here. KEQ+VD gives similar results to SMAG+VD in the channel flow case, but it is a non-equilibrium SGS model. Thus, it should be less dissipative than the model based on local equilibrium assumption (SMAG+VD). It is shown that there are lots of regions with sudden turbulence kinetic energy generation in the corrugated channel due to the momentum exchange between the corrugation and the bulk flow, so KEQ+VD may provide a better result in the current corrugated channel flow case. The reason for choosing DyK instead of DyLag is that although DyLag has a similar theory background with DyK and requires less computational time, it introduces two parameters, \mathfrak{T}_{LM} and \mathfrak{T}_{MM} , whose values are calibrated for the channel flow case, but not for the current case. Whereas for DyK, the initial k_{sgs} value can be obtained by running KEQ+VD, thus having less uncertainty than DyLag. Finally, WALE is selected because it uses a different approach to recover wall scaling for eddy viscosity without using an extra transport equation, damping function or dynamic procedure.

The $\langle u \rangle / U_{mean}$ at $x/\lambda = 0$ of C9 on mid-plane predicted by various SGS models are compared in Fig. 6.26. This plot shows the $\langle u \rangle / U_{mean}$ predicted by different SGS models are very similar. The locations of $\langle u \rangle_{max}$ predicted for all four SGS models are below the centreline of the channel ($y/h = 1.91$). The values for SMAG+VD and DyK are both $y/h = 1.813$. The value for KEQ is $y/h = 1.852$ and for WALE is $y/h = 1.89$, only 2% and 4% higher than SMAG+VD, respectively.

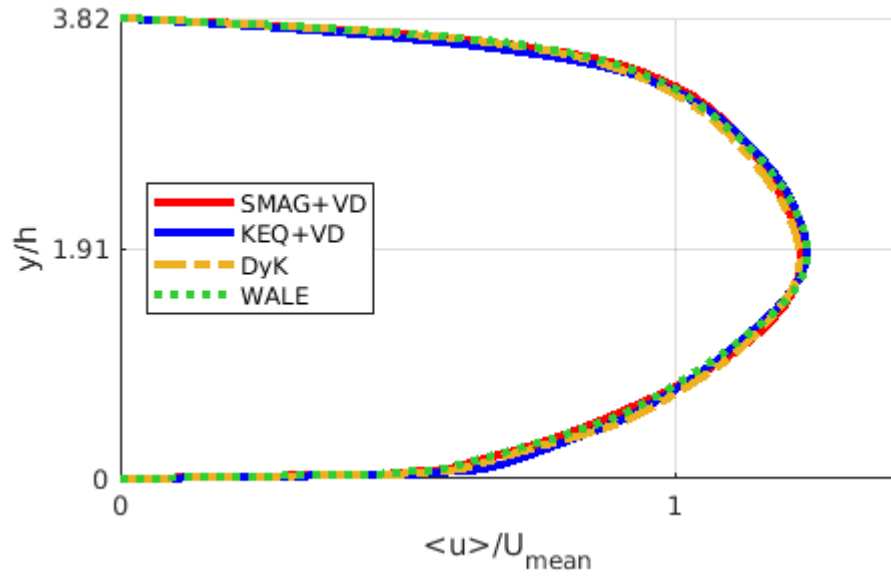


FIGURE 6.26. Comparison of $\langle u \rangle / U_{mean}$ at $z/b = 0.5$ and $x/\lambda = 0$ between the prediction of different SGS models.

The profiles of the normalised Reynolds stresses for different planes along the z -axis predicted by different SGS models are compared in Fig. 6.27. It is found that the Reynolds stresses predicted by all these SGS models follow the same trend. Despite some minor discrepancies, the locations of max Reynolds stresses obtained by these SGS models are very similar.

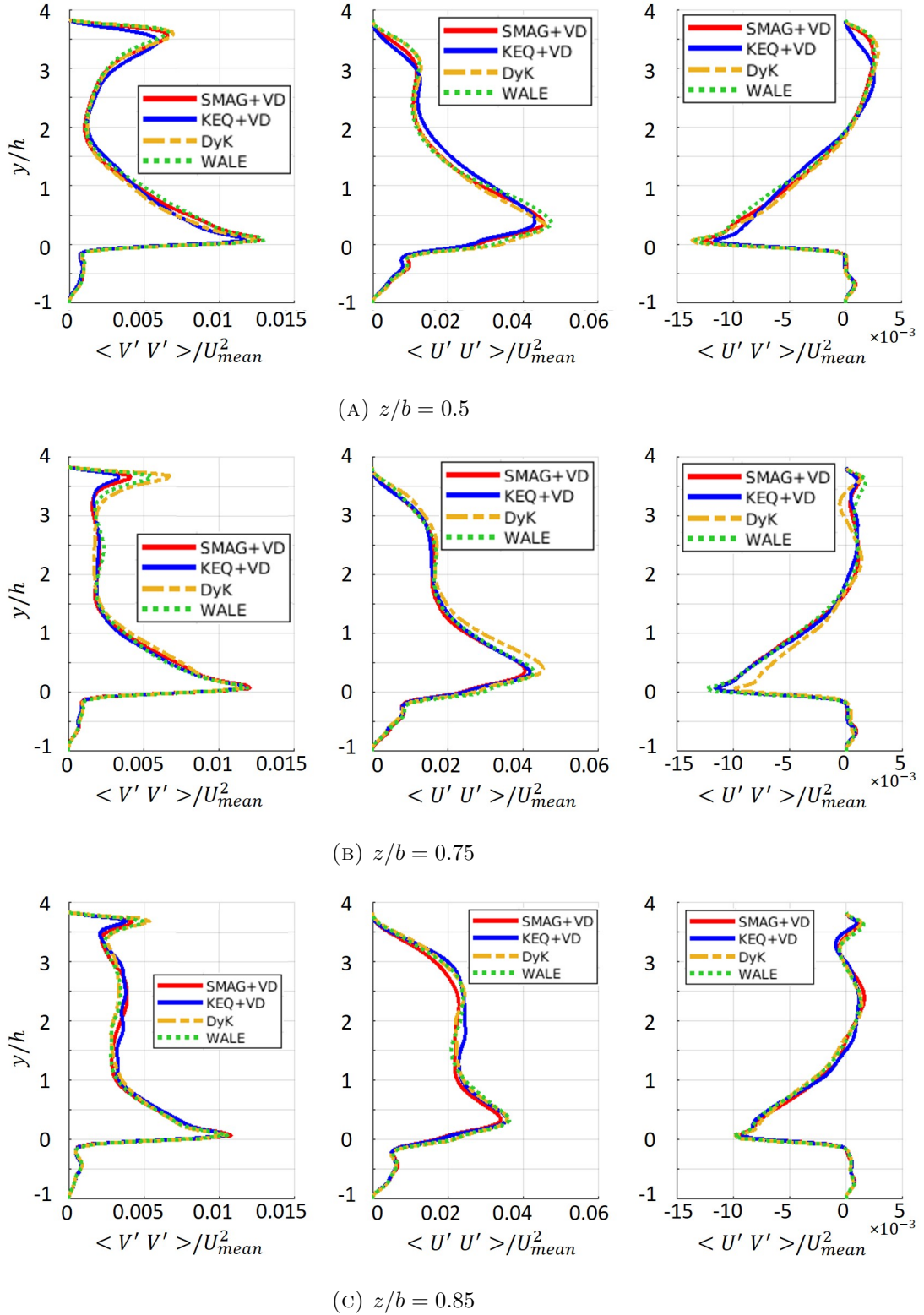


FIGURE 6.27. Comparison of $\langle u'u' \rangle$, $\langle v'v' \rangle$ and $\langle u'v' \rangle$ at different locations along z direction predicted by different SGS models.

The similarity between the results of different models is attributed to highly resolved

turbulent kinetic energy⁹ (Fig. 6.28a) and low effect of SGS viscosity (Fig. 6.28b).

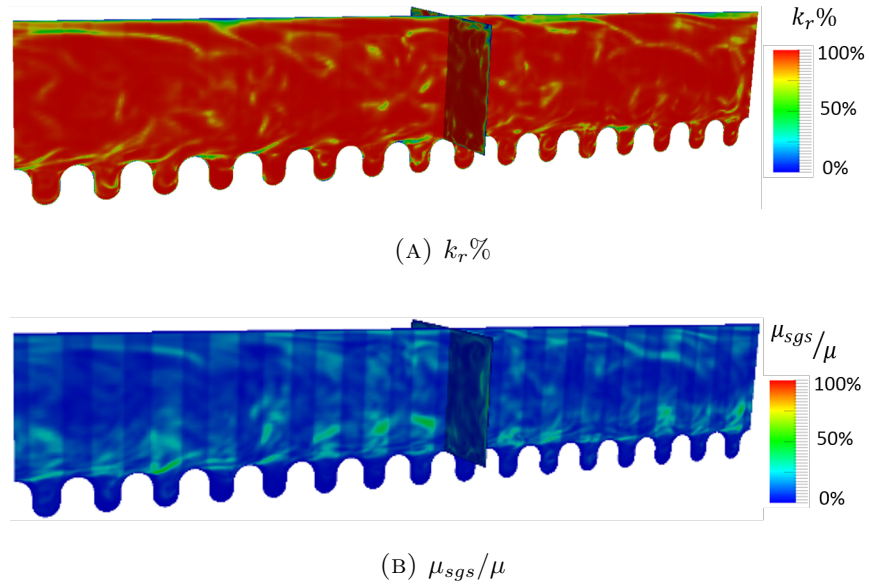


FIGURE 6.28. The contour of $k_r\%$ and μ_{sgs}/μ on mid-plane and y - z plane of $x/\lambda = 0$ predicted by SMAG+VD on 16 corrugation with periodic BC.

As stated in the section of Fundamentals of Turbulence in Chapter 2, the energy spectrum plot is able to show how the turbulent kinetic energy changes with respect to the length scale of the flow structures. It is also the key method to determine whether the LES is well resolved. Therefore, energy spectrums are calculated at $y/h = 0.265$, 0.578 and 0.819 , covering the regions which are strongly influenced by the flow ejection from the corrugations. The energy spectrum plot for these three locations are similar, thus only the energy spectrum at $y/h = 0.819$ is shown in Fig. 6.29.

⁹ $k_r\% = k_r/(k_r + k_{sgs})$

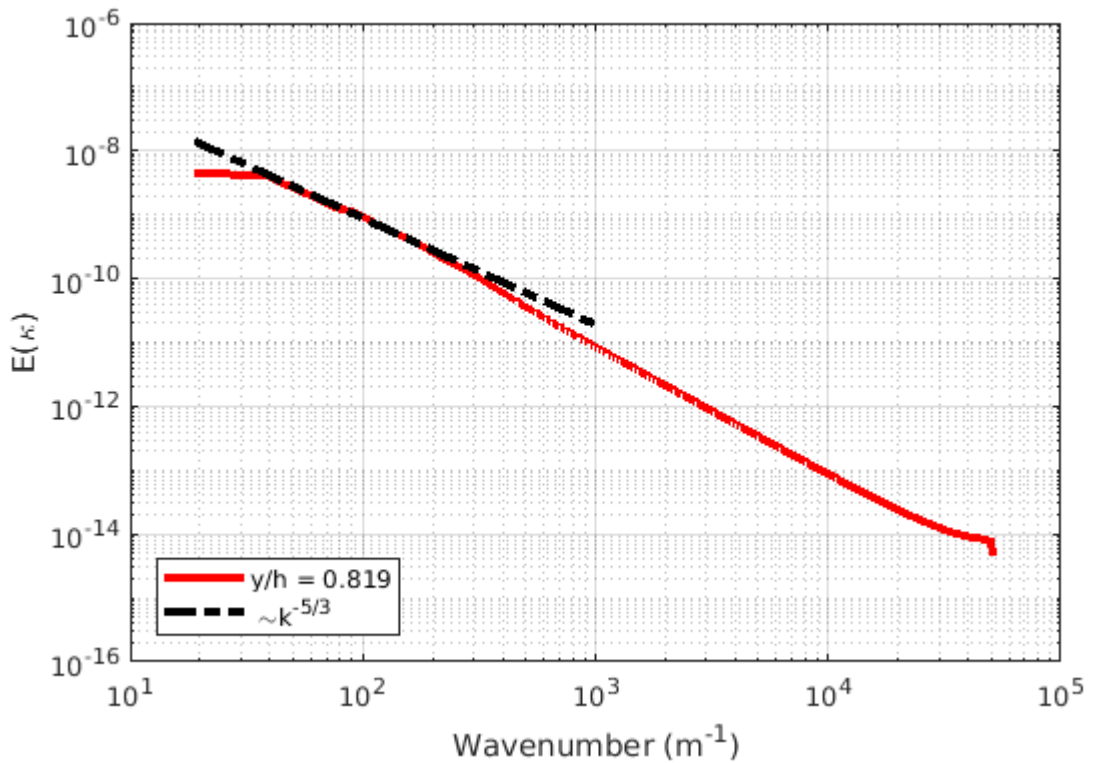


FIGURE 6.29. The energy spectrum for $y/h = 0.819$ predicted by SMAG+VD on 16 corrugations with periodic BC.

It is shown that the calculated energy spectrum matches well with the slope of $-5/3$ as presented in Eq. 2.5. This confirms that the sizes of the cut-off length in current LES locates within the range of inertial subrange, indicating all the energy containing large structures are effectively resolved. Therefore, all aforementioned findings suggest that current LES is well resolved.

Nevertheless, it should be acknowledged that the uncertainty for the LES prediction remains, as the similar results obtained across different SGS models may also be due to overly large numerical errors caused by the chosen mesh density and numerical schemes. However, the mesh quality have been verified by both icem-CFD and OpenFOAM's mesh checking tools, and the Grid 1 is shown in Section 6.3 to be able to offer a good balance between computing resource and the accuracy of the prediction. In addition, the numerical schemes are selected from the available options in OpenFOAM and by following the good practice as shown in Section 4.3. Although the higher order schemes are desirable, the current second order accuracy schemes are the best options available in the software. Therefore, at the moment, the accuracy gain by applying a higher order accuracy numerical scheme is not quantifiable.

Issues In The Experiment

The validation of current LES suggests a high confidence level on the predicted results. It is therefore likely that the issues and uncertainties in the experiment are the dominant contribution to the difference between LES predictions and PIV measurements. After a comprehensive review of experimental results and setups, a number of serious problems and open questions are highlighted in this section.

One suspicious feature of the PIV profile (Table. 6.5) is its high shape factor value at the corrugated wall ($H = 1.948$). This value suggests that the BL at the corrugated wall may be transitional, while the BL at the top wall is turbulent ($H = 1.66$). It seems to be unreasonable, as the experimental data [8] depicted strong momentum interactions between the corrugations and the bulk flow, so that the BL at the corrugated wall should become turbulent earlier or at least no later than the BL at the top wall. This issue may be caused by the inadequacy of data sampling frequency used in the PIV measurement. So, the effects of different sampling frequencies on the LES predictions is studied.

It is noted that the PIV measurement has a data sampling frequency of $8Hz$, and takes 388 data points for a total period of $48.5s$. It is unpractical to run the simulation for the same period, so $8s$ of time history data are used and expanded to $48.5s$. 12 locations on the vertical line of $x/\lambda = 0$ and mid-plane are selected for the data recording. These raw data are in a frequency of $10kHz$, as $dt = 1 \times 10^{-4}s$ in current simulation. They are then sampled at a frequency of $8Hz$. The original time history data and the sampled data are compared in Fig. 6.30 for $y/h = 1.446$.

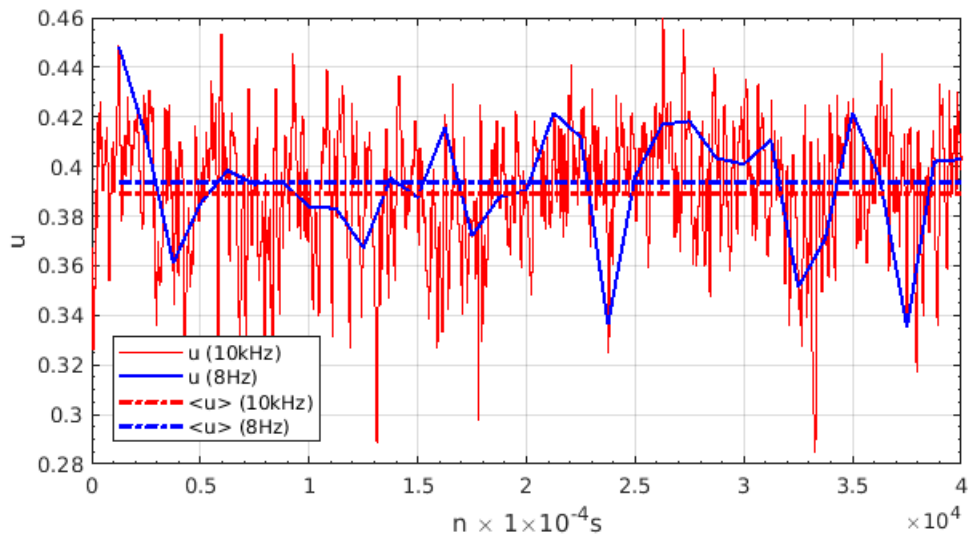


FIGURE 6.30. Comparison of different sampling frequencies on u data obtained by SMAG+VD at $y/h = 1.4458$ on $z/b = 0.5$ and $x/\lambda = 0$.

The differences between the data of the two sampling frequencies are not large. The largest discrepancy is around 4.5% at the corrugated wall region. The differences for the remaining locations are around 2%. The value of normalised $\langle u \rangle$ at the sampled locations obtained by both sampling frequencies are compared in Fig 6.31.

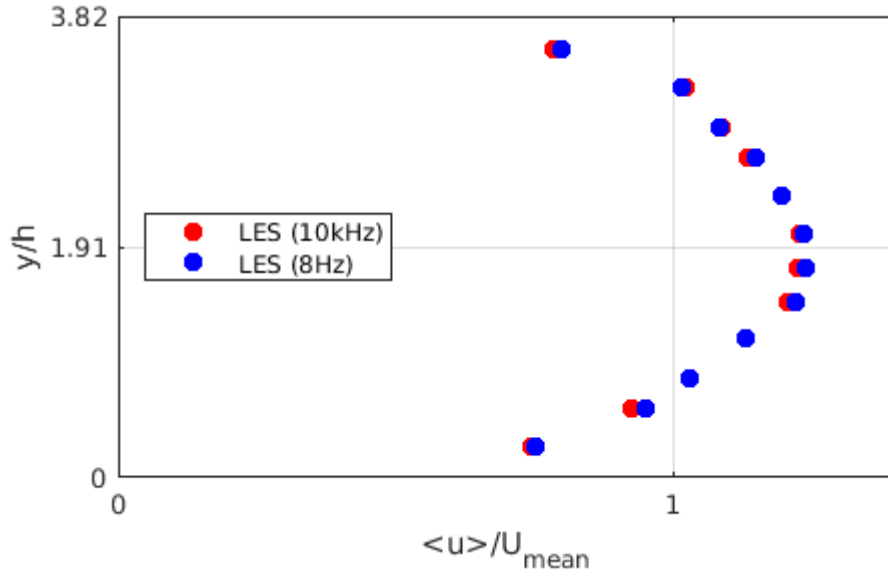


FIGURE 6.31. Comparison between $\langle u \rangle$ obtained by different sampling frequencies on $x/\lambda = 0$ at mid-plane.

The results show that the profile obtained by the $8Hz$ sampling frequency is very similar to the one produced by the $10kHz$. By repeating the same procedures, the Reynolds stresses along the line of $x/\lambda = 0.5$ at different locations along z -axis can also be calculated for both sampling frequencies. Their results are compared in Fig. 6.32.

It is found that the results from the $8Hz$ sampling frequency only match the trend of LES data close to the top wall. Large discrepancies are found at the lower half of the channel. Also, the data with $8Hz$ sampling frequency have larger differences with the PIV profile than the original data. It indicates the sampling frequency of $8Hz$ may not be able to capture the correct features of Reynolds stresses in the lower half of the channel, even though it seems to reproduce the $\langle u \rangle$ profile at a high accuracy.

However, this may raise a question that if a larger sampling frequency (smaller time step size) can result in a prediction closer to the experimental data, as Fig. 6.32 indeed shows that results for $10kHz$ are closer to the ones obtained by $8Hz$. This uncertainty caused by different time step size is partially mitigated by the study in Section 6.3.1, as the result obtained by Grid 2 are based on a time step size of $20kHz$ and its results at region close to the corrugation are very similar to the ones predicted by Grid 1 at $10kHz$ (shown

in Fig. 6.10). However, due to the limit of computing resources, the gain of accuracy from further decreasing the simulation time step size is currently not quantifiable.

Apart from the tendency of underestimation of the Reynolds stresses at the near wall region by PIV method (mentioned in Section 2.2.2), another uncertainty which should not be ignored is the spatial-averaging process during PIV data acquisition. It is understood that this spatial-averaging area is much larger than the cell used in LES. Therefore, if the method used in the PIV techniques is fully implemented on current LES data, the data at the recording points will be strongly influenced by the cells which are a certain distance away from it. This may result in larger discrepancies between the flow field and the data recorded by PIV, even for $\langle u \rangle$.

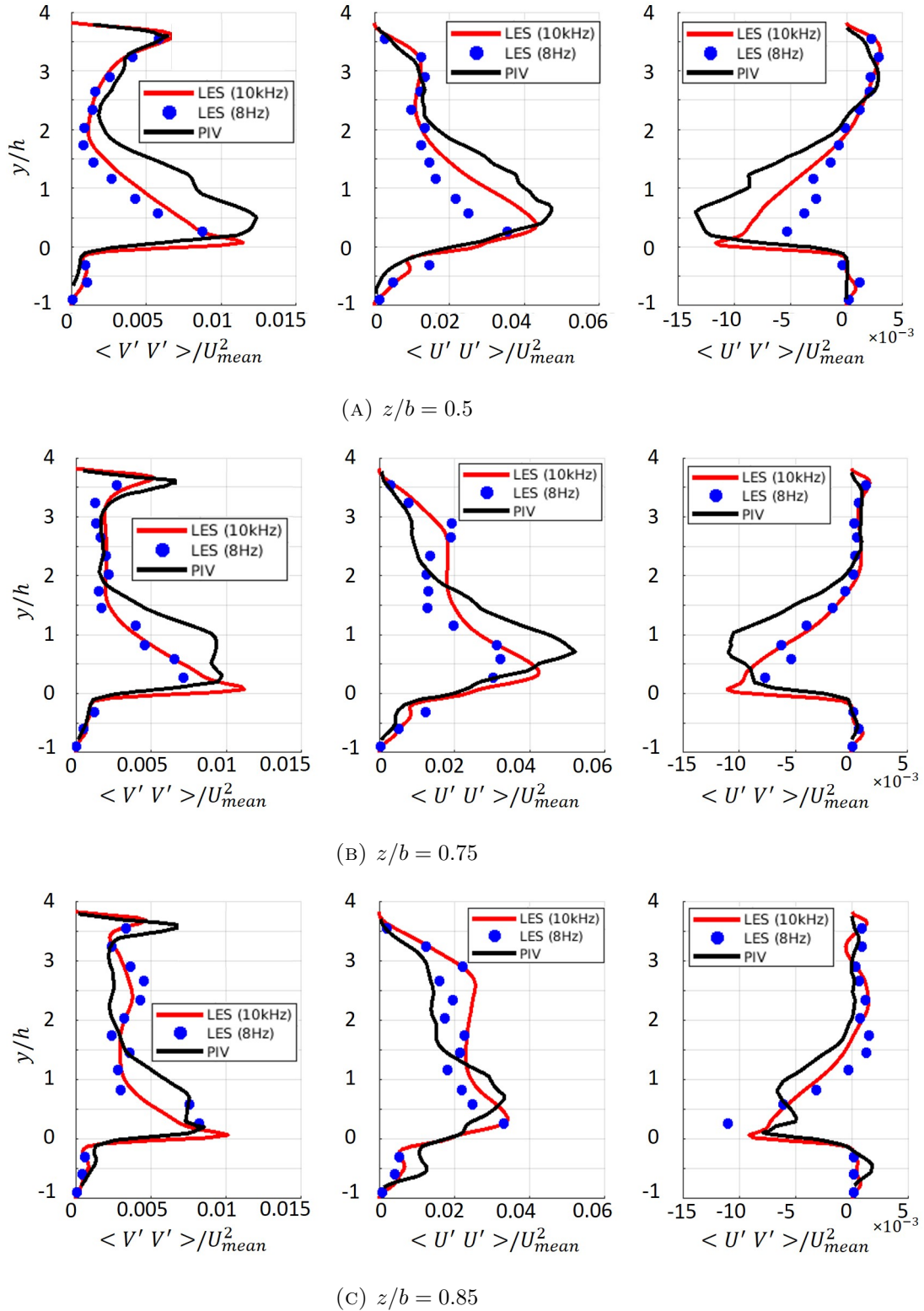


FIGURE 6.32. Comparison of various Reynolds stresses on $x/\lambda = 0.5$ at different locations along z direction calculated by different sampling frequencies.

Furthermore, apart from the errors in the PIV system (2%) and flow rate measurement (2%) of the experiment [3], some other issues may also contribute to the discrepancies

between the LES predictions and PIV data. Firstly, due to the water level changes in the reservoir, the flow rate changes 3 – 4% during a typical test. The duration of a typical test is unclear, if it is for one data set, i.e. 48.5s, this flow rate reduction will be significant, and the flow in the corrugated channel during the experiment is transient, which is not the condition simulated in current case. Secondly, due to the limitation of pressure head, experiments with $Re > 6000$ are performed by another system with a pump which can maintain the flow rate. However, the video for the case of $Re = 670$ with the pump system clearly shows a pulsation in the flow, which is also different from BCs of the current simulation. Thirdly, the temperature seems not to be monitored and controlled during the experiment. As water viscosity changes with temperature, the Re may change largely during the run. Finally, it is not clear if the flow in the channel reaches fully turbulent status when the measurements are taken. A comparison between the PIV data and LES predictions across the channel reveals that the $\langle u \rangle$ predicted by LES at C57 ($\langle u \rangle_{max} = 2.2$, only 1.7% below PIV data) has a better agreement with PIV data than at the fully turbulent region (Fig. 6.33). It may suggest that the flow is still transitional when the PIV takes the measurements. It worth mentioning that the experimental data does not contain the data for transition. However, as pointed out in 6.4.5, current mesh density should be adequate for predicting the transition satisfactorily.

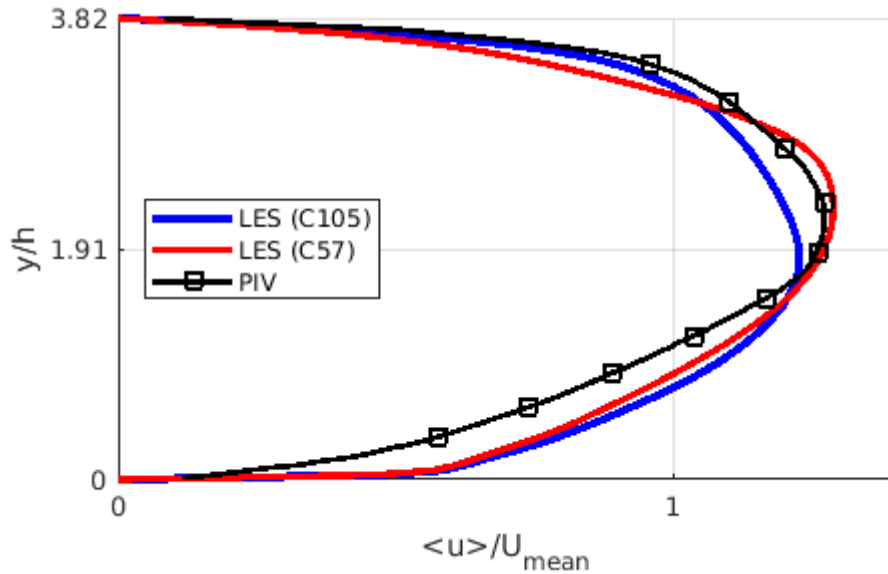


FIGURE 6.33. Comparison between $\langle u \rangle$ obtained by LES at C57 on $x/\lambda = 0$ at mid-plane and PIV data.

The various issues and open questions highlighted in the current subsection raise doubts concerning the validity of the PIV data being the benchmark for the LES predictions. In

addition, the validation of the LES results from various aspects suggest that the flow field in the corrugated channel are well resolved with a relatively high confidence level. Despite that some uncertainties remains for current numerical prediction, the discrepancies between the LES prediction and PIV data is more likely to be caused by the uncertainties in the measurements and experiment conditions. Therefore, the study of the flow field inside this corrugated channel will be based on the current LES predictions.

6.4.5 Details of Flow Development

Most of the numerical studies on corrugated channels listed in the literature review only focus on the flow field in the fully turbulent region. However, as highlighted in Section 6.4.2, the overview of the flow development in the corrugated channel suggests that the BL transition at the top wall has a profound influence on the flow characteristics in the channel, which are reflected on the changes of various BL thicknesses and $\langle u \rangle$ profile across different Zones (see Table 6.4). Therefore, the detailed flow developments across Zone 1 to 4 are discussed in this section, with focuses on turbulent structures visualisation, the mechanisms of the BL transition, and time-averaged flow field for the fully turbulent region.

Zone 1 is studied first. Fig. 6.34 shows the turbulent structures visualised by Q-criterion for the flow region between C1 and C9. Fig. 6.34a is the overview of the flow structures ($Q = 3000$) between C1 and C9 coloured by u . It was found that despite not showing here, the synthetic turbulence at the inlet decays rapidly, and its resulting large structures are not visible after the first half corrugation. However, the synthetic turbulence triggers the flow exchange between the bulk flow and the corrugation close to the exit of C1. This exchange can be seen by the structure tagged as Initial Interaction in Fig. 6.34a. The structure is rooted inside the corrugation ($y/h \sim -0.5$) and is more irregular than the two-dimensional rollers at the same places for C2 and C3.

The flow interactions between bulk flow and corrugations are stronger for the downstream. Thus the two-dimensional rollers are pushed by the flow from the corrugation to higher locations, and stretched by the bulk flow, forming the Λ -shape structures on top of the separation bubbles (C5 \sim C6). The localised view of the Λ -shape structures (coloured by v) is provided in Fig. 6.34b. The momentum interactions continue building up until the flow in the corrugation has adequate momentum to burst out. Then the Λ -shape structures are distorted and replaced by the flow ejections from the corrugation. As shown in Fig. 6.34c, no Λ -shape structures can be observed at C8 and C9, and the ejecting structures have higher u and v than structures at C5 and C6, indicating the flow ejections are penetrating the bulk flow. Fig. 6.34d also shows the flow structures at C8 and C9, but coloured by $\langle v'v' \rangle$. It shows that at C9 the flow from the corrugation is able to be ejected up to $y/h = 0.72$, but most of the ejections can only affect the flow at around $y/h = 0.36$.

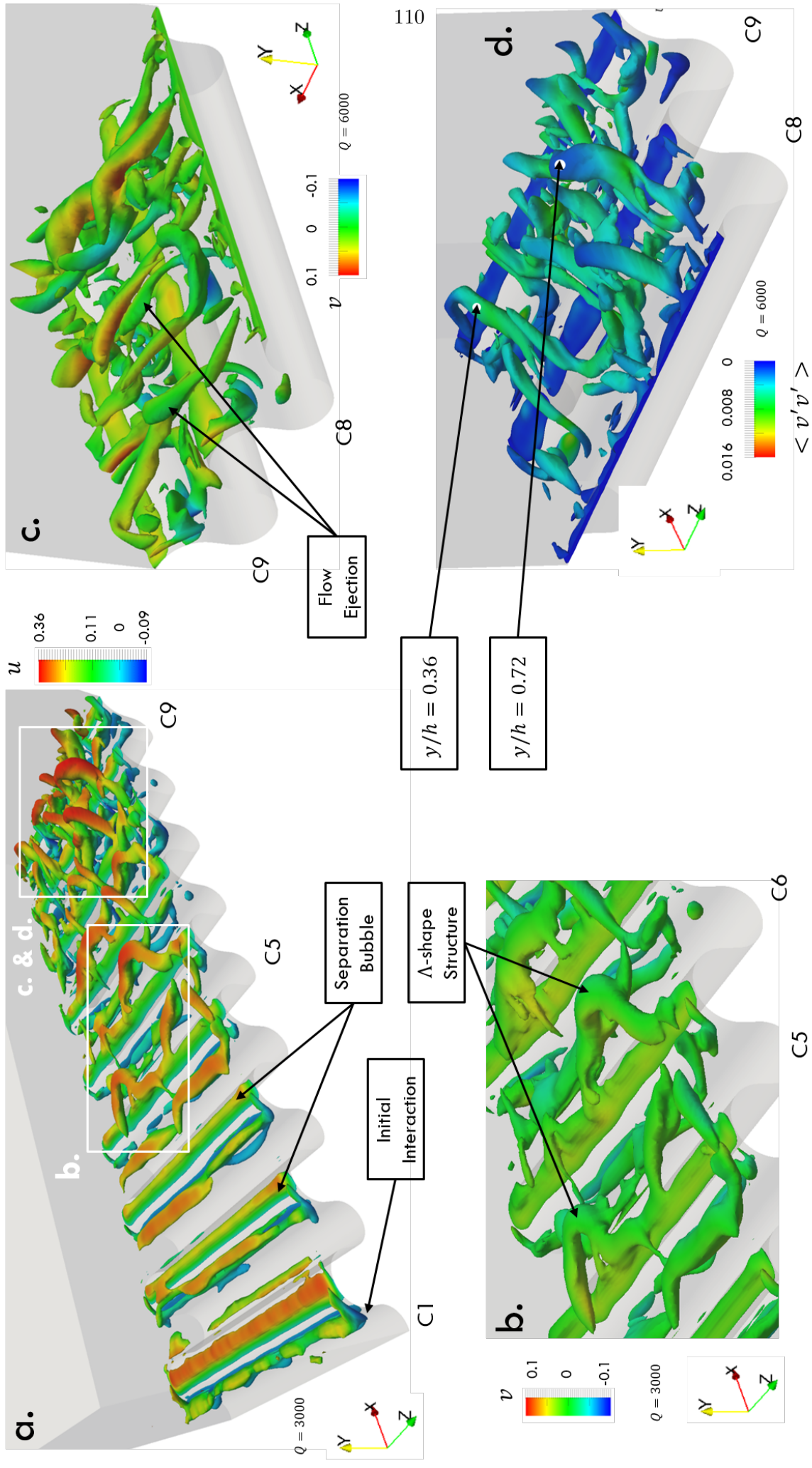


FIGURE 6.34. The iso-surface plots of Q-criterion for the flow region between C1 and C9.

The flow field between C32 and C38 in Zone 2 is also visualised by Q-criterion in Fig. 6.35. The plot indicates an increasing number of small detached structures that have an upward trend toward the top wall.

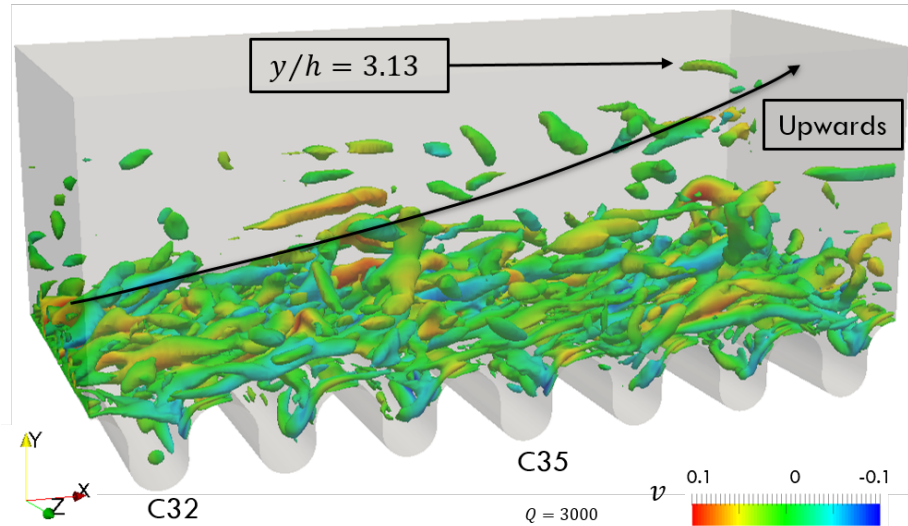


FIGURE 6.35. The iso-surface plot of Q-criterion coloured by v between C32 and C38.

Interestingly, as shown in Fig. 6.36a, these small structures are very close to the side walls. The plot (Fig. 6.36b) which combines Q-criterion plot ($Q = 350$) and the v contour on x - z plane at $y/h = 2.53$ suggests that these detached structures originate from the side walls rather than the flow ejections from the corrugations.

It is found at C38 that the highest structure reaches up to $y/h = 3.13$ at $z/b = 0.435$, which is very close to the top wall. The influence of this structure on the flow field is shown in Fig. 6.36c and Fig. 6.36d. Undulations, which are caused by this structure, are seen at the U_{mag} contours for both horizontal and vertical planes. These undulations are very similar to the one found at around C45 on the U_{mag} plot at the mid-plane (Fig. 6.15), but they are at C38 and closer to the side wall. This suggests that the instabilities and subsequent transition of the BL at the top wall are initialised by the structures originated from the side walls.

Fig. 6.37 provides the flow details of the transitional process, in which Fig. 6.37a gives the snapshot of U_{mag} at $z/b = 0.5$, Fig. 6.37b is the iso-surface plot of Q-criterion of 3000 coloured by v between C39 and C77 and Fig. 6.37c is its localised view between C54 and C73, Fig. 6.37d is the v contour on x - z plane at $y/h = 3.37$, and Fig. 6.37e same contour plot at the middle of the channel ($y/h = 1.91$).

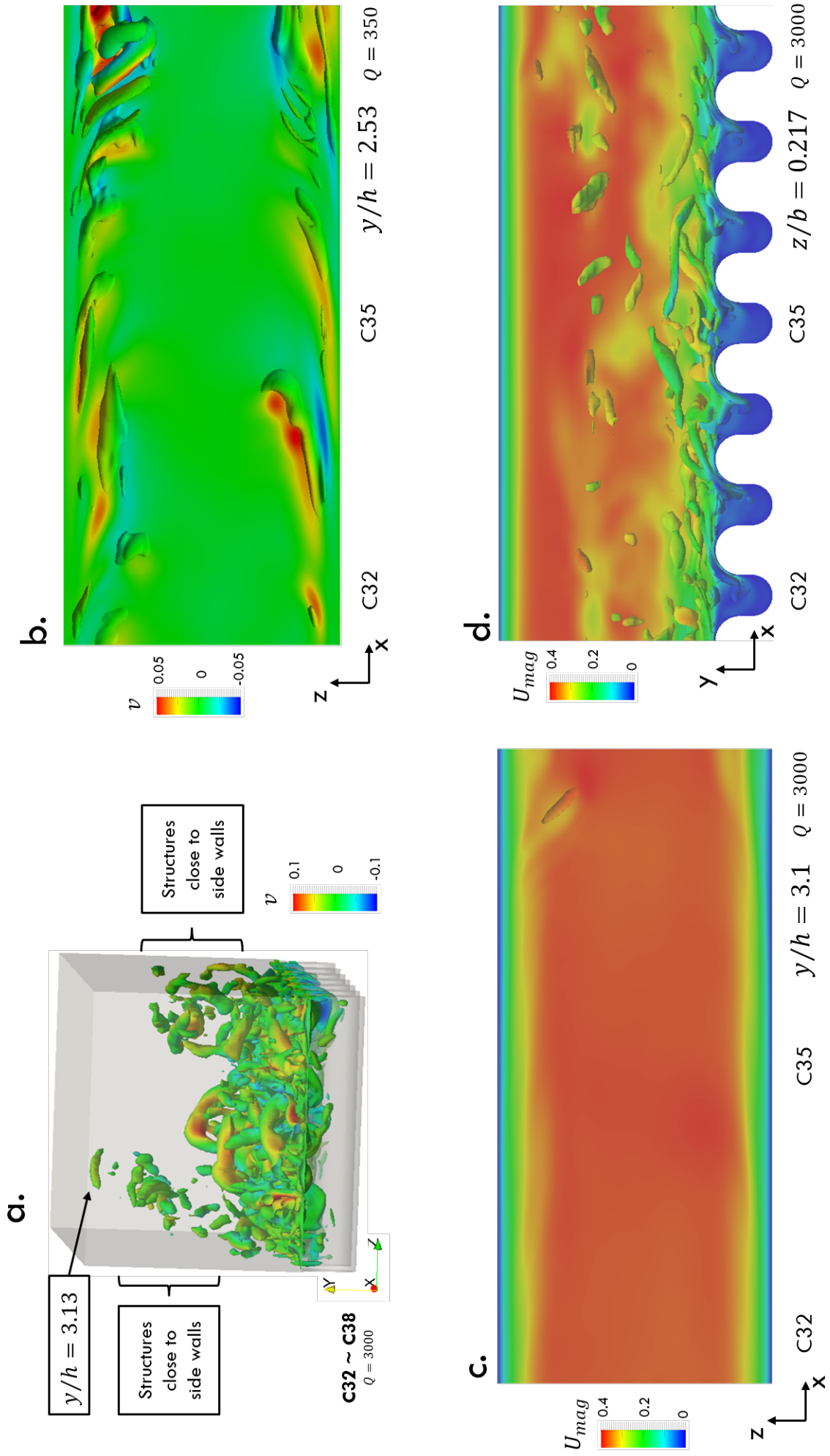


FIGURE 6.36. The iso-surface plots of Q-criterion for the flow region between C32 and C38.

It is found that the flow goes through a dramatic change during the transition. At the early stage of transition, the flow velocity within the bulk flow region is still largely uniform. Some structures are found reaching the BL of the top wall between C45 and C50 in Fig. 6.37b. These structures can also be seen as the high v spots originated from the side walls in Fig. 6.37d. It is known from Fig. 6.36 that these structures cause instabilities at the BL of the top wall. But at this time the undulations are not very apparent at the U_{mag} contour at the mid-plane. Similarly, at the middle of the channel (Fig. 6.37e), the regions close to the mid-plane have some upward-pointing high v spots, but generally have no net wall normal velocity.

Further downstream, the undulations at the top wall are more apparent from around C57 (Fig. 6.37a). It appears to be caused by the increasing number of structures hitting the BL at the top wall (Fig. 6.37b). It is found in Fig. 6.37c that between C54 and C60, most of the structures are traveling upwards towards the top wall. When reaching C60, the upwards-travelling structures becomes less, but some structures which depart from the top wall and travel down to the bulk flow start appearing. These downwards-travelling structures become dominant at around C65, which generally have a large length, with the longest one being seen across three corrugations just before C70. These downwards-traveling structures can also be seen as the negative v spots around the mid-plane region in Fig. 6.37d. Their effect on the flow field is also visible at the middle of the channel, as more and more negative v spots can also be found from C55 in Fig. 6.37e.

These downwards-travelling structures cause distortion of the BL at the top wall until around C70 (Fig. 6.37a). After C70, the BL is broken up, and the upward-travelling structures are rarely found at the region close to the top wall (Fig. 6.37c). An increasing number of negative v spots are found in the contours of x - z planes for both y/h locations, and the regions close to the mid-plane generally have negative wall normal velocity. This suggests that the BL transition at the top wall suppresses the flow development at the corrugated wall, which leads to a shifting down of $\langle u \rangle_{max}$ location and results in a more symmetric $\langle u \rangle$ profile after the transition, as seen in Fig. 6.16.

During transition process, the unstable Tollmien-Schlichting waves and hairpin vortices are not seen. Therefore, the current transition is a bypass transition. It is worth mentioning that the mesh density for the top wall is $(\Delta x^+, \Delta y^+, \Delta z^+) = ([1.6, 3.5], 0.12, 1.2)$ which is much finer than the mesh density adequate for predicting a natural transition, $(\Delta x^+, \Delta y^+, \Delta z^+) = (38.7, 0.91, 11.44)$ [149]. Further, Yang and Voke [150] found that correctly predicting the position and speed of bypass transition only needs a coarser mesh

than the one for the natural transition, as the detailed computation of the form of the instabilities is not crucial. Therefore, despite that the experimental data does not report the transition, the prediction of transition process and associated parameters should have a high confidence level.

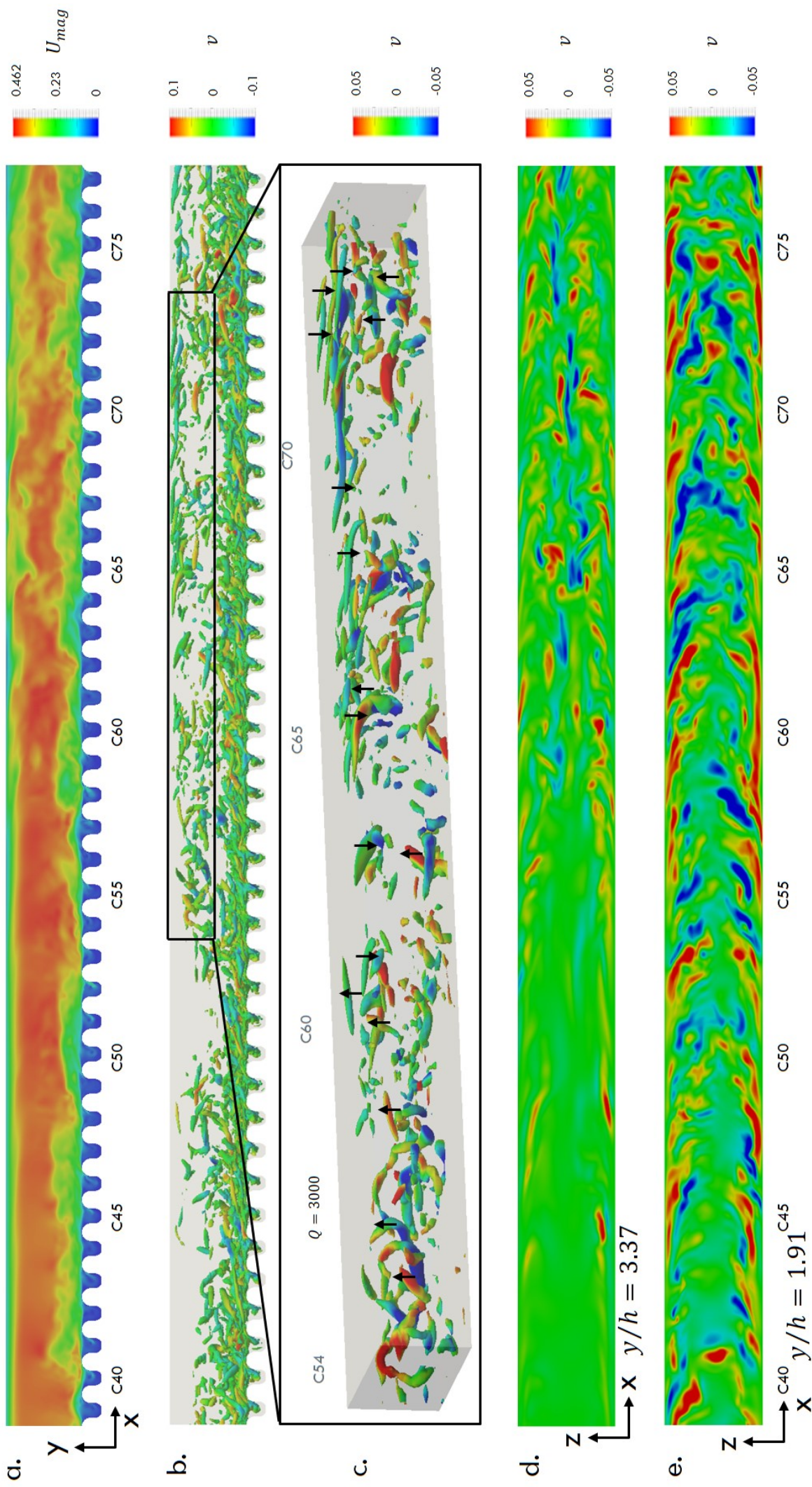


FIGURE 6.37. The localised details of the stage of Transition, at $z/b = 0.5$ predicted by SMAG+VD on 128 corrugation case.

The vector plot on x/λ for x - z plane of C101 (within fully turbulent region) coloured by the magnitude of $\langle v \rangle$ and $\langle w \rangle$ is shown in Fig. 6.38. Mean secondary flows are found at few locations, such as the upper corners, the middle of the channel, and the exit of and within the corrugation. Fig. 6.38 confirms the findings shown in Fig. 6.37d and e, i.e. the mean flows travel upwards along the side walls, create the secondary flow at the upper corners and meet at around $z/b = 0.5$ at the top wall, then travel down towards the corrugation and form another secondary flow at around $y/h = 2$.

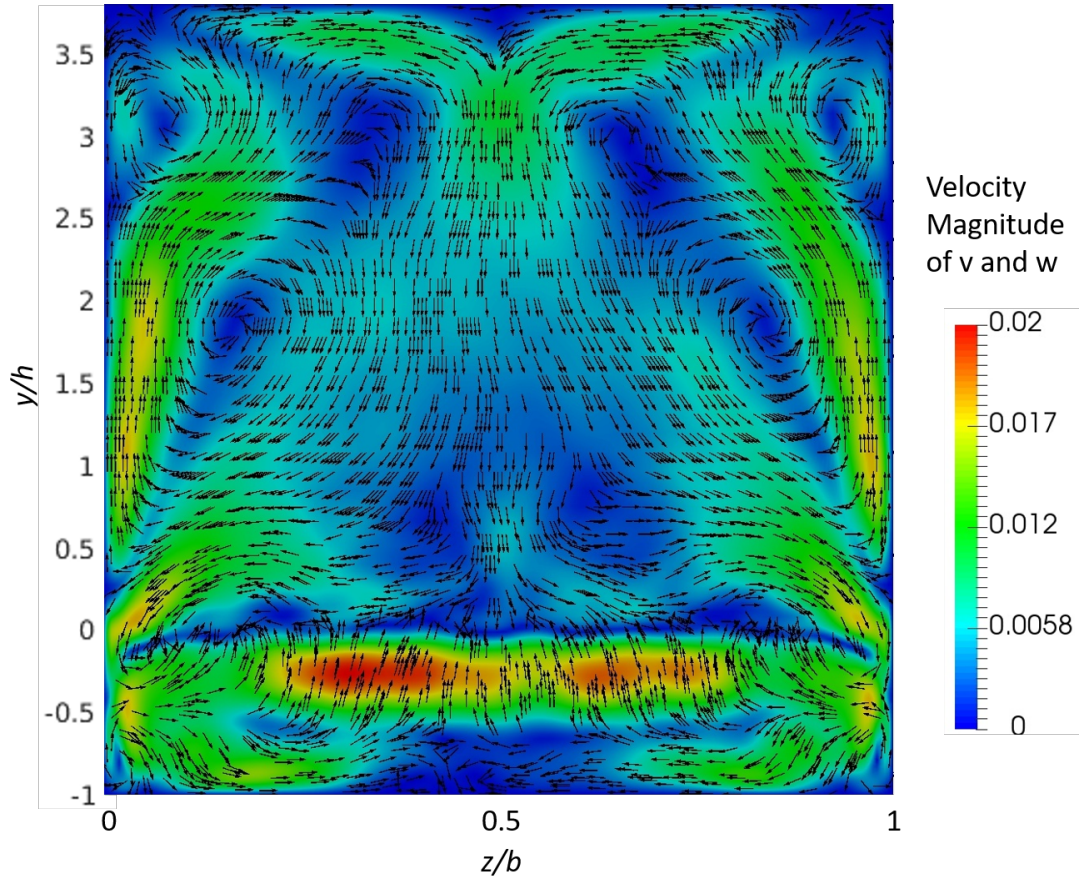


FIGURE 6.38. The vector plot on x/λ for y - z plane of C101 coloured by the magnitude of $\langle v \rangle$ and $\langle w \rangle$

The time-averaged streamlines coloured by v at C101 are shown at Fig. 6.39. Together with Fig. 6.38, they suggest that part of the mean flow which travels down from the top wall travel towards the side wall, causing net flow goes into the corrugation at the regions close to the side walls. The flow then moves transversely across the corrugation, forming a large vortex, and finally flows out of the corrugation at the middle region between $z/b = 0.2$ and 0.8 . Another part for the mean flow which travels down from the top wall does not get in to the corrugation, rather it joins the flow out of the corrugation and travel

towards mean flow direction.

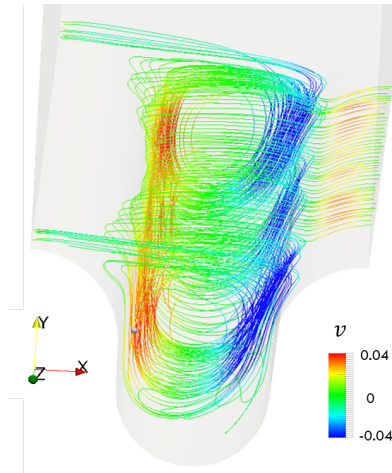


FIGURE 6.39. The time-averaged streamlines coloured by v at C101.

Contour and vector plots of $\langle U_{mag} \rangle$ at C112 and C113 (fully turbulent region) for $z/b = 0.5$ are shown in Fig. 6.40. It is found that the $\langle U_{mag} \rangle$ contours (Fig. 6.40.a) between C101 and C102 are identical. The time-averaged vector plots of $\langle U_{mag} \rangle$ (Fig. 6.40.b) and their localised views for C101 and C102 indicate that two vortices coexist in the corrugation, one of which is large and almost fills whole corrugation. This dominating vortex is centred at around $x/\lambda = 0.53$ and $y/h = -0.36$ for all corrugations. Another one is small and is flattened at the bottom of the corrugation and their locations vary slightly for different corrugations.

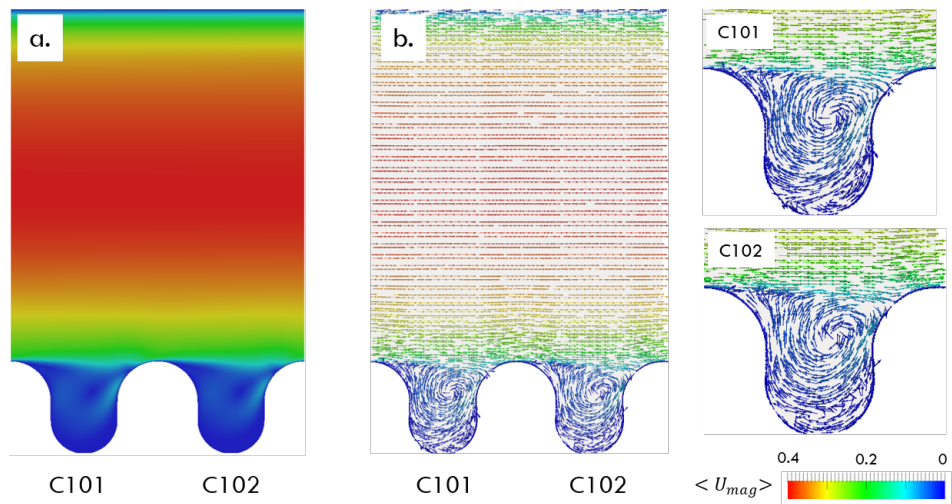


FIGURE 6.40. The snapshot of U_{mag} contour and vector at $z/b = 0.5$ for C101 and C102.

6.4.6 Hydrodynamic Interaction in Fully Turbulent Region

Hydrodynamic interactions and vortex evolution in the corrugations play a significant role in the corrugated channel flow as they are the primary mechanism under which the corrugations affect the bulk flow.

The unsteady flow patterns inside the corrugations are visualised in the work of Unal et al. [3, 12] who observed that a vortex first appears at the upstream upper corner of the corrugation, then becomes larger while travelling toward the downstream wall of the corrugation. When the vortex hits the downstream wall, part of its circulatory motions are transported over the crest and starts a new vortex in the next corrugation. The vortex weakens after hitting the wall and ejects from the corrugation into the bulk flow after the ejections at the previous corrugation. The existing flow visualisations provide valuable insights into the vortex evolution in this corrugated channel flow, but the findings are mainly descriptive, and the detailed vortex dynamics and the mechanisms of the vortex evolution are still to be understood. Therefore, this section is dedicated to study these two aspects.

Fig. 6.41 depicts the mid-plane snapshot of each stage of vortex evolution predicted by SMAG+VD on the 16 corrugations case with periodic BC. The plots in Fig. 6.41 are for the same set of cavities at different time instants from $T = 28.06s$ to $28.19s$. The time step of these plots is $0.01s$, i.e. the flow travels less than a half corrugation for each time instant. The three cavities are referred to as upstream, centre, and downstream corrugations.

A vortex evolution, similar to the one previously recorded by Unal et al [3], is clearly visible at the centre corrugation, including formation, travelling and enlargement, weakening, and ejection. At $T = 28.06s$, i.e. the first time instant, the flow is bursting from the corrugation into the bulk flow. Soon after it (at $T = 28.07s$), a small vortex/perturbation appears at the upstream upper corner of the centre corrugation due to flow separation at the top of the corrugation. At this moment the bursting of flow is still on-going. It then becomes larger and travels towards the downstream wall of the centre corrugation as seen at $T = 28.08s$. It hits the downstream upper corner of the centre corrugation $0.01s$ later, rather than reattaching at the bottom of the corrugation. The travelling of the vortex generates a local high pressure region at the downstream upper corner of the centre corrugation ($T = 28.08s$ in Fig. 6.42), and the pressure difference between this high value region and surrounding areas increases when the vortex hits that corner ($T = 28.09s$ in Fig. 6.42).

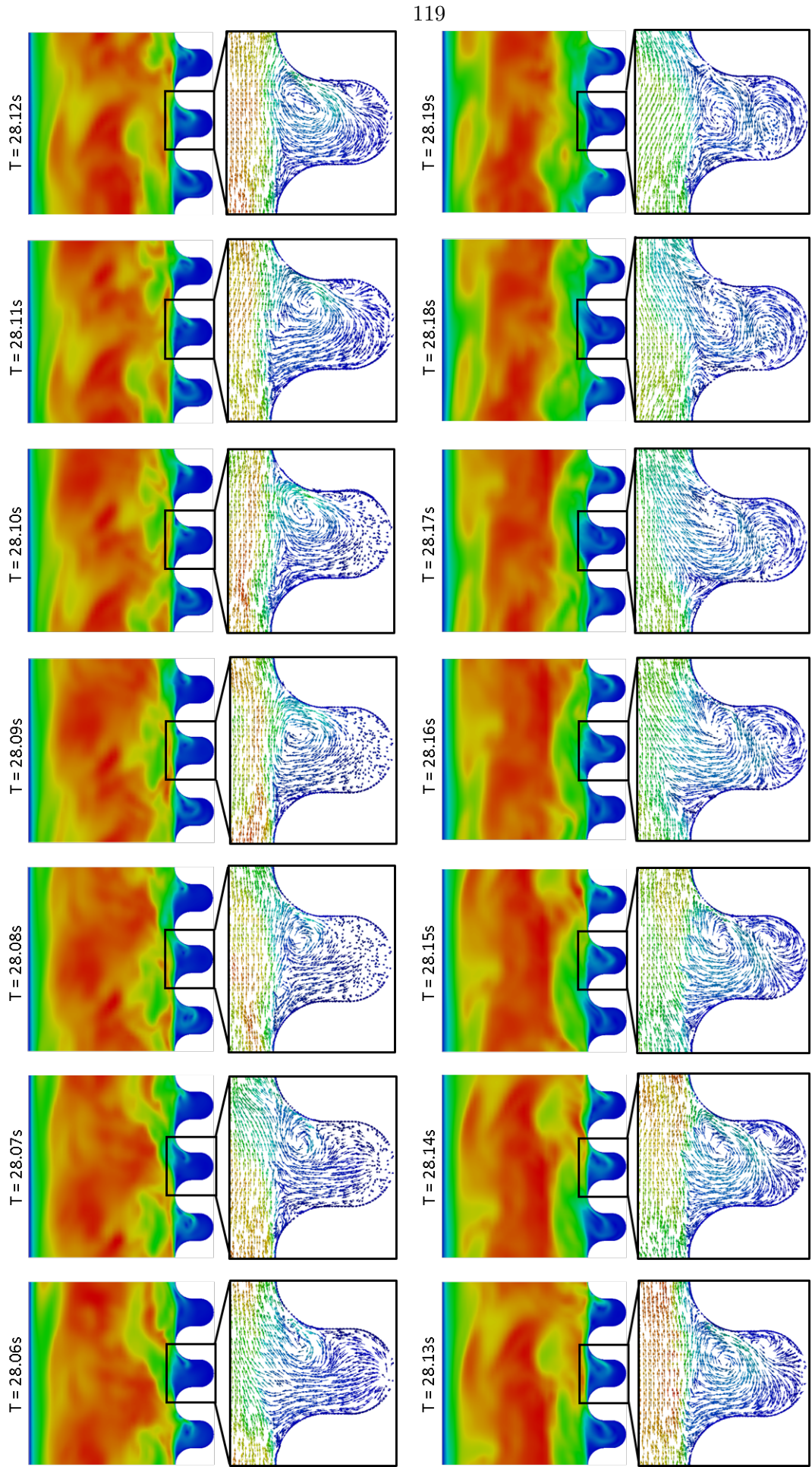


FIGURE 6.41. Plot of the vortex evolution at $z/b = 0.5$ predicted by SMAG+VD on 16 corrugations.

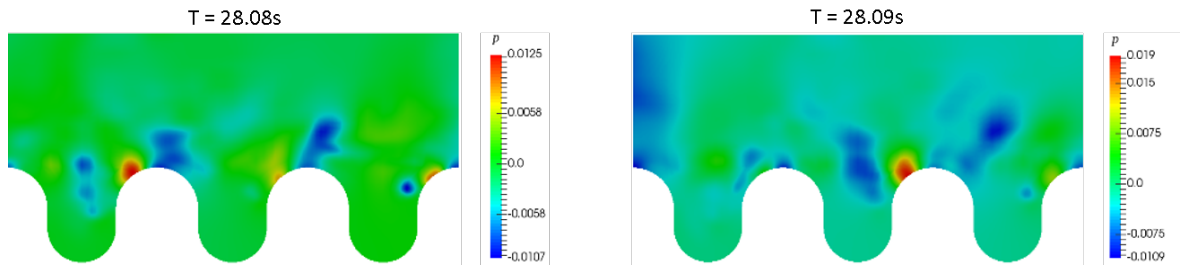


FIGURE 6.42. The pressure distribution at $z/b = 0$ of the corrugation set at $T = 28.08s$ and $28.09s$ predicted by SMAG+VD for the 16 corrugations case.

The higher pressure region will accelerate the flow in two directions. One stream will have more momentum to flow deeper into the corrugation and enlarge the vortex in the corrugation. Another stream will accelerate over the top of the corrugation, and experience flow separation at the downstream corrugation, creating a small vortex that triggers the vortex evolution process in the subsequent corrugation. This process is clearly shown in the vector plot in Fig. 6.43.

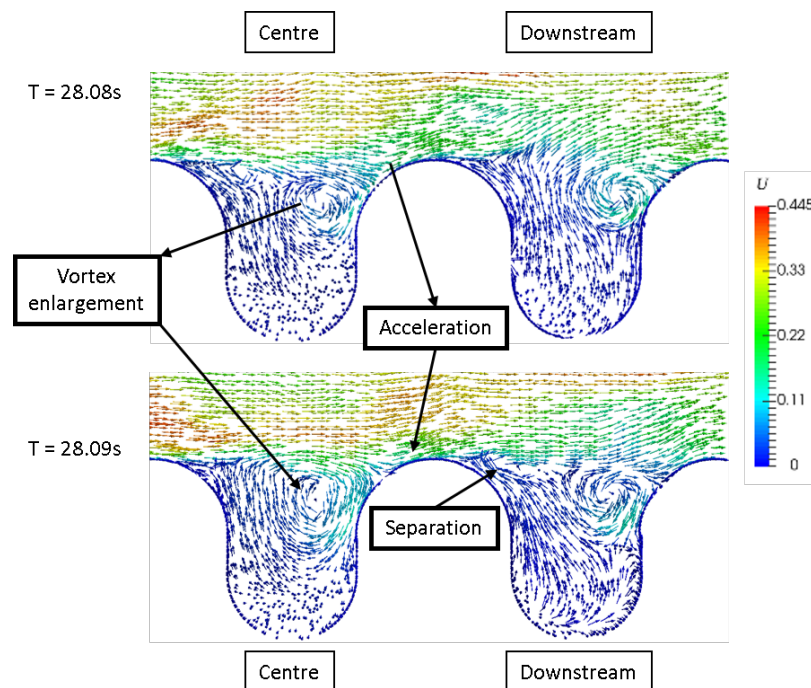


FIGURE 6.43. The velocity vector plot at $z/b = 0$ of the corrugations set at $T = 28.08s$ and $28.09s$ predicted by SMAG+VD for the 16 corrugations case.

The enlarged vortex starts becoming unstable from $T = 28.10s$, and some weak ejections are observed between $T = 28.11s$ and $T = 28.15s$. The flow in the centre corrugation starts strong ejection at $T = 28.16s$ and this lasts for $0.02s$. It is interesting to find out that the pressure also plays a vital role in this process. Fig. 6.44 shows the pressure

distribution and velocity vector plot for upstream and centre corrugations at $T = 28.11s$, $28.12s$, $29.14s$ and $28.15s$. It is found that at $T = 28.11s$, a low pressure band appears on top of the upstream corrugation and across the whole channel height. This low pressure band initialises the flow ejection at the upstream corrugation, and the flow is always ejected towards the low pressure region as the band is convected downstream by the bulk flow. When the low pressure band moves to the top of the centre corrugation, it triggers the flow ejection at that corrugation as well. This explains why flow bursts in one corrugation triggers flow ejection in the subsequent one as observed in the experiment [3].

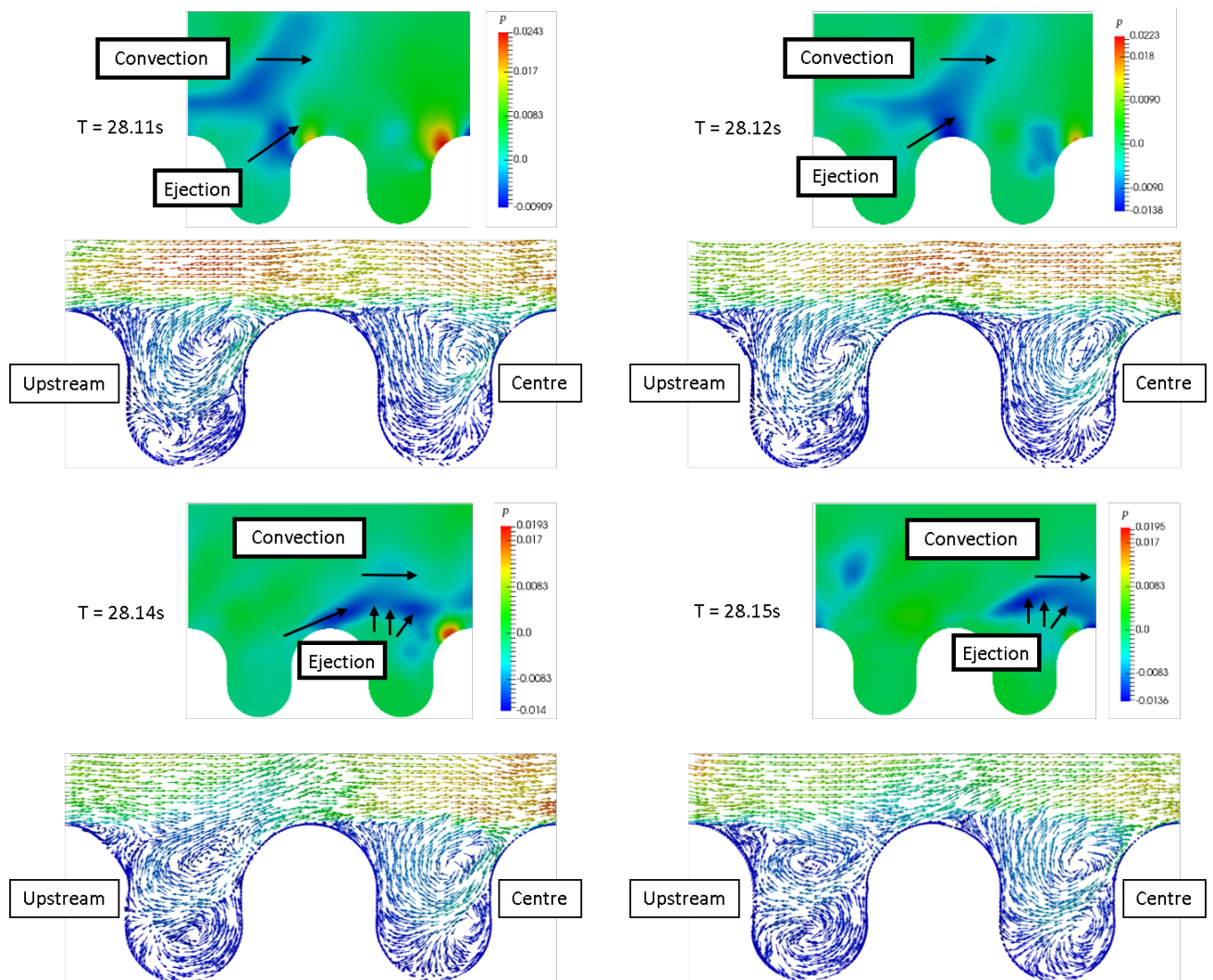


FIGURE 6.44. The pressure distribution and velocity vector plot of the corrugation set at $T = 28.11s$, $28.12s$, $29.14s$ and $28.15s$ predicted by SMAG+VD for the 16 corrugations case.

The flow feature at $T = 28.19s$ is similar to that at $T = 28.08s$, i.e. a small vortex appears at the upstream upper corner of the centre corrugation. Similarly, the enlargement

of this vortex is also observed at both $T = 28.09s$ and $T = 28.20s$, suggesting a new round of vortex evolution starts again. This indicates the total time scale of this single vortex evolution is around $0.11s$, corresponding to a flow distance of $0.033m$ or around five corrugations which matches the result obtained by 2pt-correlations (Fig. E.1). Also, given that the duration of the strong ejection is $0.02s$, the ratio between ejection period and duration is 5.5 which is the same as observed by Djenidi et al [21] on a d -type roughness wall.

In summary, the results show that a strong hydrodynamic interaction, like a chain reaction, is predicted by LES in this corrugated channel. The above findings explain the characteristics of the flow which is observed in the experimental studies with the same [3, 12] and similar shapes [27]. The travelling of the vortex from the upstream upper corner of one corrugation triggers the flow separation and initialise the vortex formation at the subsequent corrugation. In addition, the sequential flow ejection is understood to be caused by the convection of a low pressure band across the channel.

Chapter 7

Conclusions and Suggestions

A detailed numerical analysis of the flow over a corrugated channel is performed by LES. The flow configuration is a two-dimensional representation of a widely used commercial stainless steel flexible pipe. The computational domain has a rectangular cross section. The bottom wall is corrugated with periodic cavities and the top and two side walls are flat plates. Reynolds number based on bulk flow velocity and the hydraulic diameter of the channel is 5300. The main objective of this research is to study the flow characteristics in this corrugated channel, including its BL development, transition mechanisms, mean profiles of flow variables, hydrodynamic interaction and vortex evolution.

Prior to the analysis, the principles of LES are discussed together with the discussion of popular SGS and hybrid models. The widely used EVM SGS models are selected for further validation. The numerical methods are then carefully chosen to maintain a second order accuracy. After that, several EVM SGS models are tested on a plane channel flow test case with different grid densities, including SMAG and KEQ, their variants with the van-Dries damping function, SMAG+VD and KEQ+VD, and their dynamic variant, DyLag and DyK, and WALE. It is found on all mesh densities that the results obtained by SMAG+VD and KEQ+VD are similar, and that from DyLag, DyK and WALE are almost identical as well. SMAG and KEQ, however, fail completely to capture the correct result even on the finest mesh. The results also suggest that the prediction accuracy of all models improve as the mesh is refined. It is also noted that DyLag, DyK and WALE tend to over-predict the mean velocity profile and magnitude of maximum Reynolds stresses when the grid is coarse, whereas SMAG+VD and KEQ+VD tend to mispredict the location of the maximum Reynolds stresses. Finally, SMAG+VD is found to offer a satisfactory prediction at a lower computing cost, and is selected as the SGS model for the numerical analysis of the corrugated channel.

7.1 General Remarks

The numerical analysis of the corrugated channel is divided into four parts: the overview and details of the flow development predicted by LES, comparison of the fully turbulent region between the cases of 128 corrugation with turbulent inlet and 16 corrugations with periodic BC, comparison between LES predictions and PIV measurements, and hydrodynamics interaction in the fully turbulent region.

Prior to the above detailed analysis, a grid independence study is performed to assess the effect of grid densities and corrugated channel length on the predicted results. Two mesh densities are tested on 8 corrugations with periodic BC. The coarser one (Grid 1) has 0.9 million CV per corrugation and y_{max}^+ lower than 0.2 on the top and corrugation wall, and below 2 on the side walls. The finer mesh (Grid 2) doubles the mesh grid on each dimension of Grid 1. Both cases are solved using SMAG+VD. The time-averaged result obtained from both meshes are very similar, even the coarser grid can resolve most of the turbulent kinetic energy, and the resulting ν_{sgs} is generally less than 25% of ν . It is then concluded that the resolution of Grid 1 is able to support a well-resolved LES. Results obtained on three channels (8, 16 and 32 corrugations) are also compared. It is found the results predicted by 16 and 32 corrugations are identical, while the differences of the result between 8 and 16 corrugations are only marginal. Two-point correlation is performed at three locations for the 16 corrugations case. The results show that the time-averaged correlation can be found for as long as 5 corrugations, indicating the channel with 8 corrugations may not be able to accommodate the largest flow structures in the channel. Therefore the channel with 16 corrugations is selected for the analysis of the fully turbulent region of the channel.

LES is performed on the corrugated channel with 128 corrugations and synthetic turbulence inlet and convective outlet. The simulation is carried out using SMAG+VD on Grid 1. An overview of flow development is first given. The flows in the channel are divided into different Zones according to their visual features at the BL. The numerical error introduced by the inlet conditions is also discussed. A BL transition process is identified visually and proved numerically by calculating various BL thicknesses of the $\langle u \rangle$ profile across the channel. The results also suggest that the transition seems to suppress the flow development at the corrugated wall, and the BL thicknesses of both top and corrugated walls become similar after the transition.

In order to check the periodicity of the current flow configuration, features of the fully turbulent region predicted on the 128 corrugations case with turbulent inlet and

the 16 corrugations case with periodic BC are compared. It is found that the contour of different flow variables predicted on both cases share the same characteristics, including the variability of Reynolds stresses across different corrugations. A study on this variability confirms that it is caused by the nature of the current corrugated channel rather than the inadequacy of the time-averaging window. The comparison between the $\langle u \rangle$ and Reynolds stresses profiles predicted by both cases shows good agreement. It confirms that the case with 16 corrugations and periodic BC is able to reproduce the flow features of the fully turbulent region calculated by the 128 corrugations case.

The LES predictions are compared with PIV measurements on the same corrugated channel. Large discrepancies are found for both $\langle u \rangle$ and Reynolds stresses profiles. The LES predictions are then cross-checked by using different SGS models. The predictions of these SGS models are found to be very similar, which is due to the high percentage of resolved turbulent kinetic energy and a low level of ν_{sgs} . In addition, the energy spectrum across different turbulent length scales is calculated at three y/h locations, covering the region of most momentum interactions between the corrugations and the bulk flow. It is found spectrum profiles match well with the $-5/3$ slope, suggesting the flow field is well resolved by current LES. It is acknowledged that there are still uncertainties associated with error introduced by the numerical scheme and the time step size. However, these uncertainties cannot be addressed at current stage due to the limitation of the computing power and the software.

A closer examination of the experimental results and setups raises several issues and open questions on the experiment. Firstly, the calculated shape factor for the PIV data suggests that the BL at the corrugated wall may still be transitional while the BL at the top wall is turbulent when the measurement is taken. This seems unreasonable, because the BL at the corrugated wall should become turbulent quicker than that at the top wall due to the flow ejection from the corrugation. Secondly, the PIV data is recorded at $8Hz$. To assess the adequacy of this sampling frequency, LES data at several locations are recorded with $10kHz$ for $8s$ case time. These data are then sampled with $8Hz$. The results calculated by $8Hz$ are shown to be able to match the original results for $\langle u \rangle$ and follow the trend of Reynolds stresses for the upper half of the channel. However, they cannot reproduce the Reynolds stresses profile of the original LES data at the lower half of the channel, especially for the regions close to the corrugated wall. Also, the uncertainties brought by the spatial-averaging process during the PIV measurement cannot be assessed in this test, which may introduce errors for the measured $\langle u \rangle$ profile. Thirdly, the experimental

conditions seem to be either transient (in flow rate or/and Re) or pulsation, rather than steady, due to the limitation of the hardware. Fourthly, it is found the $\langle u \rangle$ profile predicted by LES at C57 (transitional) has a better agreement with the PIV data than the one at the fully turbulent region. This also raises doubts on whether the flow is fully turbulent when the PIV data is taken.

Despite that one may argue that the LES setup does not represent the experimental condition. However, the intention of the experiment was to investigate the turbulent flow field under a steady flow condition rather than a decreasing or pulsation flow condition. Therefore, the discrepancies between the LES prediction and PIV measurement are likely to be caused by the uncertainties in the experiment, and the LES predictions are used to study the detailed flow field in the channel under a steady flow condition.

The details of the flow development across the current corrugated channel are presented and discussed. Flow features for Zone 1 (C1 \sim C15) and Zone 2 (C16 \sim C41) are visualised and some small detached structures are found to have an upward trend toward the top wall. These structures are shown to cause fluctuations in the BL at the top wall and trigger the transition. It is interesting to find out that these structures are not from the flow ejection from the corrugation, rather, they are originate from the side wall. The subsequent BL transition at the top wall generates an increasing number of downward travelling structures, suppressing the flow development at the corrugated wall, thereby pushing the location of $\langle u \rangle_{max}$ down to a level slightly below the centreline of the channel.

The vector plot on $x/\lambda = 0.5$ for x - z plane shows mean secondary flows at few locations, such as the upper corners, the middle of the channel, and the exit of and within the corrugation. It demonstrates that the mean flows travel upwards along the side walls, create the secondary flow at the upper corners and meet at around $z/b = 0.5$ at the top wall, then travel down towards the corrugation and form another secondary flow at around $y/h = 2$. Together with the time-averaged streamlines for the same corrugation, it suggests that part of the mean flow which travels down from the top wall travel towards the side wall, causing net flow goes into the corrugation at the regions close to the side walls. The flow then moves transversely across the corrugation, forming a large vortex, and finally flows out of the corrugation at the middle region between $z/b = 0.2$ and 0.8 . Another part for the mean flow which travels down from the top wall does not get in to the corrugation, rather it joins the flow out of the corrugation and travel towards mean flow direction.

The time-averaged vector plot of U_{mag} is also studied on mid-plane. It is found that the

resulting vortices in the corrugation has the same characteristics as recorded in experiment. The time-averaged streamlines suggest that the outer flow goes into the corrugation from regions close to the side walls, and moves transversely across the corrugation, forming a large vortex, and finally flows out of the corrugation at the middle region.

Hydrodynamic interaction and vortex evolution are studied on the 16 corrugations case with periodic BC. The chain-reaction like behaviour and various stages of vortex evolution, which are recorded by the experiment, are reproduced by LES. It was found that after the generation of the small vortex at the upstream upper corner of the corrugation, its subsequent convection and impinging hitting on the downstream upper corner of the corrugation create a local high pressure region. Due to this, two streams of flow are accelerated, one of which goes deep inside the corrugation forming a large vortex that fills the corrugation. Another stream flows over the top of the corrugation and separates at the top of the corrugation generating small vortex at the upstream upper corner of the subsequent corrugation. Due to the lack of momentum, the large vortex in the corrugation becomes unstable. Then a low pressure band which across the whole channel height sweeps through with the bulk flow causing the flow ejection of the upstream, current and downstream corrugations. The time scale of the vortex evolution is around $0.11s$, corresponding to a flow travel distance of five corrugations which is same as the value obtained by the two-point correlation.

7.2 Recommendations for Future Work

Notwithstanding of the insight obtained by current numerical analysis on the corrugated channel, further works are recommended to supplement current research.

Current study shows that the side walls have a profound effect on the flow in current corrugated channel. It should be acknowledged that if the effect of the corrugation on the mean flow is the only area to be investigated, the distance for spanwise direction should be much longer to minimise the effect from the side walls. In other words, current configuration shared the same issues with the original periodic hill case proposed by Almeida. Therefore, a new configuration with adequately long spanwise distance (a spanwise periodicity for numerical case) or a corrugated pipe with circular cross section need to be tested in order to isolate the effect of the corrugation on the mean flow from the side walls.

Due to the uncertainties of the experiment and the LES, there are many unquantifiable factors for the discrepancies between the experimental and numerical results. Therefore, a new experiment is suggested with all aforementioned uncertainties being minimised or properly controlled, in order to provide a benchmark for LES.

It is also suggested performing a DNS with the same flow configurations to cross-check the PIV data and provide a benchmark for LES.

It is found that the high resolution of the grid is the reason of low sensitivity of flow solutions on various SGS models. Thus, the performance of these SGS models cannot be properly assessed. It is suggested coarsening the mesh to evaluate the performance of various SGS models on low mesh resolutions.

The geometry of the current corrugated wall is widely used in heat exchanger. Therefore, it would be beneficial to conduct further study on heat transfer and noise prediction on these flow configurations.

Bibliography

- [1] Lexico, “Definition of corrugated in english,” 2019. [1](#)
- [2] I. Dayyani, A. Shaw, E. S. Flores, and M. Friswell, “The mechanics of composite corrugated structures: A review with applications in morphing aircraft,” *Composite Structures*, vol. 133, pp. 358 – 380, 2015. [1](#)
- [3] E. Ünal, H. Ahn, and E. Sorguven, “Experimental investigation on flows in a corrugated channel,” *Journal of Fluids Engineering*, vol. 138, no. 7, p. 070908, 2016. [1](#), [2](#), [3](#), [22](#), [68](#), [69](#), [70](#), [82](#), [83](#), [106](#), [118](#), [121](#), [122](#)
- [4] R. Jaiman and O. Oakley, “CFD modeling of corrugated flexible pipe,” vol. 6, 01 2010. [1](#)
- [5] F. Calomino, G. Alfonsi, R. Gaudio, A. D’Ippolito, A. Lauria, A. Tafarojnoruz, and S. Artese, “Experimental and numerical study of free-surface flows in a corrugated pipe,” *Water*, vol. 10, p. 638, 05 2018. [1](#)
- [6] F. Hajabdollahi, Z. Hajabdollahi, and H. Hajabdollahi, “Optimum design of gasket plate heat exchanger using multimodal genetic algorithm,” *Heat Transfer Research*, vol. 44, no. 8, pp. 761–789, 2013. [1](#)
- [7] Koch, “Flexeramic ceramic structured packing,” 2019. [1](#)
- [8] E. Ünal, E. Sorguven, and H. Ahn, “Computational investigation of vortex structure in the corrugated channel,” vol. 7A: Fluids Engineering Systems and Technologies, 2013. [2](#), [3](#), [26](#), [69](#), [103](#)
- [9] J. Jiménez, “Turbulent flows over rough walls,” *Annual Review of Fluid Mechanics*, vol. 36, no. 1, pp. 173–196, 2004. [2](#), [7](#)
- [10] N. Kruse, S. Kuhn, and P. R. von Rohr, “Wavy wall effects on turbulence production and large-scale modes,” *Journal of Turbulence*, vol. 7, p. N31, 2006. [8](#)

- [11] M. Breuer, N. Peller, C. Rapp, and M. Manhart, “Flow over periodic hills – numerical and experimental study in a wide range of Reynolds numbers,” *Computers & Fluids*, vol. 38, no. 2, pp. 433 – 457, 2009. [2](#), [12](#), [57](#)
- [12] E. Ünal, H. Ahn, E. Sorguven, and M. Z. Gul, “Experimental investigation of vortex structure in the corrugated channel,” in *ASME 2013 International Mechanical Engineering Congress and Exposition*, American Society of Mechanical Engineers, 2013. [2](#), [68](#), [69](#), [70](#), [91](#), [118](#), [122](#)
- [13] J. Nikuradse, “Laws of flow in rough pipes,” *VDI Forschungsheft*, p. 361, 1933. [4](#)
- [14] J. W. Johnson, “Rectangular artificial roughness in open channels,” *Eos, Transactions American Geophysical Union*, vol. 25, no. 6, pp. 906–914, 1944. [4](#)
- [15] A. E. Perry, W. H. Schofield, and P. N. Joubert, “Rough wall turbulent boundary layers,” *Journal of Fluid Mechanics*, vol. 37, no. 2, p. 383–413, 1969. [4](#), [5](#), [6](#)
- [16] D. Wood and R. Antonia, “Measurements in a turbulent boundary layer over a d-type surface roughness,” *Journal of Applied Mechanics*, vol. 42, no. 3, pp. 591–597, 1975. [6](#)
- [17] H. Osaka and S. Mochizuki, “Coherent structure of a D-type rough wall boundary layer,” in *Transport Phenomena in Turbulent Flows: Theory, Experiment, and Numerical Simulation* (M. Hirata and N. Kasagi, eds.), pp. 199–211, 1988. [6](#)
- [18] L. Djenidi, R. A. Antonia, and F. Anselmet, “LDA measurements in a turbulent boundary layer over a d-type rough wall,” *Experiments in Fluids*, vol. 16, pp. 323–329, Apr 1994. [6](#)
- [19] R. Elavarasan, C. Y. Ching, and R. A. Antonia, “Turbulent boundary layer over a smooth wall with widely separated transverse square cavities,” *Applied Scientific Research*, vol. 55, pp. 227–243, Sep 1995. [7](#)
- [20] A. A. Townsend, *The structure of turbulent shear flow*. Cambridge university press, 1980. [7](#)
- [21] L. Djenidi, R. Elavarasan, and R. A. Antonia, “The turbulent boundary layer over transverse square cavities,” *Journal of Fluid Mechanics*, vol. 395, p. 271–294, 1999. [7](#), [122](#)

- [22] N. K. Ghaddar, K. Z. Korczak, B. B. Mikic, and A. T. Patera, “Numerical investigation of incompressible flow in grooved channels. part 1. stability and self-sustained oscillations,” *Journal of Fluid Mechanics*, vol. 163, p. 99–127, 1986. [7](#)
- [23] B. S. Arash Saidi, “Numerical simulation of turbulent convective heat transfer in square ribbed ducts,” *Numerical Heat Transfer, Part A: Applications*, vol. 38, no. 1, pp. 67–88, 2000. [7](#)
- [24] S. Eiamsa-ard and P. Promvonge, “Numerical study on heat transfer of turbulent channel flow over periodic grooves,” *International Communications in Heat and Mass Transfer*, vol. 35, no. 7, pp. 844 – 852, 2008. [7](#)
- [25] A. Boulemtafes-Boukadoum and A. Benzaoui, “CFD based analysis of heat transfer enhancement in solar air heater provided with transverse rectangular ribs,” *Energy Procedia*, vol. 50, pp. 761 – 772, 2014. Technologies and Materials for Renewable Energy, Environment and Sustainability (Tmrees14 - Eumisd). [8](#)
- [26] C. Lee and S. Abdel-Moneim, “Computational analysis of heat transfer in turbulent flow past a horizontal surface with two-dimensional ribs,” *International Communications in Heat and Mass Transfer*, vol. 28, no. 2, pp. 161 – 170, 2001. [8](#)
- [27] H. Stel, R. Morales, A. Franco, S. Junqueira, R. H. Erthal, and M. A. L. Gonçalves, “Numerical and experimental analysis of turbulent flow in corrugated pipes,” vol. 132, 07 2010. [8](#), [57](#), [122](#)
- [28] T. E. Stanton, D. Marshall, R. Houghton, *et al.*, “The growth of waves on water due to the action of the wind,” *Proc. R. Soc. Lond. A*, vol. 137, no. 832, pp. 283–293, 1932. [8](#)
- [29] S. Karaki and E. Y. Hsu, “An experimental investigation of the structure of a turbulent wind over water waves.,” tech. rep., Stanford Univ Calif Dept of Civil Engineering, 1968. [8](#)
- [30] J. M. Kendall, “The turbulent boundary layer over a wall with progressive surface waves,” *Journal of Fluid Mechanics*, vol. 41, no. 2, pp. 259–281, 1970. [8](#)
- [31] P. Beebe and J. E. Cermak, “Turbulent flow over a wavy boundary,” *Civil Engineering Reports; 74/72-44*, pp. 53–57, 1972. [8](#)
- [32] J. Hudson, L. Dykhno, and T. Hanratty, “Turbulence production in flow over a wavy wall,” *Experiments in Fluids*, vol. 20, no. 4, pp. 257–265, 1996. [8](#)

- [33] S. Nakagawa and T. J. Hanratty, “Particle image velocimetry measurements of flow over a wavy wall,” *Physics of Fluids*, vol. 13, no. 11, pp. 3504–3507, 2001. [8](#)
- [34] K. Krettenauer and U. Schumann, “Numerical simulation of turbulent convection over wavy terrain,” *Journal of Fluid Mechanics*, vol. 237, p. 261–299, 1992. [8](#), [9](#)
- [35] R. J. Adrian, R. T. D. S. Ferreira, and T. Boberg, “Turbulent thermal convection in wide horizontal fluid layers,” *Experiments in Fluids*, vol. 4, pp. 121–141, May 1986. [9](#)
- [36] J. W. Deardorff, “Convective velocity and temperature scales for the unstable planetary boundary layer and for rayleigh convection,” *Journal of the Atmospheric Sciences*, vol. 27, no. 8, pp. 1211–1213, 1970. [9](#)
- [37] M. Mirzaei, L. Davidson, A. Sohankar, and F. Innings, “The effect of corrugation on heat transfer and pressure drop in channel flow with different prandtl numbers,” *International Journal of Heat and Mass Transfer*, vol. 66, pp. 164 – 176, 2013. [9](#)
- [38] M. Mirzaei, A. Sohankar, L. Davidson, and F. Innings, “Large eddy simulation of the flow and heat transfer in a half-corrugated channel with various wave amplitudes,” *International Journal of Heat and Mass Transfer*, vol. 76, pp. 432 – 446, 2014. [9](#)
- [39] S. Knotek and M. Jícha, “Simulation of flow over a wavy solid surface: comparison of turbulence models,” in *EPJ Web of Conferences*, vol. 25, p. 01040, EDP Sciences, 2012. [9](#)
- [40] K. Hafez, O. Elsamni, and K. Zakaria, “Numerical investigation of the fully developed turbulent flow over a moving wavy wall using $k-\epsilon$ turbulence model,” *Alexandria Engineering Journal*, vol. 50, no. 2, pp. 145 – 162, 2011. [9](#)
- [41] W. Gong, P. A. Taylor, and A. Dörnbrack, “Turbulent boundary-layer flow over fixed aerodynamically rough two-dimensional sinusoidal waves,” *Journal of Fluid Mechanics*, vol. 312, pp. 1–37, 1996. [9](#)
- [42] D. S. Henn and R. I. Sykes, “Large-eddy simulation of flow over wavy surfaces,” *Journal of Fluid Mechanics*, vol. 383, pp. 75–112, 1999. [9](#)
- [43] V. Armenio and U. Piomelli, “A lagrangian mixed subgrid-scale model in generalized coordinates,” *Flow, Turbulence and Combustion*, vol. 65, no. 1, pp. 51–81, 2000. [9](#)

- [44] G. P. Almeida, D. F. G. Durao, and M. V. Heitor, “Wake flows behind two-dimensional model hills,” *Experimental Thermal Fluid Science*, vol. 7, pp. 87–101, July 1993. [10](#), [90](#)
- [45] G. P. Almeida, D. F. G. Durao, and M. V. Heitor, “2D model hill flows,” 1993. [10](#)
- [46] W. Rodi, J. Bonnin, and T. Buchal, “Ercoftac workshop on data bases and testing of calculation methods for turbulent flows,” in *Part of the Proceedings of the 4th ERCOFTAC/IAHR Workshop on Refined Flow Modelling*, University of Karlsruhe, 1995. [10](#)
- [47] C. Mellen, J. Fröhlich, and W. Rodi, *Large eddy simulation of the flow over periodic hills*. 2000. [10](#), [11](#)
- [48] S. Jakirlić, R. Jester-Zörker, C. Tropea, and editors, *9th ERCOFTAC/IAHR/COST Workshop on Refined Turbulence Modelling: Darmstadt University of Technology, Germany, October 4-5, 2001*. University of Technology, Darmstadt, 2001. [10](#)
- [49] R. Manceau, “Report of the 10th joint ERCOFTAC (SIG-15)/IAHR/QNET-CFD workshop on refined turbulence modelling,” 2003. [10](#)
- [50] L. Temmerman and M. A. Leschziner, “Large eddy simulation of separated flow in a streamwise periodic channel constriction,” in *TSFP Digital Library Online*, Begel House Inc., 2001. [11](#)
- [51] L. Temmerman, M. A. Leschziner, C. P. Mellen, and J. Fröhlich, “Investigation of wall-function approximations and subgrid-scale models in large eddy simulation of separated flow in a channel with streamwise periodic constrictions,” *International Journal of Heat and Fluid Flow*, vol. 24, no. 2, pp. 157 – 180, 2003. [11](#)
- [52] Y. Jang, M. Leschziner, K. Abe, and L. Temmerman, “Investigation of anisotropy-resolving turbulence models by reference to highly-resolved les data for separated flow,” *Flow, Turbulence and Combustion*, vol. 69, pp. 161–203, Nov 2002. [11](#)
- [53] K. Abe, Y. Jang, and M. Leschziner, “An investigation of wall-anisotropy expressions and length-scale equations for non-linear eddy-viscosity models,” *International Journal of Heat and Fluid Flow*, vol. 24, no. 2, pp. 181 – 198, 2003. [11](#)
- [54] S. Jakirlic, “Assessment of the RSM, URANS and hybrid models with respect to the different roadmaps including the industrial application challenges,” vol. Deliverable D3.2-36, 2012. [11](#)

- [55] J. Fröhlich, C. P. Mellen, W. Rodi, L. Temmerman, and M. A. Leschziner, “Highly resolved large-eddy simulation of separated flow in a channel with streamwise periodic constrictions,” *Journal of Fluid Mechanics*, vol. 526, p. 19–66, 2005. [11](#), [12](#)
- [56] J. Hinze, *Turbulence*. McGraw-Hill classic textbook reissue series, McGraw-Hill, 1975. [13](#)
- [57] P. Davidson, *Turbulence: An Introduction for Scientists and Engineers*. Oxford University Press, 2015. [13](#), [15](#), [16](#), [17](#)
- [58] M. Gad-el Hak, *Flow Control: Passive, Active, and Reactive Flow Management*. Cambridge University Press, 2006. [13](#)
- [59] F. White, *Viscous Fluid Flow*. College Ie, McGraw-Hill, 2006. [13](#)
- [60] O. Reynolds, “An experimental investigation of the circumstances which determine whether the motion of water shall be direct or sinuous, and of the law of resistance in parallel channels,” *Philosophical Transactions of the Royal Society of London*, vol. 174, pp. 935–982, 1883. [13](#)
- [61] O. Reynolds, “On the dynamical theory of incompressible viscous fluids and the determination of the criterion,” *Philosophical Transactions of the Royal Society of London. A*, vol. 186, pp. 123–164, 1895. [13](#)
- [62] P. Sagaut, *Large Eddy Simulation for Incompressible Flows: An Introduction*. Springer, 2006. [14](#), [15](#), [23](#), [24](#), [27](#), [28](#), [29](#), [32](#)
- [63] L. F. Richardson, *Weather Prediction by Numerical Process*, vol. 20. 01 1922. [15](#), [16](#)
- [64] A. N. Kolmogorov, “The local structure of turbulence in incompressible viscous fluid for very large Reynolds numbers,” in *Dokl. Akad. Nauk SSSR*, vol. 30, pp. 299–303, 1941. [15](#)
- [65] S. Pope, *Turbulent Flows*. Cambridge University Press, 2000. [16](#), [23](#), [35](#)
- [66] R. Lewandowski and B. Pinier, “The Kolmogorov Law of turbulence - What can rigorously be proved? part II,” in *The Foundations of chaos revisited: from Poincaré to recent advancements*, pp. 71–89, Springer, 2016. [16](#)
- [67] D. Wilcox, *Turbulence Modeling for CFD*. No. v. 1 in Turbulence Modeling for CFD, DCW Industries, 2006. [17](#)

- [68] J. D. Anderson, “Ludwig Prandtl’s boundary layer,” *Physics Today*, vol. 58, no. 12, pp. 42–48, 2005. [17](#)
- [69] C. Mayes, H. Schlichting, E. Krause, H. Oertel, and K. Gersten, *Boundary-Layer Theory*. Physic and astronomy, Springer Berlin Heidelberg, 2003. [17](#), [18](#), [19](#), [87](#)
- [70] T. Irps and V. Kanjirakkad, “On the interaction between turbulence grids and boundary layers,” *EPJ Web of Conferences*, vol. 114, p. 02048, 2016. [18](#)
- [71] M. Langari and Z. Yang, “Numerical study of the primary instability in a separated boundary layer transition under elevated free-stream turbulence,” *Physics of Fluids*, vol. 25, no. 7, p. 074106, 2013. [18](#)
- [72] H. Versteeg and W. Malalasekera, *An Introduction to Computational Fluid Dynamics: The Finite Volume Method*. Pearson Education Limited, 2007. [19](#), [22](#), [29](#), [33](#), [35](#), [37](#), [38](#), [45](#), [50](#), [51](#), [54](#), [55](#), [82](#), [145](#)
- [73] N. Hamilton, M. Tutkun, and R. B. Cal, “Low-order dynamical system model of a fully developed turbulent channel flow,” *Physics of Fluids*, vol. 29, no. 6, p. 065107, 2017. [20](#), [63](#)
- [74] A. Sayma, *Computational fluid dynamics*. Bookboon, 2009. [21](#), [22](#), [44](#), [45](#)
- [75] J. Anderson, *Computational Fluid Dynamics*. Computational Fluid Dynamics: The Basics with Applications, McGraw-Hill Education, 1995. [21](#)
- [76] UK Government, “Government boost for jet engines with £10 million investment for next generation technology,” *UK Government Press Release*, Feb 2016. [21](#)
- [77] Dantec Dynamic A/S, “Measurement principles of CTA,” 2018. [21](#)
- [78] A. Drózdź and V. Uruba, “Comparison of PIV and hot-wire statistics of turbulent boundary layer,” *Journal of Physics: Conference Series*, vol. 530, p. 012044, 08 2014. [21](#)
- [79] S. Scharnowski, M. Bross, and C. J. Kähler, “Accurate turbulence level estimations using PIV/PTV,” *Experiments in Fluids*, vol. 60, p. 1, Nov 2018. [22](#)
- [80] E. Shaughnessy, I. Katz, and J. Schaffer, *Introduction to fluid mechanics*. No. v. 1, Oxford University Press, 2005. [22](#)
- [81] M. Dhaubhadel, “CFD applications in the automotive industry,” *Journal of fluids engineering*, vol. 118, no. 4, pp. 647–653, 1996. [22](#)

- [82] B. Xia and D. Sun, “Applications of computational fluid dynamics (CFD) in the food industry: a review,” *Computers and Electronics in Agriculture*, vol. 34, no. 1, pp. 5 – 24, 2002. [22](#)
- [83] G. Inci and E. Sorgüven, “Effect of lvad outlet graft anastomosis angle on the aortic valve, wall, and flow,” *ASAIO journal*, vol. 58, no. 4, pp. 373–381, 2012. [22](#)
- [84] J. Smagorinsky, “General circulation experiments with the primitive equations,” *Monthly Weather Review*, vol. 91, no. 3, pp. 99–164, 1963. [27](#), [34](#)
- [85] Y. Zhiyin, “Large-eddy simulation: Past, present and the future,” *Chinese Journal of Aeronautics*, vol. 28, no. 1, pp. 11 – 24, 2015. [27](#), [29](#), [46](#)
- [86] A. N. Kolmogorov, “The local structure of turbulence in incompressible viscous fluid for very large Reynolds numbers,” *Proceedings: Mathematical and Physical Sciences*, vol. 434, no. 1890, pp. 9–13, 1991. [27](#)
- [87] K. Ma, W. L. Wei, L. L. Wang, and X. J. Zhao, “Large eddy numerical simulation of flows over a backward-facing step,” in *2011 International Symposium on Water Resource and Environmental Protection*, vol. 4, pp. 3024–3026, May 2011. [28](#)
- [88] A. Leonard, *Energy Cascade in Large-Eddy Simulations of Turbulent Fluid Flows*, vol. Volume 18, Part A, pp. 237–248. Elsevier, 1975. [32](#)
- [89] J. H. Ferziger, “Large eddy numerical simulations of turbulent flows,” *AIAA Journal*, vol. 15, no. 9, pp. 1261–1267, 1977. [32](#), [53](#)
- [90] R. Peyret and E. Krause, *Advanced Turbulent Flow Computations*. Springer Vienna, 2014. [32](#)
- [91] E. Villiers, *The Potential of Large Eddy Simulation for the Modeling of Wall Bounded Flows*. Thesis, 2006. [32](#), [44](#), [45](#), [46](#), [53](#), [55](#), [57](#), [79](#)
- [92] L. Berselli, T. Iliescu, and W. Layton, *Mathematics of Large Eddy Simulation of Turbulent Flows*. Springer, 2006. [33](#)
- [93] R. A. Clark, J. H. Ferziger, and W. C. Reynolds, “Evaluation of subgrid-scale models using an accurately simulated turbulent flow,” *Journal of Fluid Mechanics*, vol. 91, pp. 1–16, 1979. [33](#)

- [94] G. P. Galdi and W. J. Layton, “Approximation of the larger eddies in fluid motions II: A model for space-filtered flow,” *Mathematical Models and Methods in Applied Sciences*, vol. 10, no. 03, pp. 343–350, 2000. [33](#)
- [95] J. Bardina, J. Ferziger, and W. Reynolds, *Improved subgrid-scale models for large-eddy simulation*. Fluid Dynamics and Co-located Conferences, American Institute of Aeronautics and Astronautics, 1980. [33](#), [37](#), [38](#)
- [96] U. Piomelli, “Large-eddy simulation: achievements and challenges,” *Progress in Aerospace Sciences*, vol. 35, no. 4, pp. 335–362, 1999. [33](#)
- [97] V. M. Canuto and Y. Cheng, “Determination of the Smagorinsky—Lilly constant CS,” *Physics of Fluids*, vol. 9, no. 5, pp. 1368–1378, 1997. [34](#), [37](#)
- [98] F. Nozaki, “Smagorinsky SGS model in OpenFOAM,” 2016. [34](#)
- [99] E. Leveque, F. Toschi, L. Shao, and J. P. Bertoglio, “Shear-improved Smagorinsky model for large-eddy simulation of wall-bounded turbulent flows,” *Journal of Fluid Mechanics*, vol. 570, pp. 491–502, 2007. [35](#)
- [100] U. Schumann, “Subgrid scale model for finite difference simulations of turbulent flows in plane channels and annuli,” *Journal of Computational Physics*, vol. 18, no. 4, pp. 376–404, 1975. [35](#), [36](#), [57](#)
- [101] A. Yoshizawa, “Statistical theory for compressible turbulent shear flows, with the application to subgrid modeling,” *Physics of Fluids*, vol. 29, no. 7, pp. 2152–2164, 1986. [35](#), [36](#), [61](#)
- [102] C. Fureby, G. Tabor, H. G. Weller, and A. D. Gosman, “A comparative study of subgrid scale models in homogeneous isotropic turbulence,” *Physics of Fluids*, vol. 9, no. 5, pp. 1416–1429, 1997. [35](#), [36](#), [38](#)
- [103] P. Moin and J. Kim, “Numerical investigation of turbulent channel flow,” *Journal of Fluid Mechanics*, vol. 118, pp. 341–377, 1982. [36](#), [57](#)
- [104] R. S. Rogallo and P. Moin, “Numerical-simulation of turbulent flows,” *Annual Review of Fluid Mechanics*, vol. 16, pp. 99–137, 1984. [36](#)
- [105] J. W. Deardorff, “A numerical study of three-dimensional turbulent channel flow at large Reynolds numbers,” *Journal of Fluid Mechanics*, vol. 41, no. 02, pp. 453–480, 1970. [36](#)

- [106] E. R. Van Driest, “On turbulent flow near a wall,” *Journal of the Aeronautical Sciences*, vol. 23, no. 11, pp. 1007–1011, 1956. [36](#)
- [107] J. Ferziger and M. Peric, *Computational Methods for Fluid Dynamics*. Springer Berlin Heidelberg, 2001. [36](#), [44](#), [45](#), [49](#), [50](#), [53](#), [54](#), [55](#), [145](#)
- [108] O. Penttinen, “A pimplefoam tutorial for channel flow with respect to different les models,” in *Proceedings of CFD with OpenSource Software*, Chalmers University of Technology, 2011. [36](#)
- [109] M. Germano, U. Piomelli, P. Moin, and W. H. Cabot, “A dynamic subgrid-scale eddy viscosity model,” *Physics of Fluids A*, vol. 3, no. 7, pp. 1760–1765, 1991. [37](#), [38](#)
- [110] D. K. Lilly, “A proposed modification of the Germano subgrid-scale closure method,” *Physics of Fluids A*, vol. 4, no. 3, pp. 633–635, 1992. [37](#), [38](#)
- [111] U. Piomelli, W. H. Cabot, P. Moin, and S. Lee, “Subgrid-scale backscatter in turbulent and transitional flows,” *Physics of Fluids A*, vol. 3, no. 7, pp. 1766–1771, 1991. [38](#)
- [112] T. S. Lund, S. Ghosal, and P. Moin, “Numerical experiments with highly variable eddy viscosity models,” *Engineering Applications of Large Eddy Simulations*, vol. 162, pp. 7–11, 1993. [38](#)
- [113] U. Piomelli, “Local space-time averaging in the dynamic subgrid scale model,” *American Phys. Soc.*, vol. 35, no. 10, 1991. [38](#), [57](#), [58](#), [61](#)
- [114] S. Ghosal, T. S. Lund, P. Moin, and K. Akselvoll, “A dynamic localization model for large eddy simulation of turbulent flows,” *Journal of Fluid Mechanics*, vol. 286, p. 229, 1995. [38](#)
- [115] C. Meneveau, T. S. Lund, and W. H. Cabot, “A lagrangian dynamic subgrid-scale model of turbulence,” *Journal of Fluid Mechanics*, vol. 319, pp. 353–385, 1996. [38](#)
- [116] W. Kim and S. Menon, “A new dynamic one-equation subgrid-scale model for large eddy simulations,” in *33rd Aerospace Sciences Meeting and Exhibit*, p. 356, 1995. [39](#)
- [117] OpenCFD, *OpenFOAM: The Open Source CFD Toolbox. User Guide Version 1.4*, OpenCFD Limited. Reading UK, Apr. 2007. [39](#), [81](#)

- [118] F. Nicoud and F. Ducros, “Subgrid-scale stress modelling based on the square of the velocity gradient tensor,” *Flow, turbulence and Combustion*, vol. 62, no. 3, pp. 183–200, 1999. [39](#)
- [119] J. W. Deardorff, “The use of subgrid transport equations in a three-dimensional model of atmospheric turbulence,” *Journal of Fluids Engineering*, vol. 95, no. 3, pp. 429–438, 1973. [40](#)
- [120] C. Fureby, G. Tabor, H. G. Weller, and A. D. Gosman, “Differential subgrid stress models in large eddy simulations,” *Physics of Fluids*, vol. 9, no. 11, pp. 3578–3580, 1997. [40](#)
- [121] F. R. Menter, “Best practices for scale-resolving simulations (srs) with ANSYS CFD,” report, 2012. [40](#)
- [122] ANSYS, “ANSYS Fluent theory guide,” 2013. [40](#)
- [123] R. I. Issa, B. Ahmadi-Befruji, K. R. Beshay, and A. D. Gosman, “Solution of the implicitly discretised reacting flow equations by operator-splitting,” *J. Comput. Phys.*, vol. 93, pp. 388–410, Apr. 1991. [42](#), [54](#)
- [124] J. Tu, *Computational fluid dynamics : a practical approach*. third ed., 2018. [44](#), [45](#)
- [125] L. C. Berselli, T. Iliescu, and W. J. Layton, *Mathematics of large eddy simulation of turbulent flows*. Springer Science & Business Media, 2005. [44](#)
- [126] R. Verzicco and P. Orlandi, “A finite-difference scheme for three-dimensional incompressible flows in cylindrical coordinates,” *Journal of Computational Physics*, vol. 123, no. 2, pp. 402 – 414, 1996. [44](#)
- [127] E. Saiki and S. Biringen, “Numerical simulation of a cylinder in uniform flow: Application of a virtual boundary method,” *Journal of Computational Physics*, vol. 123, no. 2, pp. 450 – 465, 1996.
- [128] E. Fadlun, R. Verzicco, P. Orlandi, and J. Mohd-Yusof, “Combined immersed-boundary finite-difference methods for three-dimensional complex flow simulations,” *Journal of Computational Physics*, vol. 161, no. 1, pp. 35 – 60, 2000.
- [129] E. A. Muravleva and M. A. Olshanskii, “Two finite-difference schemes for calculation of bingham fluid flows in a cavity,” 2008. [44](#)

- [130] K. B. Ølgaard, A. Logg, and G. N. Wells, “Automated code generation for discontinuous galerkin methods,” *SIAM Journal on Scientific Computing*, vol. 31, no. 2, pp. 849–864, 2008. [45](#)
- [131] COMSOL, “The finite element method (FEM),” 2018. [45](#)
- [132] U. Gaitonde, Y. Gong, and F. Tanner, “Quality criteria for large eddy simulation,” *First year transfer report. School of MACE, University of Manchester*, 2008. [46](#)
- [133] D. B. Spalding, “A novel finite difference formulation for differential expressions involving both first and second derivatives,” *International Journal for Numerical Methods in Engineering*, vol. 4, no. 4, pp. 551–559. [54](#)
- [134] F. Moukalled, L. Mangani, and M. Darwish, *The Finite Volume Method in Computational Fluid Dynamics: An Advanced Introduction with OpenFOAM and Matlab*. Springer Publishing Company, Incorporated, 1st ed., 2015. [54](#)
- [135] H. Nilsson, “CFD with opensource software 2018,” 2018. [55](#), [145](#)
- [136] C. Fureby, A. Gosman, G. Tabor, H. Weller, N. Sandham, and M. Wolfshtein, “Large eddy simulation of turbulent channel flows,” *Turbulent shear flows*, vol. 11, 1997. [57](#)
- [137] W. Cabot, “Large-eddy simulations with wall models,” 1995. [57](#), [79](#)
- [138] T. Wei and W. W. Willmarth, “Reynolds-number effects on the structure of a turbulent channel flow,” *Journal of Fluid Mechanics*, vol. 204, p. 57–95, 1989. [57](#)
- [139] K. Shah and J. Ferziger, “A new non-eddy viscosity subgrid-scale model and its application to channel flow,” 1995. [57](#), [58](#), [59](#), [61](#)
- [140] T. Gefeng, Y. Zhiyin, and M. J. J., “Numerical methods for large-eddy simulation in general co-ordinates,” *International Journal for Numerical Methods in Fluids*, vol. 46, no. 1, pp. 1–18. [57](#), [148](#)
- [141] M. Lee and R. D. Moser, “Direct numerical simulation of turbulent channel flow up to $Re_\tau \approx 5200$,” *Journal of Fluid Mechanics*, vol. 774, pp. 395–415, 2015. [57](#)
- [142] I. Veloudis, Z. Yang, and J. McGuirk, “Les of wall-bounded flows using a new subgrid scale model based on energy spectrum dissipation,” *Journal of Applied Mechanics*, vol. 75, no. 2, p. 021005, 2008. [58](#), [61](#)

- [143] L. Davidson, “Large eddy simulations: How to evaluate resolution,” *International Journal of Heat and Fluid Flow*, vol. 30, no. 5, pp. 1016 – 1025, 2009. The 3rd International Conference on Heat Transfer and Fluid Flow in Microscale. [58](#), [75](#)
- [144] B. Santos, “Contrib/perturbu,” December 2017. [59](#)
- [145] A. Syrakos, S. Varchanis, Y. Dimakopoulos, A. Goulas, and J. Tsamopoulos, “A critical analysis of some popular methods for the discretisation of the gradient operator in finite volume methods,” vol. 29, 06 2016. [71](#)
- [146] A. J. Ward-Smith, R. P. Benedict, and W. M. Hagist, “Internal Fluid Flow: The Fluid Dynamics of Flow on Pipes and Ducts and Fundamentals of Pipe Flow,” *Journal of Fluids Engineering*, vol. 104, pp. 129–129, 03 1982. [97](#)
- [147] E. S. Menon, “Chapter 8 - pipeline hydraulic analysis,” in *Pipeline Planning and Construction Field Manual* (E. S. Menon, ed.), pp. 123 – 175, Boston: Gulf Professional Publishing, 2011. [97](#)
- [148] Witzemann, “Metal Hoses Manual,” pp. 78–125, 03 2013. [97](#)
- [149] T. Sayadi and P. Moin, “Predicting natural transition using large eddy simulation,” *Center for Turbulence Research Annual Research Briefs*, pp. 97–108, 2011. [113](#)
- [150] Z. Yang and P. R. Voke, “Large-eddy simulation studies of bypass transition,” in *Engineering Turbulence Modelling and Experiments* (W. RODI and F. MARTELLI, eds.), pp. 603 – 611, Oxford: Elsevier, 1993. [113](#)
- [151] P. R. Spalart, J. Wh, M. Strelets, and S. R. Allmaras, “Comments on the feasibility of LES for wings, and on a Hybrid RANS/LES approach,” 1997. [143](#)
- [152] F. R. Menter and M. Kuntz, *Adaptation of Eddy-Viscosity Turbulence Models to Unsteady Separated Flow Behind Vehicles*, vol. 19 of *Lecture Notes in Applied and Computational Mechanics*, book section 30, pp. 339–352. Springer Berlin Heidelberg, 2004. [143](#)
- [153] P. R. Spalart, S. Deck, M. L. Shur, K. D. Squires, M. K. Strelets, and A. Travin, “A new version of detached-eddy simulation, resistant to ambiguous grid densities,” *Theoretical and Computational Fluid Dynamics*, vol. 20, no. 3, pp. 181–195, 2006. [144](#)

- [154] M. L. Shur, P. R. Spalart, M. K. Strelets, and A. K. Travin, “A hybrid RANS-LES approach with delayed-DES and wall-modelled LES capabilities,” *International Journal of Heat and Fluid Flow*, vol. 29, no. 6, pp. 1638–1649, 2008. [144](#)
- [155] D. Cokljat, D. Caridi, G. Link, R. Lechner, and F. R. Menter, “Embedded LES methodology for general-purpose CFD solvers,” in *Proc. Turbulent Shear Flow Phenomena, Proc. 6th Int. Symp. Turbulence and Shear Flow Phenomena*, pp. 1191–1196, 2009. [144](#)
- [156] F. R. Menter, A. Garbaruk, P. Smirnov, D. Cokljat, and F. Mathey, *Scale-Adaptive Simulation with Artificial Forcing*, vol. 111 of *Notes on Numerical Fluid Mechanics and Multidisciplinary Design*, book section 20, pp. 235–246. Springer Berlin Heidelberg, 2010. [144](#)

Appendix A

Conventional Hybrid Model

A.1 Detached Eddy Simulation

Detached Eddy Simulation (DES) was proposed by Spalart et al [151]. In this model, the wall BLs are computed completely by the RANS model and the free shear flow away from walls is covered by LES model. The switch between RANS and LES is based on grid resolution. Theoretically, any RANS turbulence model can be incorporated in DES. Within DES model, the RANS and LES switch criterion is

$$\begin{cases} C_{DES}\Delta_{max} > \ell & \leftrightarrow \text{flow solved in RANS model} \\ C_{DES}\Delta_{max} \leq \ell & \leftrightarrow \text{flow solved in LES model} \end{cases} \quad (\text{A.1})$$

Where $\Delta_{max} = \max(\Delta_x, \Delta_y, \Delta_z)$ and ℓ is the turbulence length scale which is evaluated by relevant RANS parameters (using $k - \epsilon$ and $k - \omega$ two equation RANS models as examples)

$$\ell = \frac{k^{3/2}}{\epsilon} = \frac{k^{1/2}}{\beta^*\omega} \quad (\text{A.2})$$

It is defined that when the grid resolution $\Delta_{max} \leq \ell$ the model will be switched from RANS to LES. It requires a grid and time step resolution to be of LES quality in the detached region. For a normal RANS grid with the wall-parallel (x and z directions) grid spacing usually exceeds BL size, and the DES model will stay in RANS mode for the entire BL. However, care must be taken in this case as if $\Delta_{max} > \ell$ the LES mode will be activated inside the attached BL even though the grid is not fine enough for resolving turbulence. Menter and Kuntz [152] reported this Grid-Induced Separation (GIS), and that the BL can separate at arbitrary locations due to various mesh resolutions. In order to overcome this drawback, they introduced a concept of "shielding" of the BL which was

extended to Delayed-DES (DDES) by Spalart et al [153]. DDES modifies the dissipation term in the k -equation by introducing a function F_{DDES} which is set to be 1 within the wall BL and 0 in the detached region.

A.2 Wall Modelled Large Eddy Simulation

Wall Modelled Large Eddy Simulation (WMLES) has a different feature to DES as its switch between RANS and LES model is dependent on wall distance. In this model, kinematic turbulent viscosity is given as [154]

$$\nu_t = f_D \min[(\kappa y)^2, (C_s \Delta)^2] S \quad (\text{A.3})$$

Where y is the wall distance, f_D is a wall damping function, κ is von Karman constant, C_s is the Smagorinsky constant and s is the strain rate. The very near-wall region is represented by RANS and the mode will be switched to LES when the mesh resolution is sufficient for resolving turbulence scale.

A.3 Embedded/Zonal Large Eddy Simulation

Other than using mesh resolution and wall distance as the switch trigger between RANS and LES, WMLES, E/ZLES predefines the region for LES and RANS before calculation and turbulence is imposed at the interface between the two regions [155, 156].

Appendix B

Pressure Correction Equation for PISO Algorithm

The current study is based on incompressible flow for which the governing equations do not have coupling between density and pressure, and the energy equation and the rest of the system. However, such pressure-velocity system contains two complex couplings, i.e. the non-linear convection term and the pressure-velocity coupling [135].

Since there is no pressure equation for incompressible flow, a pressure correction equation needs to be derived by the continuity and momentum equations. The derivation process can start by discretising the momentum equation as

$$a_P \mathbf{u}_P + \sum_N a_N \mathbf{u}_N = \mathbf{Q} - \nabla p \quad (\text{B.1})$$

where p is the index of an arbitrary cell centre; N denotes the neighbour cell centres surrounding that arbitrary cell centre; a_P and a_N are coefficients which are obtained by discretisation of the momentum equation¹; \mathbf{Q} is the source term which contains all other terms in the equation.

An operator \mathbf{H} can be introduced

$$\mathbf{H} = \mathbf{Q} - \sum_N a_N \mathbf{u}_N \quad (\text{B.2})$$

then

$$\mathbf{u}_P = (a_P)^{-1} [\mathbf{H} - \nabla p] \quad (\text{B.3})$$

¹The details of calculation a_P and a_N can be found in different CFD text books [72, 107]

Substituting this in the continuity equation ($\nabla \cdot \mathbf{u} = 0$), the pressure correction equation for incompressible flow can be obtained as

$$\nabla \cdot [(a_P)^{-1} \nabla p] = \nabla \cdot [(a_P)^{-1} \mathbf{H}] \quad (\text{B.4})$$

Appendix C

Channel Flow Result Verification

Result verification is presented in this section. The two key aspects of the result verification for the current simulation are:

1. whether the statistical variable obtained by OpenFOAM is correct;
2. whether the flow reaches the statistically steady state at the end of simulation;

This section will be dedicated to answer the above three questions. Fig C.1 depicts the comparison between the mean variables obtained by OpenFOAM and calculated by the instantaneous velocity data.

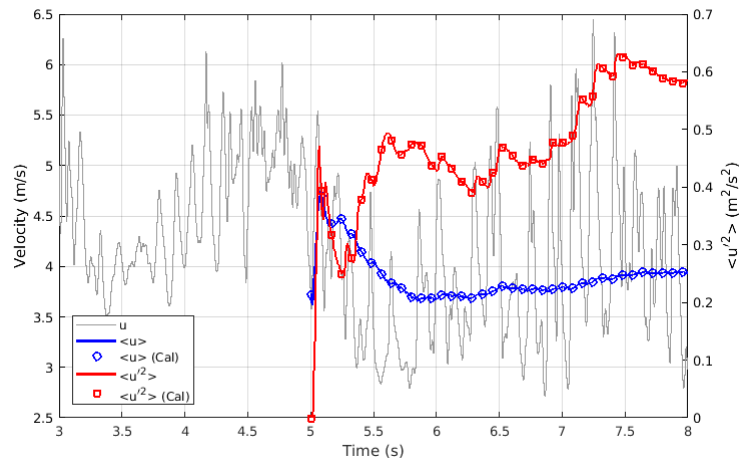


FIGURE C.1. Velocity time history profile at $y/h = 0.412$ for SMAG+VD on Mesh1.

The grey line represents the time history of the instantaneous stream-wise velocity, u . The blue and red lines are the cumulative average of velocity and fluctuation at streamwise directions obtained by OpenFOAM, i.e. $\langle u \rangle$ and $\langle u'^2 \rangle$ respectively. The blue and red circles are the moving average of u and u'^2 calculated by u by using Matlab code. It

verifies that the mean value calculated by OpenFOAM is numerically accurate. Data at different locations for other cases appear to show the same behaviour. It is noted that although the flow through time is 50% more than the comparable case conducted by Tang, et al. [140], the $\langle u \rangle$ and $\langle u'^2 \rangle$ has not yet become a straight line at the end of simulation. However, this does not necessarily indicate the flow has not reached statically steady state. Because the data to be analysed are not based on single point, rather they are spatially averaged along x and z directions (on which periodic BC are applied) and then temporally averaged prior to the analysis. Therefore, Fig. C.2 to Fig. C.4 present the spatially and temporally averaged variables along y axis for different flow times obtained by different models on different mesh densities. Among them, Fig C.2 is for SMAG+VD on Mesh1, Fig C.3 is for KEQ on Mesh2, and Fig C.4 is for DyK on Mesh3.

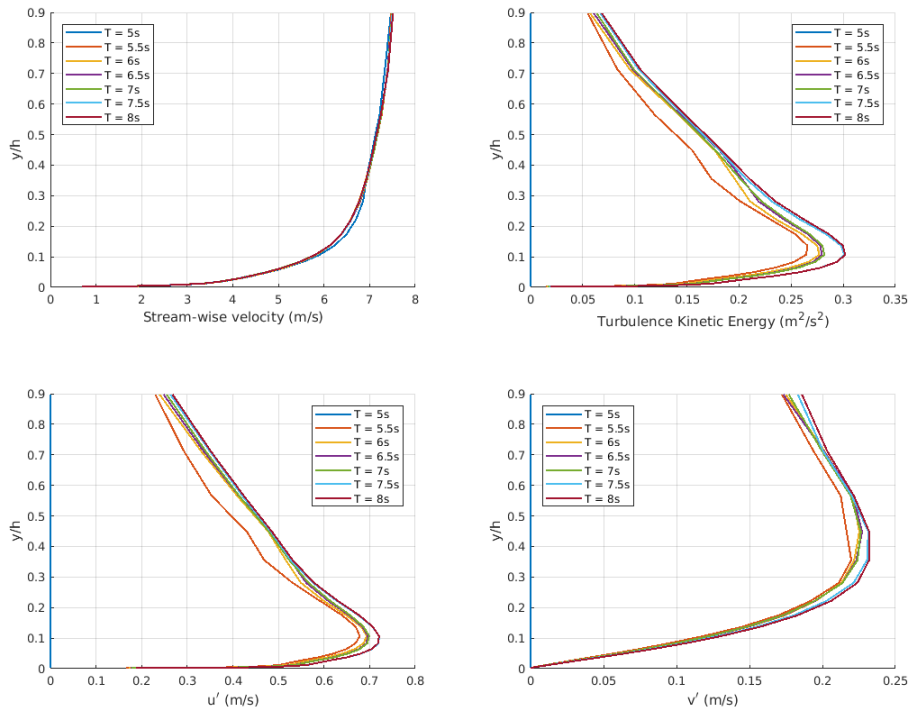


FIGURE C.2. Spatially and temporally averaged variables along y axis at different flow times for SMAG+VD on Mesh1.

Fig. C.2 to Fig. C.4 show that most of the variables reach a statistically steady state at around $T = 7s$. Some variables reach this state even at $T = 5.5s$ or $6s$. Also, the figures indicate that the finer the mesh, the quicker the flow reaches a statistically steady state. This confirmed that the result obtained at $T = 8s$ is appropriate to be used in data analysis.

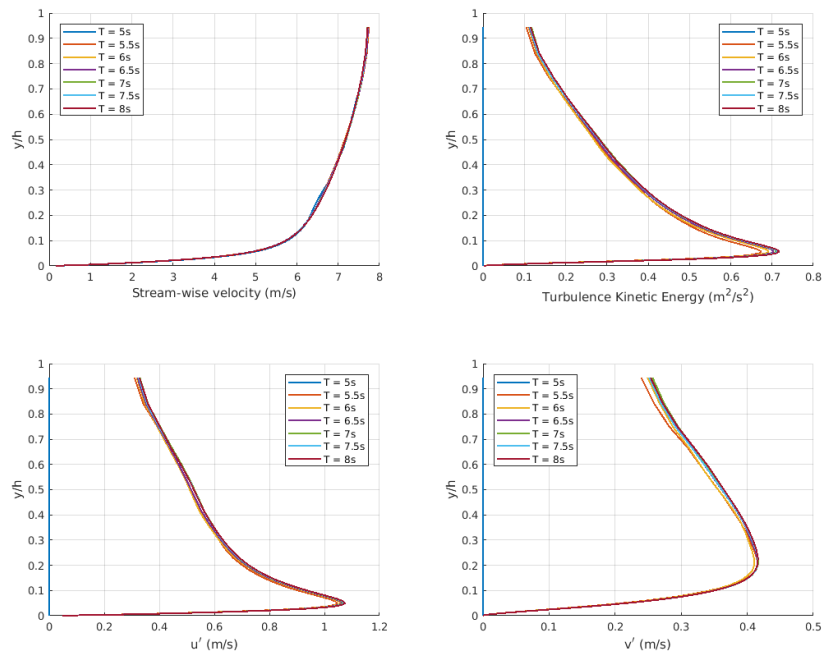


FIGURE C.3. Spatially and temporally averaged variables along y axis at different flow times for KEQ on Mesh2.

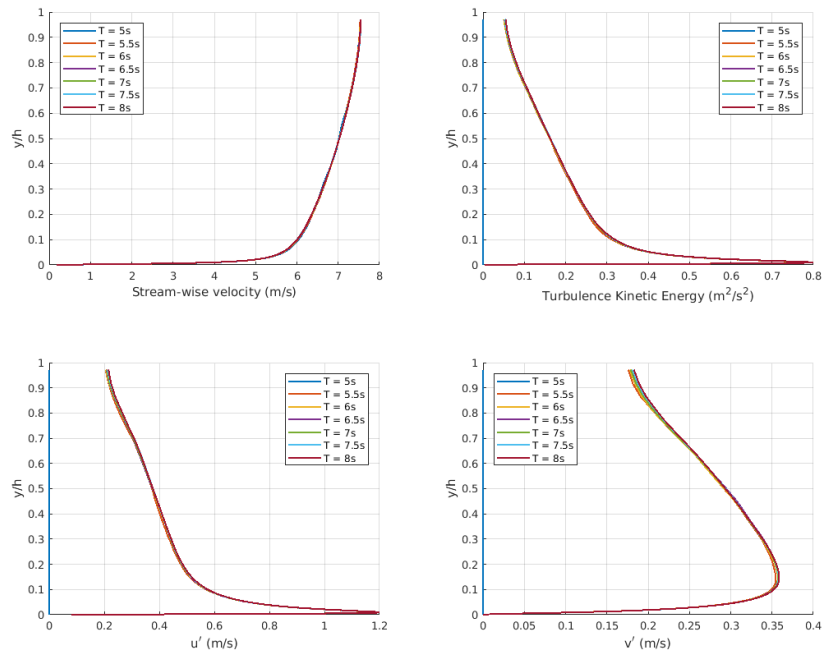


FIGURE C.4. Spatially and temporally averaged variables along y axis at different flow times for DyK on Mesh3.

Appendix D

Comparison of Computing Speeds

D.1 Computational Cost of Various SGS models

Calculation speed (clock time) of each SGS model under different mesh densities are recorded and summarised in Fig. D.1. All simulations are conducted on same the hardware configuration (128 cores on the HPC in the University of Sussex), numerical method (as stated in previous sections), and case setup (taking average between $t = 5$ and 8 with 12 point sampling). The time duration is 1s simulation time, corresponding to 50,000 time steps. It is found that taking average has no obvious effect on calculation speed. The gray bar represents Mesh1, the white bar plus the gray bar is for Mesh2 and the combination of the three colours is for Mesh3. All time cost is normalised by the time cost of SMAG model on Mesh1, $T_{SMAG} = 2800s$.

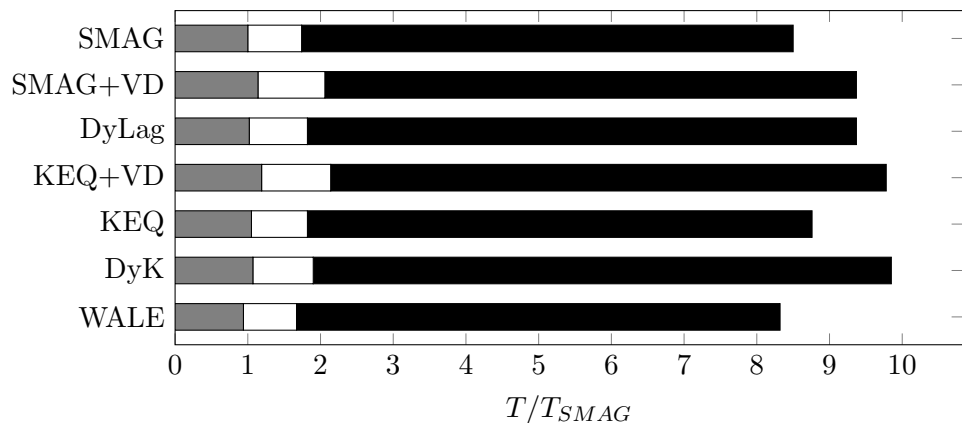


FIGURE D.1. Time cost of various SGS model for channel flow

It is found out that WALE requires the least computing resource, only 94% of the time cost of SMAG under Mesh1, 96% under Mesh2 and 98% under Mesh3. Whereas, under

Mesh1 and Mesh2, the greatest calculation resource is required by KvD, which are 19.4% and 23.7% more than SMAG respectively. Under Mesh3, DyK spends the longest time to finish its calculation, which is 15% more than the time of SMAG.

D.2 Computational Speeds of Various HPC

A computational speed between the HPC in Sussex University and the ARCHER (the UK national supercomputing services) is compared¹. The result is in Table. D.1. It is shown that the computational time savings on ARCHER is obvious, but the scalability on ARCHER over 384 cores are not good for current case. So current simulation is run on 386 cores.

HPC with CPU No.	Case Time (<i>s</i>)	Physical Time (<i>s</i>)	Physical Time per 1 <i>s</i> Case Time (<i>h</i>)
Sussex, 128	1	106967	29.71
ARCHER, 192	0.054	3000	15.43
ARCHER, 384	0.1	3414	9.31
ARCHER, 768	1	30584	8.50

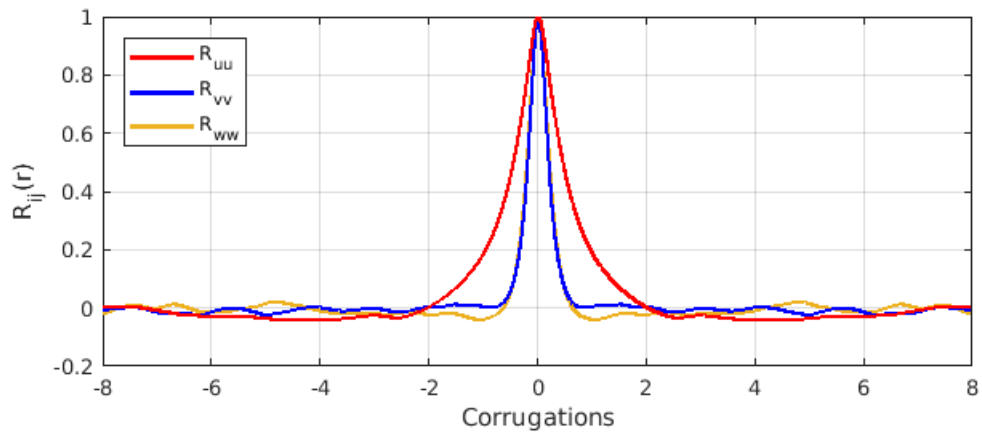
TABLE D.1. Time cost on different HPC systems for SMAG

¹The calculation on Sussex HPC starts from $T = 12s$ and finishes at $T = 13.5s$. There are some numerical instabilities at the beginning as a result of mapping the 32 corrugation case onto the 64 corrugation case as its initial condition. So the time consuming data from $T = 12.5$ and $13.5s$ is used to compare with the simulation on ARCHER.

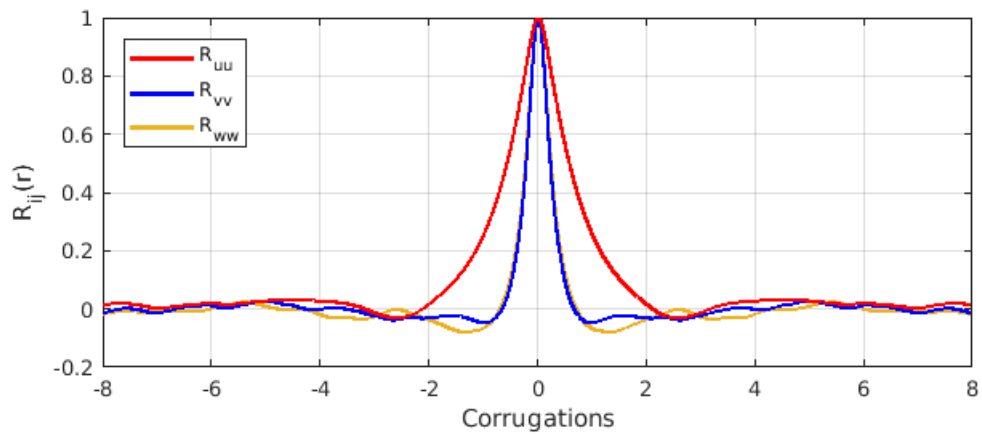
Appendix E

Results of Two-point correlation

The results of the two-point correlation along the line of $y/h = 0.265$ and $y/h = 0.819$ are shown in Fig. E.1.



(A) $y/h = 0.265$



(B) $y/h = 0.819$

FIGURE E.1. The normalised 2pt correlation of velocity along x direction at $y/h = 0.265$ and $y/h = 0.819$ predicted by SMAG+VD on 16 corrugations with periodic BC.

Appendix F

Discrepancies of Reynolds Stresses Between Each Corrugation

It is found in the predictions of both 128 and 16 corrugations cases that the high turbulent intensity regions show discrepancies between each corrugation. This may be due to the nature of current flow or the inadequacy of time-averaging window. Both possibilities are studied in current section.

Firstly, the profiles of $\langle u'u' \rangle$ and $\langle v'v' \rangle$ at 5 corrugations (black lines in Fig. F.1) are compared. The selected corrugation are C2, C5, C8, C11 and C14.

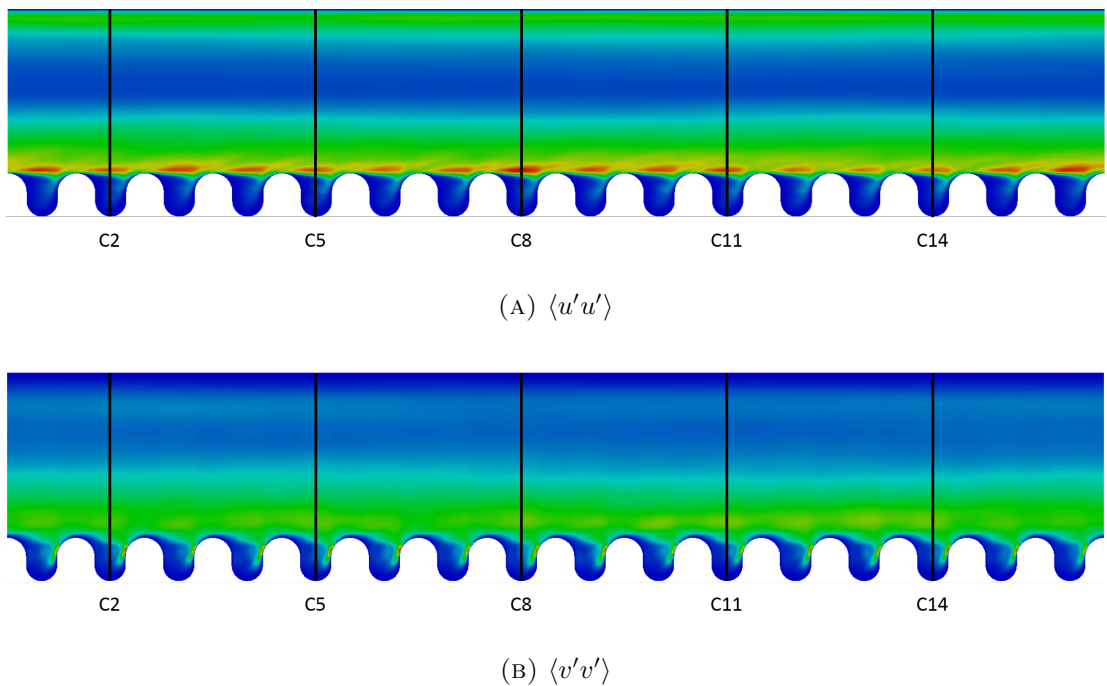


FIGURE F.1. The location of data sampling lines.

The comparison between $\langle u'u' \rangle$ of the selected sampling lines is presented in Fig. F.2. The result confirms the visual observation in Fig. F.1a that the profile of $\langle u'u' \rangle$ varies across different corrugations. Although they generally follow the same shape, large discrepancies are appeared at around $y/h = 0.071$, 0.363 , 1 and 3.58 , and the difference between the max and min value at these locations are 16.6% , 42.9% (not shown explicitly in Fig. F.1a), 17.6% and 7.4% , respectively. Nevertheless, the locations of $\langle u'u' \rangle_{max}$ are same for each corrugation, which are $y/h = 0.071$ for the corrugated wall and $y/h = 3.576$ for the top wall. The values for 128 corrugations case are the same.

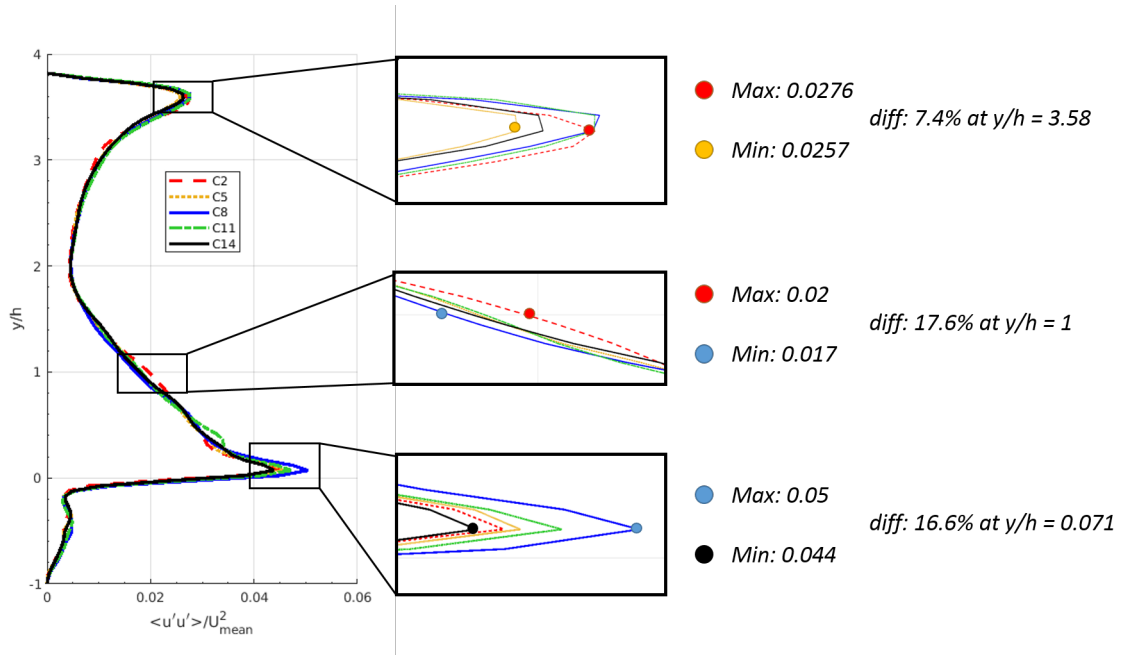


FIGURE F.2. Comparison between $\langle u'u' \rangle$ of the selected corrugations for SMAG+VD.

Fig. F.3 depicts the comparison between $\langle v'v' \rangle$ of the selected corrugations. The shape of profile at each corrugation largely agrees with each other. However, discrepancies can be found at around $y/h = 0.36$, 1.68 and 3 , the difference between the max and min value at these locations are 9.8% , 14.5% and 14.3% , respectively. Also, similar to the profile of $\langle u'u' \rangle$, the locations of $\langle v'v' \rangle_{max}$ are same for all corrugation, which are $y/h = 0.363$ for the corrugated wall and $y/h = 3.04$ for the top wall. These values for the 128 corrugations case are the same.

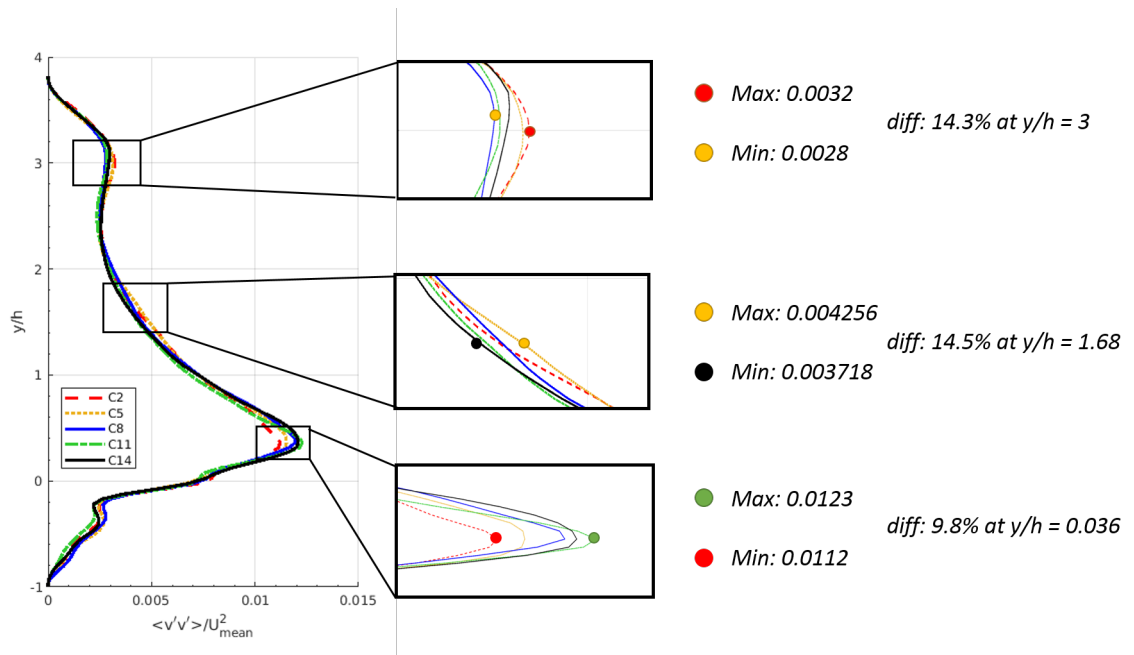


FIGURE F.3. Comparison between $\langle v'v' \rangle$ of the selected corrugations for KEQ+VD.

As shown in Section 6.2, the above discrepancies are not caused by inadequacy of the time-averaging window. It is therefore concluded that the discrepancies of the high turbulent intensity region between each corrugation are caused by the nature of this type of flow. The comparison between the Reynolds stresses obtained by difference cases will be based on the spatial-averaging values.